Theses and Dissertations

December 2012

Lithium-Ion Ultracapacitor Energy Storage Integrated with a Variable Speed Wind Turbine for Improved Power Conversion Control

Goran Mandic
University of Wisconsin-Milwaukee

LITHIUM-ION ULTRACAPACITOR ENERGY STORAGE INTEGRATED WITH A

VARIABLE SPEED WIND TURBINE FOR IMPROVED

POWER CONVERSION CONTROL

By

Goran Mandic

A Dissertation Submitted in

Partial Fulfillment of the

Requirements for the Degree of

Doctor of Philosophy

in Engineering

at

The University of Wisconsin-Milwaukee

December 2012

ABSTRACT
LITHIUM-ION ULTRACAPACITOR ENERGY STORAGE INTEGRATED WITH A
VARIABLE SPEED WIND TURBINE FOR IMPROVED
POWER CONVERSION CONTROL

By

Goran Mandic

The University of Wisconsin-Milwaukee, 2012
Under the Supervision of Professor Dr. Adel Nasiri

The energy of wind has been increasingly used for electric power generation worldwide
due to its availability and ecologically sustainability. Utilization of wind energy in
modern power systems creates many technical and economical challenges that need to be
addressed for successful large scale wind energy integration. Variations in wind velocity
result in variations of output power produced by wind turbines. Variable power output
becomes a challenge as the amount of output power of the wind turbines integrated into
power systems increases. Large power variations cause voltage and frequency deviations
from nominal values that may lead to activation of relay protective equipment, which
may result in disconnection of the wind turbines from the grid. Particularly community
wind power systems, where only one or a few wind turbines supply loads through a weak
grid such as distribution network, are sensitive to supply disturbances.

While a majority of power produced in modern power systems comes from
synchronous generators that have large inertias and whose control systems can
compensate for slow power variations in the system, faster power variations at the scale

of fraction of a second to the tens of seconds can seriously reduce reliability of power system operation. Energy storage integrated with wind turbines can address this challenge. In this dissertation, lithium-ion ultracapacitors are investigated as a potential solution for filtering power variations at the scale of tens of seconds.

Another class of issues related to utilization of wind energy is related to economical operation of wind energy conversion systems. Wind speed variations create large mechanical loads on wind turbine components, which lead to their early failures. One of the most critical components of a wind turbine is a gearbox that mechanically couples turbine rotor and generator. Gearboxes are exposed to large mechanical load variations which lead to their early failures and increased cost of wind turbine operation and maintenance. This dissertation proposes a new critical load reduction strategy that removes mechanical load components that are the most dangerous in terms of harmful effect they have on a gearbox, resulting in more reliable operation of a wind turbine.

Dedicated to my son

Stefan Mandić

TABLE OF CONTENTS

LIST OF FIGURES

LIST OF ABBREVIATIONS

WPP – Wind Power Plant

AGC – Automatic Generator Controller

PCC – Point of Common Coupling

STATCOM – Static Synchronous Compensator

DC – Direct Current

AC – Alternating Current

LVRT – Low Voltage Ride Through

ANN – Artificial Neural Network

SMES – Superconducting Magnetic Energy Storage

CAES – Compressed Air Energy Storage

ESS – Energy Storage System

POI – Point of Interconnection

CSI – Current Source Inverter

EDLC – Electrolytic Double Layer Capacitor

LIC – Lithium Ion Capacitor

PMSG – Permanent Magnet Synchronous Generator

LSS – Low Speed Shaft

HSS – High Speed Shaft

MPPT – Maximum Power Point Tracking

LPF – Low-Pass Filter

PLL – Phase Locked Loop

SVPWM – Space-Vector Pulse Width Modulation

RMS – Root Mean Square

RRO – Regional Reliability Organization

NREL – National Renewable Energy Laboratory

ACKNOWLEDGEMENTS

1. Introduction and literature review

Wind is a clean and inexhaustible source of energy that has been increasingly utilized worldwide. Global increase in energy demand, coupled with concerns about effects of pollution and CO_2 emissions associated with use of fossil fuels, are among the major driving forces behind recent exponential growth of global wind power installation. Several countries have already set goals on percentage of total electrical power production to be from wind power plants (WPP). One example is the United States, where the goal is to reach 20% of the total electric power production to be from WPPs by 2030. Despite advantages of wind energy, the technical challenges to integrate large amount of wind energy are many. Variations in wind speed are the source for many technical issues that have to be addressed in order to make utilization of this source of energy technically and economically reliable. Problems associated with variability of wind speed can be divided into two main categories: electrical and mechanical. The problems from the electrical category are related to electrical power fluctuations that are correlated to fluctuations in wind speed. In the case of large scale wind energy integration, power fluctuations can cause frequency and voltage deviations. Also, uncertain nature of wind results in difficulties in power system operation planning, optimal scheduling, and unit commitment. Frequency and voltage variations can also be significant in cases when wind turbines are connected to a weak grid or in the distributed power generation systems when wind power supplies local loads at the distribution level. Due to all these problems associated with grid integration of wind energy, utility companies are developing technical requirements that have to be met in order to connect wind turbines into a grid. The major technical requirements are defined by the standard

IEEE1547-2004 and the FERC Oder No. 661A that describe requirements that any grid connected power source has to satisfy. Also, additional requirements are set by various utility companies and regional reliability organizations (RRO).

1.1. Problems associated with wind speed variations

Frequency deviations can cause protective relay equipment to trip which may have severe impact on power system stability and may lead to power outages [1]-[3]. In [1], impact of power variations caused by WPPs in power system consisting of several thermal power plants is analyzed. The authors analyze filtering capabilities of governor control and automatic generator control systems to filter power fluctuations. The spectrum of power output of the wind turbine can be divided in three regions, where slow power variations can be compensated by automatic generator control (AGC), fast power variations by governor control system, while filtering medium frequency power fluctuations in range of 0.01Hz-0.1Hz remains poor, thus limiting the maximum wind power penetration without causing significant frequency deviations. The governor systems of large synchronous generators are responsible for frequency control of a power system. Power variations cause increased wear on governor systems of generators in conventional power plants in power systems with large wind power penetration [2]. The power filtering capability of thermal power plants, however, is limited. In [2], based on detailed model of small power system consisting of thermal power plant and wind farms the authors show that maximum allowed frequency deviation of 1% from the nominal value limits the peak power fluctuation from WPPs to 5% of total rated power of thermal power plants. This means significant limit on maximum wind power penetration in a

power system without limiting power variations by using energy storage. Reliability analysis of power system with wind turbines given in [4] shows that at lower wind speeds, when power variations are significant relative to the total power output of a wind turbine, power system reliability decreases. The authors conclude that energy storage can increase power system reliability during low wind speed condition. Effects of turbulence level and control method of a wind turbine are analyzed in [5]. In [6], the authors analyze various methods for output power smoothing that do not require energy storage. Power injected to the grid by a wind turbine can be controlled directly, including the constant output power regime. However, rotational speed depends on the power loading of the generator, as well as on the wind speed. Therefore, constant output power control is very sensitive to wind speed variations, as they may lead to reaching of upper or lower rotational speed limits. The authors propose the second output power control method where the power reference is a linear function of wind speed. Although this method reduces power fluctuations, it reduces the efficiency of power conversion from the wind flow, since the wind turbine does not operate in at the maximum power point. As shown in [6], maximum power point tracking results in increased power variations. In order to operate a wind turbine at maximum efficiency, while reducing output power fluctuations, various energy storage systems have been proposed as an addition to the wind turbine power conversion system. A WPP output power control by using AGC can result in reduced power variations by providing output power setpoints to each wind turbine in a WPP [7]. This method takes into account power smoothing effect by aggregating power outputs at the point of common interconnection (POI) of the WPP. Set points are computed based on total power demand from the WPP. The method proposed in [8]

combines blade pitch control and primary speed control of the generator to reduce power fluctuations that result in frequency deviations. Method presented in reference [9] is based on prediction of wind speed to optimize output power setpoint that would result in reduced frequency deviations.

All methods that do not require additional energy storage have advantage of not requiring installation of additional hardware. Only modification in control algorithm can increase the level of installed wind power within a power system. However, they cannot operate at the optimal power extraction points resulting in reduced efficiency of wind to electrical power conversion.

1.2. Energy storage for wind applications

Energy storage absorbs energy that cannot be supplied to the grid, for various reasons such as potential frequency deviations that they can cause, limited power transmission capacity of the line connecting the WPP to the power system, disturbances in the power system such as short circuit or ground faults, or imposed limits from power system operation and dispatching control, such as power ramp rate limit or power shifting when a wind turbine has to provide power even if there is not enough wind. Figure 1.1 illustrates energy storage applications based on power and energy density in a power system.
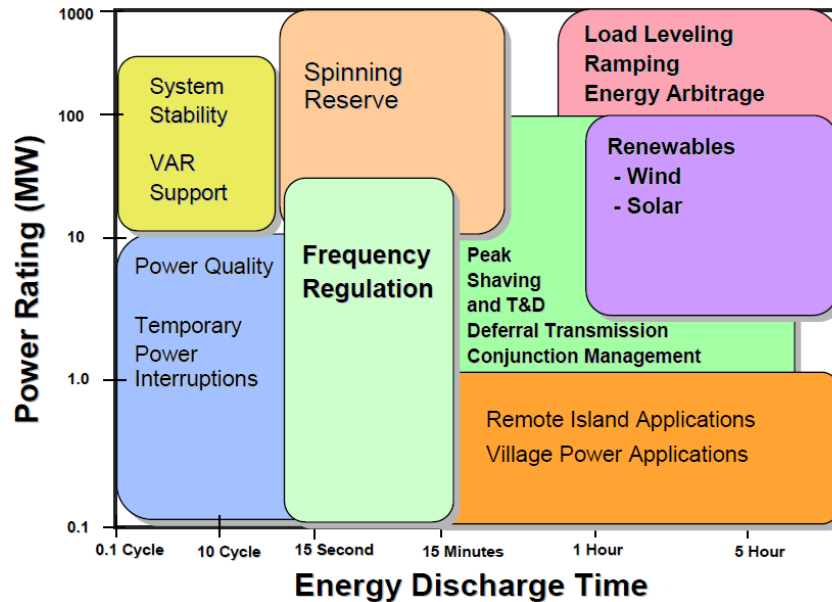
Figure 1.1. Energy storage applications in a power system [11]

Reference [12] gives an overview of various energy storage systems and their use with renewable energy sources. Benefits of using energy storage in a real WPP are discussed in [13] and [14]. In [13], the authors analyze increase of power system reliability and system efficiency by using energy storage. The energy storage in [14] is used to store energy during the peak power production. It can be used later when power production is low due to reduced wind speed. As a result, the wind turbine with storage increases the power system availability. The principle of storing energy in order to be used later is called power shifting. Reduction in the peak power delivered to the grid results in reduction in the reactive power demand by the induction generators used in the wind turbines. A battery bank connected through a bidirectional AC/DC converter to the POI of a WPP and associated control system is proposed in [15]. This configuration of AD/DC converter and energy storage in DC link is called static synchronous compensator (STATCOM) and is often used to compensate reactive power. However, large energy storage on the DC side of STATCOM can be used as an energy buffer as well. In [15],

the authors propose control method of the energy storage that optimizes usage of the storage capacity under constraints such as limits on charge and discharge rates and upper and lower limits on state of charge. Another configuration based on battery bank and STATCOM connected at the terminals of a wind turbine is proposed in [16]. The energy storage improves transient stability of a wind turbine during low voltage disturbances in the power network, by providing reactive power to maintain voltage at the connecting bus, while absorbing active power from the wind turbine, enabling low voltage ride-through capability (LVRT) of a wind turbine. Energy storage based on a zinc-bromine flow battery for wind energy integration is proposed in [17]. Control system, based on artificial neural network (ANN) manages energy storage increasing predictability of the power production by the wind turbine. Increased predictability of the power production increases reliability of the power system operation and ease unit commitment and dispatch planning of the power system operation. Another method for improved stability of the WPPs and reduction of power variations by using batteries is reported in [18]. A method for optimal schedule control of a large battery energy storage based on particle swarm optimization is proposed in [19]. The optimization algorithm improves reliability of the power output of the WPP while minimizing the cost of the system operation.

Superconducting magnetic energy storage (SMES) as a solution for wind turbine storage system is proposed in [20]. The authors propose installing the SMES in a WPP comprised of variable speed wind turbines with generator side AC/DC converters share the same DC link. The SMES is installed in the DC link before the common inverter connected to the grid. Energy is stored in magnetic field of the SMES providing the buffer for output power smoothing. The proposed system can cancel up to 80% of rated

power fluctuation within one minute interval. A hybrid system comprised of a SMES and battery is proposed in [21]. Higher energy density of the battery provides compensation capability for slow power fluctuations, while high power density of the SMES enables compensation of higher frequency power fluctuations. The advantage of this solution is reduced size of SMES resulting in lower cost. Analysis based on detailed modeling and simulations of benefits of using SMES in large WPPs is given in [22]. Another application of SMES for increased stability of a wind turbine connected to the grid is proposed in [23]. Despite high efficiency and high power density of SMES systems, the cost of such systems still limits their practical applicability. Kinetic energy of a flywheel as an energy storage for wind turbines has been investigated by many researchers. In [24], a flywheel driven by induction machine connected to the DC link of a full rated power conversion system of a variable speed wind turbine is used as an energy buffer for power fluctuations that are not to be injected to the grid. The flywheel control system can keep DC link voltage constant, or filter output power by using fuzzy control based control system. Another application of flywheel for wind power integration is proposed in [25]. Flywheel connected through the DC/AC converter to the DC link of the power conversion system of a wind turbine improves stability of the turbine against sudden changes in power production or power demand as well as disturbances in the power grid. A fuel cell as a supplement to the inertia of a wind turbine for frequency control of a wind turbine is proposed in [26]. The fuel cell is controlled as virtual inertia added to the inertia of the rotor for frequency control. Hydrogen for the fuel cell has to be obtained from natural gas on other means unrelated to electrical power generation, which is the major drawback of the proposed method. Hydrogen for fuel cell can be provided as a

product of electrolysis. In [27], a method for reducing long term wind power variations is proposed. When power produced by a wind turbine is above the power level required by load, excessive power is used in the electrolyzer that produces hydrogen. Stored hydrogen is later used in a fuel cell to produce electric power when load demand exceeds power produced by wind turbine. A research on use electrolytic hydrogen as a storage at the power system level is reported in [28]. The amount of power stored as hydrogen, or converted back to electric power by the fuel cell is determined by the day-ahead forecasting and optimization of the cost of operation of the power system. In both cases, energy storage is used as a mean of increased predictability of a wind power sources and, therefore, easier power system operation planning in systems with larger level of wind power penetration. One of the methods to store energy in power system is in the form of potential energy of compressed air. In [29], the operation of a power system with large scale wind energy integration and large compressed air energy storage (CAES) is analyzed. All methods that deal with very low frequency power variations, called long term power variations, require large energy density storage systems. On the other hand, methods that deal with higher frequencies, called short term power variations, typically require larger power density as large amounts of power have to be stored or released in short time intervals. In the research reported in this thesis, ultracapacitors are used as high power density energy storage. Ultracapacitors as energy storage for wind power applications have been proposed by several researchers. In [31] a variable speed doubly-fed induction generator is equipped with ultracapacitor energy storage system (ESS) connected to the DC link of the rotor back to back power conversion circuit. The ultracapacitor module is connected to the DC link through the buck/boost DC/DC

converter. The ultracapacitor ESS is sized according to the LVRT requirement and maximum DC voltage of the ultracapacitor module. The ESS management system is a fuzzy rule based controller that operates the ESS in order to minimize output power variations and to satisfy the LVRT requirements. The controller uses prediction algorithm and state of charge of the ultracapacitor module to calculate the reference for the output power that will be supplied to the grid. The systems shows good performance when prediction of the wind power is accurate. However, the method shows great sensitivity to the accuracy of the prediction algorithm. Also, the membership functions of fuzzy sets that describe voltage and state of charge of the ultracapacitor module have to be tuned by trial and error procedure until desired performance is obtained. Another method of ultracapacitor storage integration into WECS is proposed in [32]. The authors propose adding an ultracapacitor module is connected through a DC/DC converter and a current source inverter (CSI) to the AC terminals of an induction generator based wind turbine. The ultracapacitor storage system is used to smooth power fluctuations from the wind turbine by injecting or absorbing higher frequency power fluctuations. A low pass filter is used to calculate the reference for the current controller of the CSI. Also, the energy storage system with associated power conversion circuit controls reactive power at the AC terminals of the wind turbine. ELDC ultracapacitors are chosen for the storage module. Similar configuration is proposed in [33], with voltage source inverter instead of CSI. Power smoothing is achieved by injecting or absorbing the difference between power from the wind turbine, and the same power after low-pass filtering. Even though these methods effectively reduce power fluctuations in the range of several seconds (1-10s), the main disadvantage of these methods is the need of use two additional

conversion stages – DC/DC in addition to DC/AC converter. The power losses on these converter stages considerably reduce efficiency. Also, control system is more complex and therefore, less reliable. Another method for output power smoothing using ultracapacitor energy storage is described in [34]. The authors propose a system that comprises the ultracapacitor module as a short term, and a battery for long term energy storage. The ultracapacitor module is connected to the DC link of a permanent magnet synchronous generator (PMSG) based wind turbine through bidirectional DC/DC converter. The battery is connected to the DC link through the second DC/DC link converter. Power smoothing is achieved by using two high pass filters with different cut-off frequencies. The high-pass filter with lower cut-off frequency computes the amount of power that will be stored or supplied by the energy storage as a whole; the battery with the ultracapacitor module. The amount of power to be stored or supplied by the ultracapacitor module is calculated by the high-pass filter with higher cut-off frequency. The difference between this power and total power demand for the energy storage is stored or released from the battery. This system offers more power smoothing capacity due to the battery. Another system that also uses bidirectional DC/DC converter in the DC link of the PMSG based wind turbine and ultracapacitor energy storage is described in [35]. Power reference for the grid side converter is a moving average of the power coming from the generator. Main disadvantage of both of these solutions is that they require additional DC/DC converter. An alternative that does not need a DC/DC converter is proposed in [36]. The ultracapacitor energy storage module is connected directly to the DC link of a double conversion circuit of a DFIG based wind turbine. The control of the grid side converter adjusts total output power of the generator according to

the moving average over the period of sixty seconds of the mechanical power on the generator's shaft. This method reduces power variations as long as the DC link voltage is within the upper and lower limits. If DC link voltage reaches limit, the moving average output power smoothing is bypassed, and output power is equal the generated power, as if there is no energy storage buffer. If the moving average reference becomes less then generated power, and DC link voltage is on its lower limit, it means that there is enough storage reserve to absorb the difference in power. The same holds when moving average power reference is greater than the generated power and DC link voltage is at its upper limit. There is enough energy stored in the ultracapacitor module that can cover the difference, while DC link voltage reduces. In both cases, the moving average power smoothing is restored. A method that addresses reducing power fluctuations at a WPP level is proposed in [37]. The method is similar to methods from [33] and [34] since it also utilizes ultracapacitor module connected through the DC/DC converter and three phase inverter/rectifier to absorb or deliver power in order to reduce power fluctuations. However, due to spatial distribution of wind turbines resulting in smoothing effect of the total power produced by the WPP at the point of common interconnection (POI), the authors claim that it is more optimal solution to place large centralized energy storage at the POI. Localized ultracapacitor storage may unnecessarily remove power fluctuations that would be compensated by power fluctuations from other wind turbines, resulting in reduced effective energy capacity of the ultracapacitor storage that contributes to the total reduction of the power variations at the POI. Centralized energy storage reduces power fluctuations measured at POI, and it also can be used to POI voltage as well by controlling reactive power flow. The power smoothing algorithm in [37] utilizes a high-

pass filter to determine power flow through the ultracapacitor bank resulting in low-pass filtered total output power of the WPP. Even though this method addresses the problem of suboptimal usage of localized storage capacity, the major point in favor for using decentralized energy storage systems at each wind turbine is increased reliability. If there is a failure at the energy storage system of one wind turbine, other storage modules still provide power smoothing capabilities for the entire WPP. Control strategy for power smoothing at the POI level, by using localized ultracapacitor storage systems at each wind turbine, is proposed in [38]. At the wind turbine level, the ultracapacitor energy storage is installed at the DC link, through the buck/boost DC/DC converter, of the rotor double conversion circuit of the DFIG generator. Centralized controller computes power reference for the DC/DC controllers for each wind turbine. Result is large power smoothing effect on the entire WPP. Power fluctuations that are compensated by aggregating effect of distribution of wind turbines are not measurable by the centralized controller at the POI level. Therefore, central controller does not try to compensate these fluctuations, resulting in increased capacity for reducing power fluctuations that can be observed at POI. The power smoothing algorithm of the centralized controller keeps the output power constant. In this thesis, a novel method for output power smoothing of a wind turbine is proposed. The ultracapacitor bank is used as energy storage due to large power density that ultracapacitors provide. The set point for the output power is based on filtrated signal of the input power from the generator. However, unlike other power smoothing methods reported in literature, no additional DC/DC converter is used due to direct connection of the ultracapacitor bank to the DC link of the wind turbine power conversion system. Also, low pass filter used to calculate set point of the output power is

adaptive, with cut-off frequency related to the state of charge of the energy storage. Additional mean of the DC link voltage optimization is introduced to addresses issues with existing methods in cases when there is no enough energy capacity in the ultracapacitor storage resulting in DC link voltage reaching upper or lower limits for safely operation. The proposed method has been evaluated by excessive simulations under various wind profiles, and experimental verification in the laboratory.

1.3. Wind turbine gearbox

The mechanical issues caused by variable wind speed are mainly result of increased stress on individual components of a wind turbine, such as tower, blades, and drivetrain. Mechanical failures are responsible for more than 50% of down time of a wind turbine [41]. Also, repair or replacement of mechanical part of wind turbine is very costly and time consuming. Long down times, as periods when turbines do not produce energy, increase return of investment periods. One of the major mechanical related issues in modern wind turbines is premature failures of gearboxes. Gearbox is a mechanical component of the turbine that adapts torque and rotational speed demand from the generator to the torque and speed characteristics of the rotor. High gear ratio is achieved by using multiple gear stages that form complete gearbox. With the use of a gearbox, the rotational speed of the wind turbines main shaft (low speed shaft-LSS) can be increased significantly, allowing the use of a high rotational speed generator. Gearbox related failures are also responsible for over 20% of downtime of the wind turbines [41]. Despite 20 years of expected lifetime for gearboxes, they usually need replacement after only 6 to

8 years [41]. All of these factors significantly contribute to operational and maintenance costs. In the past fifteen years, significant improvements have been made on the control algorithms for wind turbine generators. Early turbine developments focused on the optimization of energy harvesting and grid compliance. More recently, the direct drive wind turbine generator concept has been pursued by several turbine manufacturers. With direct drive, the generator is connected directly to the low speed shaft. The blades drive the generator directly, dispensing the need for a gearbox. As the size of the wind turbines increases, the blade length is also increased but the rotational speed must be limited due to blade tip noise. As a consequence of low rotational speed requirement for direct drive wind turbines, the generators have larger dimensions and heavier weights. Thus, the tower structure to support the generators must be reinforced to carry the weight and to withstand additional aerodynamic loads. As power level of wind turbines increases, the direct drive concept becomes impractical, making the use of gearboxes necessary again [45]. Both direct drive and gearbox based drivetrain and mechanical coupling between the generator shaft and the turbine rotor are flexible. Mechanical torque acting on the drivetrain causes torsional deformations thus resulting in mechanical stress. Torsional vibrations are the results of torsional deformation and they are measures of mechanical stress.

The torsional vibration damping in high performance electric drives has been investigated by many researchers [47-50], [52], [54], [58], [64], [65], [66]. Flexible coupling between an electric motor and mechanical load is a source of vibration modes that can significantly degrade performance of the system. Methods for vibration damping

in electric drive systems are based on motor torque control that avoids excitation of resonant modes, or compensates for vibrations caused by load.

Methods for torsional vibration damping in wind turbine drivetrains are reported in several papers. In [46] the problem of active damping of tower and drivetrain resonant vibrations is addressed. The method for drivetrain resonant vibration is based on generator torque control in such a way that provides active vibration damping of a dominant resonant mode. In [53] the indirect torque control method for fixed-speed wind turbine with a static synchronous compensator (STATCOM) is proposed. In this method, the generator torque control is achieved by controlling reactive current in a way that smoothes transient torque during grid fault recovery. A method for active torsional vibration damping for variable speed wind turbines with full rated power conversion is proposed in [55]. In this method, torsional vibrations are compensated by using speed feedback loop that compensates generator speed variations. The compensation torque component is proportional to the speed deviation. Another torsional vibration damping control strategy is proposed in [61] where the authors analyze effects of pitch angle to the drivetrain dynamics. Active damping strategy is based on introducing compensation torque that is calculated from the rotational speed information. All these methods are focused on reduction of vibrations at the lowest resonant frequency since the drivetrain dynamics is represented by dual-mass spring damper system.

In this thesis, a novel generator torque control strategy that reduces mechanical stress in the gearbox of a variable speed wind turbine is proposed. This control strategy reduces torsional vibrations by modulating generator torque so that it increases the damping of several resonant modes, not only the dominant one. The control strategy has band pass

filter properties thus avoiding interference with the generator speed controller that operates wind turbine at the maximum power point (MPPT). Proposed control strategy is verified by using computer simulations. Model of the gearbox used in simulations is of the higher order and it captures more details of the real gearbox dynamics than widely used two mass models. Simulation results show that appropriate control of the generator torque can reduce resonant vibrations, therefore increasing operational lifetime of the gearbox.

2. Wind energy conversion systems

Wind turbines convert mechanical energy of moving mass of air around properly shaped blades connected to the rotor into rotational movement that can be used to perform useful work. By coupling a rotating shaft of a wind turbine to an electric generator, mechanical energy of wind is converted into electric energy. However, this electric energy will depend on airflow. In order to study behavior of a wind turbine, detailed mathematical models can be very useful. This chapter is devoted to development of a detailed model in Matlab/Simulink software package. The developed model is very detailed and it includes the mechanical model of a three blade wind turbine, the drivetrain, the permanent magnet generator with interior mounted permanent magnets, the power conversion stage with grid connected inverter, and all control systems. The model captures complex dynamics of all subsystems and their interactions. Design of all control loops is also covered in this chapter. Model described here is further used in development of active vibration damping control, described in the chapter 3, and output power smoothing algorithm using the ultracapacitor energy storage, described in the chapter 4.

2.1. Modeling of a wind turbine

A wind turbine is a complex, flexible mechanical system whose dynamics can be described by a set of nonlinear differential equations that forms a mathematical model of a wind turbine. These differential equations describe laws of aerodynamics, mechanics, and mechanical elasticity. The order of the mathematical model depends on the level of

detail the model represents a real wind turbine. Multi-body models divide complex mechanical systems into smaller parts whose interactions are described by differential equations. More accurate models are built by dividing the mechanical system under consideration into smaller parts resulting in larger number of differential equations. The process of numerical solving of such system of differential equation on a computer is called simulation, and it is widely used in industry and research. There are many software packages that can simulate wind turbine models of various level of complexity. These software packages are called simulation codes. A good reference on various simulation codes and their comparison is [68]. One of simulation codes that offer medium level complexity with relatively easy integration with Matlab/Simulink is FAST (Fatigue, Aerodynamics, Structures, and Turbulence) wind turbine simulation code, developed at the National Renewable Energy Laboratory (NREL), that is used for the purpose of model development for the research reported in this dissertation.

2.1.1 Fatigue, Aerodynamics, Structures, and Turbulence (FAST) simulation code

The FAST is an aeroelastic simulation code that can simulate behavior of two and tree bladed horizontal axis wind turbines. FAST stands for Fatigue, Aerodynamics, Structures and Turbulence. The FAST simulation code uses medium-complexity multibody dynamic model of a wind turbine [68]. It has several modes of operation that can be divided into two groups. First group of modes of operation consists of simulation modes. In a simulation mode, FAST solves the system of nonlinear differential equations of motion and calculates trajectories of state variables. There are two simulation modes available to a user. The first one is standalone mode when FAST simulates wind turbine operation by

using torque and pitch control routines, either those available with FAST or written by the user and compiled with rest of the FAST code. This simulation mode is very fast, but it is the most complicated for use due to need of writing code that simulates behavior of torque and pitch controllers. Moreover, loading torque of a wind turbine depends on the type of the generator and its interface to the electrical grid. Detail model of the system can be very complex and it can be very time consuming for implementation in a code written by the user. Therefore, second mode of operation is provided. In the second mode, FAST simulator can be called from Matlab/Simulink model by means of S-function interface available in Simulink for calling external functions that are not part of standard Matlab installation. In this mode, the user has a full set of libraries and models available in Simulink to implement more detailed control functions as well as other parts of the wind turbine, such as generator, power conversion circuit and the grid interface. This mode of operation is mainly used in research presented in this thesis, with models of entire systems and control algorithms described in the latter chapters. Second group of operation modes of FAST belongs to the analysis group of modes. There are two operation modes in this group. One is the linearization mode, when FAST calculates linearized state space models of a wind turbine. A wind turbine is a highly nonlinear system. The wind turbine characteristics depend on the rotor position with linearization points that can be defined for various azimuth angles of the rotor. In this mode, the user can specify the number of linearization points over the full rotational angle of a wind turbine rotor. Final stage of operation in this mode is calculation of the azimuth averaged model that calculates the time invariant linear state space model of the wind turbine. This model can be used for advanced control designs by using modern control theory

techniques. Finally, the last mode of operation of FAST is ADAMS pre-processing. In this mode, FAST generates configuration data files of a wind turbine to be used in ADAMS software (Automatic Dynamic Analysis of Mechanical Systems) for more complex simulation of a wind turbine. By using ADAMS, it is possible to simulate very complex behavior of a wind turbine since ADAMS enables additional degrees of freedom that are not available in FAST. One example of the degree of freedom not available in FAST but available in ADAMS is blade torsion mode [68]. Integral part of FAST is AeroDyn, a set of subroutines that calculate aerodynamic forces resulting from wind flow around the turbine's blades [75]. Modes of operation of FAST are illustrated in figure 2.1.
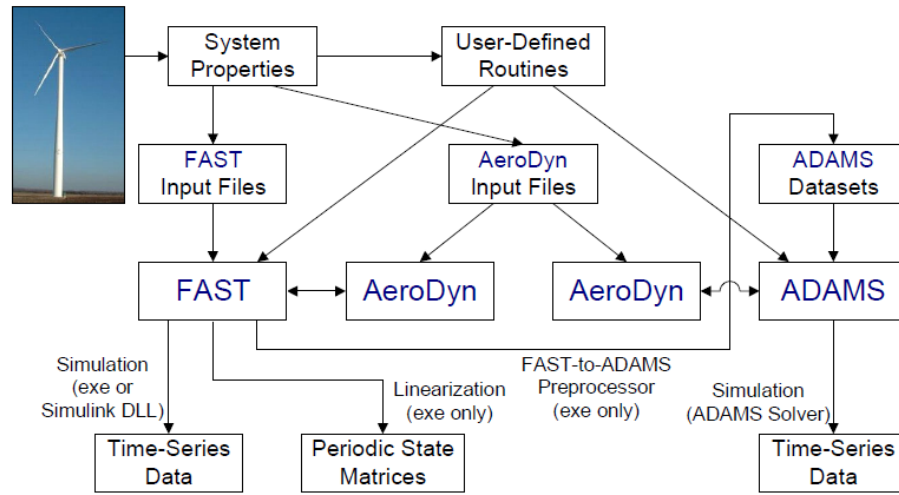
Figure 2.1. Modes of operation of FAST [62]

System of nonlinear aeroelastic differential equations that models a wind turbine, written in the matrix form is:

$$M(q,u,t) \cdot \ddot{q} + f(q,\dot{q},u,u_d,t) = \mathbf{0} \qquad (1)$$

M is the matrix of masses and moments of inertia

q is the state vector that contains displacements for each degree of freedom enabled in the model

$\dot{q}$ is the vector of the first derivatives of the state vector q

$\ddot{q}$ is the vector of the second derivatives of the state vector q

u is the control input vector

u_d is the disturbance input vector

Support platform has 6 degrees of freedom (DOF), divided into two groups. First group consists of translational DOFs: surge, sway, and heave). Second group contains rotational DOFs: rol, pitch, and yaw. The tower has 4 DOFs. The tower posses two bending modes. Each mode has longitudinal and transverse directions. Each blade has first and second flapwise bending modes. In addition, each blade has also the edgewise bending mode. Therefore, three bladed turbine has 9 blade bending DOFs. Flexible blades are modeled as linear systems. Mode shapes of a blade are needed for FAST to perform simulations. These shapes are contained in the input files specified in the BLADE sections of the main FAST input file. Mode shapes are approximate by sixth order polynomial, where zero and first coefficients are equal to zero, due to rigid connection to the bottom of the tower to the platform, which results in zero deflection and zero slope at the bottom. Coordinate system originates at the bottom of the tower. Flexible blades and tower are modeled using linear approximation, valid for small displacements. AeroDyn is a set of software routines that calculates the aerodynamic forces acting on the wind turbine blades and it uses the full field stochastic wind data. TurbSim is a program that can generate this data according to various stochastic models of wind [64]. AeroDyn can read single point wind files with wind speed data at the hub height. It can also read multiple-point wind files

generated by TurbSim. Input files for FAST and AeroDyn for the NREL 750kW test wind turbine are listed in the Appendix. In the following section, static characteristic of this wind turbine, obtained by using FAST, are presented.

2.1.2. Power characteristics of the 750kW wind turbine

Power produced by airflow around rotor blades of a wind turbine depends on wind speed and rotational speed [84].

$$P_a(v_w, \lambda) = \frac{1}{2} \cdot A \cdot C_p(\lambda, \beta) \cdot \rho \cdot v_w^3 \tag{2}$$

Power coefficient Cp depends on tip speed ratio and blade pitch angle. Figure 2.2 shows how Cp of the NREL 750kW test wind turbine depends on tip speed ratio.
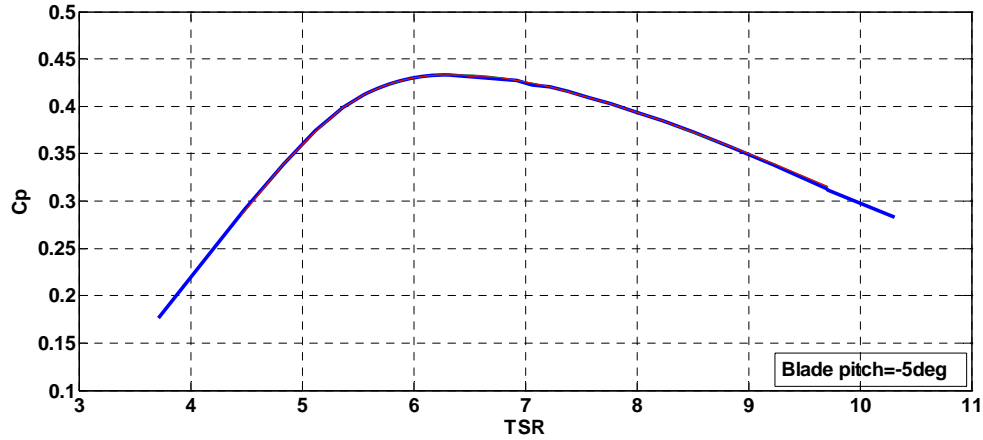
Figure 2.2. Power coefficient Cp as a function of tip speed ratio

The peak of the Cp curve is the maximum efficiency point of wind to mechanical power conversion process. Figure 2.3 shows dependence of the power coefficient on blade pitch angle.
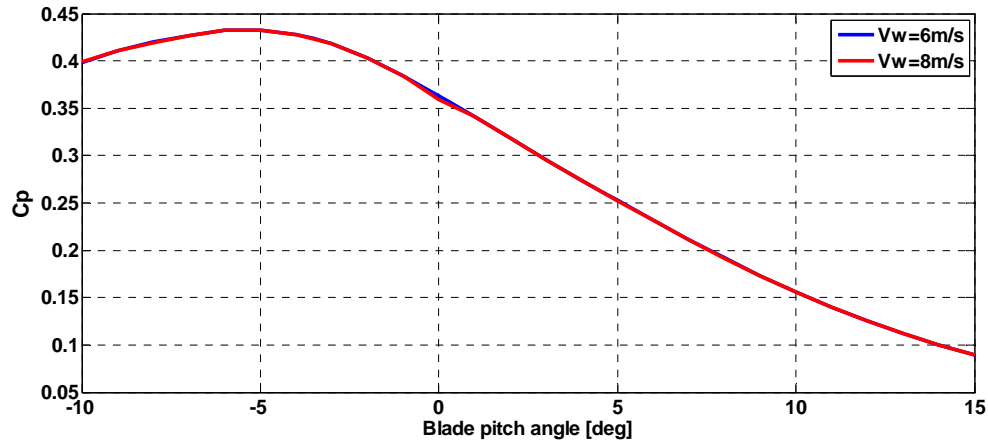
Figure 2.3. Power coefficient Cp as a function on the blade pitch angle

The goal of the control system of a wind turbine is to maximize this coefficient by keeping the tip speed ratio constant, and at the value that maximizes Cp. Torque characteristics of the NREL 750kW test wind turbine obtained by simulations using FAST are shown in figure 2.4. Torque curves, as functions of rotational speed, are different for various wind velocities.
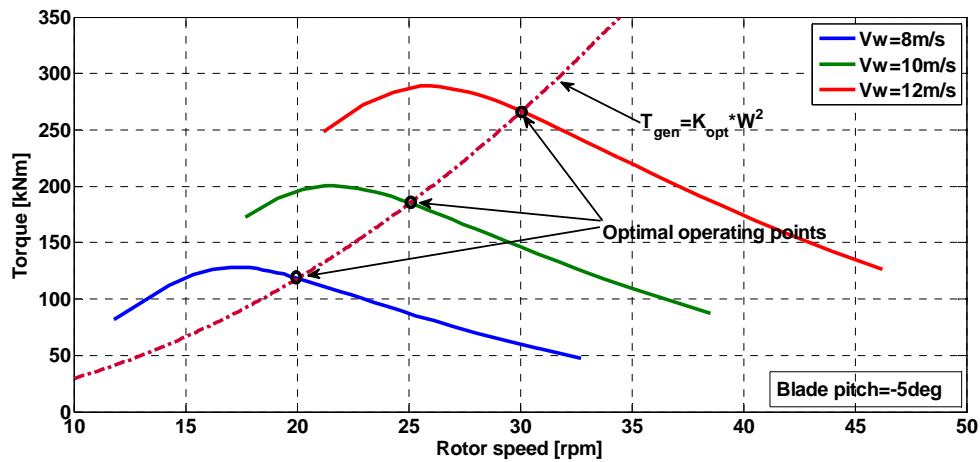
Figure 2.4. Torque characteristics of the NREL 750kW wind turbine

operated in variable speed mode for various wind velocities

Rotational speed of a wind turbine is constant when aerodynamic torque created by the wind flow is balanced by the electromechanical torque on the generator shaft, which can

be coupled to the main rotor of the wind turbine directly or through a gearbox. For stable operation, the slope of the generator torque characteristic has to be larger than the slope of the aerodynamic torque of the wind turbine. This condition can be written as:

$$\frac{dT_{gen}}{d\Omega} > \frac{dT_{aero}}{d\Omega} \tag{3}$$

In order to maintain a stable operation it is necessary that the generator torque characteristic satisfies the condition (3). In variable speed wind turbines, there is always power electronics converter that can control generator torque and by controlling the generator torque, rotational speed of the wind turbine is controlled. The main goal of the generator speed controller is to keep the wind turbine speed at the optimal point, where the power production is maximized, while satisfying the condition (3) for stable operation. One solution widely accepted in industry is to adopt a static torque characteristic that is a quadratic function of the rotational speed:

$$T_{gen} = K \cdot \Omega^2 \tag{4}$$

The slope of this function is:

$$\frac{dT_{gen}}{d\Omega} = 2 \cdot K \cdot \Omega \tag{5}$$

The function (5) is always positive, since direction of wind turbine rotation is always the same and assuming that the coefficient K is positive. By tuning the coefficient K, various operating points can be selected. In order to maximize power production of the wind turbine, it is desirable to choose torque characteristics that will result in the operating points that will maximize output power at every wind speed. Starting from the aerodynamic power equations for wind turbines:

$$P_a(v_w, \lambda) = \frac{1}{2} \cdot A \cdot C_p(\lambda, \beta) \cdot \rho \cdot v_w^3 \qquad (6)$$

The torque equation can be derived as:

$$T_a(v_w, \lambda) = \frac{P_a}{\omega} = \frac{1}{2} \cdot A \cdot C_p(\lambda, \beta) \cdot \rho \cdot v_w^3 \cdot \frac{1}{\omega} \qquad (7)$$

It follows that:

$$T_a(\omega, \lambda) = \frac{1}{2} \cdot \pi \cdot R^2 \cdot C_p(\lambda, \beta) \cdot \rho \cdot \frac{R^3 \cdot \omega^3}{\lambda^3} \cdot \frac{1}{\omega} \qquad (8)$$

$$T_a(\omega, \lambda) = \frac{1}{2} \cdot \pi \cdot R^5 \cdot C_p(\lambda, \beta) \cdot \rho \cdot \frac{1}{\lambda^3} \cdot \omega^2 \qquad (9)$$

For the optimal operation, the last equation can be rewritten as:

$$T_{gen\_opt} = K_{opt} \cdot \Omega^2 \qquad (10)$$

From where it follows:

$$K_{opt} = \frac{1}{2} \cdot \pi \cdot R^5 \cdot C_{p\max} \cdot \rho \cdot \frac{1}{\lambda_{opt}^3} \qquad (11)$$

From the characteristics of the NREL 750kW turbine, the optimal generator torque coefficient is:

$$K_{opt} = \frac{1}{2} \cdot \pi \cdot R^5 \cdot C_{p\max} \cdot \rho \cdot \frac{1}{\lambda_{opt}^3} = 26888.94 \left[\frac{Nm}{(rad/s)^2} \right] \qquad (12)$$

If the generator is coupled to the main shaft through a gearbox, the coefficient K should be divided by the gear ratio of the gearbox:

$$K_{opt\_gen} = \frac{K_{opt}}{n_{gearbox}} \qquad (13)$$
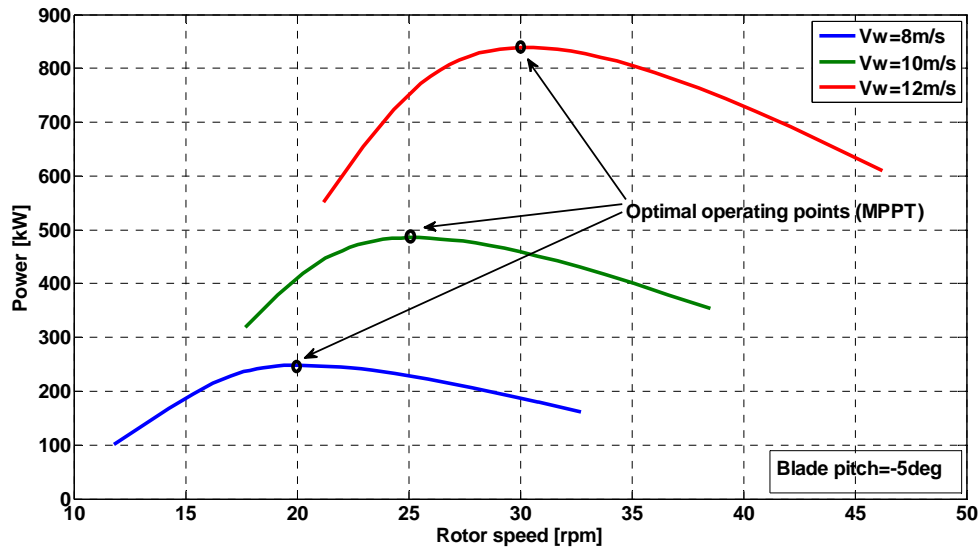
Figure 2.5. Power characteristics of the NREL 750kW wind turbine

for various wind velocities operated in variable speed mode

Power characteristics of the 750kW wind turbine for various wind speeds are shown in figure 2.5, as the wind turbine is operated in variable speed mode. The electromechanical torque of the generator should be varied with variations in wind speed in such a way that ensures convergence of rotational speed to values that result in the peak power for particular wind speed. Quadratic torque speed characteristic (10) with optimally selected coefficient K (13) guarantees this convergence in steady state.

Stochastic nature of the wind speed variations may result in suboptimal power extraction when wind speed changes rapidly, not allowing rotational speed of the turbine to converge towards the optimal power points. To overcome this issue, various maximum power point tracking algorithms have been proposed [72],[73],[74]. For the purpose of the research reported in this thesis, quadratic generator torque characteristic is chosen, as it is the case in majority implementations in industry.

The shaft of the wind turbine is mechanically coupled to the generator. Generators have their own specifications on power rating and maximum rotational speed. In order to match characteristics of wind turbine to the characteristics of the generator, torque speed characteristic cannot follow the equation (10) for all operational range of wind speeds. When rotational speed of the generator reaches its maximum speed, further increase of rotational speed should not be allowed. To keep rotational speed constant for higher wind speeds, blade pitch angle should be adjusted by the blade pitch controller which then keeps rotational speed constant by varying the blade pitch angle with variations in wind speed. Electromechanical torque of the generator is at its maximum, and rated electrical power is delivered to the power grid. This mode of operation is called region 3 operation. Before the generator reaches the maximum rotational speed allowed, it first reaches its rated speed. At rated speed, voltage on the generator's terminal is equal to the rated voltage of the generator. Further increase of the voltage is not allowed, and filed weakening technique of the generator magnetic field has to be applied. The region of rotational speeds from the speed when field weakening begins to the speed when turbine operates in the region 3 is called the region 2 ½. This region has linear torque speed characteristic for smooth transition between regions 2 and 3. In region 2, torque speed characteristic follows the equation (10). Complete torque speed characteristics of the 750kW wind turbine is shown in figure 2.6.
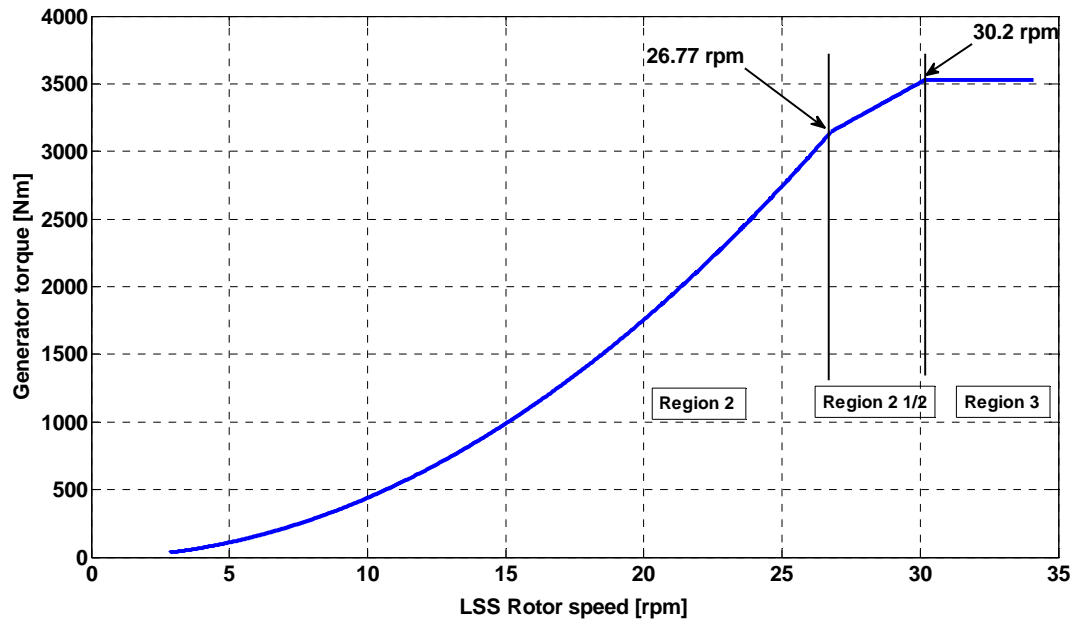
Figure 2.6. Torque-speed characteristic of the 750kW wind turbine

The power-wind speed characteristic of the 750kW wind turbine with the torque speed characteristic from figure 2.6 is shown in figure 2.7.
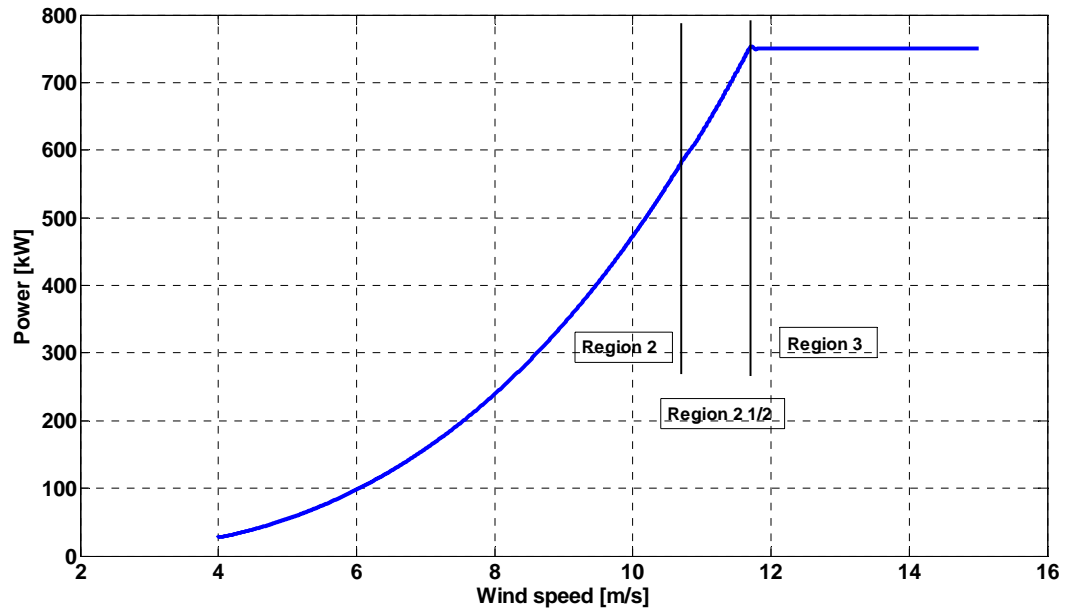
Figure 2.7. Power characteristic of the 750kW wind turbine

Simulink implementation of the torque reference generator according to the torque speed characteristic from figure 2.6 is shown in figure 2.8.
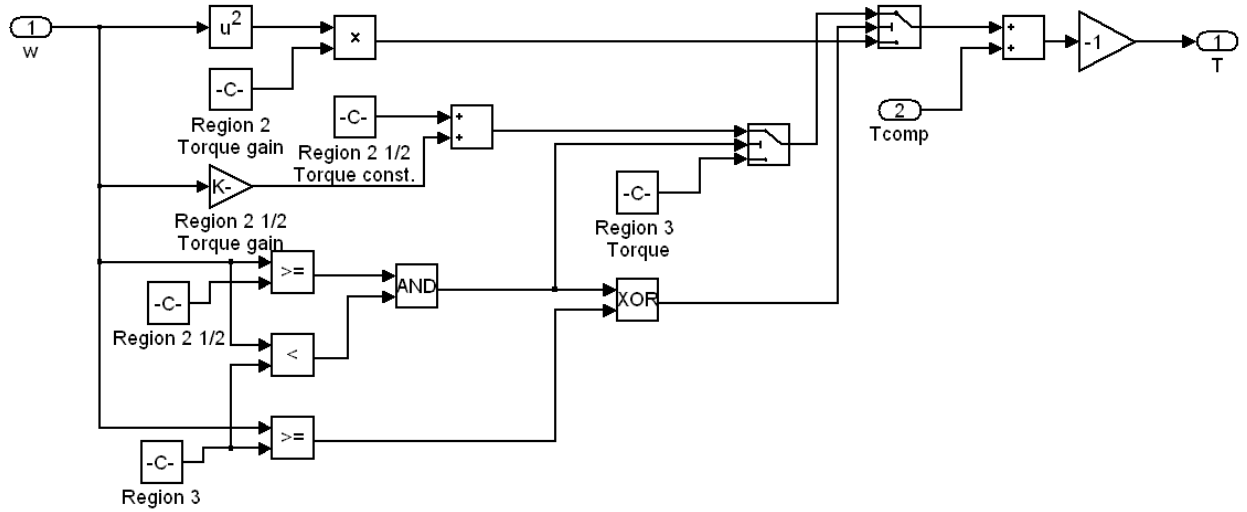
Figure 2.8. Torque reference calculation

2.2. Blade pitch control

When wind speed reaches or exceeds wind speed at which the turbine extracts rated power, blade pitch control has to be utilized to limit the mechanical power produced by the turbine. According to figure 2.3 and equation (1) power coefficient and mechanical power of a wind turbine depends on blade pitch angles. In order to keep power constant, blade pitch angle has to be increased to reduce power coefficient. The most widely used technique is collective blade pitch control where pitch angles of each blade on a rotor changes equally [82]. Another approach is to control pitch angles of each blade individually [85]. In this thesis the collective blade pitch control approach has been adopted. Linearization capability of FAST allows computation of a linear state space models that can be used for control design. This functionality is used for the pitch control development for the wind turbine model used in this research.
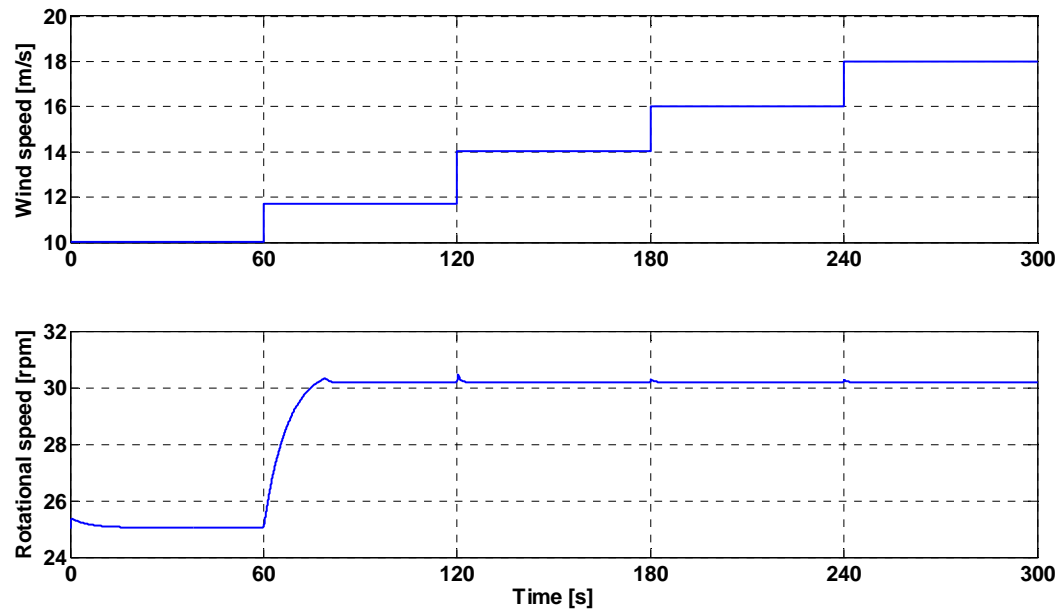
Figure 2.9. Blade pitch angle control in region 3

The effectiveness of blade pitch control is tested by simulation. Figure 2.9. shows response of the wind turbine to wind speed changes. Blade pitch controller keeps rotational speed constant when wind speed is above rated value, which is 11.5m/s for NREL 750kW wind turbine. Structure of the controller is shown in figure 2.10.
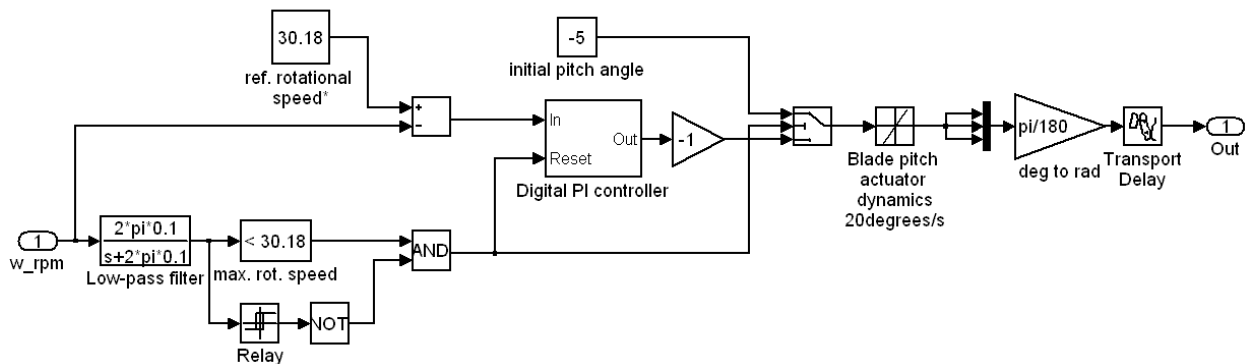
Figure 2.10. Blade pitch angle controller

2.3. Generator and a double power conversion system – Modeling and control

In the following sections, a full rated double power conversion system of a permanent magnet synchronous generator for a 750kW variable speed wind turbine is described. This type of wind turbine configuration is also known as type 4 wind turbine generator. Detailed mathematical models are developed and control system designed for grid and generator side converters. Finally, complete model is implemented in Simulink and integrated with FAST wind turbine model forming the complete multiphysics model of a 750kW wind turbine. Block diagram of the double conversion system with controllers for generator and grid side converters is shown in figure 2.11.
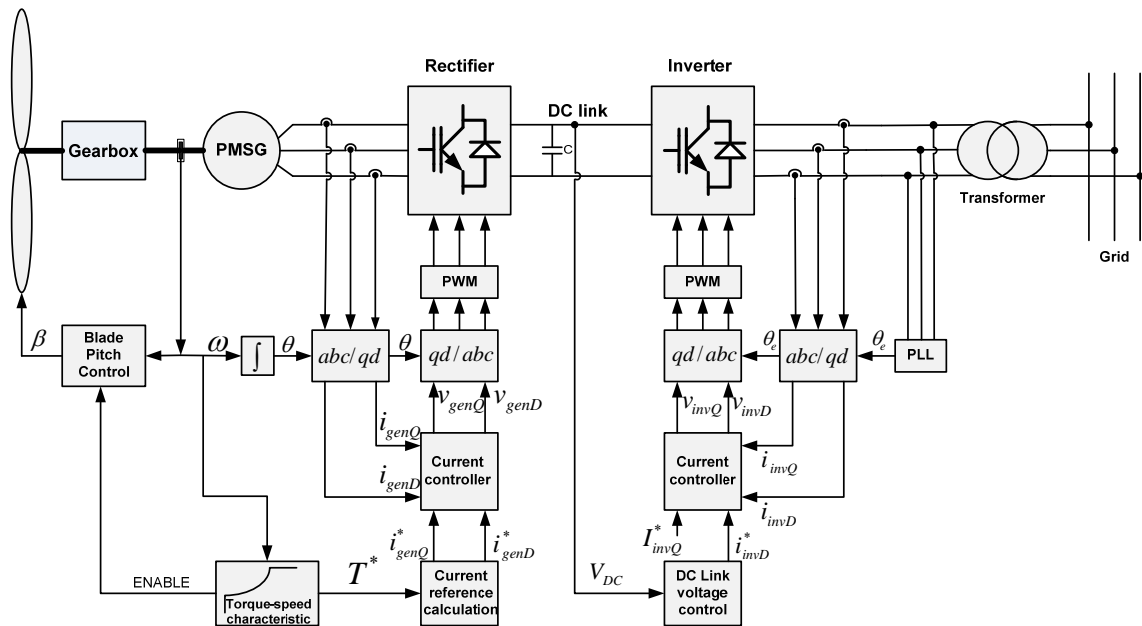
Figure 2.11. Complete control structure of the PMSG based variable speed wind turbine

Permanent magnet synchronous generator (PMSG) is mechanically coupled to the shaft of the drivetrain. Voltage and frequency of the synchronous generator is proportional to rotational speed, which varies with variations in wind speed. The active rectifier converts

three phase voltages of the generator to DC voltage that supplies the grid side converter (inverter). The inverter converts DC voltage to three phase voltages supplying power to the grid. Therefore, this system converts electric power of the generator from AC to DC and then back from DC to AC with different parameters. Voltage and frequency of the inverter can be regulated independently of the generator speed, which is the main reason for using such complex double conversion systems in modern variable speed wind turbines. The active rectifier enables control of the generator's currents, by using vector control technique. Since generator's electromechanical torque depends on current, and rotational speed of the turbine depends on the balance between mechanical torque of the rotor and generator, by controlling generator's current it is possible to control rotational speed. Vector control strategy in the rotating QD (quadrature-direct) reference frame is used to control generator currents. References for the generator current controller are provided by the rotational speed controller with implemented torque speed characteristic from figure 2.6. Grid side converter uses similar vector control technique that enables independent control of active and reactive power. A phase locked loop (PLL) provides phase angle of the grid voltages needed for synchronization of inverter voltages. DC link voltages is kept constant by the DC link voltage controller which calculates reference for the grid current controller. In following sections, each of the blocks from figure 2.11 is described in detail.

2.3.1. Phase-locked Loop (PLL) for grid synchronization of a three phase inverter

Phase locked loop (PLL) is a structure that computes phase angle and frequency of a measured signal. For power converters connected to the grid, PLL is necessary in for proper synchronization of the converter and the grid. The good overviews of main types of PLL used in grid tied applications are given in [98] and [99]. The most common type of PLL in three phase systems is illustrated in figure 2.12 [99]. Three phase voltage measurement are inputs to abc to DQ transformation block. Transformation matrix from abc to QD0 is:

$$T_{abc}^{qd0} = \frac{2}{3} \cdot \begin{bmatrix} \cos(\theta) & \cos\left(\theta - \frac{2 \cdot \pi}{3}\right) & \cos\left(\theta + \frac{2 \cdot \pi}{3}\right) \\ \sin(\theta) & \sin\left(\theta - \frac{2 \cdot \pi}{3}\right) & \sin\left(\theta + \frac{2 \cdot \pi}{3}\right) \\ \frac{1}{2} & \frac{1}{2} & \frac{1}{2} \end{bmatrix} \qquad (14)$$

This block needs the phase angle θ as an input. Phase angle is integral of the sum of base frequency and frequency correction. Frequency correction is the output of the compensator, which can be PI controller. If the goal is to keep the D axis of the rotating reference frame aligned to the rotating voltage vector, then voltage vector component along the Q axis should be equal to zero. Therefore, the Q component from the abc/QD block is compared to zero, and difference is fed to the PI controller. PI controller computes frequency correction which when added to the base frequency and integrated gives the phase angle.
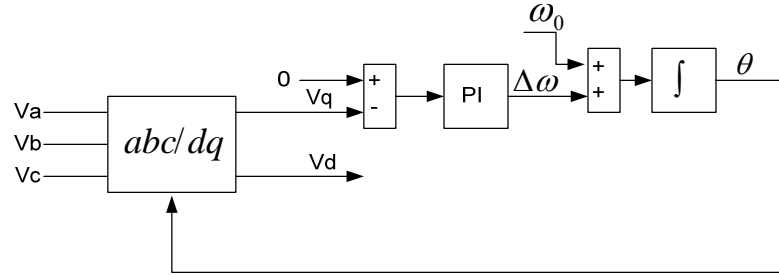
Figure 2.12. Three-phase PLL based on the DQ transformation

Due to nonlinear nature of the abc/DQ transformation, the PLL from figure 2.12 is a nonlinear system. It has however, two equilibrium points. In one point Vd is equal to zero, while in another point Vq is equal to zero. Proper selection of the parameters of the PI controller can result in making one of these points unstable and another stable, resulting in convergence to the stable point regardless on the initial conditions.   The parameters of the PI controller are chosen based on the small signal analysis. Simulink implementation of the PLL block for 750kW wind turbine model is shown in figure 2.13.
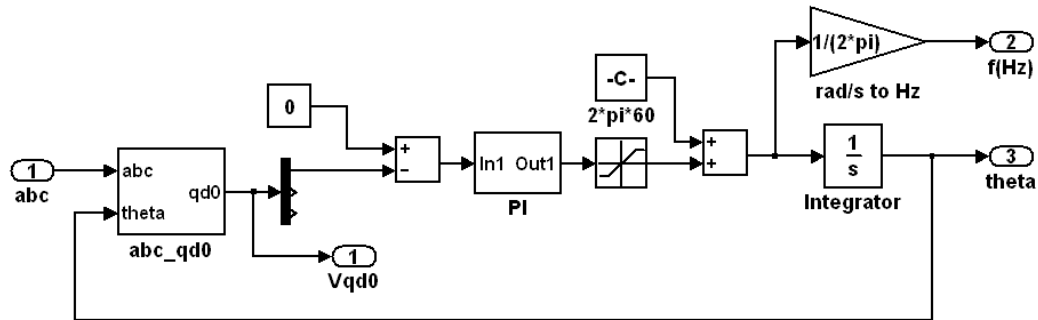
Figure 2.13. Simulink implementation of the PLL

2.3.2. Modeling of a three phase grid connected inverter

Inverters convert voltage or current from direct current (DC) source into alternating current (AC) form to supply load. Inverters have been widely used in variable speed electric drives, uninterruptible power supplies (UPS), inductive heating in metal processing, hybrid and electric vehicles, high voltage DC power transmission, and grid integration of renewable energy systems. Schematic diagram of a two level inverter connected to the grid is shown in figure 2.14.
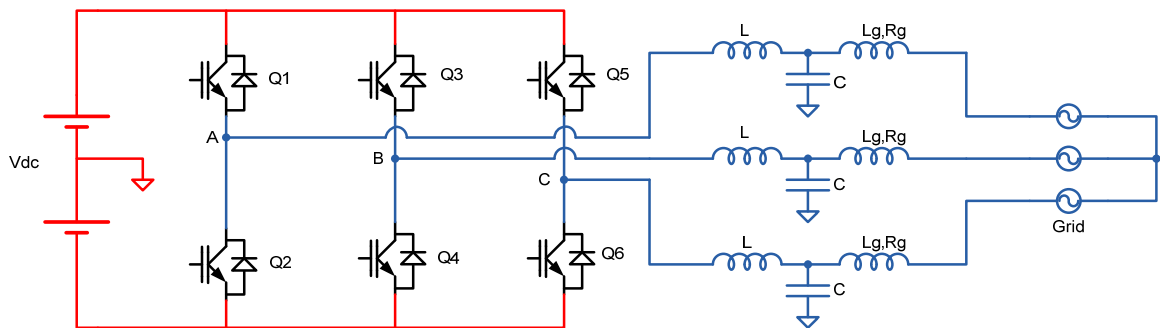
Figure 2.14. Three phase grid connected inverter

Inverters belong to the class of power electronic circuits and they use semiconductor switching components (bipolar transistors (BJT), MOSFETs, IGBTs, thyristors) that operate as switches, only in discrete regimes: conduction, or inactive state. Switching signals that control states of semiconductor switches are generated in the control circuit, amplified and scaled in the gate driver circuit. There are several methods for generating switching patterns, but most widely used method is Pulse Width Modulation (PWM), and it will only be discussed in this thesis. Switch pairs (Q1,Q2; Q3,Q4; Q5,Q6) form phase legs. If upper switch is conducting, the voltage of the corresponding phase terminal is at the positive potential of the DC source. When lower switch is conducting, phase terminal

is at the negative potential of the DC source. By fast switching between positive and negative terminal and controlling the duration of each state, it is possible to control the average voltage at the phase terminal. The principle of PWM is illustrated in figure 2.15. Average voltage over one switching cycle (Tsw) can be positive or negative. Therefore by controlling average voltage to follow sinusoidal function in time, it is possible to generate AC voltage waveform.
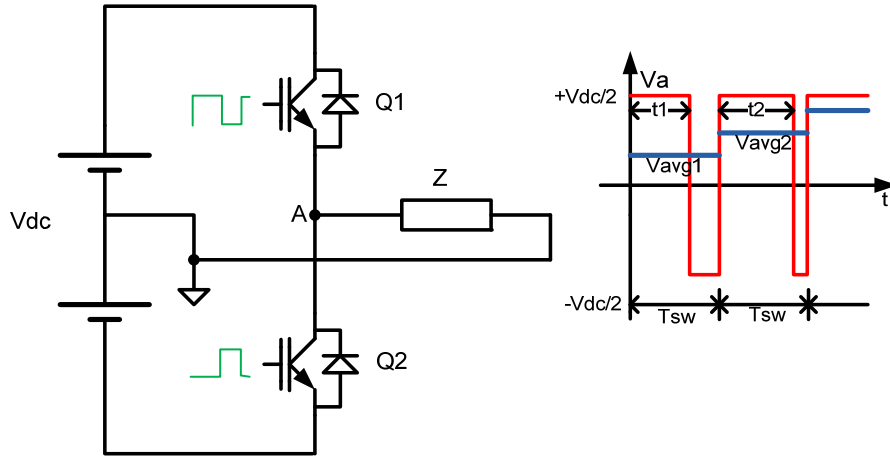
Figure 2.15. The principle of pulse width modulation (PWM)

$$V_{avg1} = \frac{1}{T_{sw}} \cdot \left(\int_0^{t_1} \frac{V_{dc}}{2} \cdot dt + \int_{t_1}^{T_{sw}} \left(-\frac{V_{dc}}{2} \right) \cdot dt \right) = \frac{V_{dc}}{2 \cdot T_{sw}} \cdot \left(2 \cdot t_1 - T_{sw} \right) \tag{15}$$

$$V_{avg2} = \frac{1}{T_{sw}} \cdot \left(\int_0^{t_2} \frac{V_{dc}}{2} \cdot dt + \int_{t_2}^{T_{sw}} \left(-\frac{V_{dc}}{2} \right) \cdot dt \right) = \frac{V_{dc}}{2 \cdot T_{sw}} \cdot \left(2 \cdot t_2 - T_{sw} \right) \tag{16}$$

It is important to note here that when upper switch is conducting, lower switch has to be turned off, and vice versa. Therefore, only duration of conducting of one transistor determines voltage at the phase terminal. In real case, there is additional time that has to be inserted between turning off upper switch and turning on the lower switch on order to provide enough time for upper switch to stop conducting before lower switch begins to

conduct. Each switch has reverse biased diode connected in parallel. Reverse diodes provide path for the currents in filter inductors when the switch is turned off.

Voltage waveform on the phase leg is rectangular, and therefore with high harmonic contents. On the other side, grid voltage ideally contains only main harmonic of 60/50 Hz. Large voltage harmonics result in high ripple current that is injected to the grid. In order to reduce harmonics, passive filters are used between phase terminals of the VSI and the grid. In figure 2.14 this filters consist of LC resonant circuit. Additional impedance between inverter and the grid, Lg and Rg, is impendence of cable that connects inverter to the grid. However, in order to provide better filtering of high frequency harmonics, additional filter inductance is added after capacitor, forming the LCL filter.

One phase of the grid connected inverter from the phase to the grid terminal is shown in figure 2.16. Due to symmetry, other two phases do not need to be considered at this point. Voltage at the phase input is denoted as V_{inv} and it has PWM shaped rectangular waveform. Grid voltage is denoted V_{grid} and it is assumed that has no other harmonics except the main.
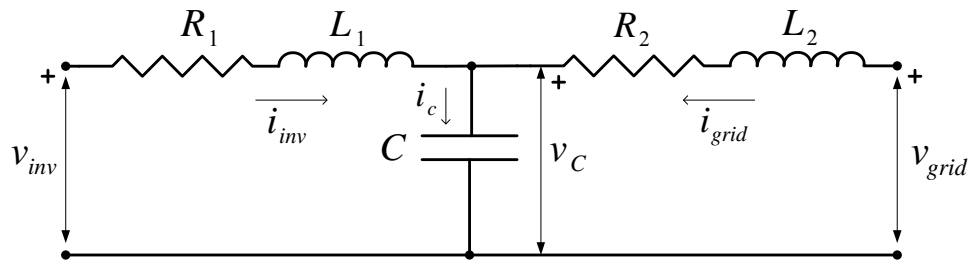
Figure 2.16. The LCL filter

If there is significant inductive line impedance between inverter and the grid, it can be modeled by adding the impedance parameters to R2-L2 part of the circuit. From the

Kirchhoff's laws, and knowing that capacitor current is the derivative of the capacitor voltage following equations can be formulated:

$$i_{inv} = i_C + i_{grid} \tag{17}$$

$$v_{inv} = R_1 \cdot i_{inv} + L_1 \cdot \frac{di_{inv}}{dt} + v_C \tag{18}$$

$$v_{grid} = -R_2 \cdot i_{grid} - L_2 \cdot \frac{di_{grid}}{dt} + v_C \tag{19}$$

$$i_C = C \cdot \frac{dv_C}{dt} \tag{20}$$

By substituting (20) into (17) it follows:

$$C \cdot \frac{dv_C}{dt} = i_{inv} - i_{grid} \tag{21}$$

Equations (18), (19), and (21) form a system that models behavior of LCL filter per one phase. The system can be written in the state space form, with i_{inv}, i_{grid}, and v_C as state variables.

$$\begin{bmatrix} \dfrac{di_{inv}}{dt} \\ \dfrac{di_{grid}}{dt} \\ \dfrac{dv_C}{dt} \end{bmatrix} = \begin{bmatrix} -\dfrac{R_1}{L_1} & 0 & -\dfrac{1}{L_1} \\ 0 & -\dfrac{R_2}{L_2} & \dfrac{1}{L_2} \\ \dfrac{1}{C} & -\dfrac{1}{C} & 0 \end{bmatrix} \cdot \begin{bmatrix} i_{inv} \\ i_{grid} \\ v_C \end{bmatrix} + \begin{bmatrix} \dfrac{1}{L_1} & 0 \\ 0 & -\dfrac{1}{L_2} \\ 0 & 0 \end{bmatrix} \cdot \begin{bmatrix} v_{inv} \\ v_{grid} \end{bmatrix} \tag{22}$$

$$\begin{bmatrix} i_{inv} \\ i_{grid} \\ v_C \end{bmatrix} = \begin{bmatrix} 1 & 0 & 0 \\ 0 & 1 & 0 \\ 0 & 0 & 1 \end{bmatrix} \cdot \begin{bmatrix} i_{inv} \\ i_{grid} \\ v_C \end{bmatrix} \tag{23}$$

Equations (22) and (23) are the state space model of the form:

$$\dot{x} = A \cdot x + B \cdot u$$

$$y = C \cdot x$$

$$x = y = \begin{bmatrix} i_i \\ i_{grid} \\ v_C \end{bmatrix}; u = \begin{bmatrix} v_{inv} \\ v_{grid} \end{bmatrix}; A = \begin{bmatrix} -\dfrac{R_1}{L_1} & 0 & -\dfrac{1}{L_1} \\ 0 & -\dfrac{R_2}{L_2} & \dfrac{1}{L_2} \\ \dfrac{1}{C} & -\dfrac{1}{C} & 0 \end{bmatrix}; B = \begin{bmatrix} \dfrac{1}{L_1} & 0 \\ 0 & -\dfrac{1}{L_2} \\ 0 & 0 \end{bmatrix}; C = \begin{bmatrix} 1 & 0 & 0 \\ 0 & 1 & 0 \\ 0 & 0 & 1 \end{bmatrix} \quad (24)$$

From the state space model, it is possible to derive transfer function model in Laplace domain:

$$G(s) = \begin{bmatrix} \dfrac{I_i(s)}{V_i(s)} & \dfrac{I_i(s)}{V_{grid}(s)} \\ \dfrac{I_{grid}(s)}{V_i(s)} & \dfrac{I_{grid}(s)}{V_{grid}(s)} \\ \dfrac{V_C(s)}{V_i(s)} & \dfrac{V_C(s)}{V_{grid}(s)} \end{bmatrix} = C \cdot (s \cdot I - A)^{-1} \cdot B \quad (25)$$

Equation (25) results in the following transfer function matrix:

$$G(s) = \begin{bmatrix} \dfrac{\dfrac{1}{L_1} \cdot s^2 + \dfrac{R_2}{L_1 \cdot L_2} \cdot s + \dfrac{1}{L_1 \cdot L_2 \cdot C}}{s^3 + \left(\dfrac{R_1}{L_1} + \dfrac{R_2}{L_2}\right) \cdot s^2 + \left(\dfrac{1}{L_1 \cdot C} + \dfrac{1}{L_2 \cdot C} + \dfrac{R_1 \cdot R_2}{L_1 \cdot L_2}\right) \cdot s + \dfrac{R_1 + R_2}{L_1 \cdot L_2 \cdot C}} & -\dfrac{\dfrac{1}{L_1 \cdot L_2 \cdot C}}{s^3 + \left(\dfrac{R_1}{L_1} + \dfrac{R_2}{L_2}\right) \cdot s^2 + \left(\dfrac{1}{L_1 \cdot C} + \dfrac{1}{L_2 \cdot C} + \dfrac{R_1 \cdot R_2}{L_1 \cdot L_2}\right) \cdot s + \dfrac{R_1 + R_2}{L_1 \cdot L_2 \cdot C}} \\ \dfrac{\dfrac{1}{L_1 \cdot L_2 \cdot C}}{s^3 + \left(\dfrac{R_1}{L_1} + \dfrac{R_2}{L_2}\right) \cdot s^2 + \left(\dfrac{1}{L_1 \cdot C} + \dfrac{1}{L_2 \cdot C} + \dfrac{R_1 \cdot R_2}{L_1 \cdot L_2}\right) \cdot s + \dfrac{R_1 + R_2}{L_1 \cdot L_2 \cdot C}} & -\dfrac{\dfrac{1}{L_2} \cdot s^2 + \dfrac{R_1}{L_1 \cdot L_2} \cdot s + \dfrac{1}{L_1 \cdot L_2 \cdot C}}{s^3 + \left(\dfrac{R_1}{L_1} + \dfrac{R_2}{L_2}\right) \cdot s^2 + \left(\dfrac{1}{L_1 \cdot C} + \dfrac{1}{L_2 \cdot C} + \dfrac{R_1 \cdot R_2}{L_1 \cdot L_2}\right) \cdot s + \dfrac{R_1 + R_2}{L_1 \cdot L_2 \cdot C}} \\ \dfrac{\dfrac{1}{L_1 \cdot C} \cdot s + \dfrac{R_2}{L_1 \cdot L_2 \cdot C}}{s^3 + \left(\dfrac{R_1}{L_1} + \dfrac{R_2}{L_2}\right) \cdot s^2 + \left(\dfrac{1}{L_1 \cdot C} + \dfrac{1}{L_2 \cdot C} + \dfrac{R_1 \cdot R_2}{L_1 \cdot L_2}\right) \cdot s + \dfrac{R_1 + R_2}{L_1 \cdot L_2 \cdot C}} & \dfrac{\dfrac{1}{L_2 \cdot C} \cdot s + \dfrac{R_1}{L_1 \cdot L_2 \cdot C}}{s^3 + \left(\dfrac{R_1}{L_1} + \dfrac{R_2}{L_2}\right) \cdot s^2 + \left(\dfrac{1}{L_1 \cdot C} + \dfrac{1}{L_2 \cdot C} + \dfrac{R_1 \cdot R_2}{L_1 \cdot L_2}\right) \cdot s + \dfrac{R_1 + R_2}{L_1 \cdot L_2 \cdot C}} \end{bmatrix} \quad (26)$$

These transfer functions completely describe dynamical response from each input in the system to each output. They are especially important for parameter choosing for LCL filter. In order to choose parameters for the LCL filters several parameters are needed: the

power level, grid voltage level, maximum voltage drop on the filter, maximum current ripple allowed. Power and voltage level are the parameters of the particular system, while maximum voltage drop and current ripple are defined by the standard IEEE-519.

The transfer function from inverter voltage to the grid current is of special interest in LCL parameter calculation:

$$G_{21}(s) = \frac{I_{grid}(s)}{V_i(s)} = \frac{\dfrac{1}{L_1 \cdot L_2 \cdot C}}{s^3 + \left(\dfrac{R_1}{L_1} + \dfrac{R_2}{L_2}\right) \cdot s^2 + \left(\dfrac{1}{L_1 \cdot C} + \dfrac{1}{L_2 \cdot C} + \dfrac{R_1 \cdot R_2}{L_1 \cdot L_2}\right) \cdot s + \dfrac{R_1 + R_2}{L_1 \cdot L_2 \cdot C}} \qquad (27)$$

The goal of design procedure is to calculate values for L1, L2 and C. Assuming that resistances R1 and R2 are low, they can be neglected.

$$R_1 \approx 0$$
$$R_2 \approx 0$$

By making this assumption, the characteristic polynomial of the transfer function is:

$$f(s) = s^3 + \left(\frac{1}{L_1 \cdot C} + \frac{1}{L_2 \cdot C}\right) \cdot s \qquad (28)$$

By solving the characteristic equation, system poles can be found:

$$s^3 + \left(\frac{1}{L_1 \cdot C} + \frac{1}{L_2 \cdot C}\right) \cdot s = 0 \qquad (29)$$

$$s_1 = 0 \qquad (30)$$

$$s_{2,3} = \pm j \cdot \sqrt{\frac{(L_1 + L_2)}{C \cdot L_1 \cdot L_2}} \qquad (31)$$

Approximated resonant frequency of the LCL filter is:

$$\omega_{res} = \sqrt{\frac{(L_1 + L_2)}{C \cdot L_1 \cdot L_2}} \qquad \left[\frac{rad}{s}\right] \qquad (32)$$

Next step is to calculate total inductance L1+L2. By neglecting current through capacitor, total voltage drop across the series connection of inductances between inverter and grid is

$$\Delta V \approx \omega \cdot (L_1 + L_2) \cdot I_{RMS} \tag{33}$$

For 750kVA inverter connected to the 690V three-phase utility grid, the RMS current is:

$$I_{RMS} = \frac{750000}{\sqrt{3} \cdot 690} = 627.6A \tag{34}$$

This current is relatively high and it can create large voltage drop across inductors if inductance is too large. On the other hand, larger inductance results in smaller current ripple. One of the main factors that limit the allowed voltage drop across the filter inductance is DC link voltage which should be kept as low as possible to reduce voltage stress on the switching components. By allowing voltage drop to be maximum 15% of the phase to neutral voltage, the voltage drop is:

$$\Delta V_{max} = 0.15 \cdot \frac{690}{\sqrt{3}} = 59.76V \tag{35}$$

Now, the total inductance can be calculated:

$$L_1 + L_2 = \frac{\Delta V_{max}}{\omega \cdot I_{RMS}} = \frac{59.76}{2 \cdot \pi \cdot 60 \cdot 627.6} = 252.56 \mu H \approx 250 \mu H \tag{36}$$

Assuming that L1 and L2 are related as :

$$L_2 = \beta \cdot L_1 \tag{37}$$

$$L_{tot} = L_1 + L_2 = (1 + \beta) \cdot L_1 \tag{38}$$

$$L_1 = \frac{L_1 + L_2}{(1 + \beta)} = \frac{L_{tot}}{(1 + \beta)} \tag{39}$$

β is a coefficient of proportionality between two inductances. The resonant frequency is

$$\omega_{res} = \sqrt{\frac{1+\beta}{C \cdot \beta \cdot L_1}} \tag{40}$$

The next step is to calculate the capacitor value and coefficient β. It is desirable to choose the smaller value for the capacitor, for the same resonant frequency.

$$\omega_{res} = \sqrt{\frac{(1+\beta)^2}{C \cdot \beta \cdot L_{tot}}} \tag{41}$$

$$C = \frac{(1+\beta)^2}{\omega_{res}^2 \cdot \beta \cdot L_{tot}} \tag{42}$$

The coefficient β that minimizes capacitance can be found by calculating the first derivative of the equation above.

$$\frac{dC}{d\beta} = \frac{2 \cdot (1+\beta) \cdot \omega_{res}^2 \cdot \beta \cdot L_{tot} - (1+\beta)^2 \cdot \omega_{res}^2 \cdot L_{tot}}{\omega_{res}^4 \cdot \beta^2 \cdot L_{tot}^2} \tag{43}$$

From this equation the coefficient β that minimizes capacitor is:

$$2 \cdot (1+\beta) \cdot \omega_{res}^2 \cdot \beta \cdot L_{tot} - (1+\beta)^2 \cdot \omega_{res}^2 \cdot L_{tot} = 0 \tag{44}$$

The solution of this equation is $\beta = 1$. Therefore, inductances L1 and L2 should be equal and their values are:

$$L_1 = L_2 = \frac{L_{tot}}{2} = 125 \, \mu H \tag{45}$$

$$|G_{21}(j \cdot \omega)| = \frac{|I_{grid}(j \cdot \omega)|}{|V_i(j \cdot \omega)|} = \frac{\dfrac{1}{L_1 \cdot L_2 \cdot C}}{\left| -j \cdot \omega^3 - \left(\dfrac{R_1}{L_1} + \dfrac{R_2}{L_2} \right) \cdot \omega^2 + \left(\dfrac{1}{L_1 \cdot C} + \dfrac{1}{L_2 \cdot C} + \dfrac{R_1 \cdot R_2}{L_1 \cdot L_2} \right) \cdot j \cdot \omega + \dfrac{R_1 + R_2}{L_1 \cdot L_2 \cdot C} \right|} \tag{46}$$

$$G_{21}(\omega) = \cfrac{\cfrac{1}{L_1 \cdot L_2 \cdot C}}{\sqrt{\left(\cfrac{R_1 + R_2}{L_1 \cdot L_2 \cdot C} - \left(\cfrac{R_1}{L_1} + \cfrac{R_2}{L_2}\right) \cdot \omega^2\right)^2 + \left(\omega^3 - \omega \cdot \left(\cfrac{1}{L_1 \cdot C} + \cfrac{1}{L_2 \cdot C} + \cfrac{R_1 \cdot R_2}{L_1 \cdot L_2}\right)\right)^2}} \qquad (47)$$

The switching frequency in for this project is 4kHz. In chapter 4, the maximum DC link voltage with fully charged ultracapacitor bank is defined to be 1730V. The peak voltage across the total inductance of the filter is equal to one half of the DC link voltage. This voltage create current ripple that has to be limited to 1% of the rated RMS current according to the IEEE-519 standard. Therefore, the gain of G21 transfer function at switching frequency of 4kHz should be:

$$G_{21}(2 \cdot \pi \cdot 4000) = \frac{6.27}{865} = 0.00725 \qquad (48)$$

From this result, the capacitance is calculated as 250µF, resulting in resonant frequency of LCL filter of 1237Hz. Final values for parameters of the LCL filter are given in the table.

L1	L2	C
125µH	125µH	250µF

2.3.3. Inverter model in QD coordinates and controller design

Similarly to the generator side converter, QD reference frame is chosen for inverter controller as well. A system of differential equations that describes three phase LCL filter is given below.

$$
\begin{bmatrix} \dfrac{di_{inv}^{ABC}}{dt} \\[2mm] \dfrac{di_{grid}^{ABC}}{dt} \\[2mm] \dfrac{dv_{C}^{ABC}}{dt} \end{bmatrix} = \begin{bmatrix} -\dfrac{R_1}{L_1} & 0 & -\dfrac{1}{L_1} \\[2mm] 0 & -\dfrac{R_2}{L_2} & \dfrac{1}{L_2} \\[2mm] \dfrac{1}{C} & -\dfrac{1}{C} & 0 \end{bmatrix} \cdot \begin{bmatrix} i_{inv}^{ABC} \\[2mm] i_{grid}^{ABC} \\[2mm] v_{C}^{ABC} \end{bmatrix} + \begin{bmatrix} \dfrac{1}{L_1} & 0 \\[2mm] 0 & -\dfrac{1}{L_2} \\[2mm] 0 & 0 \end{bmatrix} \cdot \begin{bmatrix} v_{inv}^{ABC} \\[2mm] v_{grid}^{ABC} \end{bmatrix} \tag{49}
$$

$$
i_{inv}^{ABC} = \begin{bmatrix} i_{inv}^{A} \\ i_{inv}^{B} \\ i_{inv}^{C} \end{bmatrix} \quad i_{grid}^{ABC} = \begin{bmatrix} i_{grid}^{A} \\ i_{grid}^{B} \\ i_{grid}^{C} \end{bmatrix} \quad v_{inv}^{ABC} = \begin{bmatrix} v_{inv}^{A} \\ v_{inv}^{B} \\ v_{inv}^{C} \end{bmatrix} \quad v_{grid}^{ABC} = \begin{bmatrix} v_{grid}^{A} \\ v_{grid}^{B} \\ v_{grid}^{C} \end{bmatrix} \quad v_{C}^{ABC} = \begin{bmatrix} v_{C}^{A} \\ v_{C}^{B} \\ v_{C}^{C} \end{bmatrix}
$$

By applying abc to QD transformation to the first set of differential equations, following equations in QD coordinates can be derived:

$$
\frac{di_{inv}^{ABC}}{dt} = -\frac{R_1}{L_1} \cdot i_{inv}^{ABC} - \frac{1}{L_1} \cdot v_{C}^{ABC} + \frac{1}{L_1} \cdot v_{inv}^{ABC} \tag{50}
$$

$$
i_{inv}^{ABC} = T_{qd0}^{abc} \cdot i_{inv}^{qd0} \tag{51}
$$

$$
i_{inv}^{qd0} = T_{abc}^{qd0} \cdot i_{inv}^{abc} \tag{52}
$$

Where inverse transformation from QD0 to abc domain is (53):

$$T_{qd0}^{abc} = \begin{bmatrix} \cos(\theta) & \sin(\theta) & 1 \\ \cos\left(\theta - \dfrac{2\cdot\pi}{3}\right) & \sin\left(\theta - \dfrac{2\cdot\pi}{3}\right) & 1 \\ \cos\left(\theta + \dfrac{2\cdot\pi}{3}\right) & \sin\left(\theta + \dfrac{2\cdot\pi}{3}\right) & 1 \end{bmatrix} \tag{53}$$

By applying the abc to QD coordinate transformation, it follows:

$$\frac{d}{dt}\left[T_{qd0}^{abc} \cdot i_{inv}^{qd0}\right] = -\frac{R_1}{L_1} \cdot T_{qd0}^{abc} \cdot i_{inv}^{qd0} - \frac{1}{L_1} \cdot T_{qd0}^{abc} \cdot v_C^{qd0} + \frac{1}{L_1} \cdot T_{qd0}^{abc} \cdot v_{inv}^{qd0} \tag{54}$$

$$\frac{d}{dt}\left[T_{qd0}^{abc}\right] \cdot i_{inv}^{qd0} + T_{qd0}^{abc} \cdot \frac{d}{dt} i_{inv}^{qd0} = -\frac{R_1}{L_1} \cdot T_{qd0}^{abc} \cdot i_{inv}^{qd0} - \frac{1}{L_1} \cdot T_{qd0}^{abc} \cdot v_C^{qd0} + \frac{1}{L_1} \cdot T_{qd0}^{abc} \cdot v_{inv}^{qd0} \tag{55}$$

Knowing that:

$$\frac{d}{dt}\left[T_{qd0}^{abc}\right] = \frac{d}{dt}\begin{bmatrix} \cos(\theta) & \sin(\theta) & 1 \\ \cos\left(\theta - \dfrac{2\cdot\pi}{3}\right) & \sin\left(\theta - \dfrac{2\cdot\pi}{3}\right) & 1 \\ \cos\left(\theta + \dfrac{2\cdot\pi}{3}\right) & \sin\left(\theta + \dfrac{2\cdot\pi}{3}\right) & 1 \end{bmatrix} = \omega \cdot \begin{bmatrix} -\sin\theta & \cos\theta & 0 \\ -\sin\left(\theta - \dfrac{2\cdot\pi}{3}\right) & \cos\left(\theta - \dfrac{2\cdot\pi}{3}\right) & 0 \\ -\sin\left(\theta + \dfrac{2\cdot\pi}{3}\right) & \cos\left(\theta + \dfrac{2\cdot\pi}{3}\right) & 0 \end{bmatrix} = \omega \cdot T_{qd0}^{'} \tag{56}$$

It follows:

$$T_{qd0}^{abc} \cdot \frac{d}{dt} i_{inv}^{qd0} = -\frac{R_1}{L_1} \cdot T_{qd0}^{abc} \cdot i_{inv}^{qd0} - \frac{1}{L_1} \cdot T_{qd0}^{abc} \cdot v_C^{qd0} + \frac{1}{L_1} \cdot T_{qd0}^{abc} \cdot v_{inv}^{qd0} - \omega \cdot T_{qd0}^{'} \cdot i_{inv}^{qd0} \tag{57}$$

By multiplying both sides of this equation by T_{abc}^{qd0}, knowing that $T_{qd0}^{abc} \cdot T_{abc}^{qd0} = I$ and

$$T_{qd0}^{abc} \cdot T_{qd0}^{'} = \begin{bmatrix} 0 & 1 & 0 \\ -1 & 0 & 0 \\ 0 & 0 & 0 \end{bmatrix} \tag{58}$$

$$\frac{d}{dt} i_{inv}^{qd0} = -\frac{R_1}{L_1} \cdot i_{inv}^{qd0} - \frac{1}{L_1} \cdot v_C^{qd0} + \frac{1}{L_1} \cdot v_{inv}^{qd0} - \omega \cdot \begin{bmatrix} 0 & 1 & 0 \\ -1 & 0 & 0 \\ 0 & 0 & 0 \end{bmatrix} \cdot i_{inv}^{qd0} \tag{59}$$

Resulting in the flowing set of differential equations for inverter current components in QD0 system:

$$\frac{di_{inv}^q}{dt} = -\frac{R_1}{L_1} \cdot i_{inv}^q - \frac{1}{L_1} \cdot v_C^q + \frac{1}{L_1} \cdot v_{inv}^q - \omega \cdot i_{inv}^d$$

(60)

$$\frac{di_{inv}^d}{dt} = -\frac{R_1}{L_1} \cdot i_{inv}^d - \frac{1}{L_1} \cdot v_C^d + \frac{1}{L_1} \cdot v_{inv}^d + \omega \cdot i_{inv}^q$$

(61)

$$\frac{di_{inv}^0}{dt} = -\frac{R_1}{L_1} \cdot i_{inv}^0 - \frac{1}{L_1} \cdot v_C^0 + \frac{1}{L_1} \cdot v_{inv}^0$$

(62)

Similar derivation process for grid currents and capacitor voltages leads to:

$$\frac{di_{grid}^{ABC}}{dt} = -\frac{R_2}{L_2} \cdot i_{grid}^{ABC} + \frac{1}{L_2} \cdot v_C^{ABC} - \frac{1}{L_2} \cdot v_{grid}^{ABC}$$

(63)

$$\frac{d}{dt}\left[T_{qd0}^{abc} \cdot i_{grid}^{qd0}\right] = -\frac{R_2}{L_2} \cdot T_{qd0}^{abc} \cdot i_{grid}^{qd0} + \frac{1}{L_2} \cdot T_{qd0}^{abc} \cdot v_C^{qd0} - \frac{1}{L_2} \cdot T_{qd0}^{abc} \cdot v_{grid}^{qd0}$$

(64)

Final system of differential equations for grid currents of the LCL filter is:

$$\frac{di_{grid}^q}{dt} = -\frac{R_2}{L_2} \cdot i_{grid}^q + \frac{1}{L_2} \cdot v_C^q - \frac{1}{L_2} \cdot v_{grid}^q - \omega \cdot i_{grid}^d$$

(65)

$$\frac{di_{grid}^d}{dt} = -\frac{R_2}{L_2} \cdot i_{grid}^d + \frac{1}{L_2} \cdot v_C^d - \frac{1}{L_2} \cdot v_{grid}^d + \omega \cdot i_{grid}^q$$

(66)

$$\frac{di_{grid}^0}{dt} = -\frac{R_2}{L_2} \cdot i_{grid}^0 + \frac{1}{L_2} \cdot v_C^0 - \frac{1}{L_2} \cdot v_{grid}^0$$

(67)

Capacitor voltages in QD0 coordinates:

$$\frac{dv_C^{ABC}}{dt} = \frac{1}{C} \cdot i_{inv}^{ABC} - \frac{1}{C} \cdot i_{grid}^{ABC}$$

(68)

$$\frac{d}{dt}\left[T_{qd0}^{abc} \cdot v_C^{qd0}\right] = \frac{1}{C} \cdot T_{qd0}^{abc} \cdot i_{inv}^{qd0} - \frac{1}{C} \cdot T_{qd0}^{abc} \cdot i_{grid}^{qd0}$$

(69)

$$\frac{dv_C^q}{dt} = \frac{1}{C} \cdot i_{inv}^q - \frac{1}{C} \cdot i_{grid}^q - \omega \cdot v_C^d \tag{70}$$

$$\frac{dv_C^d}{dt} = \frac{1}{C} \cdot i_{inv}^d - \frac{1}{C} \cdot i_{grid}^d + \omega \cdot v_C^q \tag{71}$$

$$\frac{dv_C^0}{dt} = \frac{1}{C} \cdot i_{inv}^0 - \frac{1}{C} \cdot i_{grid}^0 \tag{72}$$

Simulink implementation of inverter and grid current computation based on differential equations in QD0 domain is shown in figure 2.17. Figure 2.18 shows capacitor voltage computations based on the model (70)-(72). Finally, complete model of the three phase LCL filter connected to the utility grid is shown in figure 2.19. Inputs to the model are inverter and grid voltages and the phase angle θ from PLL.

(a)   (b)
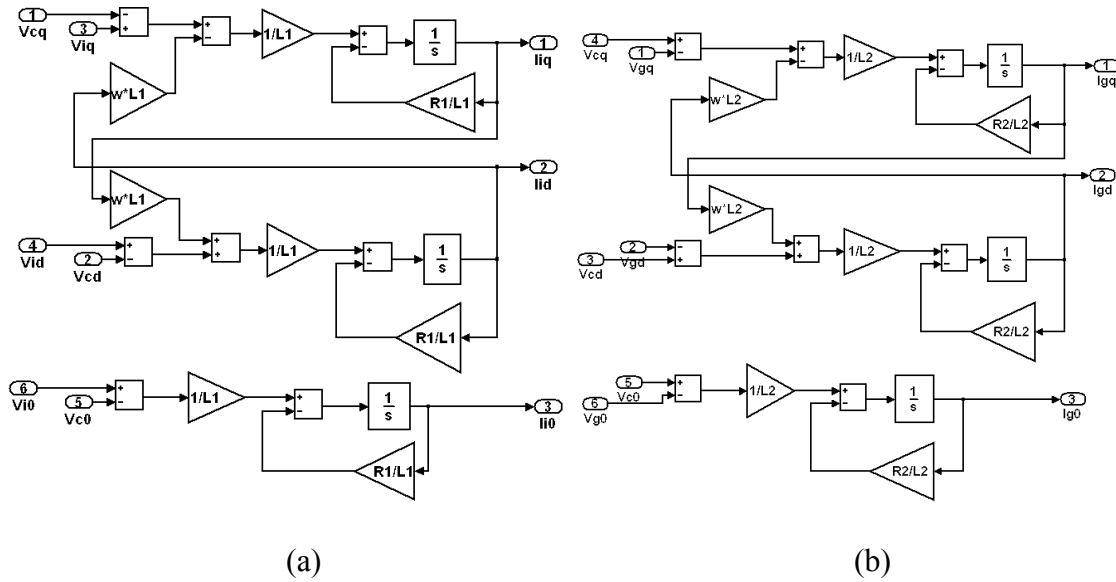
Figure 2.17. Simulink block diagrams of filter inductances of

the LCL filter in QD coordinates
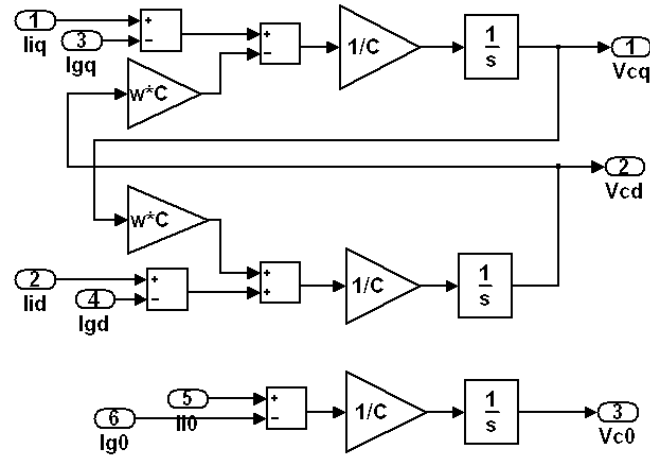
Figure 2.18. Capacitor voltage computation in QD coordinates
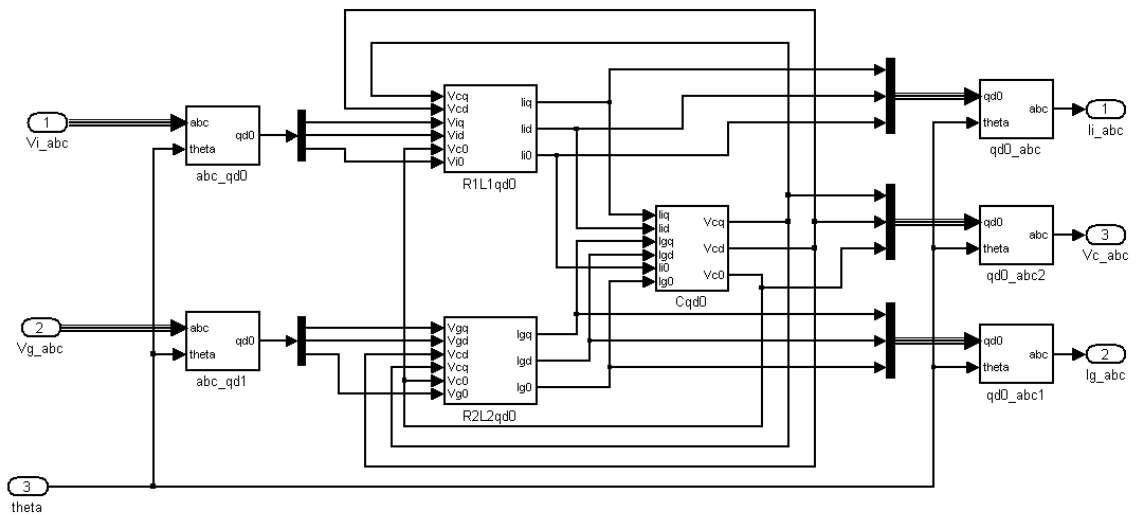
Figure 2.19. Complete Simulink model of the grid connected LCL filter

The outputs of the model are inverter currents, grid currents and capacitor voltages, all in abc domain.

The inverter control is based on the current feedback from the current sensors typically located between inverter and filter inductance of the LCL filter. The concept of vector control allows decoupled control of direct and quadrature components of current which is directly reflected to decoupled active and reactive power control. The basic principle of current control using vector control technique is to find voltage vector that will produce

desired currents. From differential equations for inductor currents, by applying Laplace transformation following expression are derived:

$$s \cdot I_{inv}^q(s) = -\frac{R_1}{L_1} \cdot I_{inv}^q(s) - \frac{1}{L_1} \cdot V_C^q(s) + \frac{1}{L_1} \cdot V_{inv}^q(s) - \omega \cdot I_{inv}^d \qquad (73)$$

It follows that:

$$I_{inv}^q(s) \cdot \left(s + \frac{R_1}{L_1}\right) = -\frac{1}{L_1} \cdot V_C^q(s) + \frac{1}{L_1} \cdot V_{inv}^q(s) - \omega \cdot I_{inv}^d \qquad (74)$$

$$I_{inv}^q(s) = \frac{-\frac{1}{L_1} \cdot V_C^q(s) + \frac{1}{L_1} \cdot V_{inv}^q(s) - \omega \cdot I_{inv}^d}{\left(s + \frac{R_1}{L_1}\right)} = \frac{V_{inv}^q(s) - V_C^q(s) - \omega \cdot L_1 \cdot I_{inv}^d}{L_1 \cdot s + R_1} \qquad (75)$$

From the equation above, it follows that inductor current on Q axis depends on inverter voltage on this axis, inverter current on D axis, and capacitor voltage on Q axis. Inverter voltage on Q axis that would produce desired current is:

$$V_{inv}^q(s) = I_{inv}^q(s) \cdot (L_1 \cdot s + R_1) + V_C^q(s) + \omega \cdot L_1 \cdot I_{inv}^d(s) \qquad (76)$$

From the equation (76), voltage drop across the inductor impedance, $I_{inv}^q(s) \cdot (L_1 \cdot s + R_1)$, has to be known in order to compute voltage V_{inv}^q that results in current I_{inv}^q. This method is the open loop control, and its main disadvantage is dependence on accuracy of parameters L1 and R1, especially since R1 depends on temperature which changes due to changes in RMS current during inverter operation. Feedback control overcomes this difficulty, and it is always used in current control of grid connected inverters. In QD reference frame current control, feedback loop is used to calculate only voltage component that correspond to the voltage drop across the inductor L1,R1. Other two components, capacitor voltage on Q axes and cross coupling term from

Q axis current are added to the voltage drop term forming the voltage reference for the Q axis. Voltage component across R1 and L1 is:

$$V_{RL}^{q}(s) = I_{inv}^{q}(s) \cdot (L_1 \cdot s + R_1)$$

(77)

The transfer function from voltage component on the inductor terminals to the current through the inductor is:

$$G_{RL}^{q}(s) = \frac{I_{inv}^{q}(s)}{V_{RL}^{q}(s)} = \frac{1}{L_1 \cdot s + R_1}$$

(78)

Due to the nature of PWM generation of voltages of a three phase converter, there is a transport delay between voltage reference computed by the controller and actual voltage on the converter's terminals. This delay is equal to one half of the switching frequency. For low switching frequencies, used in high power applications, this delay becomes significant and needs to be taken into account for closed loop controller design. Taking the transport delay of the converter into account, following voltage equation on the Q axis holds:

$$V_{inv}^{q-real}(s) = V_{inv}^{q}(s) \cdot e^{-s \cdot \frac{T_s}{2}}$$

(79)

Transport delay in voltage causes the transport delay in current caused by that voltage. Therefore, the closed loop transfer function that takes into account the converter's transport delay is:

$$G_{RL}^{q-real}(s) = \frac{1}{L_1 \cdot s + R_1} \cdot e^{-s \cdot \frac{T}{2}}$$

(80)

One of the methods to model transportation delay with a transfer function is Padé approximation. The first order Padé approximation of the transportation delay is:

$$G_{Pade}(s) = \frac{-\dfrac{T_S}{4} \cdot s + 1}{\dfrac{T_S}{4} + 1} \tag{81}$$

Finally, the transfer function of the plant that includes transport delay is:

$$G_{RL}^{q\_real}(s) = G_{RL}^{q}(s) \cdot G_{Pade}(s) \tag{82}$$

$$G_{PI}(s) = \frac{K_P \cdot s + K_i}{s} \tag{83}$$

If PI controller (83) is used to control the current trough the inductor, the following transfer function of the closed loop system describes the dynamic response of the current to the current reference command in the Q axis:

$$G_{Icl}^{q}(s) = \frac{I_{inv}^{q}(s)}{I_{inv}^{q*}(s)} = \frac{G_{PI}(s) \cdot G_{RL}^{q}(s) \cdot G_{Pade}(s)}{1 + G_{PI}(s) \cdot G_{RL}^{q}(s) \cdot G_{Pade}(s)} \tag{84}$$

Now, selection of parameters Kp and Ki determine dynamic response of the system and they have to be carefully chosen to keep system stable with large stability margin while keeping good transient response for reference tracking. For the aperiodic response and good gain margin for stable operation, following parameters have been selected for the 750kW wind turbine inverter.

Kp	Ki
0.3721	15.28

The transfer function from the current reference to inductor current on D axis is the same as for the Q axis. The block diagram of current controller in QD coordinates is shown in figure 2.20. Current controllers computes voltage references v_{inv}^{q*} and v_{inv}^{d*} that are

converted back to abc domain and after proper scaling, which depends on the DC link voltage, used to compute duration of PWM pulses for switches in the power converter.
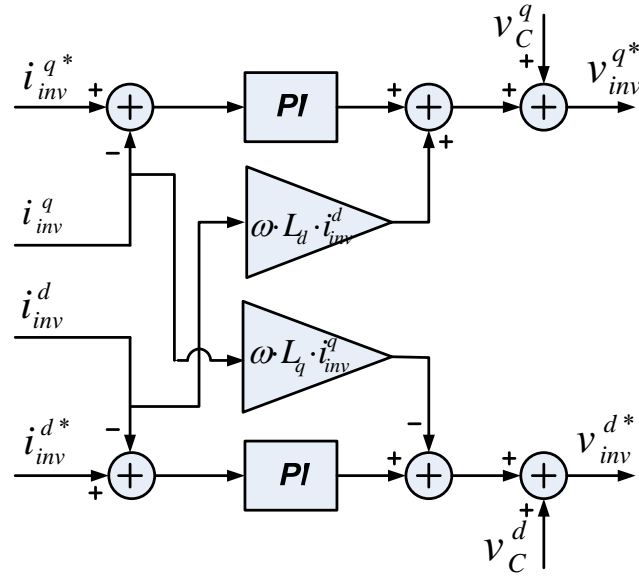
Figure 2.20. Inverter current controller

Space vector PWM algorithm form the Appendix A then produces actual phase voltages on the converter's terminals.

2.3.4. Permanent Magnet Synchronous Generator

Permanent magnet synchronous generators (PMSG) have been increasingly used in wind energy industry due to their advantages over other types of generators. Main advantage of PMSG over induction generators is no need for reactive power. A PMSG has permanent magnets on rotor that produce magnetic flux, meaning that no coil is needed on the rotor which results in higher efficiency compared to standard synchronous generators. Permanent magnets can be mounted on the rotor of the PMSG in two ways: surface mounted or interior mounted (IPM). Also, geometric distribution of magnetic flux

can be trapezoidal or sinusoidal. Machines with trapezoidal distribution of magnetic flux are mostly used as brushless DC motors (BLDC), while sinusoidal distribution is mainly used in generators. Stator voltage equations of a PMSG are:

$$v_a = R_s \cdot i_a + \frac{d\psi_a}{dt} \tag{85}$$

$$v_b = R_s \cdot i_b + \frac{d\psi_b}{dt} \tag{86}$$

$$v_c = R_s \cdot i_c + \frac{d\psi_c}{dt} \tag{87}$$

Flux linkage equations:

$$\psi_a = (L_\gamma + L_{aa}(\theta_e)) \cdot i_a + L_{ab}(\theta_e) \cdot i_b + L_{ac}(\theta_e) \cdot i_c + \psi_{PMa}(\theta_e) \tag{88}$$

$$\psi_b = L_{ab}(\theta_e) \cdot i_a + (L_\gamma + L_{bb}(\theta_e)) \cdot i_b + L_{bc}(\theta_e) \cdot i_c + \psi_{PMb}(\theta_e) \tag{89}$$

$$\psi_c = L_{ac}(\theta_e) \cdot i_a + L_{bc}(\theta_e) \cdot i_b + (L_\gamma + L_{cc}(\theta_e)) \cdot i_c + \psi_{PMc}(\theta_e) \tag{90}$$

Ideally, flux linkages produced by permanent magnets on the rotor, ψ_{PMa}, ψ_{PMb}, and ψ_{PMc} are sinusoidal. Non-ideal space distribution can be approximated by Fourier series of flux linkage harmonics:

$$\psi_{PMa}(\theta_e) = \psi_{PMa1}(\theta_e) + \psi_{PMa2}(2 \cdot \theta_e + \zeta_2) + \psi_{PMa3}(3 \cdot \theta_e + \zeta_3) + \dots \tag{91}$$

Electromechanical torque is:

$$T_{em} = -\frac{\partial W_{em}}{\partial \theta_e} \tag{92}$$

The energy of the electromagnetic field is given by the following equation (93):

$$W_{em} = \frac{1}{2} \cdot L_{aa}(\theta_e) \cdot i_a^2 + \frac{1}{2} \cdot L_{bb}(\theta_e) \cdot i_b^2 + \frac{1}{2} \cdot L_{cc}(\theta_e) \cdot i_c^2 + L_{ab}(\theta_e) \cdot i_a \cdot i_b + L_{bc}(\theta_e) \cdot i_b \cdot i_c + L_{ac}(\theta_e) \cdot i_c \cdot i_a +$$
$$+ \psi_{PMa}(\theta_e) \cdot i_a + \psi_{PMb}(\theta_e) \cdot i_b + \psi_{PMc}(\theta_e) \cdot i_c$$

By applying the same coordinate transformation from abc to QD reference frame, following equations can be derived:

$$v_d = R_s \cdot i_d + L_d \cdot \frac{di_d}{dt} - \omega_e \cdot L_q \cdot i_q \tag{94}$$

$$v_q = R_s \cdot i_q + L_q \cdot \frac{di_q}{dt} + \omega_e \cdot (L_d \cdot i_d + \psi_{PM}) \tag{95}$$

$$T_e = \frac{3}{2} \cdot P \cdot \left(\psi_{PM} \cdot i_q + (L_d - L_q) \cdot i_d \cdot i_q \right) \tag{96}$$

Inductances of the model in the QD reference frame are:

$$L_q = L_s + L_{mq} \tag{97}$$

$$L_d = L_s + L_{md} \tag{98}$$

Finally, the PMSG dynamic model in the QD reference frame is:

$$\frac{di_d}{dt} = \frac{1}{L_d} \left(v_d - R_s \cdot i_d + \omega_e \cdot L_q \cdot i_q \right) \tag{99}$$

$$\frac{di_q}{dt} = \frac{1}{L_q} \left(v_q - R_s \cdot i_q - \omega_e \cdot (L_d \cdot i_d + \psi_{PM}) \right) \tag{100}$$

$$T_e = \frac{3}{2} \cdot P \cdot \left(\psi_{PM} \cdot i_q + (L_d - L_q) \cdot i_d \cdot i_q \right) \tag{101}$$

The Simulink implementation of the PMSG model is shown in figure 2.21.

Figure 2.21.Simulink model of a PMSG

In the Laplace domain, the state space equations can be written as:

$$V_d(s) = R_s \cdot I_d(s) + L_d \cdot s \cdot I_d(s) - \omega_e \cdot L_q \cdot I_q(s) \tag{102}$$

$$V_q(s) = R_s \cdot I_q(s) + L_q \cdot s \cdot I_q(s) + \omega_e \cdot (L_d \cdot I_d(s) + \psi_{PM}) \tag{103}$$

In order to design current controller in the QD reference frame for vector control of the

PMSG, following equations in Laplace domain are of interest:

$$I_d(s) = \frac{V_d(s) + \omega_e \cdot L_q \cdot I_q(s)}{R_s + L_d \cdot s} \tag{104}$$

$$I_q(s) = \frac{V_q(s) - \omega_e \cdot (L_d \cdot I_d(s) + \psi_{PM})}{R_s + L_q \cdot s} \tag{105}$$

Voltage and torque equations of a permanent magnet synchronous machine in the D-Q

reference frame:

$$v_d = R_s \cdot i_d + L_d \cdot \frac{di_d}{dt} - \omega_e \cdot L_q \cdot i_q \tag{106}$$

$$v_q = R_s \cdot i_q + L_q \cdot \frac{di_q}{dt} + \omega_e \cdot (L_d \cdot i_d + \psi_{PM}) \tag{107}$$

$$T_e = \frac{3}{2} \cdot P \cdot \left(\psi_{PM} \cdot i_q + \left(L_d - L_q \right) \cdot i_d \cdot i_q \right) \tag{108}$$

Assuming that D and Q axes are real and imaginary axes in the complex plane, the PMSG voltage equation can be rewritten as a following phasor equation:

Phasor diagram of the PMSG is shown in Figure 2.22.
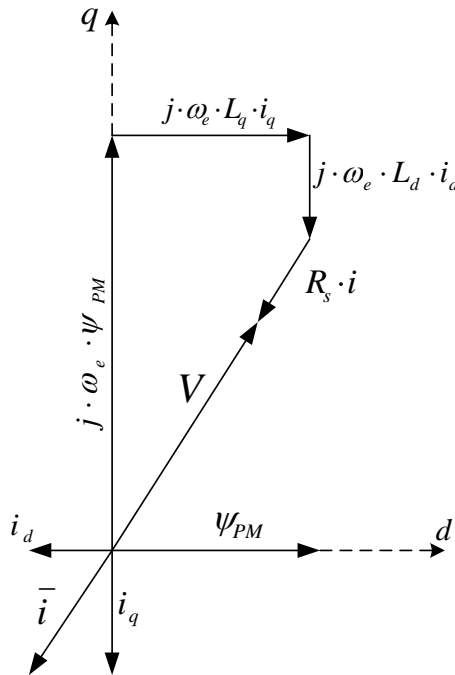
Figure 2.22. Phasor diagram of a PMSG

Interior mounted permanent magnet machines have different inductances along D and Q axes. If the D axis is oriented along the magnetic flux produced by the permanent magnet, then total inductance along this axis is lower than the inductance in the orthogonal Q axes due to low magnetic permeability of magnetic materials compared to the permeability of ferromagnetic core of the machine. For the purpose of this research, a 750kW PMSG is chosen as a generator of the wind turbine under consideration. Since

this wind turbine contains gearbox, a high speed PMSG is needed. Also, the rated voltage of this machine should be near 690V, as it is typical standard voltage level for WECS of similar sizes. Requirements for the generator needed for this system are very similar to the requirements for high power permanent magnet motor drives used in ship propulsion. One such motor is described in [40]. Parameters of the generator chosen for the development of the wind turbine model for this research are:

Rs=10mΩ

Ld=700μH

Lq=2mH

Ψ=1.428 T

The same method used for inverter controller design can be applied here. The transfer functions of interest for generator current controller design are the same as in the inverter control Q and D loops. Only difference is in the values of parameters. Due to difference in Ld and Lq inductance, different are the PI controller parameters. The parameters of the Id and Iq PI current controllers are given in tables 2.1 and 2.2 respectively.

Table 2.1

Kp	Ki
2.976	2.87

Table 2.2

Kp	Ki
0.907	26.07

Space vector PWM strategy from the Appendix A is applied for the generator side converter. The Simulink implementation of the current controller of the generator side converter is shown in figure 2.23.
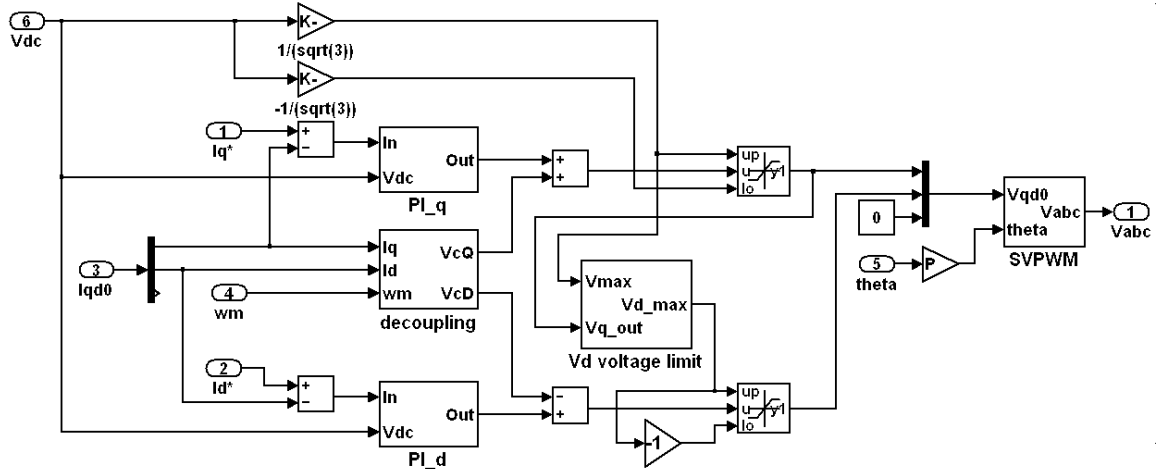
Figure 2.23. Current controller of a PMSG in QD reference frame

Structure of the decoupling block is shown in figure 2.24 and space vector modulator (SVPWM) in figure A.4 (Appendix A).
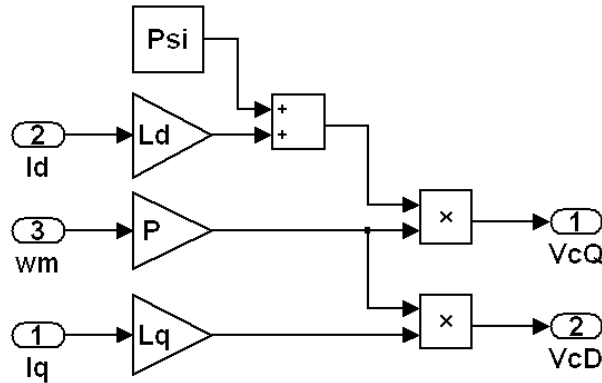
Figure 2.24 . The decoupling block of the PMSG current controller

The main challenge in utilization of IPM synchronous generator (IPMSG) is the fact that both Id and Iq current components produce torque. Therefore, it is necessary to define the method how to divide total demanded torque from the torque speed controller to the two torque components of the IPMSG. In this project, the following method has been proposed. The main constraints of IPMSG operations are maximum voltage and rotational speed. From the phasor diagram, voltage on the IPMSG terminal is:

$$V = \sqrt{\left(\omega_e \cdot \psi_{PM} - \omega_e \cdot L_d \cdot I_d\right)^2 + \left(\omega_e \cdot L_q \cdot I_q\right)^2} - R_s \cdot \sqrt{I_d^2 + I_q^2} \qquad (109)$$

This voltage is limited by the voltage in DC link for normal rectifier operation. If space vector modulation is used, the peak voltage on the IPMSG terminal is:

$$V \le \frac{V_{DC}}{\sqrt{3}} \qquad (110)$$

The terminal voltage reaches the maximum values at the rated rotational speed. In order to allow operation on increased rotational speed, field weakening has to be applied. The current Id is used for this purpose. Following equation is used to compute Id current reference:

$$I_d^*(t) = K_1 \cdot \omega_r + K_2 \cdot \omega_r^2 \qquad (111)$$

Constants K1 and K2 are calculated based on voltage constraint equations (109) and (110). From the torque equation of PMSG, and knowing the Id current reference, the Iq reference can be calculated. Simulink block that computes Iq current reference is shown in figure 2.25.
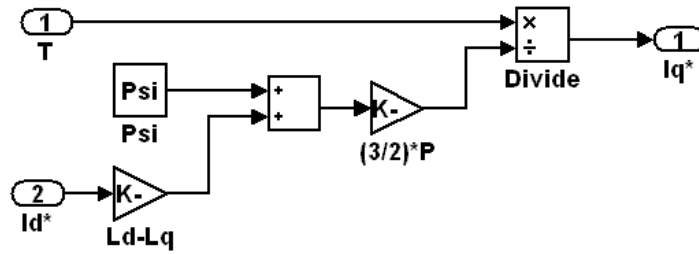
Figure 2.25. Iq reference calculation for the generator current controller

2.3.5. Modeling of the DC link of the double power conversion system

The voltage of the DC link depends on the balance between DC currents of the rectifier and inverter. Maximum magnitude of line to neutral voltage of a three phase PWM converter modulated by space-vector modulation is given by the equation (110). From (11) it follows that line to line RMS voltage of the three phase power converter is equal to:

$$V_{L-L} = \frac{V_{DC}}{\sqrt{2}} \qquad (112)$$

For generators with rated line to line voltage V_{L-L}^n, the minimum DC link voltage is

$$V_{DC}^{min} = \sqrt{2} \cdot V_{L-L}^n \qquad (113)$$

This is the theoretical minimum, and it has to be increased to include voltage drops across semiconductor switching components and line resistances. The model of DC link is shown in figure 2.29. The currents of the DC link sides of each power converter can be calculated by applying the energy conservation law. The computation of the DC link current of the generator side converter (rectifier) is shown in figure 2.26. Similarly, the computation of the DC link current of the grid side converter is shown in figure 2.27.
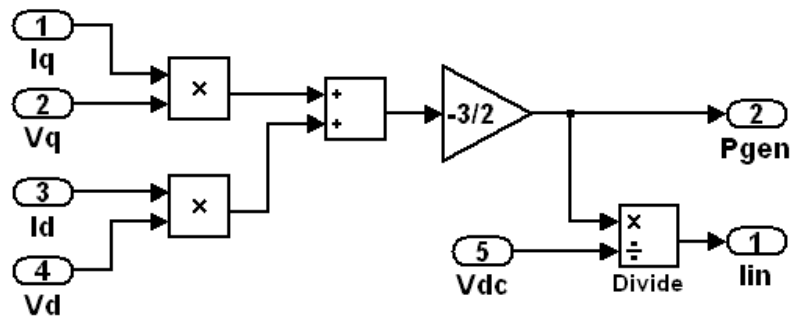
Figure 2.26. DC link current, generator side
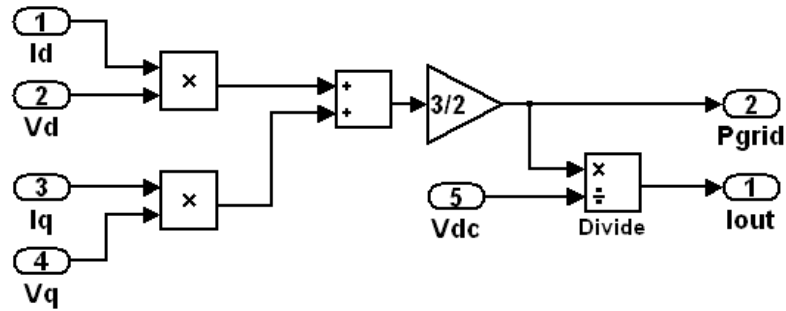
Figure 2.27. DC link current, inverter side

The model of the DC link capacitor is shown in figure 2.28. Figure 2.29 shows the complete model of the DC link of the wind turbine.
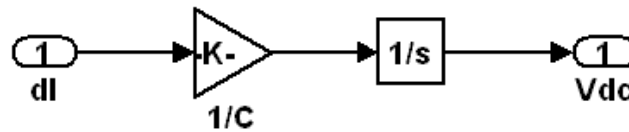
Figure 2.28. Simulink model of the DC link capacitor
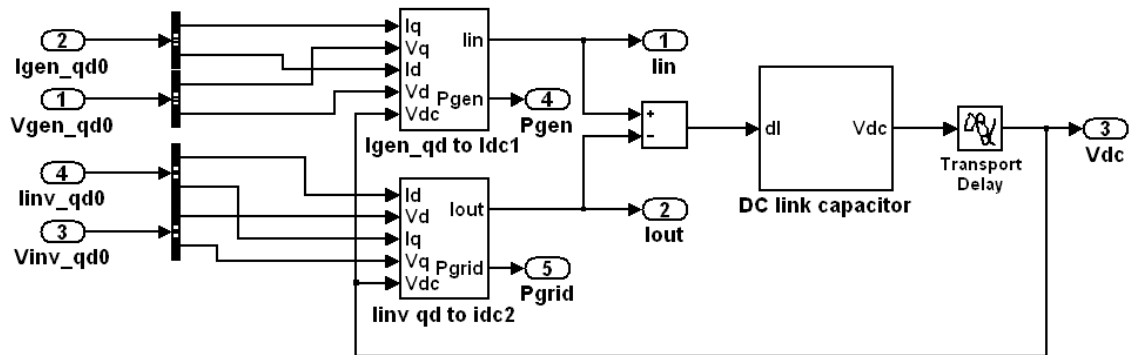
Figure 2.29. Complete simulink model of the of DC link of the double conversion system

Simulink models of each block from the figure 2.10 have been developed in this chapter. Complete model of the electrical subsystem for integration with FAST wind turbine simulation model is shown in figure 2.30. Figure 2.30 shows complete Simulink model of the double conversion system that is expanded in following chapters to include drivetrain model with active vibration damping controller as well as lithium-ion ultracapacitor energy storage. Complete model of a wind turbine is shown in figure 3.19.
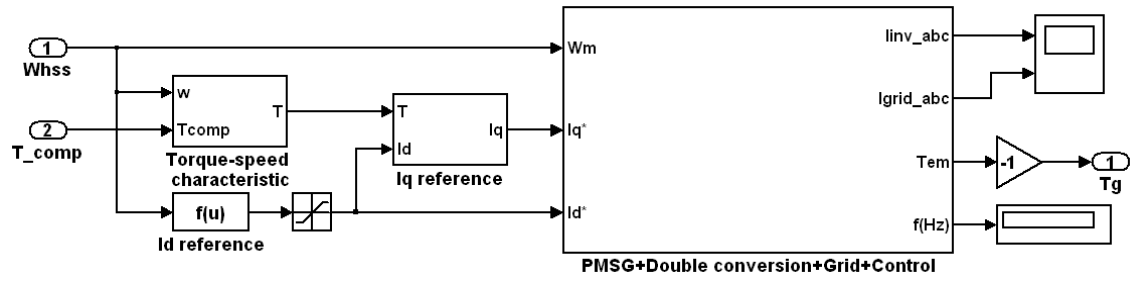
Figure 2.30. Simulink block of the electrical subsystem of the 750kW turbine

3. Mechanical stress reduction of a variable speed wind turbine drivetrain

In wind turbines, the gearbox connects the main rotor, called low-speed shaft (LSS), and the generator on the high speed shaft (HSS), as shown in Figure 3.1. The gear ratio depends on size of the turbine and rated rotational speed of the generator. Larger wind turbines rotate slowly and higher gear ratios are required. Variations in wind velocity cause variable torque on the main shaft of the turbine. This torque is balanced by the electromechanical torque of the generator and friction. Torque difference between the main shaft and the generator shaft is acting on the gearbox, causing torsion deflection. In steady state, when rotational speed is constant, the torsion angle between the main shaft and the generator shaft would remain constant. However, due to variations in torque from the main shaft, as well as variations of the generator torque, torsion angle between two shafts varies. These variations in torsion angle are unwanted vibrations that increase dynamic loads and fatigue of the gearbox components. The most dangerous vibrations are those whose frequencies are equal to the natural frequencies of the gearbox. Therefore, in order to reduce mechanical stress on the gearbox components, it is desirable to reduce vibrations at the resonant frequencies. A novel generator torque control method aimed at reducing resonant vibrations of the gearbox components is proposed in this chapter. This control strategy reduces resonant torsion vibrations of the shafts between gear stages by introducing compensating torque as additional electromechanical torque of the generator with goal to counteract torque components from the main shaft that cause torsional vibrations at resonant frequencies of the drivetrain. The compensating torque consists of torque components with frequencies equal to the resonant frequencies of the drivetrain whose amplitudes are variable in time. The amplitudes of compensating torque

components have to be proportional to the amplitudes of torque components from the main shaft that are going to be compensated, with matching phase angle in order to avoid increase instead of decrease of unwanted torsional vibrations. The average of the compensating torque is equal to zero thus not affecting rotational speed control of the wind turbine. Compensating torque is generated by adjusting the generator current reference, responsible for torque-speed characteristic as described in the previous chapter. Due to the limited bandwidth of the generator current control loop, not all vibrations can be compensated. However, all torsional vibration components that are within the current controller bandwidth can be effectively damped. This chapter first explains the multibody spring damper model of a typical three stage wind turbine gearbox. Parameters of the model are calculated from the real field test data of a 750kW wind turbine. It is followed by description of the control strategy that damps resonant vibrations of the drivetrain. The effectiveness of the proposed strategy is verified by extensive Matlab/Simulink computer simulations.
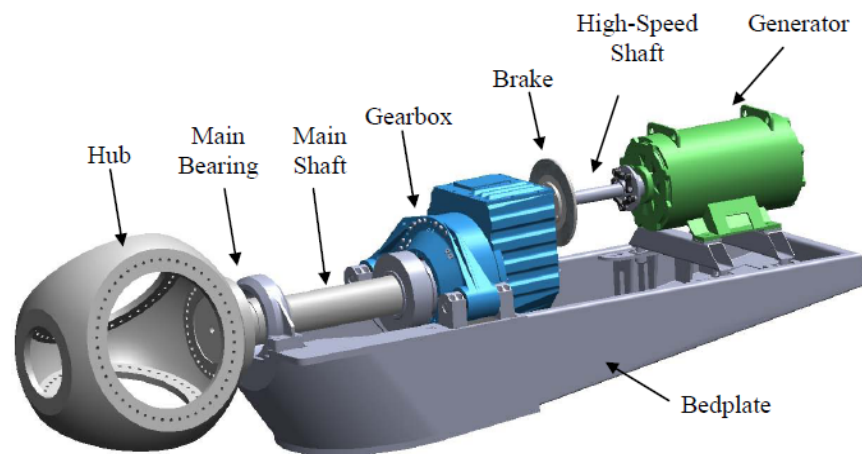
Figure 3.1. Wind turbine drivetrain [42]

3.1. Modeling of a wind turbine drivetrain

   Wind turbine gearbox is a complex mechanical system that can be modeled in several ways, depending on required level of accuracy. The simplest model, widely used in available design codes, uses dual-mass spring damper system. This model approximates entire drive train as two ineartias connected by flexible shaft. This model has two degrees of freedom and, therefore, two natural frequencies. One natural frequency is equal to zero, representing rigid body mode, while another one is equal to the global resonant frequency of the gearbox. The moment of inertia of the gearbox is lumped to one of inertias at the flexible shaft's ends. This type of model is widely used in many aerodynamic wind turbine simulation codes [68]. Although very simple, this model gives insight into global behavior of the drivetrain. On the other hand, this model provides no information about internal dynamics of the gearbox itself. Next step in modeling of the drivetrain is to increase the number of degrees of freedom of the model. Typical gearbox configuration used in wind industry has multiple gear stages. More detailed model assumes that each gear set is a lumped moment of inertia, while shafts that connect them are flexible linear spring damper systems. This model captures more details of the gearbox internal dynamics, compared to the dual-mass model. However, it does not capture dynamical behavior of individual gears, flexibility of gear teeth and the nonlinearities in the gear teeth interactions. Next level in modeling includes modeling of the gear mesh flexibility as a linear spring damper system, for each coupled gear pairs. This model can be further expanded by taking into account nonlinear effects of gear teeth bending thus forming more accurate nonlinear model. Also, interactions between gearbox

shafts, bearings, and housing can be modeled as linear or nonlinear spring damper systems resulting in very high order model that captures many details of dynamical behavior within the gearbox. Finally, the most detailed model can be obtained by using finite element analysis. This model can provide detailed data about loads and fatigue of gearbox components indentifying the most critical points. However, models based on finite elements are numerically complex and it would be very difficult to integrate such models with the model of the other components of a wind turbine. Such complete model would be computationally demanding and impractical for use since simulations would take large amounts of time. Compromise solution is to use reasonably detailed multiple degree of freedom spring damper model of a gearbox that can be integrated with the complete model of a wind turbine. Simulation results of such model, particularly torque profiles at various points within the drivetrain, can be further used as input for more detailed nonlinear of finite element based models to further investigate mechanical loading and dynamical behavior of gearbox components.
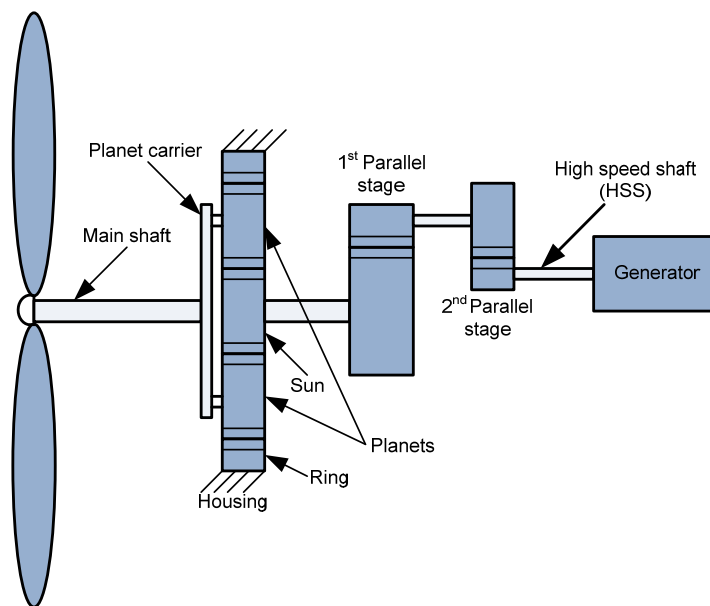
Figure 3.2. Wind turbine drivetrain with a three stage gearbox

Good references on detailed gearbox modeling are [42] and [43]. For the purpose of this research on drivetrain mechanical stress reduction, a medium level model of the gearbox is developed. In the 750kW wind turbine used as a test case in this research, the gearbox has three stages, as illustrated in Figure 3.2. First stage is a planetary gear set needed to handle greater torque loads. Second and third are parallel stages to provide higher gear ratios. The flexible multibody model which models only flexibility of drivetrain shafts is illustrated in Figure 3.3.

$$\Delta\theta_1 = \theta_R - \theta_1'$$
$$\Delta\theta_2 = \theta_1' - \theta_2'$$
$$\Delta\theta_3 = \theta_2' - \theta_3'$$
$$\Delta\theta_4 = \theta_3' - \theta_G'$$
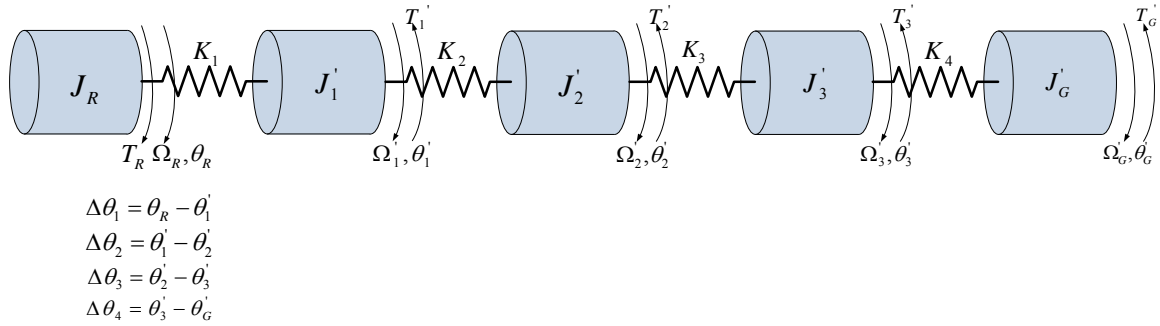
Figure 3.3. Five-mass model of the drivetrain

In this model, rotor of a wind turbine and main shaft (LSS) is represented as moment of inertia J_R. Planetary gear set consists of the ring that is coupled with the gearbox housing. Ring itself has gear teeth on its inner side. Inside the ring, three or more gears rotate. These gears are called planets and they are mechanically coupled by planet carrier. The planet carrier is also the input, or low speed shaft of the system. The planets are coupled through gear teeth contact to the innermost gear called sun. The sun's shaft is a high speed shaft or output of the assembly. Planet carrier, planets and sun are shown in figure 3.4. Planetary gear stage is represented as a lumped moment of inertia J_1'. This moment of inertia is scaled to the LSS side, by multiplying moment of inertia of the sun and output shaft of the planetary stage by square of the gear ratio n_1 of this gear set.

$$J_1^{'} = J_{Planet.} + n_1^2 \cdot J_{sun} \tag{1}$$
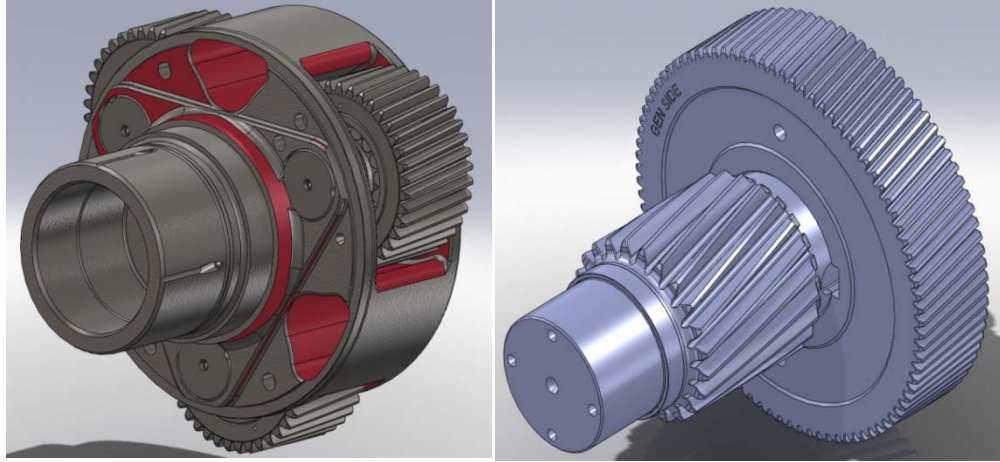
Figure 3.4. Planet carrier and planets (left), sun and first parallel

stage pinion (right)

Flexible shaft that connects rotor inertia and the planetary gear stage is represented as spring damper system with stiffness coefficient K_1. The sun and the first parallel stage pinion are connected by the flexible shaft with stiffness coefficient $K_2^{'}$. First parallel stage that consists of pinion and wheel is represented as a lumped moment of inertia $J_2^{'}$. This moment of inertia is also scaled to the LSS side of the drivetrain.
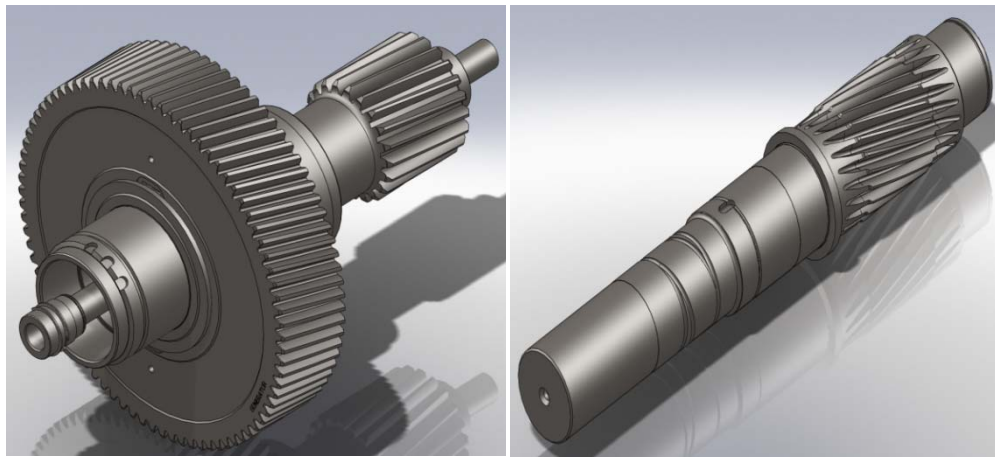
Figure 3.5. First parallel stage wheel with second parallel stage pinion (left).
Second parallel stage wheel (right)

$$J_2' = n_1^2 \cdot \left(J_{1stPinion} + n_2^2 \cdot J_{1stWheel} \right) \qquad (2)$$

Where $J_{1stPinion}$ and $J_{1stWheel}$ are moments of inertia of first parallel gear set pinion and wheel respectively. Gear ratio of the first parallel gear stage is n_2. First parallel stage's wheel is coupled to the second parallel stage wheel. Figure 5 shows these gear sets. Flexible shaft between first and second parallel gear stages is represent by stiffness coefficient K_3'. Second parallel gear stage is represented by lumped moment of inertia J_3' which is also scaled to the LSS side of the drivetrain.

$$J_3' = n_1^2 \cdot n_2^2 \cdot \left(J_{2ndPinion} + n_3^2 \cdot J_{2ndWheel} \right) \qquad (3)$$

Gear ratio of the second parallel gear set is n_3. Finally, the second parallel gear set's wheel is coupled to the generator by the flexible shaft represented by the stiffness coefficient K_4'. This shaft is the high speed shaft of the system. The generator is represented by the moment of inertia J_G which scaled to the LSS side.

$$J_G' = n_1^2 \cdot n_2^2 \cdot n_3^2 \cdot J_G \qquad (4)$$

Following set of differential equations is a mathematical representation of this five-mass model of the drivetrain:

$$J_R \cdot \frac{d\omega_R}{dt} = T_R - K_1 \cdot (\theta_R - \theta_1') - D_1 \cdot \left(\omega_R - \omega_1' \right) \qquad (5)$$

$$J_1' \cdot \frac{d\omega_1'}{dt} = K_1 \cdot (\theta_T - \theta_1') + D_1 \cdot \left(\omega_T - \omega_1' \right) - K_2' \cdot \left(\theta_1' - \theta_2' \right) - D_2 \cdot \left(\omega_1' - \omega_2' \right) \qquad (6)$$

$$J_2' \cdot \frac{d\omega_2'}{dt} = K_2' \cdot (\theta_1' - \theta_2') + D_2 \cdot \left(\omega_1' - \omega_2' \right) - K_3' \cdot \left(\theta_2' - \theta_3' \right) - D_3 \cdot \left(\omega_2' - \omega_3' \right) \qquad (7)$$

$$J_3' \cdot \frac{d\omega_3'}{dt} = K_3' \cdot (\theta_2' - \theta_3') + D_3 \cdot \left(\omega_2' - \omega_3' \right) - K_4' \cdot \left(\theta_3' - \theta_G' \right) - D_4 \cdot \left(\omega_3' - \omega_G' \right) \qquad (8)$$

$$J_G' \cdot \frac{d\omega_G'}{dt} = K_4' \cdot (\theta_3' - \theta_G') + D_4 \cdot \left(\omega_3' - \omega_G' \right) - T_G' \qquad (9)$$

$$\omega_R = \frac{d\theta_R}{dt} \tag{10}$$

$$\omega_1' = \frac{d\theta_1'}{dt} \tag{11}$$

$$\omega_2' = \frac{d\theta_2'}{dt} \tag{12}$$

$$\omega_3' = \frac{d\theta_3'}{dt} \tag{13}$$

$$\omega_G' = \frac{d\theta_G'}{dt} \tag{14}$$

This system of ten linear differential equations can be rewritten in the state space form as:

$$\dot{x} = A \cdot x + B \cdot u \tag{15}$$

$$y = C \cdot x \tag{16}$$

Where the system matrix is:

$$
A = \begin{bmatrix}
-\dfrac{D_1}{J_R} & \dfrac{D_1}{J_R} & 0 & 0 & 0 & -\dfrac{K_1}{J_R} & \dfrac{K_1}{J_R} & 0 & 0 & 0 \\[2mm]
\dfrac{D_1}{J_1'} & \left(-\dfrac{D_1}{J_1'}-\dfrac{D_2}{J_1'}\right) & \dfrac{D_2}{J_1'} & 0 & 0 & \dfrac{K_1}{J_1'} & \left(-\dfrac{K_1}{J_1'}-\dfrac{K_2}{J_1'}\right) & \dfrac{K_2'}{J_1'} & 0 & 0 \\[2mm]
0 & \dfrac{D_2}{J_2'} & \left(-\dfrac{D_2}{J_2'}-\dfrac{D_3}{J_2'}\right) & \dfrac{D_3}{J_2'} & 0 & 0 & \dfrac{K_2}{J_2'} & \left(-\dfrac{K_2'}{J_2'}-\dfrac{K_3'}{J_2'}\right) & \dfrac{K_3'}{J_2'} & 0 \\[2mm]
0 & 0 & \dfrac{D_3}{J_3'} & \left(-\dfrac{D_3}{J_3'}-\dfrac{D_4}{J_3'}\right) & \dfrac{D_4}{J_3'} & 0 & 0 & \dfrac{K_3'}{J_3'} & \left(-\dfrac{K_3'}{J_3'}-\dfrac{K_4'}{J_3'}\right) & \dfrac{K_4'}{J_3'} \\[2mm]
0 & 0 & 0 & \dfrac{D_4}{J_G'} & -\dfrac{D_4}{J_G'} & 0 & 0 & 0 & \dfrac{K_4'}{J_G'} & -\dfrac{K_4'}{J_G'} \\[2mm]
1 & 0 & 0 & 0 & 0 & 0 & 0 & 0 & 0 & 0 \\
0 & 1 & 0 & 0 & 0 & 0 & 0 & 0 & 0 & 0 \\
0 & 0 & 1 & 0 & 0 & 0 & 0 & 0 & 0 & 0 \\
0 & 0 & 0 & 1 & 0 & 0 & 0 & 0 & 0 & 0 \\
0 & 0 & 0 & 0 & 1 & 0 & 0 & 0 & 0 & 0
\end{bmatrix} \tag{17}
$$

The state vector is:

$$x = \begin{bmatrix} \omega_R & \omega_1' & \omega_2' & \omega_3' & \omega_G' & \theta_R & \theta_1' & \theta_2' & \theta_3' & \theta_G' \end{bmatrix}^T \tag{18}$$

Inputs to the system are torque of the wind turbine rotor and electromechanical torque of the generator:

$$u = \begin{bmatrix} T_R & T_G' \end{bmatrix}^T \qquad (19)$$

Output of the system are rotational speed of the LSS and HSS, as well as torsion angles of the shafts.

$$y = \begin{bmatrix} \omega_R & \omega_G' & \theta_R - \theta_1' & \theta_1' - \theta_2' & \theta_2' - \theta_3' & \theta_3' - \theta_G' \end{bmatrix}^T \qquad (20)$$

$$C = \begin{bmatrix} 1 & 0 & 0 & 0 & 0 & 0 & 0 & 0 & 0 & 0 \\ 0 & 0 & 0 & 0 & 1 & 0 & 0 & 0 & 0 & 0 \\ 0 & 0 & 0 & 0 & 0 & 1 & -1 & 0 & 0 & 0 \\ 0 & 0 & 0 & 0 & 0 & 0 & 1 & -1 & 0 & 0 \\ 0 & 0 & 0 & 0 & 0 & 0 & 0 & 1 & -1 & 0 \\ 0 & 0 & 0 & 0 & 0 & 0 & 0 & 0 & 1 & -1 \end{bmatrix} \qquad (21)$$

Eigenvalues of the matrix A are natural frequencies of the model. Complex conjugate pairs correspond to resonant vibrations of the torsion angles. Pair of eigenvalues equal to zero correspond to rigid body modes of LSS and HSS. This model is implemented in Matlab/Simulink and integrated into complete wind turbine model described in the previous chapter.

3.2. Model parameters calculation

This section briefly describes calculation of parameters for the derived five mass model of the drivetrain, while more details can be found in reference [67]. Field test data of a 750kW experimental wind turbine are the basis for parameter calculation as well as SolidWorks model of the gearbox of this wind turbine. Test data and SolidWorks model are provided by NREL. The experimental wind turbine is tested on the dynamometer as a fixed speed induction generator with dual speed operations. The dual speed operation is accomplished by switching the stator pole winding arrangement from six poles to four pole configuration. The 750kW experimental turbine can run at two rotational speeds, one for high speed (four pole winding configuration) and another one for low wind velocities (six pole winding configuration). Induction generator is connected directly to the grid, without any power conversion system. This turbine belongs to the fixed speed class of turbines since it operates at constant rotational speed despite wind speed variations except for changes between high and low wind speed cases. First data set is obtained by applying a mechanical brake on the HSS of the drivetrain (figure 3.6). Wind speed was constant, and after applying the brake torque measured on the LSS showed oscillatory response as a result of torsional vibrations in the drivetrain. By approximating the frequency of this oscillatory response with its first harmonic, the dominant natural frequency of the drivetrain can be determined. When brake is engaged, the generator inertia does not contribute to the dynamic response. Therefore, the system can be represented as a single degree of freedom model with rotor inertia on one side, and flexible shaft fixed on the another side.
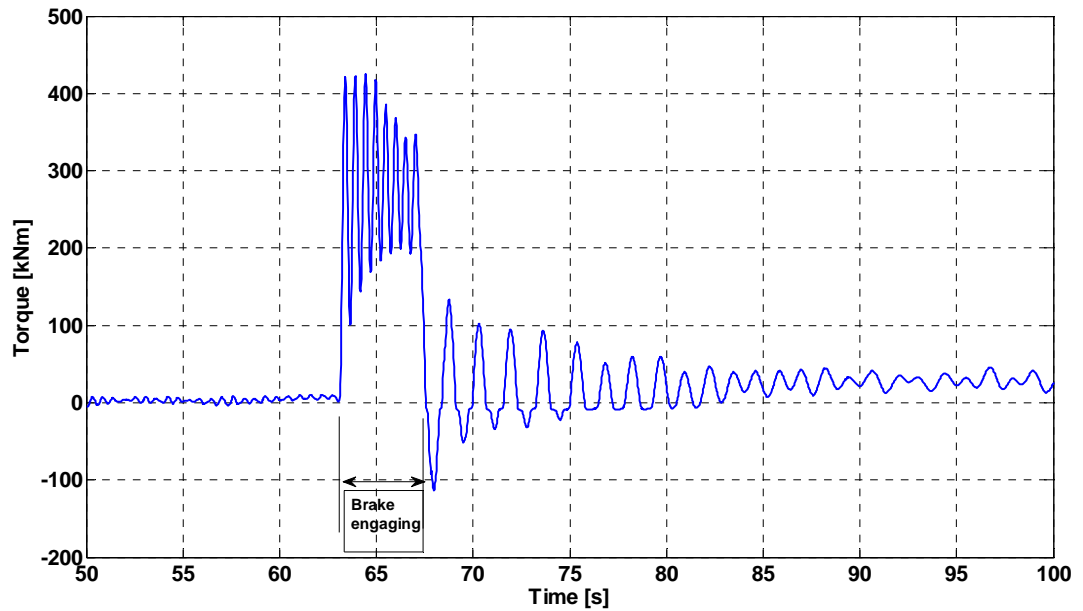
Figure 3.6. Breaking event

Next dataset used for parameter calculation is shown in figure 3.7. The turbine rotational speed is changed from low to high speed and oscillatory response is recorded. In this case, generator inertia and electromechanical torque contribute to the response.
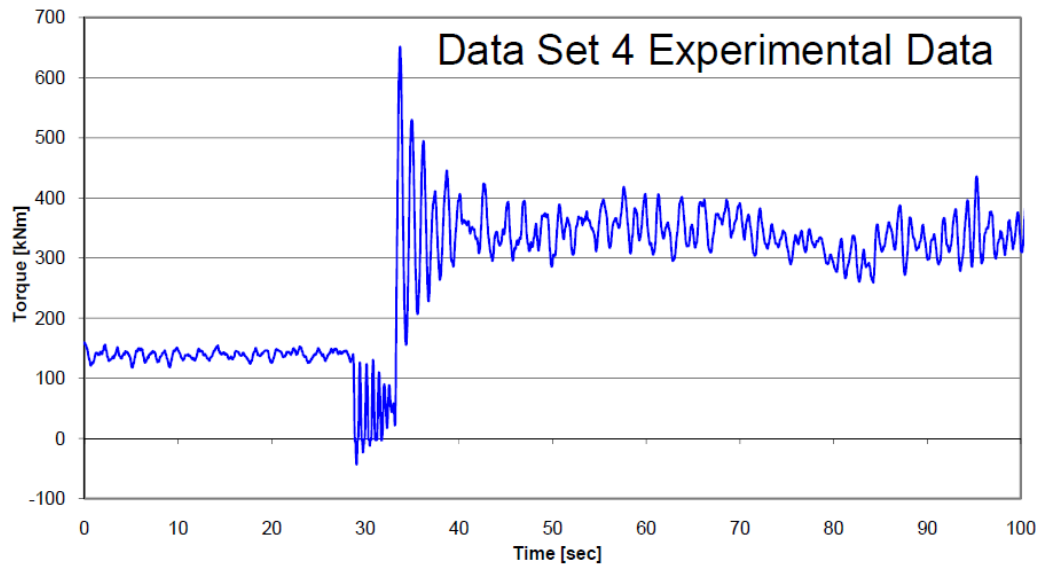
Figure 3.7. Change in rotational speed

From this data, parameters of the equivalent two mass model can be calculated, by approximating oscillatory response with its dominant resonant frequency component. In the two mass model two moments of inertia are connected by the flexible shaft with total equivalent stiffness coefficient. From the SolidWorks model, moments of inertia of gearbox components, shown in figures 3.4 and 3.5 are extracted. Stiffness coefficients of shafts connecting gear sets are calculated from the material characteristics used in this gearbox. The inertias, stiffness coefficients, and gear ratios are given in tables 3.1, 3.2, and 3.3.

I_h	998138.4	I_{P_1}	0.4
I_{PC}	116.72	I_{G_2}	3.42
I_S	1.02	I_{P_2}	0.08
I_{G_1}	31.72	I_{Ge}	24

Table 3.1. Moments of inertia of the gearbox components

k_1	3.69E+07
k_2	2.45E+07
k_3	2.70E+08
k_4	2.08E+06

Table 3.2. Equivalent stiffness coefficients

N_1	4.714
N_2	3.565
N_3	4.00

Table 3.3. Gear ratios of the gear stages

Inertia of the rotor J_R is calculated from the FAST model of the 750kW NREL experimental turbine. From these data, equivalent stiffness and moment of inertia of a single degree of freedom model is calculated. The calculated natural frequency of this model showed good matching to the experimental data [67], confirming accuracy of stiffness coefficients from the table 2. From the available data, it is not possible to calculate damping coefficients $D_1 - D_4$. However, the worst case is if these values are equal to zero meaning that there is no damping of torsional vibrations due to friction. For

the purpose of model development used in this research, these coefficients are set to 100, which is smaller than the least stiffness coefficient, K4 for four orders of magnitude. This low frictional damping in the system results in more challenging task for the vibration damping controller, as major contribution to damping has to be result of generator torque control strategy. Finally, by substituting values for moments of inertia, stiffness, and damping coefficients to the state space model described in the previous sections, following natural frequencies are calculated:

f1	0
f2	2.96Hz
f3	292Hz
f4	371Hz
f5	2214Hz

Table 3.4. Natural frequencies of the five mass drivetrain model.

With known parameters of the model, the active vibration damping controller can be designed and tested by computer simulations of the full model of the 750kW wind turbine.

3.3. Active generator torque control for drivetrain vibration damping

This section describes the principles of resonant oscillation damping of the gearbox by controlling the generator torque. It also shows a design procedure for the controller that damps the resonant oscillations at three natural frequencies of the previously derived gearbox model. Aerodynamic torque at the turbine shaft causes rotation of the drivetrain. Aerodynamic torque on the rotor is balanced by the electromechanical torque of the generator. Torque difference between the aerodynamic torque and generator torque causes acceleration or deceleration of the shaft. Besides the average value, the aerodynamic torque contains variable components, as a result of variations in wind speed. Below rated speed, generator torque of a variable speed wind turbine is usually controlled to follow the cube of the rotational speed. Due to the large inertia of the wind turbines, rotational speed variations are much slower than variations of the aerodynamic torque. The torque difference between the low and high speed shafts causes rotational motion, and the variable (higher frequency) components within the torque may excite the gearbox modes, increasing the wear and tear of the gears. Torque oscillations at the natural frequencies can be very harmful to the gearbox and it should be minimized. To reduce these unwanted torque components, the torque command to the power converter includes the damping components to remove or reduce the torque components that may excite the gearbox modes. A simplified block diagram of the proposed control strategy is shown in Figure 3.8. As shown in figure 8, stress damper controller has to estimate the amount of unwanted and potentially harmful torque components that are acting on the gearbox. This can be done by measuring torque at the LSS as well as HSS. Installing torque sensors can

be very impractical. Therefore, the method proposed in this paper uses indirect effects caused by the torque difference acting on the gearbox to identify harmful components that should be removed.
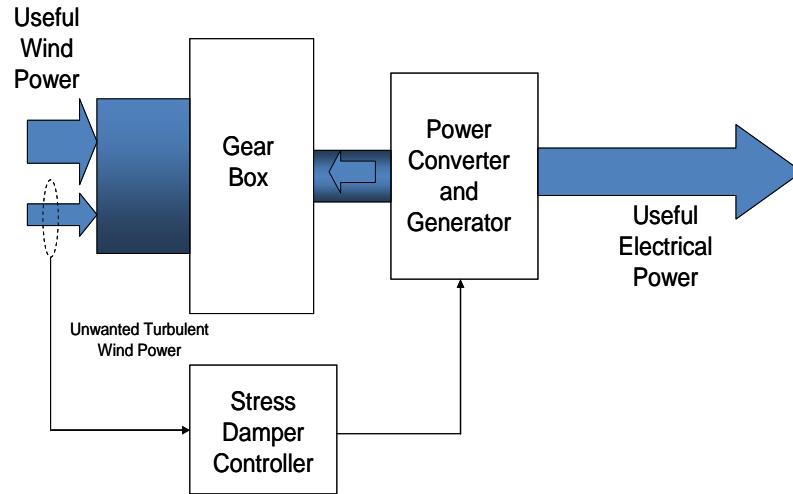
Figure 3.8. Active vibration damping concept

From the equations (13) to (18), it can be seen that acceleration of a HSS (equation 14) contains the information about all angles and rotational speeds of various gearbox stages. By appropriate filtering of the acceleration signal, the information about resonant oscillations within the gearbox can be extracted. This information can then be used to calculate the compensation torque that would reduce these oscillations. The concept of the stress reduction control strategy based on the processing of the acceleration signal is illustrated in Figure 3.9. The rotational speed of HSS is first processed through a washout block which calculates acceleration of the shaft. The acceleration signal is next processed through parallel band-pass filters where the central frequency of each band-pass filter (BPF) is set to one particular resonant frequency of the gearbox. The output of each filter provides the level of oscillation at each resonant frequency. These signals are processed through compensators (CMP) that produce output torque components that should be

added to the generator torque in order to increase damping of the resonant oscillations. Compensators are low pass filters, as illustrated in the design example. Due to the limited bandwidth of the generator current controller, only resonant oscillations at frequencies within the one half of the frequency bandwidth of the current controller are compensated.
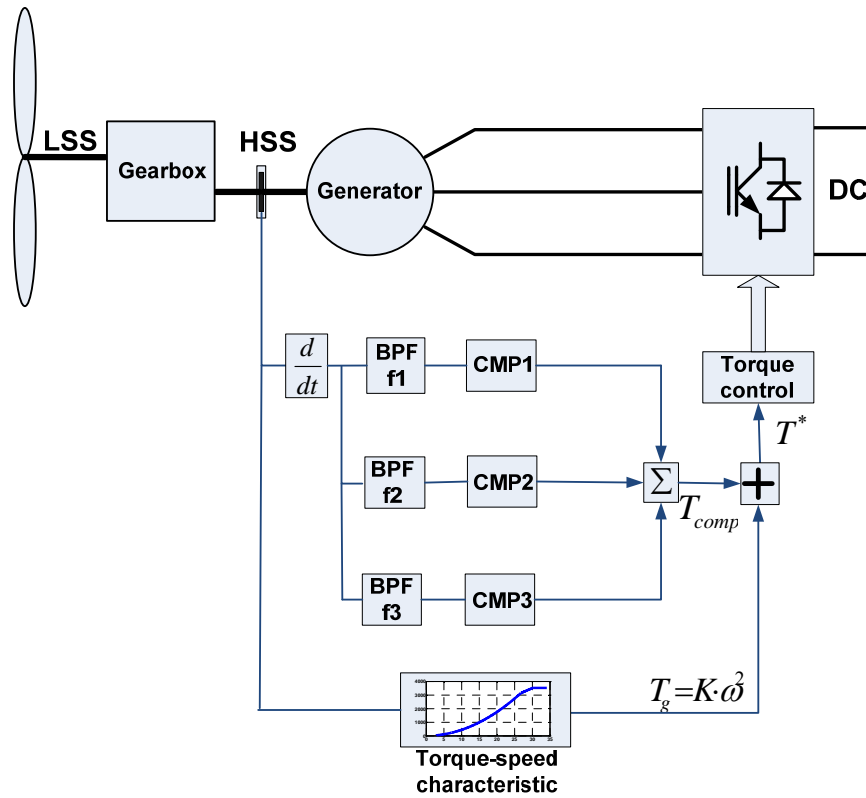
Figure 3.9. Resonant vibration damping controller

The compensating torque that is added to the optimum torque reference prevents the harmful torque components from entering the gearbox. By decreasing the excitation of the resonant modes, resonant oscillations are reduced as well. Therefore, wear and fatigue of the internal components of the gearbox is reduced. Band pass filters of the controller introduce additional poles in the system. It is important that these poles are well damped and that compensators do not move these poles into right half-plane of the complex plane. Transfer functions for each of the band pass filters are given bellow:

$$G_{BPF-fri}(s) = \frac{\beta_i \cdot s}{s^2 + \alpha_i \cdot \mathbf{2} \cdot \pi \cdot f_{ri} \cdot s + (\mathbf{2} \cdot \pi \cdot f_{ri})^2}$$ (22)

The band pass filters are of the second order. Parameters α and β in transfer functions dictate pole locations, damping, and gain of each band pass filter. These parameters must be carefully chosen since they greatly affect overall system dynamics. The outputs of the band-pass filters are signals that are proportional to the level of oscillation at each resonant frequency. Series compensators should produce signals that are of right magnitude and phase that when added to the generator torque reference, results in damping of resonant oscillations. In this research, compensators are low pass filters. Low pass filters introduce phase lagging, and filter gain. Band pass filter has zero in the origin. The pole of the low pass filter limits the gain at the higher frequencies. Proper selection of cut off frequency and filter gain should result in increased damping of the drive train resonant mode.

$$G_{CMP}(s) = \frac{K_{CMP}}{s + \omega_{CMP}}$$ (23)

The main challenge in designing procedure of this controller is to choose large number of parameters needed for proper function of the system. For the system that compensates vibration at three resonant frequencies, following parameters have to be selected: $\beta_1, \beta_2, \beta_3, \alpha_1, \alpha_2, \alpha_3, K_{CMP1}, K_{CMP2}, K_{CMP3}, \omega_{CMP1}, \omega_{CMP2}$, and ω_{CMP3}. The goal of the controller synthesis is to increase damping of the resonant modes in the closed loop system. The method used in this research is based on the search algorithm that varies controller's parameters and returns values that maximize damping of resonant modes. The algorithm computes state space model of the entire closed loop system in each iteration, computes eigenvalues of the system matrix, and plots them on the complex

plane. Algorithm keeps changing parameters, and as a result, a graph that shows pole locations is produced. Parameters that maximize damping are then selected and verified in simulations. The block diagram of the building blocks that form the state space model of the entire control loop is shown in figure 3.10.
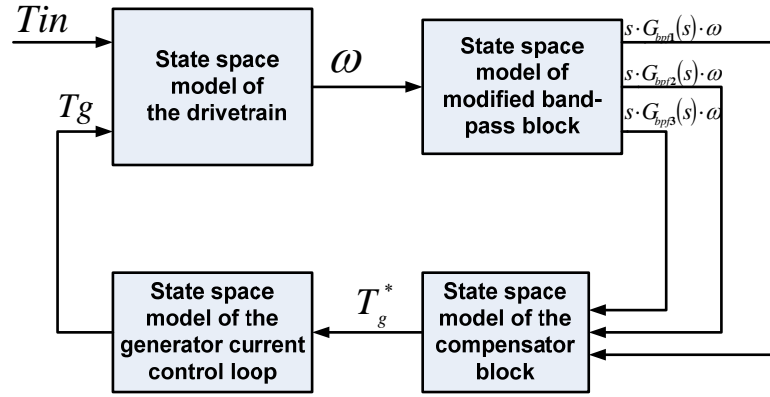
Figure 3.10. Closed loop state space model building

The state space model of the drivetrain is given by equations (15) and (16), with system matrix (17), state vector (18) and modified output matrix:

$$C=[0\ 0\ 0\ 0\ n\ 0\ 0\ 0\ 0\ 0] \qquad (24)$$

In (24) n is the gear ratio of the gearbox. From the output matrix, it is clear that only generator speed is of interest for connection with other blocks. Since in the previously developed model all states were scaled to the input shaft, generator speed state has to be multiplied by the gear ratio. Generator speed, ω on the figure 3.10 is the input to the modified bypass filter block.

Bypass filter block consists of three bypass filters, with additional differentiator at the input to compute the angular acceleration from rotational speed. This block is illustrated in figure 3.11. It should be noticed here that transfer functions from the modified band-pass block are similar to (22) with the exception of s^2 term that includes first derivative

of the speed input calculation, while (22) takes acceleration as the input. The block on figure 3.11 has one input and three outputs, and it can be easily converted to state space model. Similarly, the compensation block has three inputs and one output as a sum of outputs of the compensators (23) on each channel. Outputs are summed and result is the torque reference command for the generator current controller. Generator current control loop is described in chapter 2. As described in chapter 2, the torque reference is used to compute references for Id and Iq current components of the generator current.
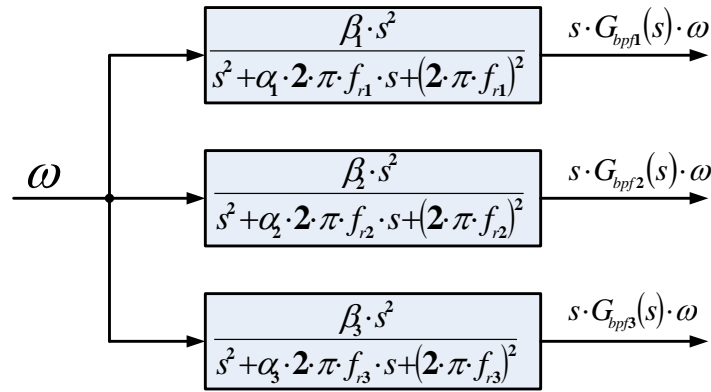
Figure 3.11. Modified band-pass filter block

The major challenge in taking the dynamics of the generator torque and current control system is difference between these two control loops due to difference in Ld and Lq inductances of the IPM generator. The transfer functions of the current control loops are given in chapter 2, and in the controller parameter optimization algorithm, they are converted to the state space form. Finally, whole model is combined in the large state space model that completely describes dynamics of the closed loop. The complete model of the closed loop system has 31 states. Eigenvalues of the system matrix are calculated in each iteration, as illustrated in figure 3.12. Algorithm stores parameter values that result in maximum damping of the resonant modes. Search for optimal values for all controller parameters would take large amount of time. To accelerate the process, some

parameters were selected in advance while others were optimized. Then some of preselected parameter were varied, and the procedure repeated until the set of parameters that result in satisfying damping of all parameters was found. Bandpass filters have effect on selective moving eigenvalues associated with drivetrain model. Therefore, when gain value for a compensator that maximizes damping of a certain mode is found, the parameters of the compensator in that channel can be frozen, while other parameters can still change until damping of other resonant modes is maximized as well.
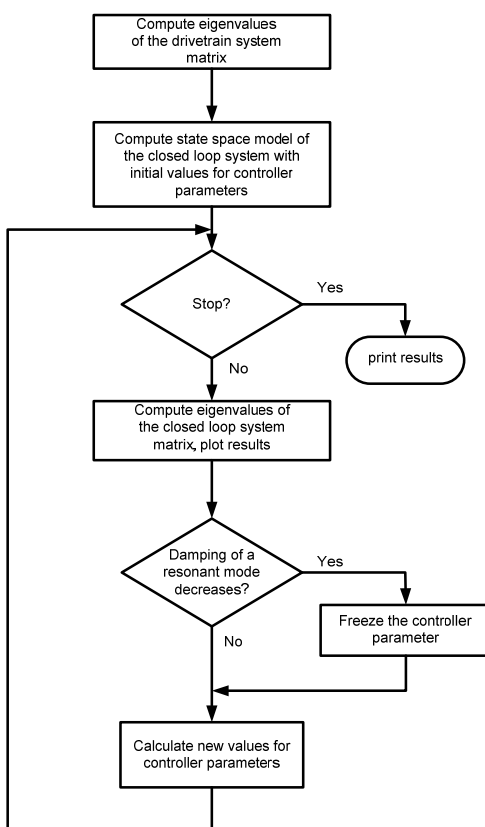
Figure 3.12. Controller parameter optimization algorithm

Pole locations of the closed loop system are shown in figure 3.13. Poles marked by green color are eigenvalues of the drivetrain system matrix computed at the beginning of the optimization. Figure 3.14 is a zoomed in look at pole locations of the drivetrain low frequency resonant modes as compensator gains change. When the gain at each channel

is increased, the drive train poles moves away from imaginary axes (indicating an increased damping of that mode). List of controller parameters is given in table 3.5.
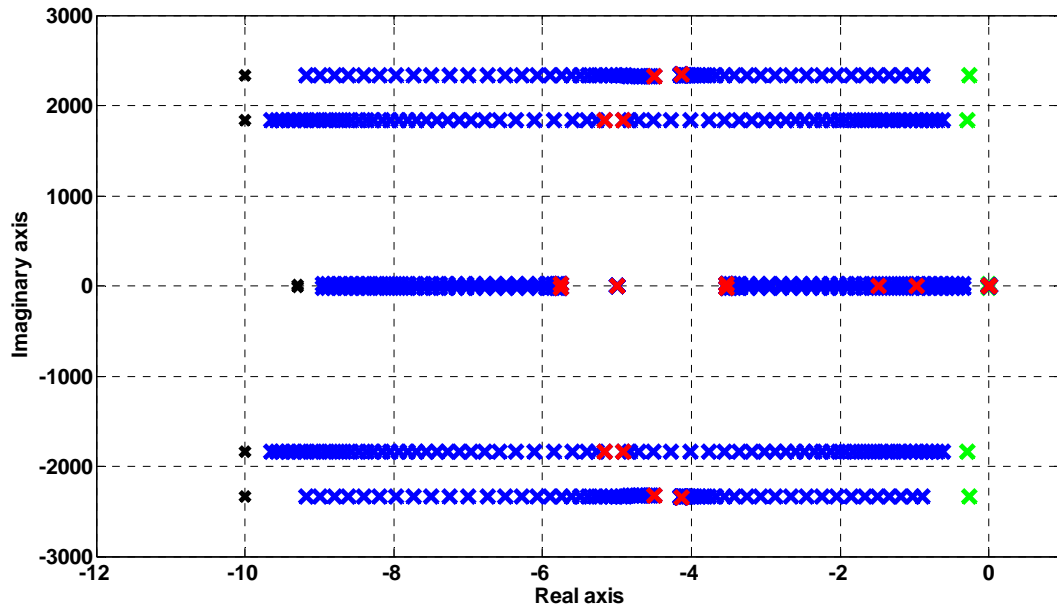
Figure 3.13. Pole locations of the closed loop system
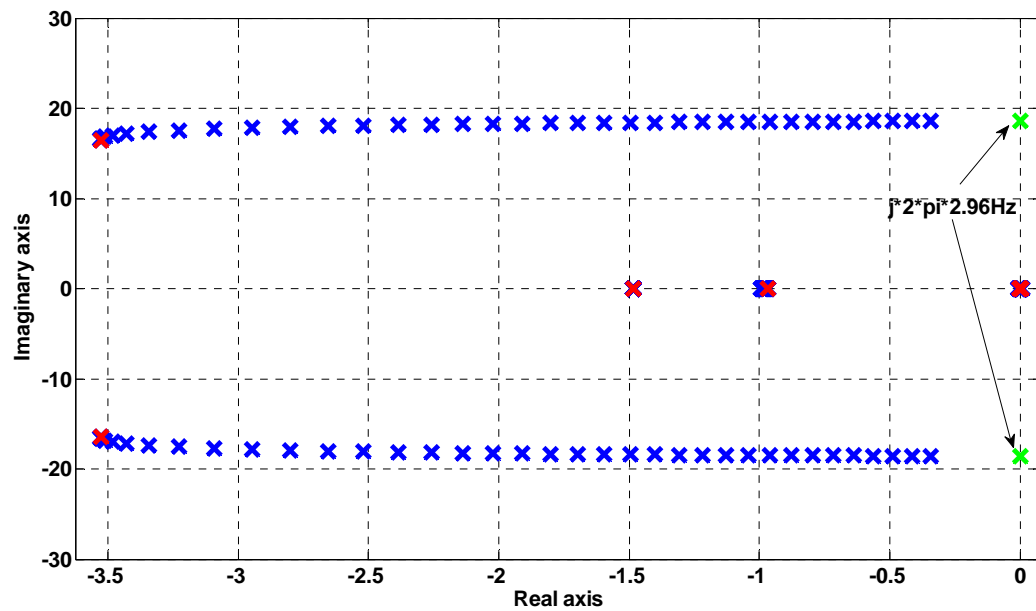
Figure 3.14. Pole locations of the low frequency resonant mode

β1	β2	β3	α1	α2	α3	Kcmp1	Kcmp2	Kcmp3	ω1	ω2	ω3
20	100	100	1	0.011	0.0086	4224	127050	316800	1	183.5	2331.1

Table 3.5. Active vibration damping controller parameters

3.4. Simulink model of a wind turbine with active drivetrain vibration damping

Figure 3.15 shows a block diagram of the complete wind turbine control system with active torque control for resonant vibration damping. This system is extension of the wind turbine model developed in chapter 2. Simulink model of the wind turbine drivetrain is shown in figure 3.16. This model is based on the system of differential equations (5)-(14). Wind turbine model implemented in FAST code has built in a two mass drivetrain model that consists of a flexible shaft that connects rotor and generator inertias. The new gearbox model replaces this functionality of FAST when run from Simulink. First, the two mass drivetrain model in FAST has to be disabled, generator inertia set to zero, and gear ratio set to 1 in the FAST input file. Now, the drivetrain model in FAST behaves like large rotor inertia with a rigid shaft. The five mass gearbox model has 10 states. First state, rotational speed, is computed in FAST, while other nine states in the simulink model from figure 3.16. The rotor speed is now used as the input to the gearbox model. The torque reaction portion of the equation (5), given in (25) is returned to FAST to complete rotor speed computation.

$$T_{react} = -K_1 \cdot (\theta_R - \theta_1^{'}) - D_1 \cdot \left(\omega_R - \omega_1^{'}\right) \tag{25}$$

The rest of the states are computed by the model from figure 3.16. The output of the gearbox model is the generator speed ω_G that is the input for generator and rest of the system model.
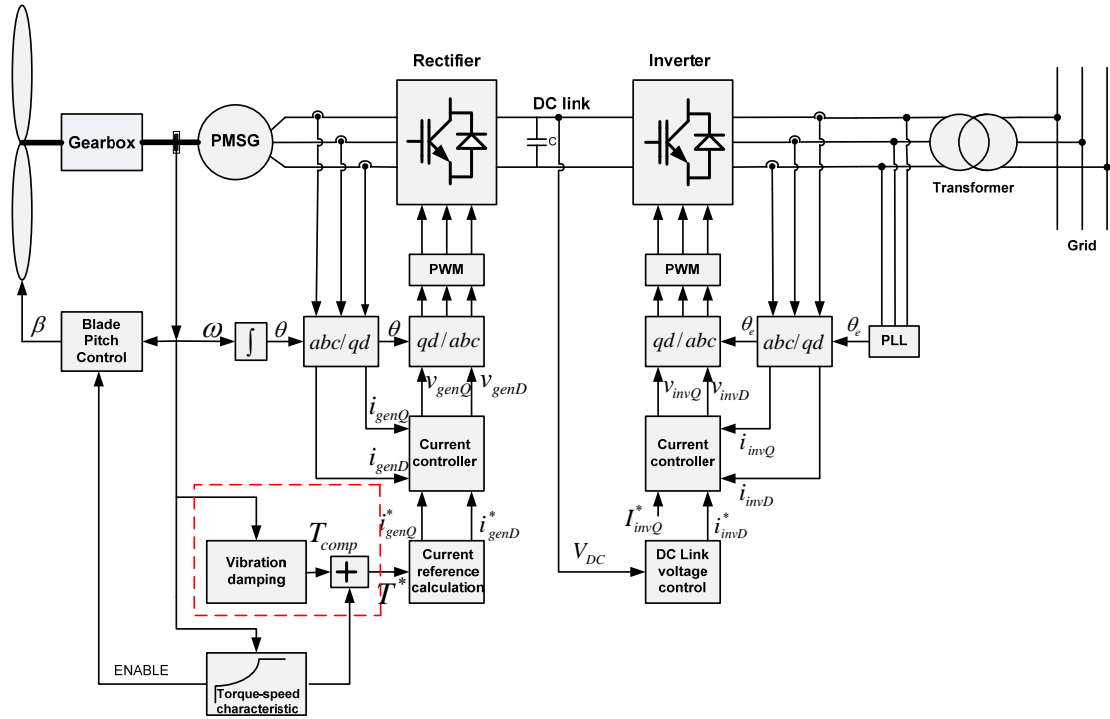
Figure 3.15. Control block diagram of a wind turbine with active drivetrain
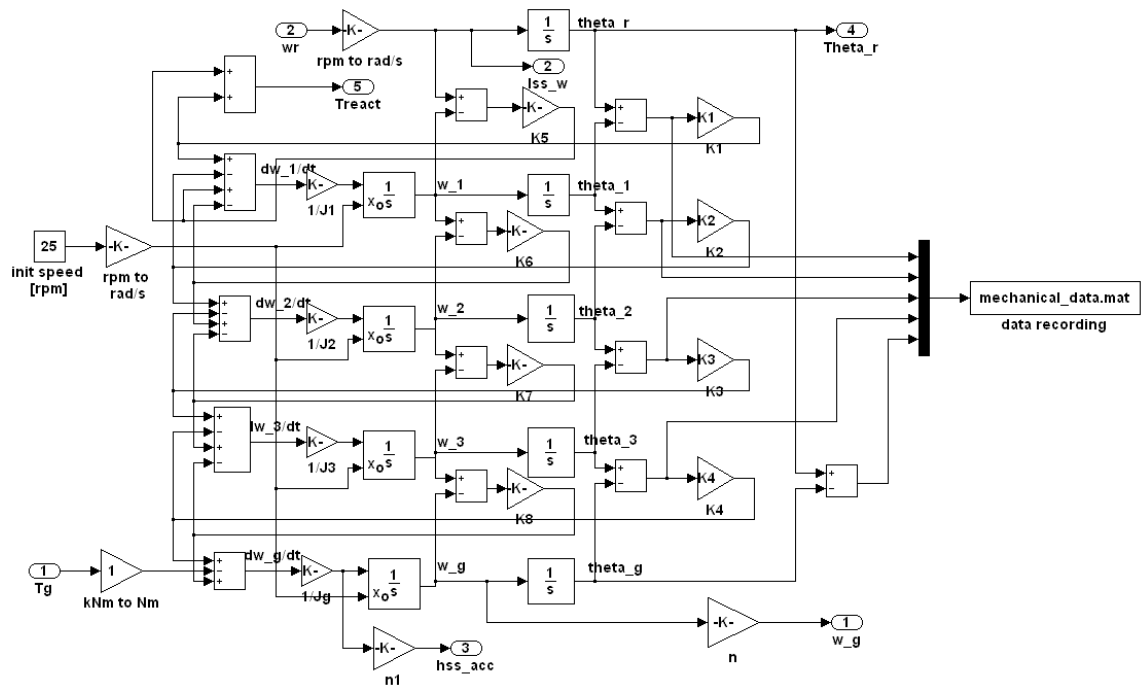
vibration damping

Figure 3.16. Simulink implementation of the gearbox model
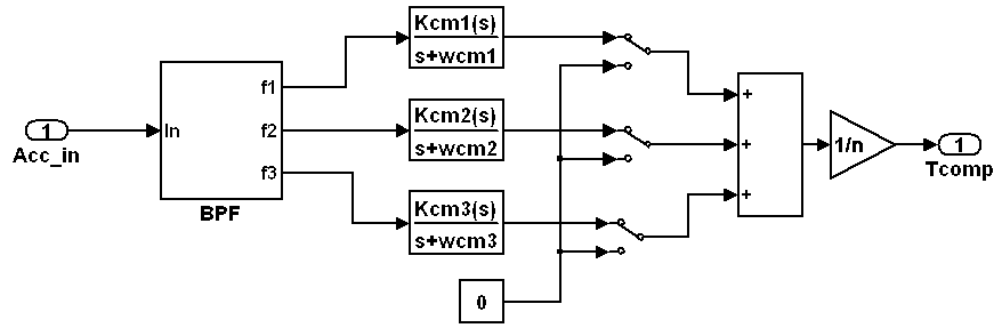
Figure 3.17. Vibration damping controller
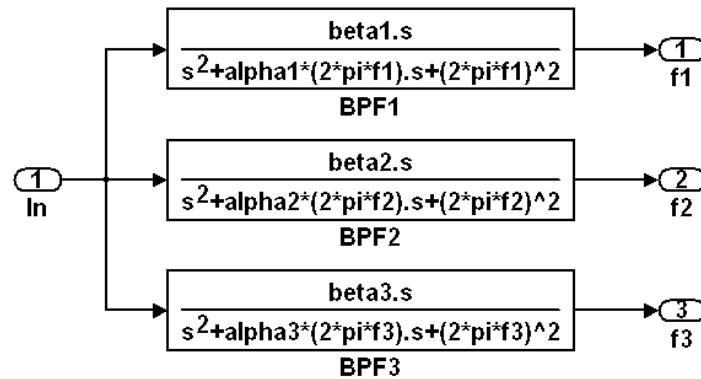
Figure 3.18. Bandpass resonance vibration filtering
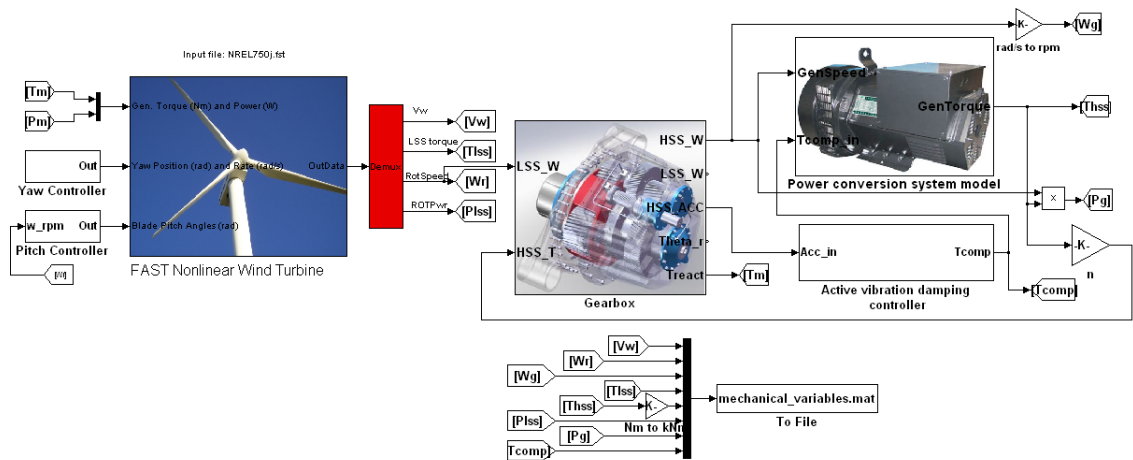
Figure 3.19. Simulink model of a wind turbine with vibration damping controller and

double conversion system

Simulink implementation of the vibration damping control blocks are shown in figures

3.17 and 3.18. Complete Simulink model of the wind turbine is shown in figure 3.19. The

torque component computed by the vibration damping controller is added to the torque reference from the turbine's torque-speed characteristic. This is the new torque reference which is further split into Id and Iq references for the generator current controller.

3.5. Simulation results

Series of simulations were run in order to test effectiveness of the proposed vibration damping control method. Various wind speed profiles were used as input to the complete wind turbine model with the drivetrain and resonant vibration damping controller. Simulation results are presented in this section.

3.5.1. Step changes of wind speed

First wind profile used for simulation has step changes of wind velocity. Wind speed rapidly changes from steady 6 m/s to steady 8 m/s. After 20 seconds, wind speed is reduced back to 6m/s. These step changes excite oscillatory modes in all flexible elements of the wind turbine model, including torsional vibrations of the gearbox. In the figure 3.20, wind speed and rotational speed are shown. Blue line represents results for the case when vibration damping controller was disabled, while red line represents results with enabled vibration damping controller.
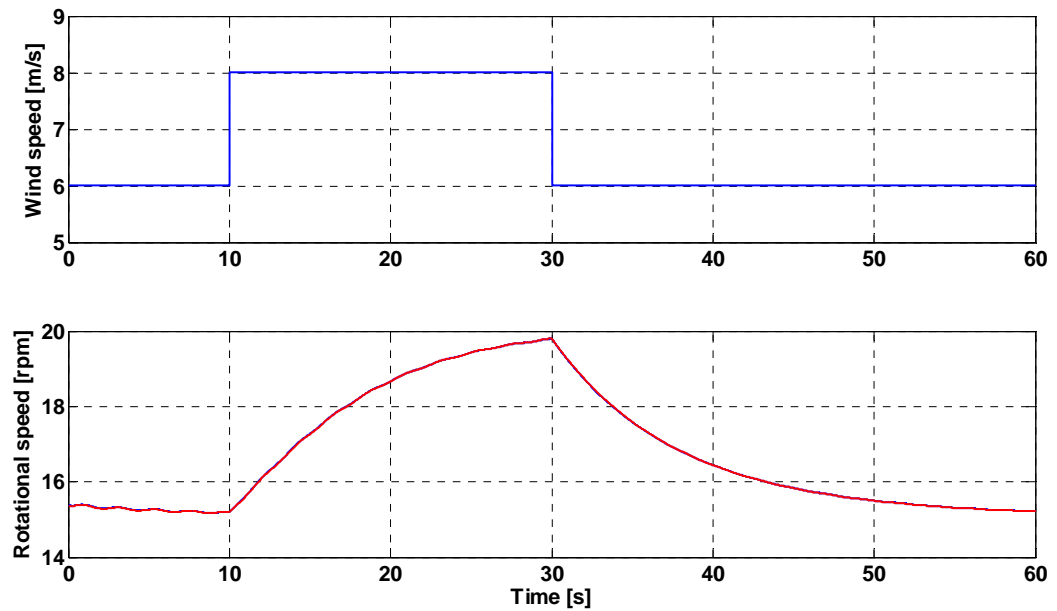
Figure 3.20. Wind speed and rotational speed

Figure 3.21 shows torsion angles of each block of the drivetrain for the cases when vibration damping controller is disabled and enabled. The figure shows that vibration damping controller significantly reduces resonant vibrations at all shafts within the drivetrain. Total torsion angle from the LSS to HSS, scaled to the LSS, is shown in figure 3.22. Figure 3.22 contains plots of the total torsion angle from LSS to HSS, and HSS torque of the generator. HSS torque shows more variations, due to the action of the vibration damping controller. However, total torsion angle shows fast reduction in oscillations. Torque difference that dictates torsion across the drivetrain is shown in the figure 3.23 together with the mechanical power at the HSS. Torque difference plot shows reduced components that cause resonant vibrations.
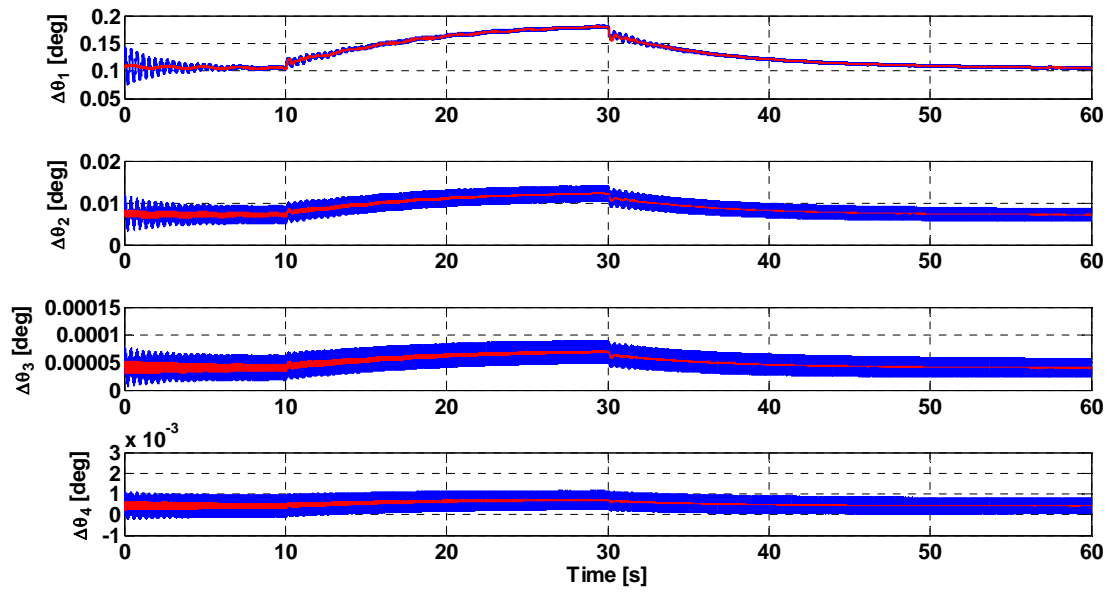
Figure 3.21. Torsional angles of the drivetrain
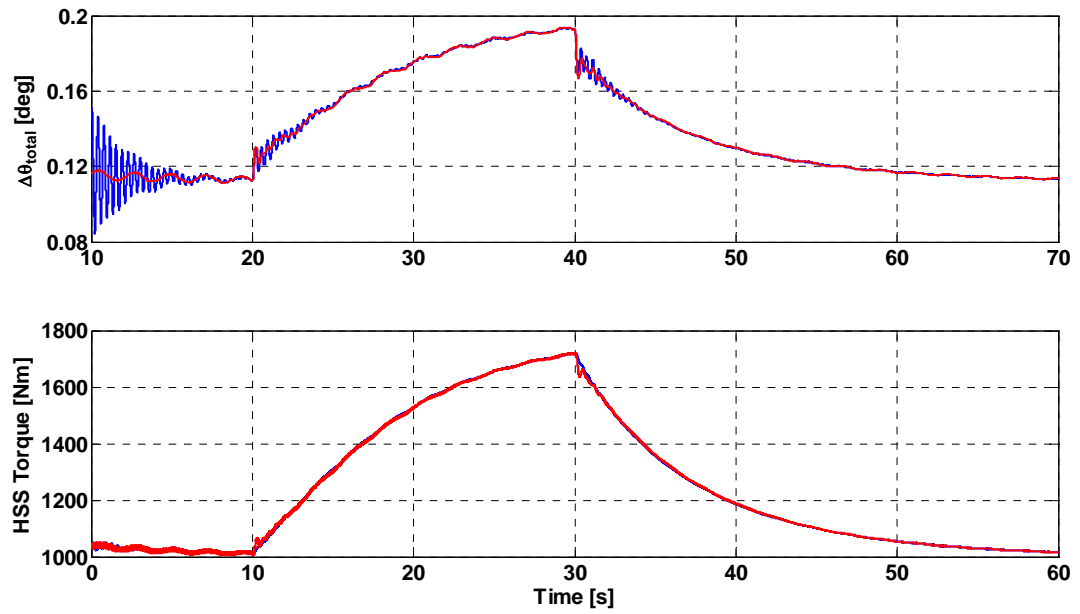
Figure 3.22. Total torsional angle of the drivetrain and generator torque
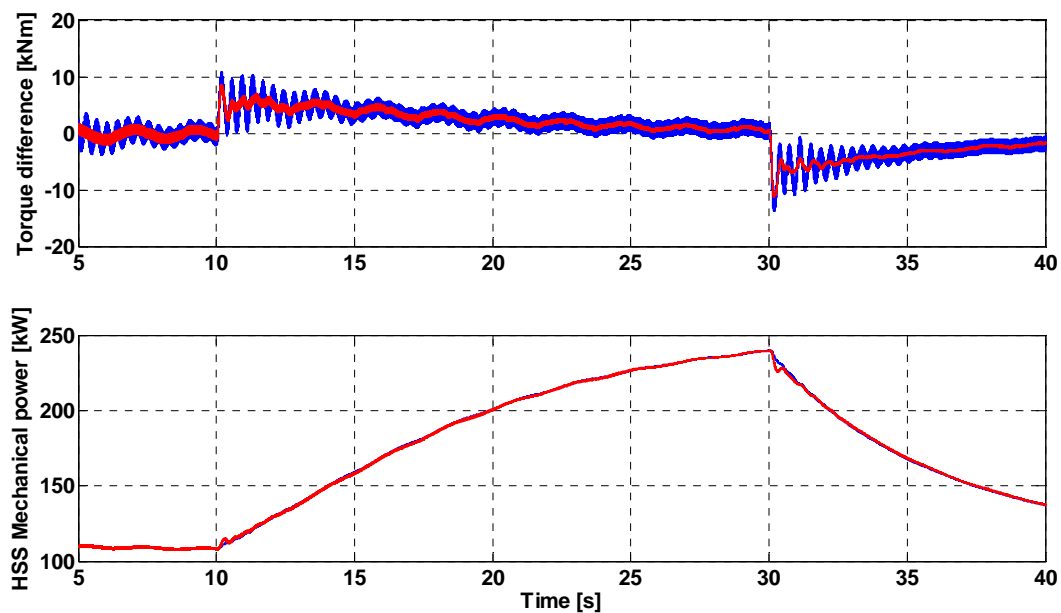
Figure 3.23. Torque difference and mechanical power on the HSS shaft
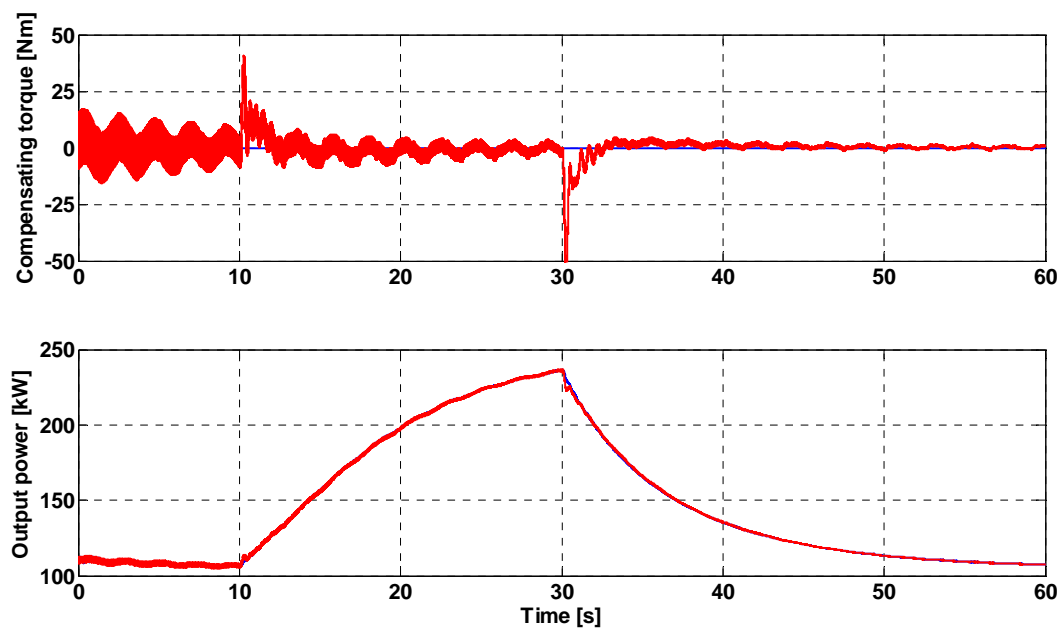
Figure 3.24. Compensating torque and output power
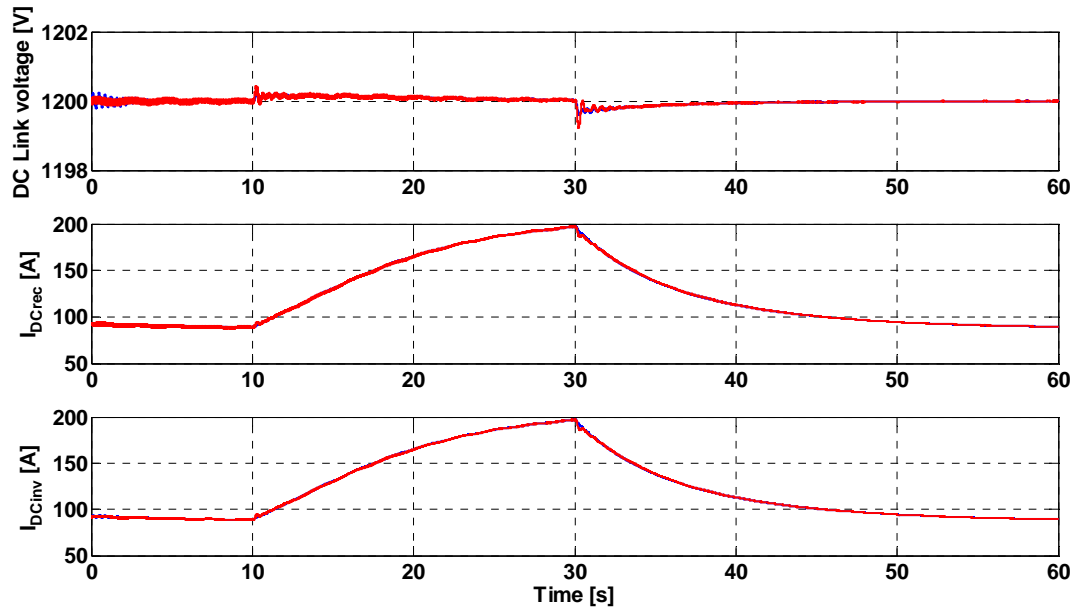
Figure 3.25. DC link voltage and currents.

Finally, figure 3.24 shows compensating torque calculated by the vibration damping controller as well as output power. The output power plot shows slight overshoot and dip, result of action of the vibration damping controller, at the points when wind speed changes rapidly. However, by integrating the ultracapacitor energy storage, as described in the next chapter, these additional power variations can be completely removed. Figure 3.25 shows DC link voltage and currents from the DC side of the rectifier and inverter. Since only standard capacitor is used in the DC link for the purpose of testing vibration damping control, DC link voltage is kept constant and therefore DC currents look the same. This is not the case with ultracapacitor energy storage integrated in the DC link, as it will be presented in the next chapter.

3.5.2. Sinusoidal wind speed profile

Next simulation was run by using the sinusoidal wind speed profile, as shown it figure 3.26. Wind speed is constant at the beginning of the simulation after 10 seconds it changes from 8ms to 9ms with additional sinusoidal component whose frequency is 2.96Hz, the resonant frequency of the first mode of the gearbox, with the amplitude of the sinusoidal component of 1m/s, thus creating large excitation for this resonant mode. As it the previous, and the following cases, rotational speed for the cases with and without resonant damping controller has nearly the same profile due to large rotor inertia. Action of the resonant damping controller does not have significant effect to the rotational speed since the compensating torque is much smaller compared to the torque caused by the wind flow. As shown in figure 3.27, resonant vibrations at each shaft of the drivetrain are reduced significantly by the action of resonant damping controller.
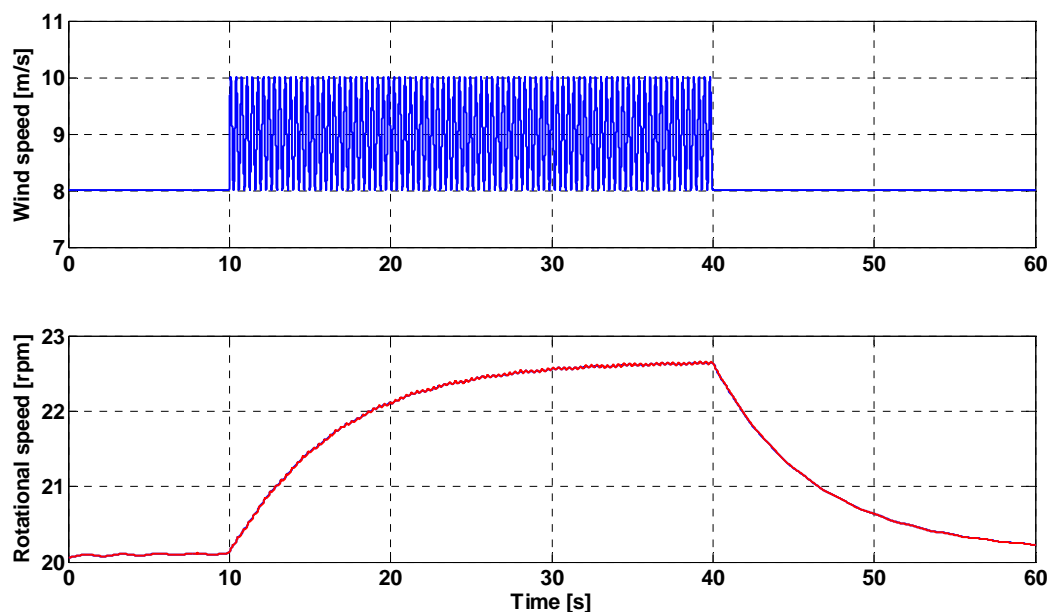
Figure 3.26. Wind speed and rotational speed. Sinusoidal wind profile.
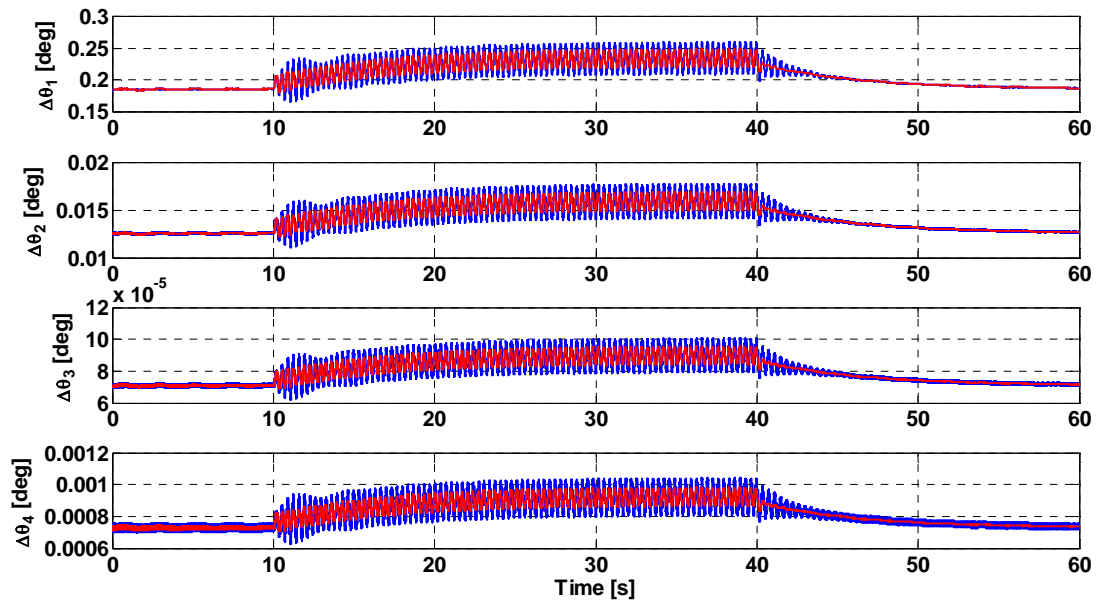
Figure 3.27. Torsional vibrations of the drivetrain. Sinusoidal wind profile
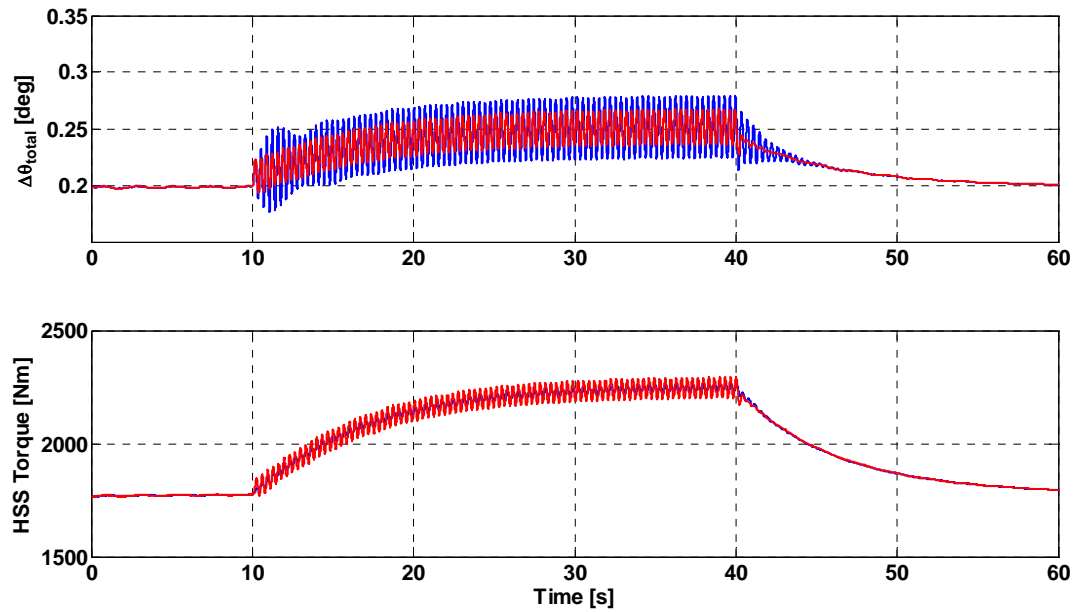
Figure 3.28. Total torsional angle of the drivetrain and HSS torque.

Sinusoidal wind profile
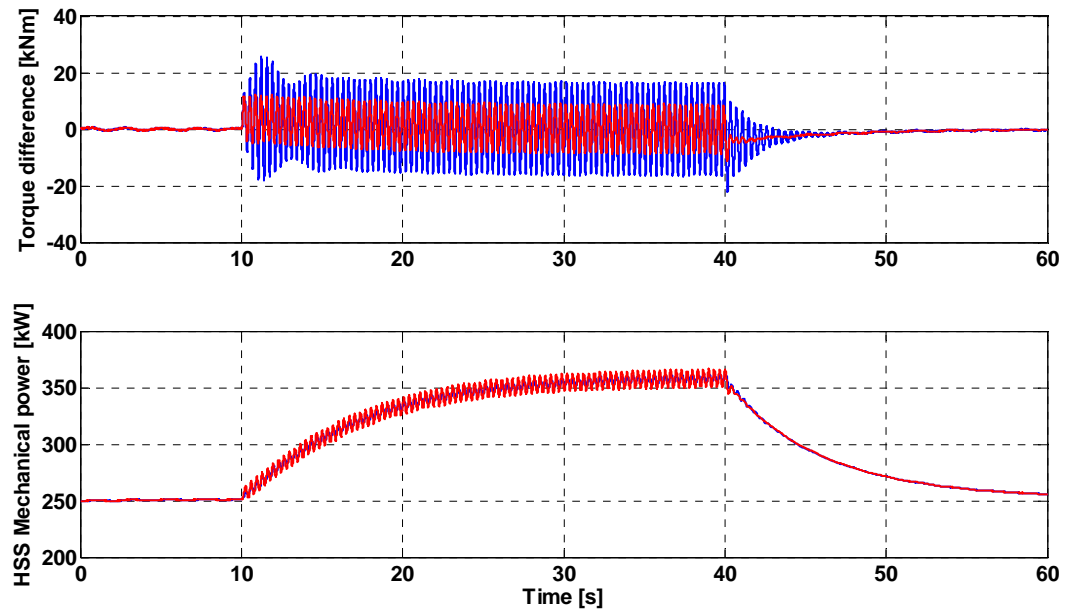
Figure 3.29. LSS-HSS torque difference and HSS mechanical power

Reduction of the overall torsion angle of the drivetrain is shown in figure 3.28 as well as HSS torque which has additional sinusoidal component produced by the vibration damping controller, as shown in figure 3.29. Figure 3.30 shows compensating torque and output power (delivered to the grid).

Figure 3.30. Compensating torque and output power. Sinusoidal wind profile
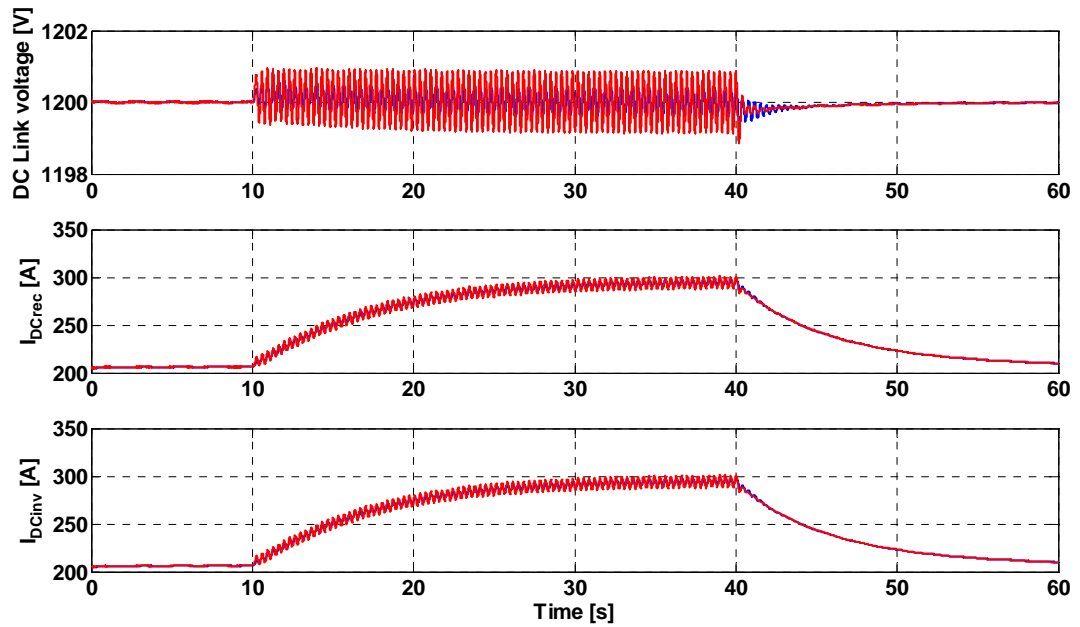
Figure 3.31. DC link voltage and currents. Sinusoidal wind profile

Finally, DC link voltage and currents are shown in Figure 3.31. DC link voltage is kept within ±1V from the reference DC link voltage of 1200V.

3.5.3 Variable wind speed- wind profile A1

Following three simulation cases use variable wind speed profile generated by TurbSim. Input files for TurbSim v1.50 used to generate the wind speed data files are given in the appendix. Wind speed profile A1 used in the first case is based on Kaimal model with turbulence level B according to IEC 61400-3 standard. Mean wind speed at the hub height is 10m/s. Turbulence type is normal.
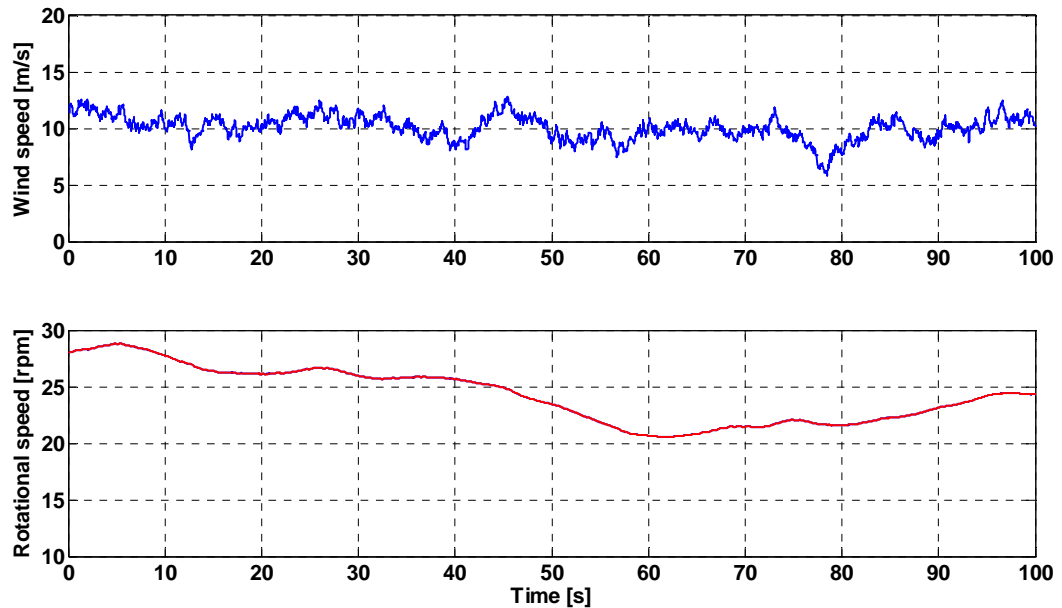
Figure 3.32. Wind and rotational speed. Wind profile A1

Figure 3.32 shows wind and rotational speed. As in previous simulation cases, red line represents results with vibration damping controller enabled versus blue line for the case when the controller is disabled.
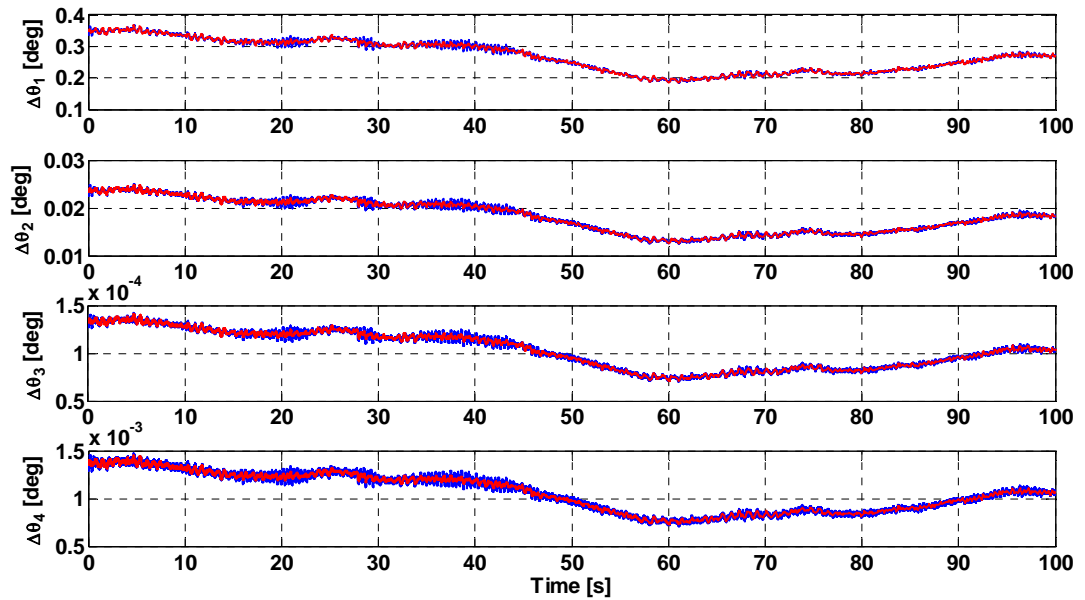
Figure 3.33. Torsion angles of the drivetrain. Wind profile A1

Figure 3.33 shows torsion angles at all shafts of the gearbox. It can be observed that red curves are less variable compared to blue curves for the case when the vibration damping controller is disabled. It is a result of reduced torque difference at resonant frequency. Torque difference and mechanical power at HSS are shown in figure 3.34.
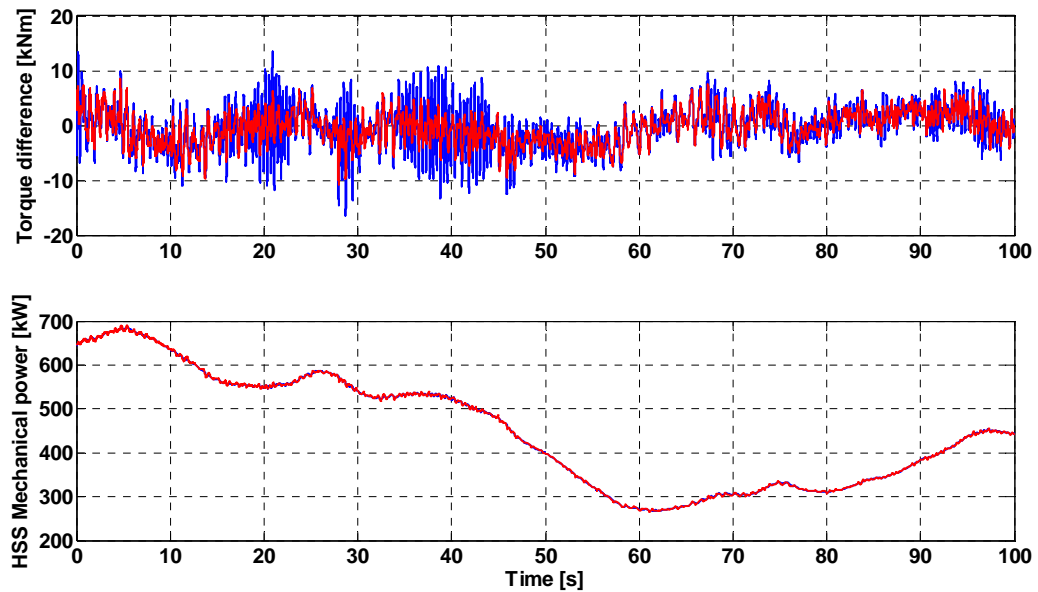
Figure 3.34. Torque difference and HSS mechanical power. Wind profile A1
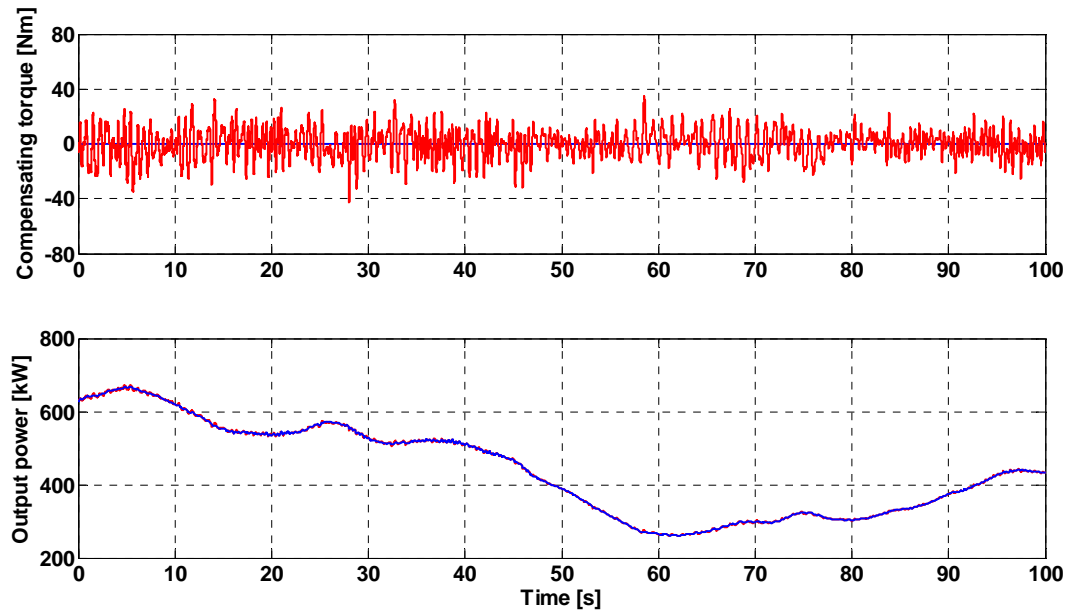
Figure 3.35. Compensating torque and output power. Wind profile A1

Compensating torque and output power are shown in figure 3.35. DC link variables are

shown in figure 3.36. Voltage of the DC link is kept constant despite variable wind speed.
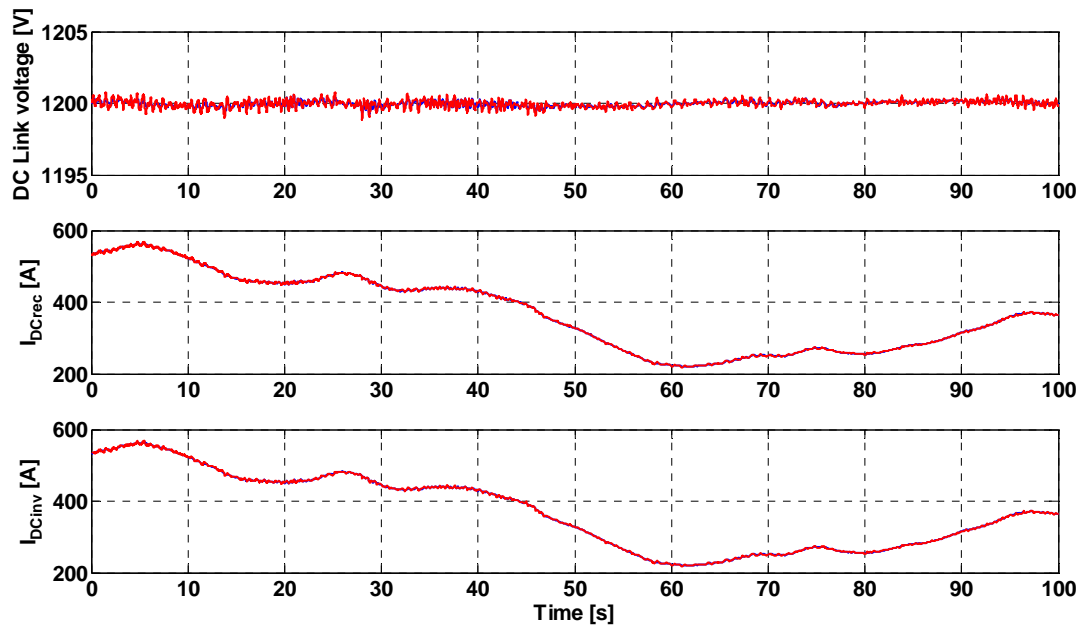
Figure 3.36. DC link voltage and currents. Wind profile A1
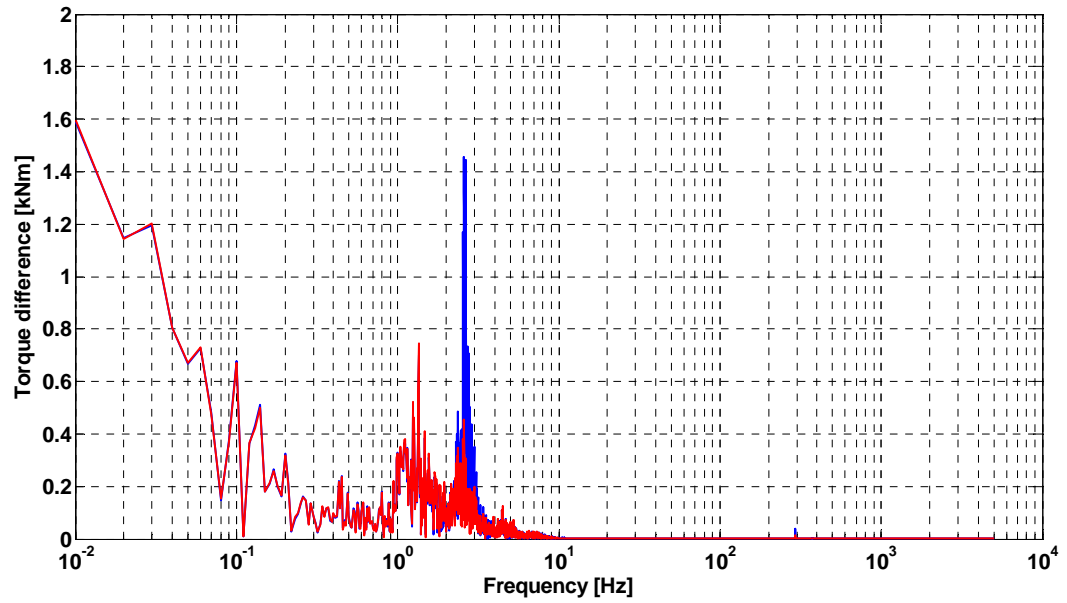
Figure 3.37. Torque difference spectrum. Wind profile A1
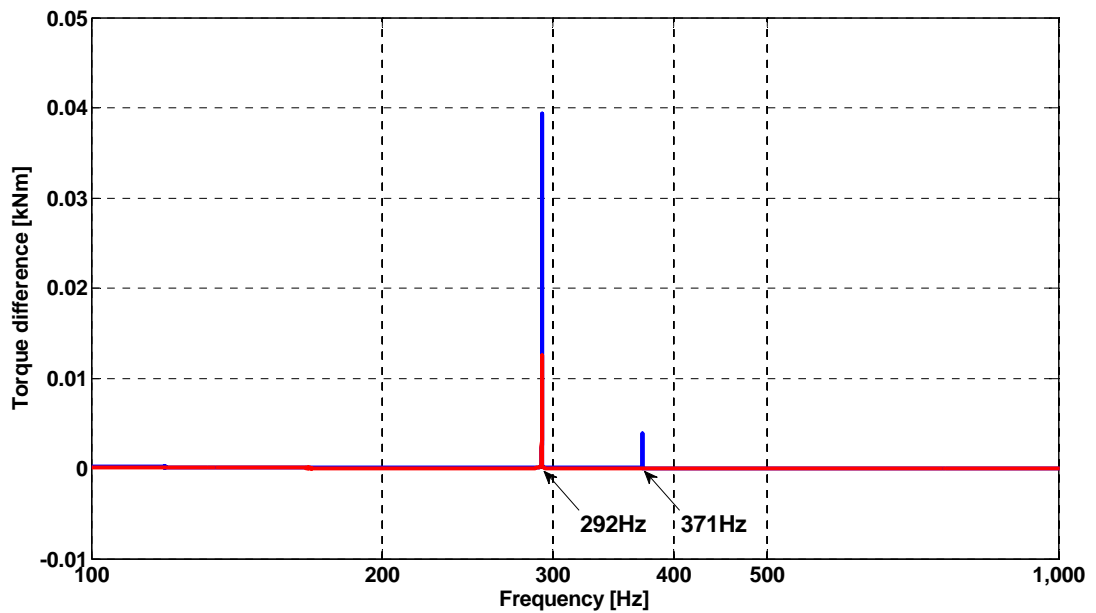
Figure 3.38. Torque difference spectrum (zoom in). Wind profile A1

In order to better assess effectiveness of the proposed resonant damping controller, spectrum of the variables of interest can provide more details. Figure 3.37 shows spectrum of the torque difference of the drivetrain. Blue curve represents the case with resonant damping controller disabled. The spectrum shows that resonant torque

components are greatly reduced by the action of the controller. Figure 3.38 is zoomed in the 100-1000Hz region to show reduction in the torque difference at higher resonant frequencies.
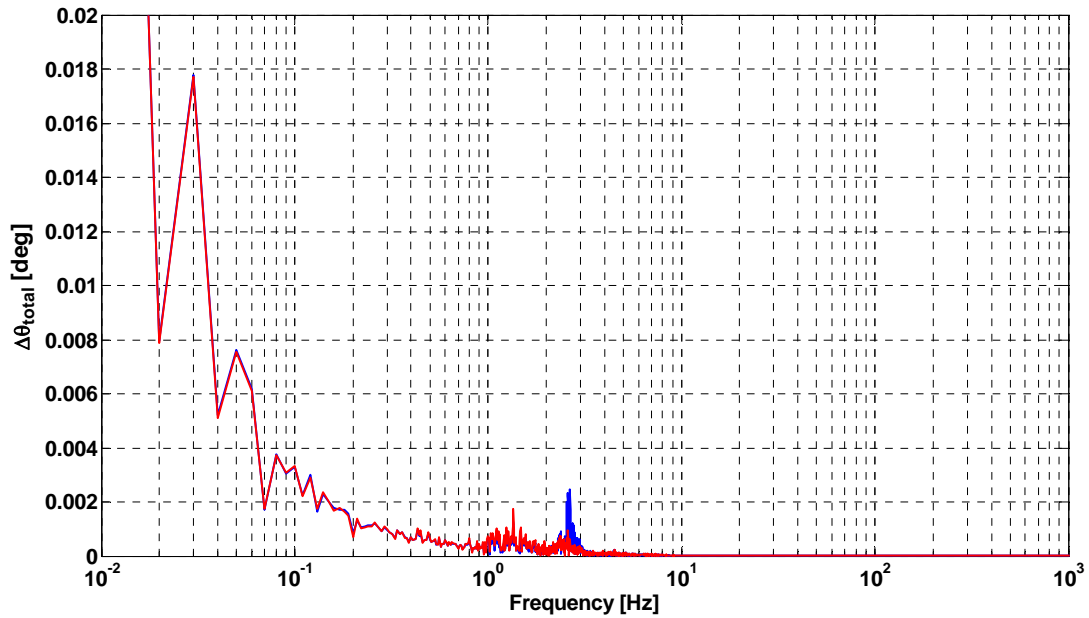
Figure 3.39. Total torsion angle spectrum. Wind profile A1

Finally, figure 3.39 shows spectrum of the total torsion angle, as a measure of vibrations across the drivetrain. It can be observed form the graph that vibration damping controller significantly reduces vibrations at the first resonant frequency (2.96Hz). Higher frequency vibrations are too small to be seen on the graph.

3.5.4. Variable wind speed – wind profile A2

Wind profile A2 has the same statistical parameters as wind profile A1, except the seed numbers used for random number generator. This resulted in wind profile shown in figure 3.40. Figures 3.42, 3.45, and 3.46 all show great reduction in torque components at

resonant frequencies by vibration damping controller. Reduction of torsional vibrations at resonant frequencies is shown in the torsion angle spectrum in figure 3.47.
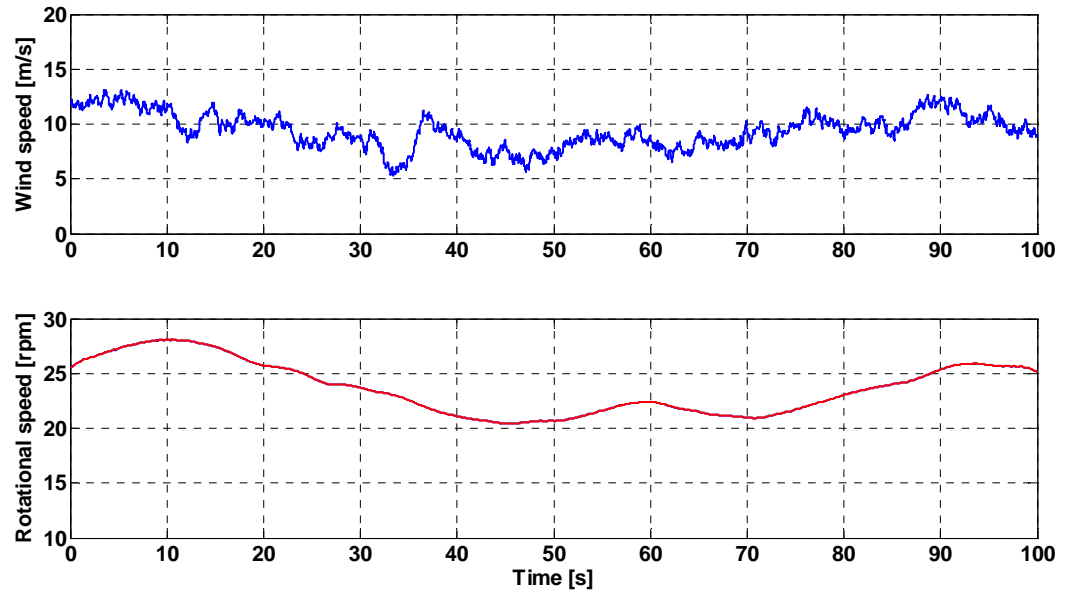
Figure 3.40. Wind and rotational speed. Wind profile A2
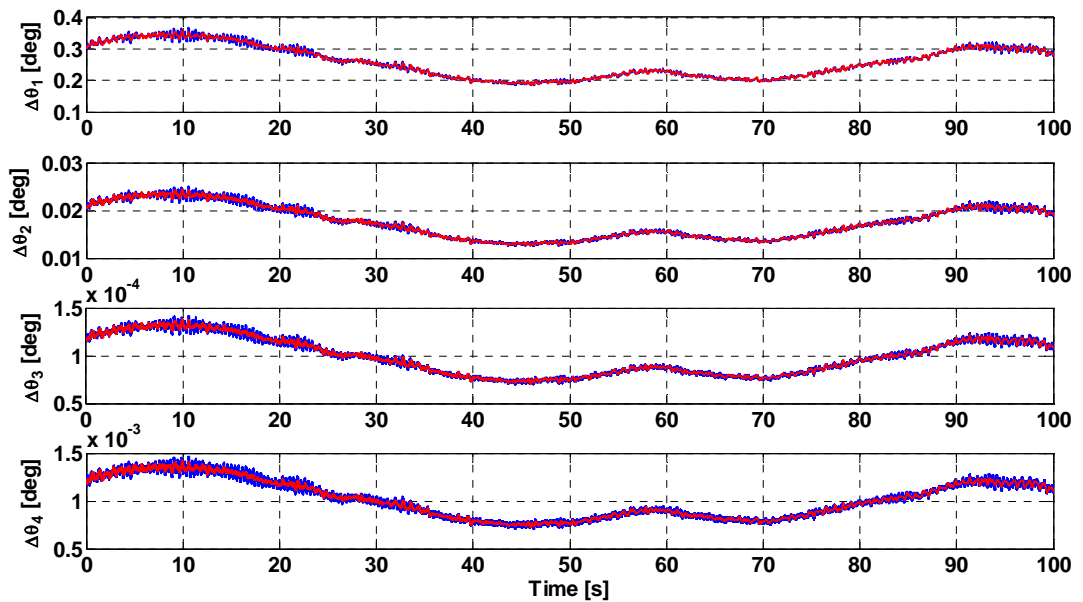
Figure 3.41. Torsion angles of the drivetrain. Wind profile A2
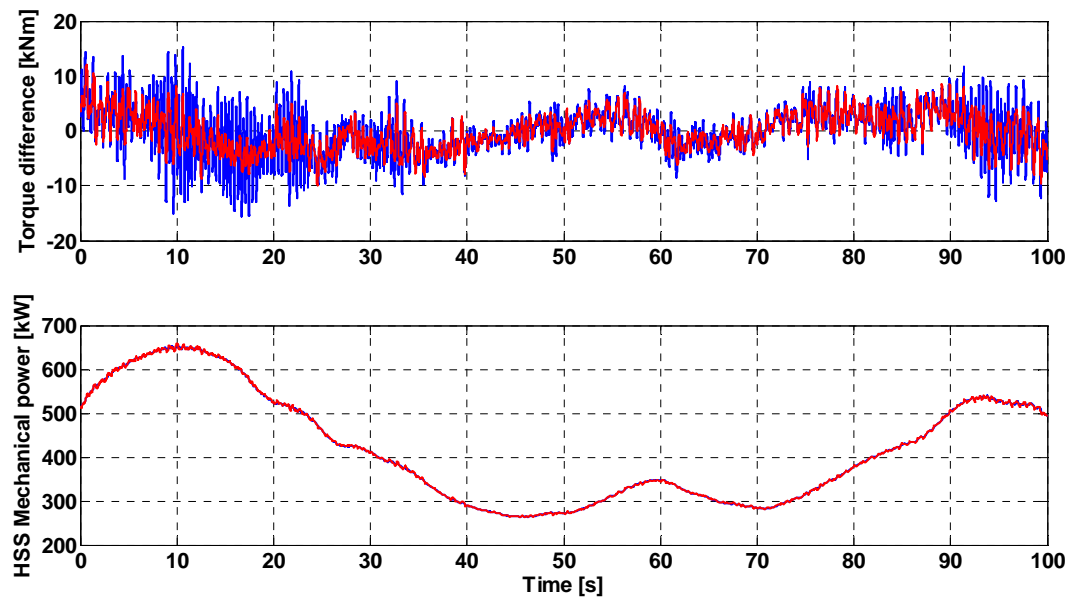
Figure 3.42. Torque difference and HSS mechanical power. Wind profile A2
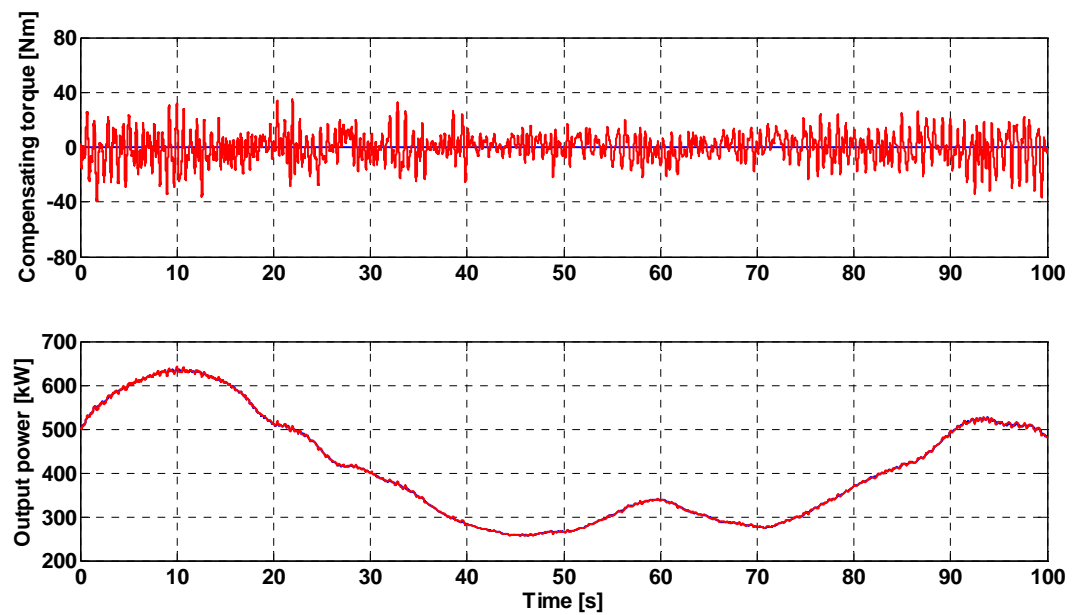
Figure 3.43. Compensating torque and output power. Wind profile A2
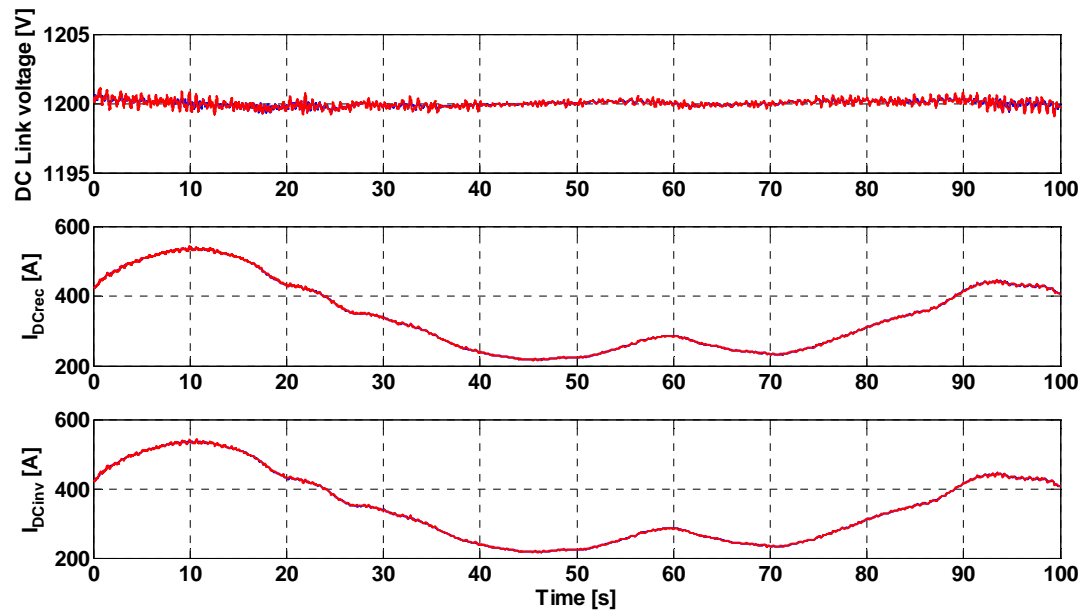
Figure 3.44. DC link voltage and currents. Wind profile A2
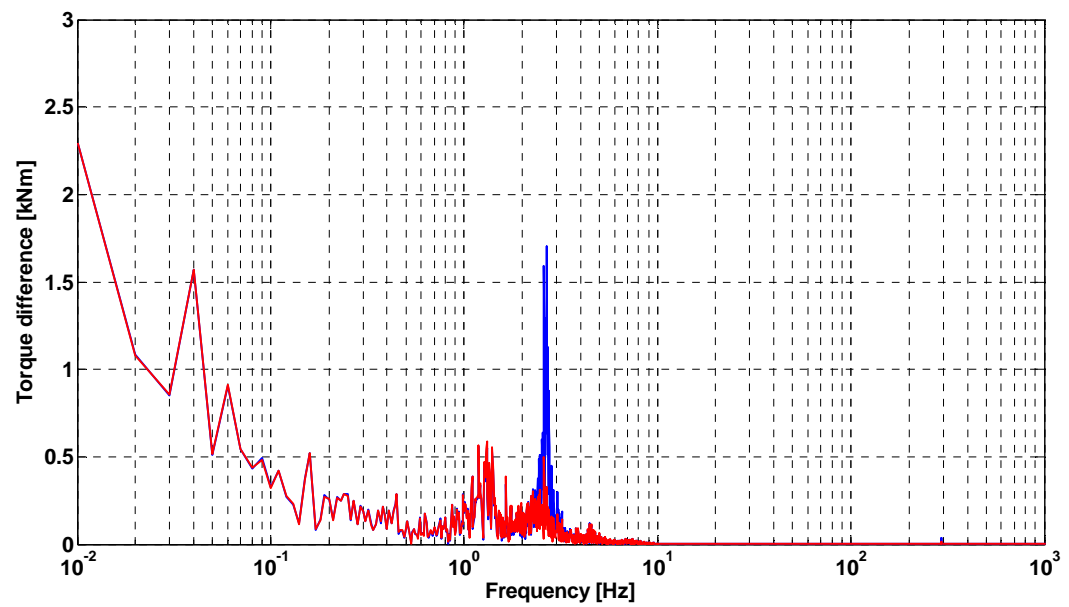
Figure 3.45. Torque difference spectrum. Wind profile A2
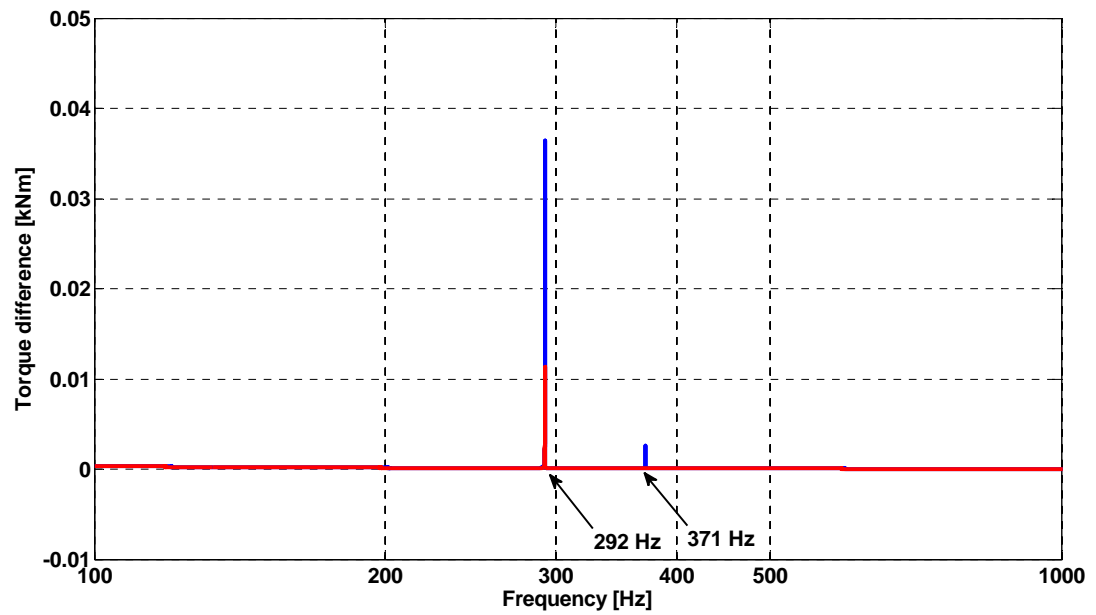
Figure 3.46. Torque difference spectrum. Wind profile A2
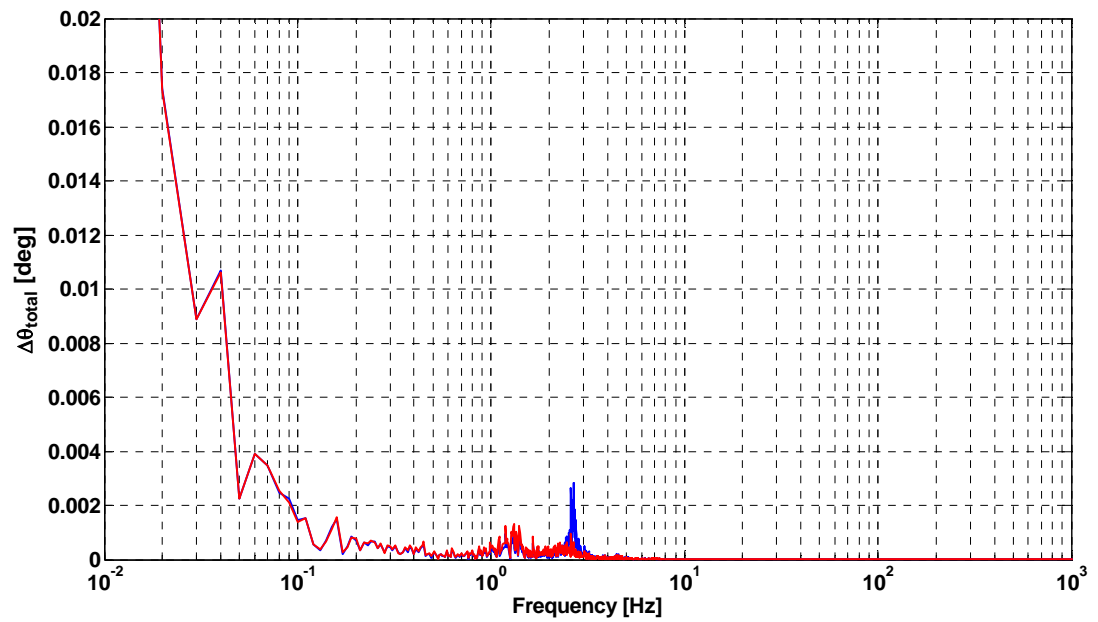
Figure 3.47. Total torsion angle spectrum. Wind profile A2

3.5.5. Variable wind speed – wind speed profile B

For additional testing of the vibration damping controller, a more variable wind speed profile is used. This wind profile, is generated by TurbSim, using the input file listed in the appendix D. This wind speed profile has lower average wind speed, but higher level of turbulence. The turbulence level is "A" according to IEC 61400-3 standard [63]. Wind speed and rotational speed of the wind turbine are shown in figure 3.48.
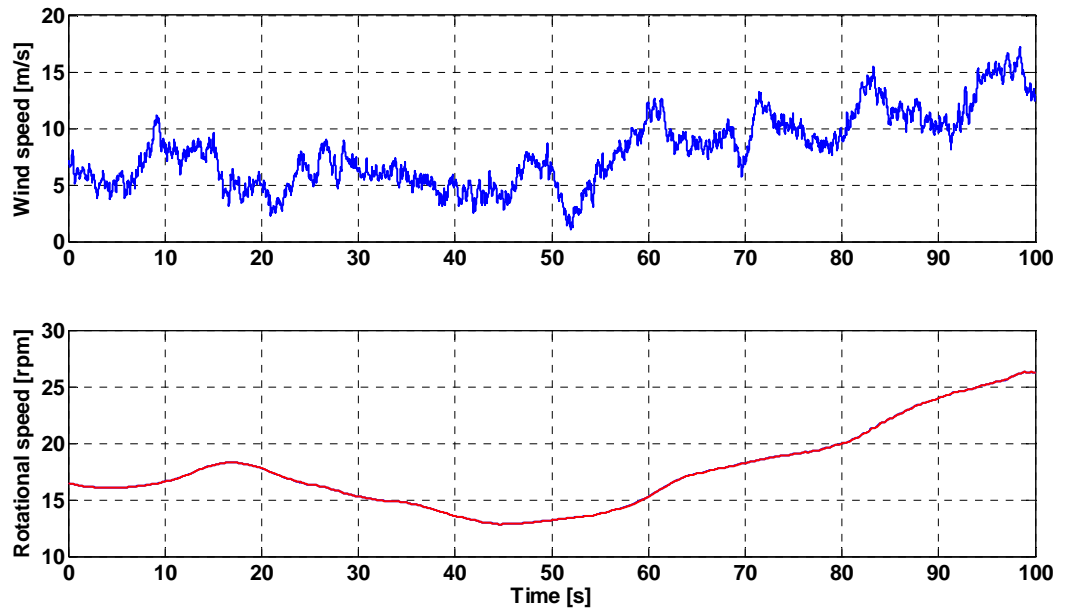
Figure 3.48. Wind and rotational speed. Wind profile B
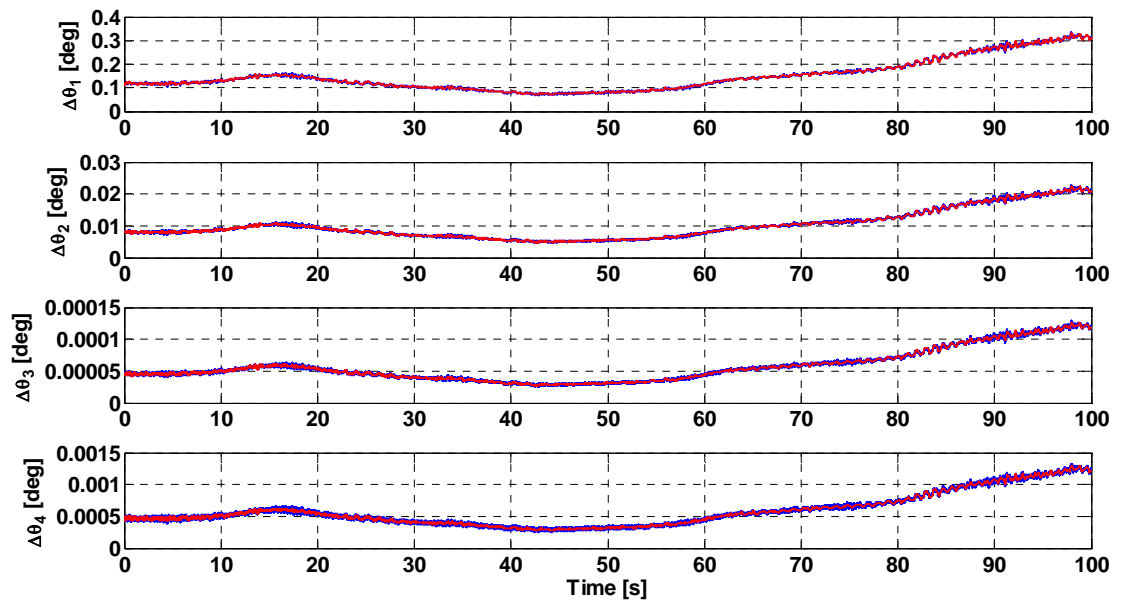
Figure 3.49. Torsion angles of the drivetrain. Wind profile B
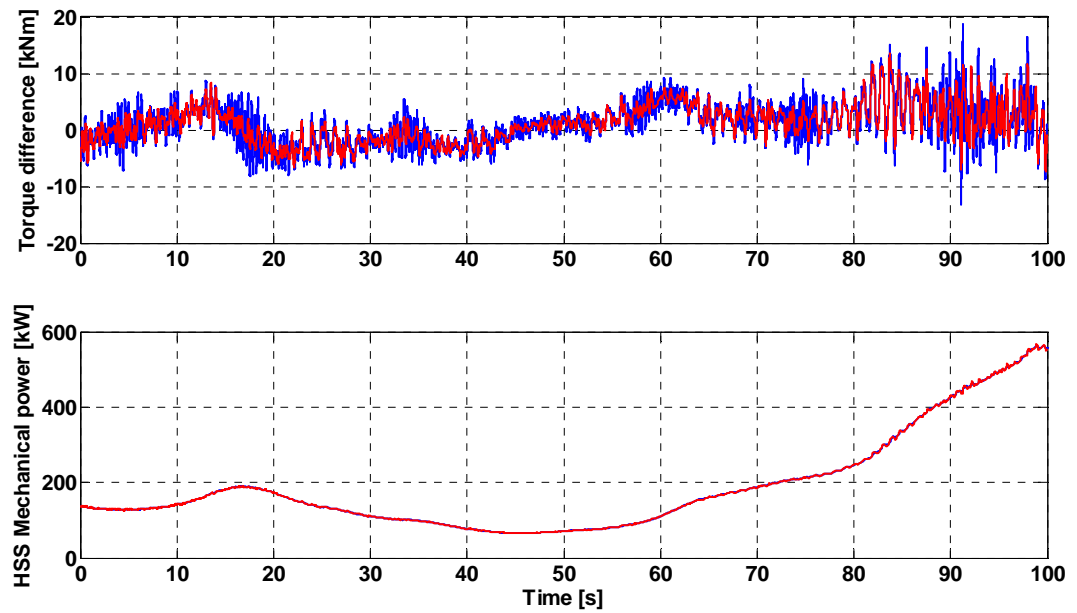
Figure 3.50. Torque difference and HSS mechanical power. Wind profile B
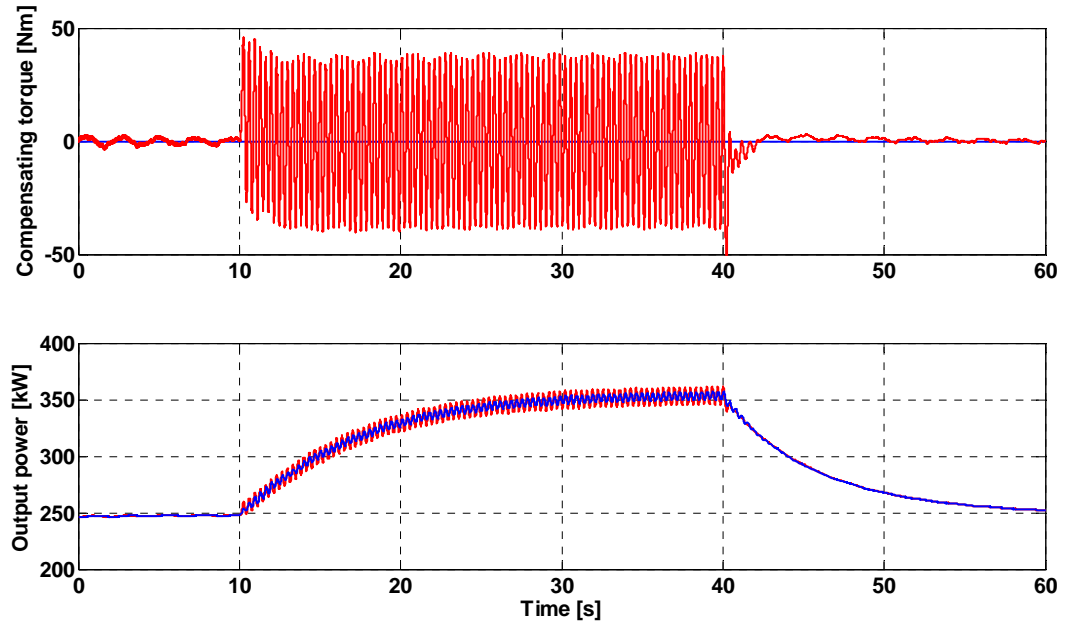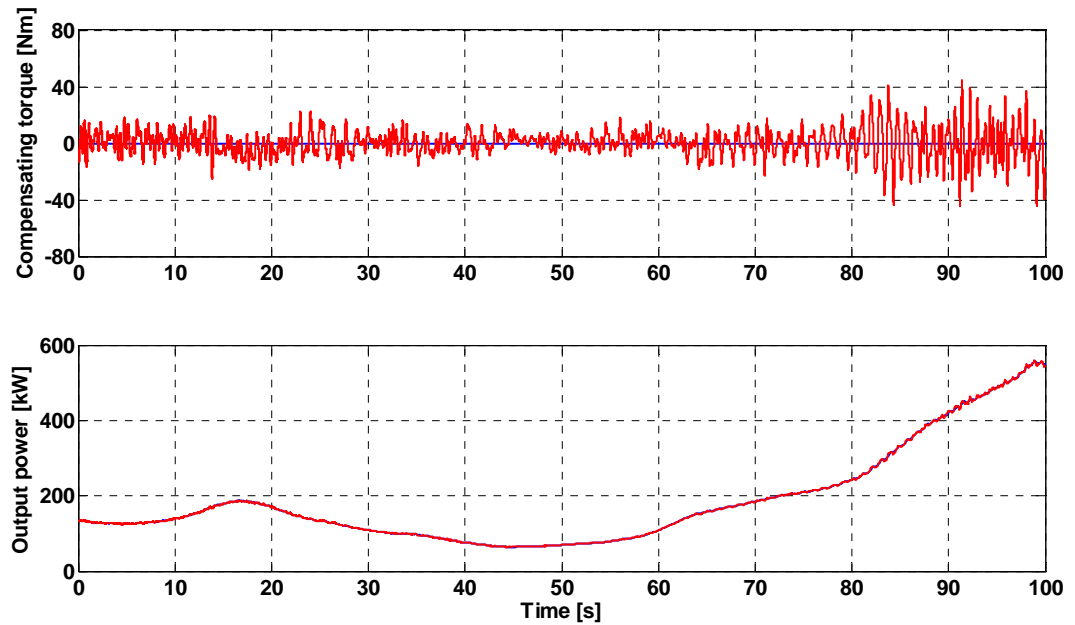
Figure 3.51. Compensating torque and output power. Wind profile B
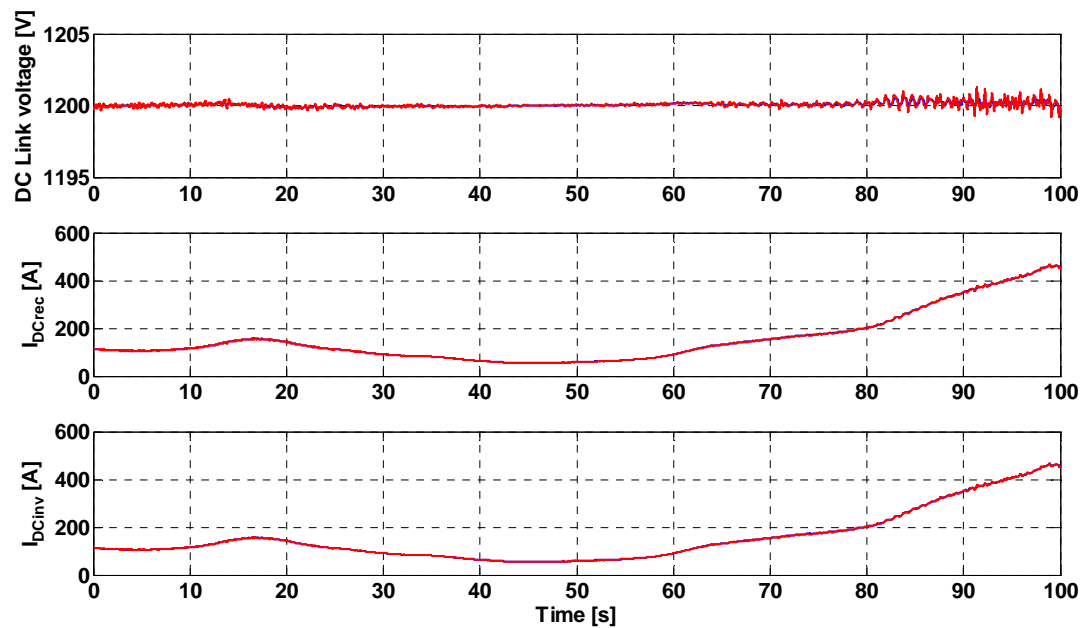
Figure 3.52. DC link voltage and currents. Wind profile B
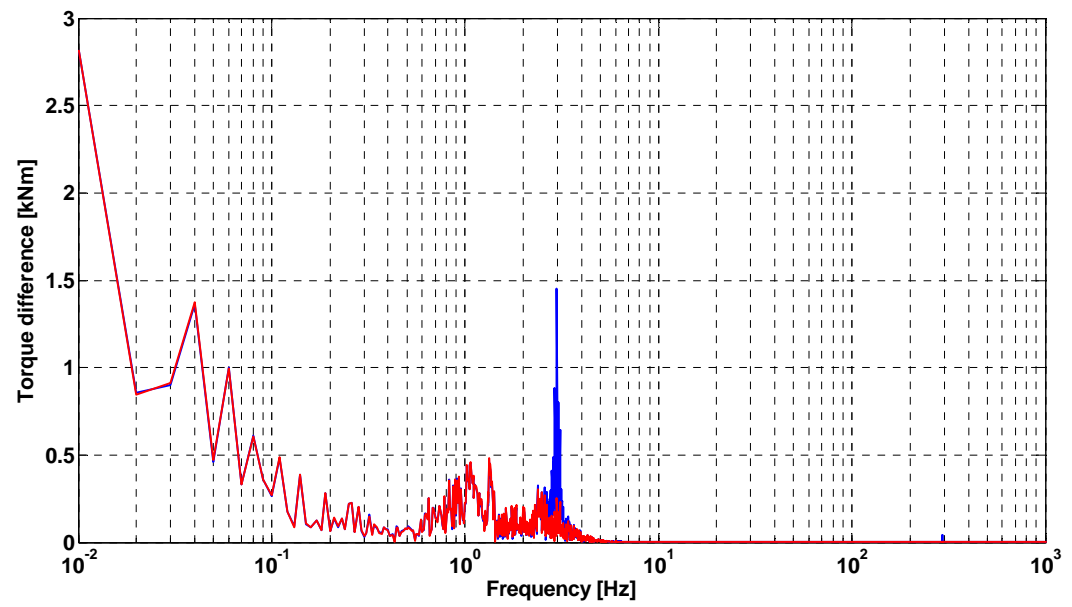
Figure 3.53. Torque difference spectrum. Wind profile B
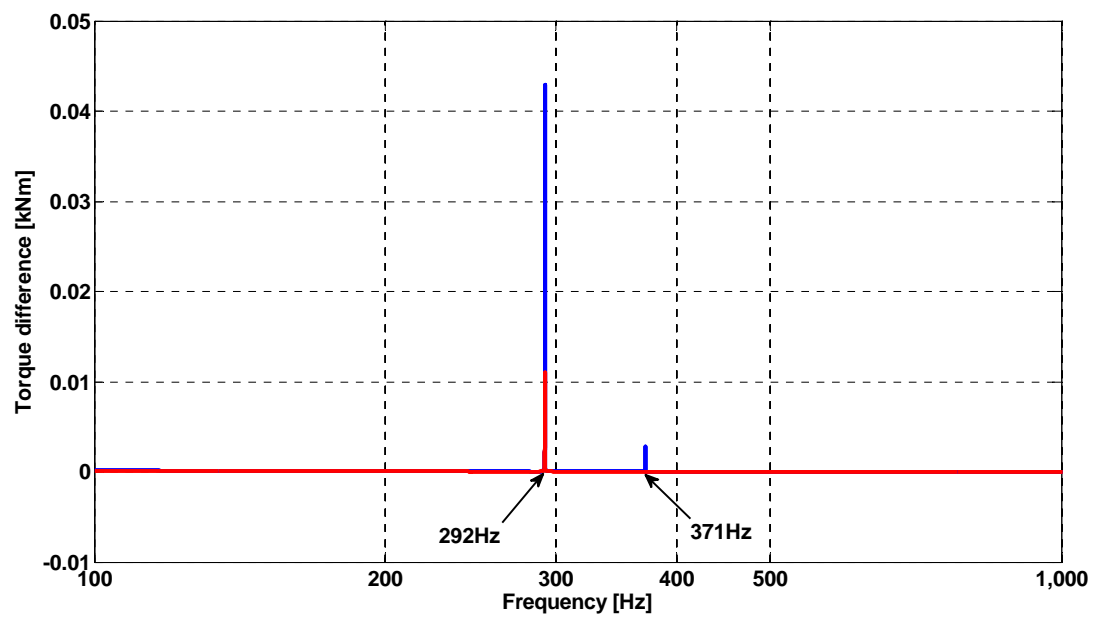
Figure 3.54. Torque difference spectrum. Wind profile B
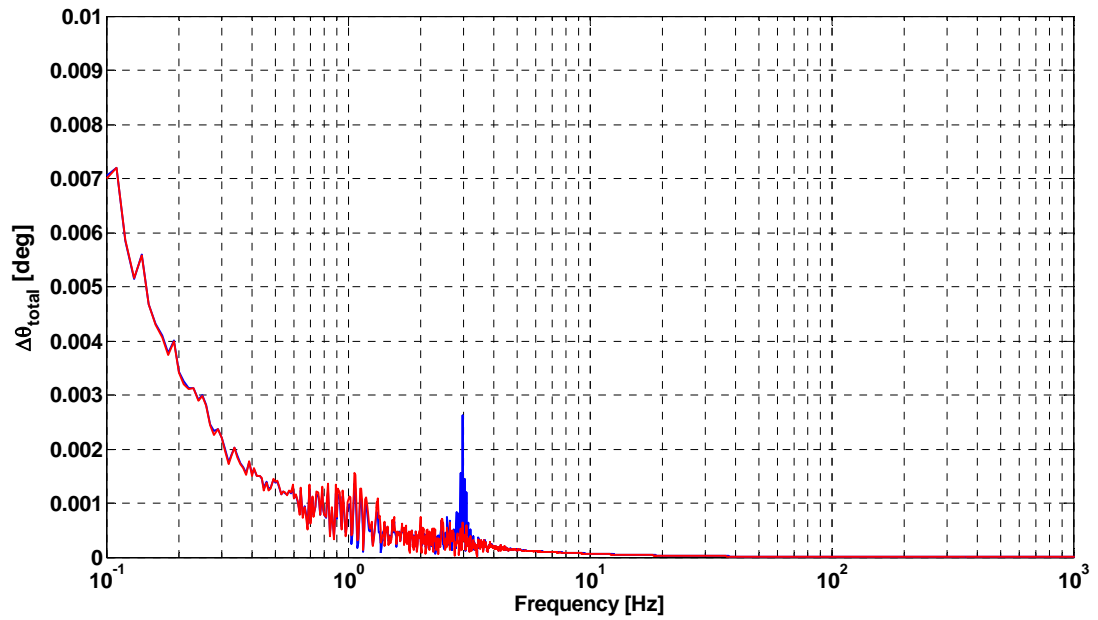
Figure 3.55. Total torsion angle spectrum. Wind profile B

As in previous simulation cases, torque difference spectral components at drivetrain resonant frequencies , shown in figure 3.53, are significantly reduced, resulting in reduced torsion vibration, as shown in figure 3.55.

3.6. Conclusion

Simulation results presented in this chapter show reduction in resonant torsional vibrations of the drivetrain for wide variety of wind speeds. The model of the drivetrain presented in this chapter is fairly complex, but it only captures torsional vibration effects. Presented vibration damping strategy is limited to torsional vibrations only. However, gear mesh flexibility results in vibrations that are of higher frequencies [42], [43]. It is not possible compensate for vibrations at these higher frequencies by controlling the generator torque, due to limited bandwidth of the generator current controller, which

cannot exceed the switching frequency of the generator side converter. However, reduced torsional vibrations would result in reduced mechanical stress on the drivetrain shafts. Further research would include analysis of effects of this control strategy on individual gears and gear teeth surfaces by using finite element analysis.

4. Ultracapacitor energy storage for reduction of output power variations of a wind turbine

In this chapter a novel method for reducing of output power variations of a variable speed wind turbine is proposed. Lithium-ion ultracapacitors are investigated as a solution for short term power fluctuation. An energy storage bank composed of series connected ultracapacitors is directly connected to the DC link of the double conversion system described in the chapter 2. This energy storage bank provides a buffer for decoupling input power from the generator and output power delivered to the grid. A filtering based method that optimizes the DC link voltage is proposed and verified by extensive simulations. Finally, an experimental setup of the scaled down double conversion system with lithium-ion ultracapacitor bank in the DC link was built and tested. Experimental results, shown at the end of this chapter, confirm capability of the ultracapacitor bank to filter large power variations.

4.1 Ultracapacitors for energy storage applications

Ultracapacitors are energy that store energy in form of potential energy of electrostatic field, in the same way as ordinary capacitors. The difference is in the fact that ultracapacitors have much larger capacitance, as their name suggests. The most attractive characteristic of ultracapacitors is that no chemical reactions are involved in energy storage/release process. The degradation processes of chemical reactants reduce lifecycle and limits power characteristics of batteries. In contrast, ultracapacitors have larger lifecycle and can be charged and discharged up to several hundred thousand times

without significant degradation in capacity. Moreover, energy can be stored or released in very short periods of time resulting in much higher power density (W/kg) of ultracapacitors compared to batteries (figure 4.3). The main disadvantage of ultracapacitors is low amount of energy per volume they can store compared to batteries, which makes them still inadequate replacement for batteries in applications that energy demand is more significant. However, large power density makes ultracapacitors ideal short-term energy storage devices in applications where large amount of power needs to be delivered or stored over short periods of time. Some examples of such applications are regenerative breaking in hybrid and electric vehicles, uninterruptible power supplies and power quality applications, consumer electronics, power tools, renewably energy systems, etc. Coupling batteries and ultracapacitors is attractive solution for applications where both energy and power density is important: industrial applications, renewable energy systems, and transportation. Ultracapacitors can greatly help solving several issues in electric power systems [30]. One of such issues addressed in this thesis is power quality improvements of wind turbines integrated into the grid and resulting impact on frequency deviations. Following two sections describe principle of operation of two classes of ultracapacitors: Electrolytic Double Layer Capacitor (EDLC), and Lithium-ion Capacitor (LIC). The ultracapacitor technology is active field of research, and promising results are achieved with carbon nanotube based ultracapacitors that potentially can achieve near 50% of energy density of electrochemical batteries while still retaining power density of other types of ultracapacitors.

4.1.1. Electrolytic Double Layer Capacitor (EDLC)

Electrolytic Double Layer Capacitor is the firstly introduced type of ultracapacitor. The principle of operation of EDLC is illustrated in Figure 4.1. Two metal electrodes are coated with activated carbon, highly porous form of carbon with large equivalent surface area. The space between activated carbon covered electrodes is filled with electrolyte with dielectric separator that prevents electrodes from mechanical contact. Separator is porous and allows transfer of positive and negative ions from one side to another. When voltage is applied at ultracapacitor terminals, positive ions are attracted toward the negative electrode while negative ions migrate toward the positive electrode. Due to activated carbon's porosity large number of ions can move close to the surface of electrode forming positive-negative charge distribution at nanometer distance, as illustrated in Figure 4.1.
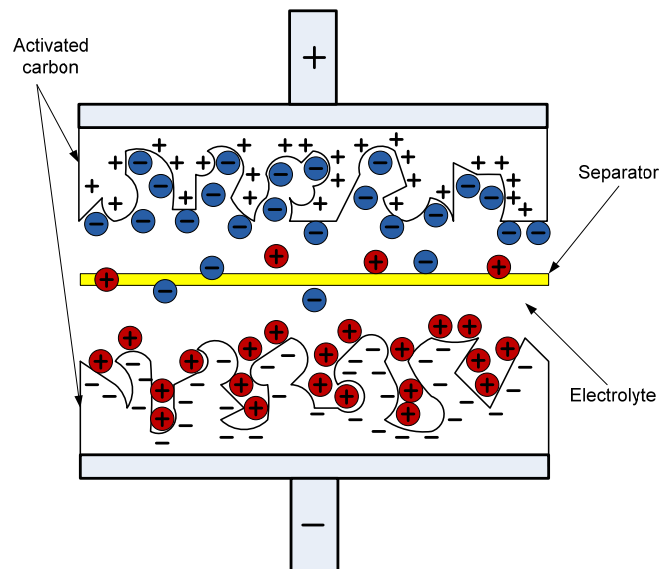
Figure 4.1. Electrolyte Double Layer Capacitor

Large surface area and small distance results in large capacitance. Each electrode with ions from electrolyte forms an equivalent capacitor resulting in two large capacitors (double layers) connected in series. Resulting capacitance is one half of the capacitance of one electrode, but voltage is doubled. In order to prevent chemical reactions between activated carbon and electrolyte voltage has to be low. Typical EDLC voltage is about 2.8V per cell. EDLC type of ultracapacitors can be completely discharged. One of the main issues in EDLC is contact resistance between a metal electrode and activated carbon coating. Special glue, called binder, has to be used and it introduces additional series resistance, thus reducing efficiency of EDLC.

4.1.2. Lithium-ion Ultracapacitors

Lithium-ion ultracapacitors have structure illustrated in figure 4.2. Positive electrode is the same as in EDLC, metal plate coated with activated carbon. Negative electrode is metal plate coated with lithium doped carbon. This electrode is very similar to the negative electrode of a lithium-ion battery. Another similarity is lithium salt organic solution as electrolyte. However, mechanism of storing energy is similar to EDLC.
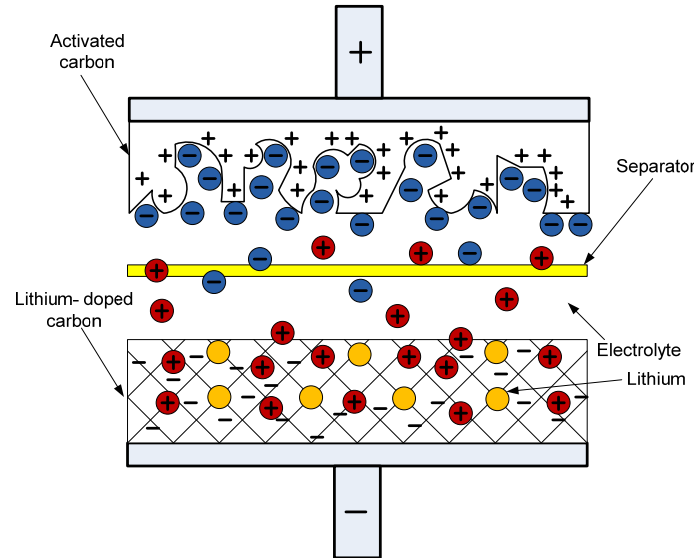
Figure 4.2. Lithium-ion ultracapacitor

During charging process, negative ions from electrolyte migrate toward the positive electrode that has large surface area due to activated carbon. At the same time, positive ions are being intercalated into carbon coated negative electrode. The process is reversed during discharging. Voltage has to be low, in order to prevent chemical reactions between electrolyte and carbon. However, main advantage of lithium ion ultracapacitors over EDLC is that voltage between electrodes can be increased nearly twice, due to lithium doping of the negative electrode. Energy stored in a capacitor is proportional to capacitance and the square of voltage across its terminals. Therefore, lithium ion ultracapacitors have close to four time larger energy density compared to EDLC, while keeping equally large power density. Figure 4.3 compares energy and power densities for several energy storage solutions. Lithium ion ultracapacitors with their large power capacity and energy capacity comparable to conventional batteries are chosen in this research as short term energy storage for wind energy conversion system.
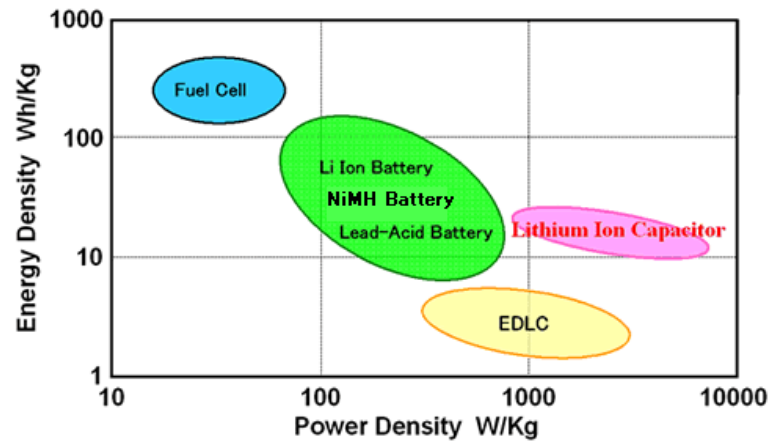
Figure 4.3. Power and energy densities (source: JM Energy Corporation)

Technical data of a 1200F LIC from JM Energy Corporation is given in the table 4.1.

Table 4.1.

Parameter / Cap. model	Operating Temperature [˚C]	Voltage range (min/max)[V]	Capacitance [F]	Energy density [Wh/kg]	Power density, at I=75A [W/kg]	Dimensions [mm]
1000F	-20 - +70	2.2/3.8V	700-1300	12	1000	138x106x5
2000F	-20 - +70	2.2/3.8V	1400-2500	14	1000	138x106x9

4.2. Dynamic Modeling of a Lithium-ion ultracapacitor

A mathematical model of ultracapacitor is a set of differential equations that give relation between voltage, current, and temperature during charging and discharging processes. There are several approaches to modeling of ultracapacitors. Models based on equivalent circuits consist of serial and parallel combinations of resistors and capacitors that form a circuit which has similar voltage and current characteristics as the ultracapacitor [86-91]. Typically, series of tests needed to be performed, during which the ultracapacitor was charged or discharged and voltage and current profiles were recorded [90],[91]. These models are easiest to implement in simulation software, and can be very

accurate [88]. However, equivalent circuit models do not give any information about physical and electrochemical processes inside the ultracapacitor. Another class of models use physical and electrochemical laws to describe behavior of ultracapacitors [92],[93]. These models can be very accurate, but they require precise data on geometry of the electrodes and chemical properties of electrolyte. However, they give complete information on behavior of ultracapacitors including thermal effects and characteristic degradation due to aging. Some methods for ultracapacitor modeling combine equivalent circuit with physical laws based models [94],[95].

The model developed for the purpose of this research is based on equivalent circuit, and it is fully described in [97]. In order to study electrical behavior of a lithium-ion ultracapacitor cell, extensive laboratory tests were performed. The ultracapacitor was charged with constant current pulses, followed by resting periods that allows the voltage at the ultracapacitor's terminals to reach steady state. These charging tests were repeated for various current levels and pulse/resting time durations. The low voltage- high power DC power supply used for these tests has capability of operating in constant current or constant voltage modes. As long as voltage at the ultracapacitor's terminals was below upper voltage limit of 3.8V, constant current mode provided constant current pulses that charged the ultracapacitor in steps. Once the voltage reached the upper voltage limit, preprogrammed in the DC power supply, constant voltage mode limited charging current in order to keep the voltage at the maximum allowed value of 3.8V, thus preventing damaging the ultracapacitor. Once the charging current in the constant voltage mode reached the preprogrammed minimum value of 2A, the charging test was completed, and the ultracapacitor was fully charged with voltage across its terminals near 3.8V. Then

discharging test was performed. To discharge ultracapacitor, the active load device was used. This device could also be put into constant current, constant voltage, or constant resistance modes of operation. Again, at the beginning of the test, constant current mode was used. The ultracapacitor was discharged by delivering constant current pulses to the active load. Each current pulse was followed by resting period that allowed the ultracapacitor voltage to stabilize. Voltage and current measurements were logged into data files during the procedure. When voltage of the ultracapacitor reached lower limit of 2.2V, the active load switched to the constant voltage mode that kept discharging of the ultracapacitor, but limiting the discharging current. Once that the discharging current drops to 2A, discharging test completes. The charging and discharging tests were repeated for various charging and discharging currents. In addition to constant current pulse charging tests, additional charging tests that utilized sinusoidal currents were performed. After collecting the data from charging and discharging tests, the parameters of the equivalent circuit were calculated. The waveforms of a charging and discharging tests are given in figure 4.4a and 4.4b.
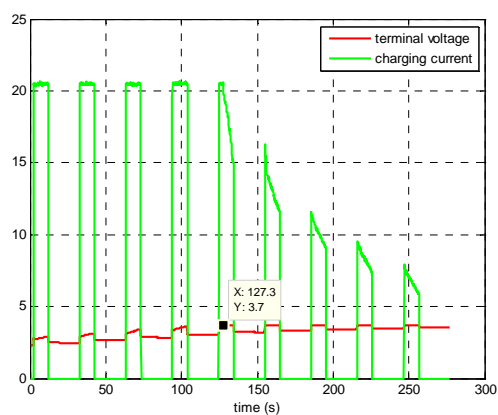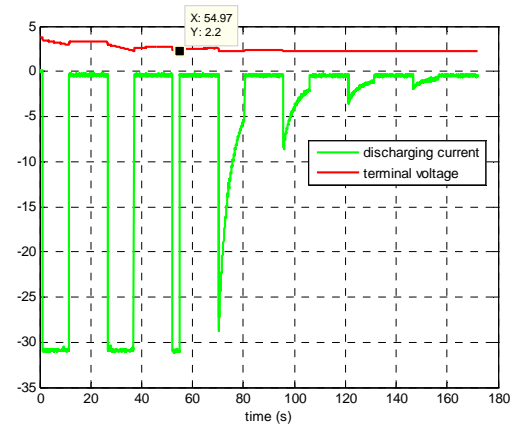
(a)　　　　　　　　　　　　　　　　(b)

Figure 4.4. Charging and discharging tests [97]

The equivalent circuit model of the ultracapacitor is shown in Figure 4.5. Parameters of this model are given in the table 4.2. From the charging and discharging test, it was observed that capacitance of the ultracapacitor is nonlinear and dependent on the open circuit voltage. For the modeling purpose, this nonlinear voltage-capacitance dependence is approximated by the 4th order polynomial with coefficients listed in the table 4.3. The additional details about testing procedure and parameter calculation are given in [97].
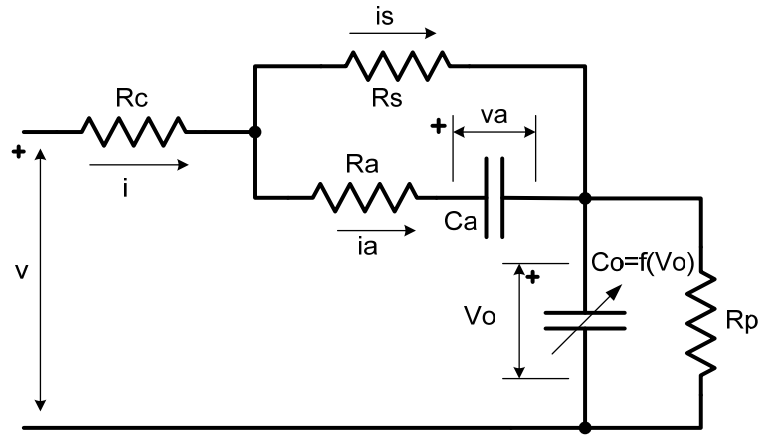
Figure 4.5. Equivalent circuit model of a lithium-ion ultracapacitor

Ra	Rs	Ca
79.9mΩ	5.34mΩ	30.6F

Capacitance Co is a function of the open circuit voltage.

$$C_O = a \cdot V_{oc}^4 + b \cdot V_{oc}^3 + c \cdot V_{oc}^2 + d \cdot V_{oc} + e$$

a	b	c	d	e
-703.3938	9359.727	-45480.9041	96048.0835	-73516.7294

Self discharging process is modeled by adding parallel resistor Rp. However, according to the manufacturer's data, estimated discharging time from 3V to 2.2V is 20 years. Also, laboratory measurements showed no change in the open circuit voltage of an

ultracapacitor cell during one month period. Therefore, it is valid to neglect this resistance in further calculation. It is however, taken into account in Simulink model of the circuit, as a resistor with very large resistance. Resistance Rc is a series resistance of terminals and connection with the rest of the circuit. From the equivalent circuit, and by neglecting Rp, it follows:

$$i - i_s + i_a = 0 \tag{1}$$

$$v - R_c \cdot i + R_s \cdot i_s + v_{Co} = 0 \tag{2}$$

$$R_s \cdot i_s - R_a \cdot i_a - v_{Ca} = 0 \tag{3}$$

$$i = C_o \cdot \frac{dv_{Co}}{dt} \tag{4}$$

$$i_a = C_a \cdot \frac{dv_{Ca}}{dt} \tag{5}$$

$$\begin{bmatrix} \dfrac{dv_{Co}}{dt} \\ \dfrac{dv_{Ca}}{dt} \end{bmatrix} = \begin{bmatrix} 0 & 0 \\ 0 & -\dfrac{1}{C_a \cdot (R_s + R_a)} \end{bmatrix} \cdot \begin{bmatrix} v_{Co} \\ v_{Ca} \end{bmatrix} + \begin{bmatrix} \dfrac{1}{C_o} \\ \dfrac{R_s}{C_a \cdot (R_s + R_a)} \end{bmatrix} \cdot [i] \tag{6}$$

$$v = \begin{bmatrix} 1 & \dfrac{R_s}{R_s + R_a} \end{bmatrix} \cdot \begin{bmatrix} v_{Co} \\ v_{Ca} \end{bmatrix} + \begin{bmatrix} R_c + \dfrac{R_a \cdot R_s}{R_a + R_s} \end{bmatrix} \cdot [i] \tag{7}$$

Equations (6) and (7) are the state space representation in the form:

$$\dot{x} = A \cdot x + B \cdot u \tag{8}$$

$$y = C \cdot x + D \cdot y \tag{9}$$

Simulink implementation of the model based on equations (1)-(5) is shown in figure 4.6. From the state space model (6), (7), it is possible to derive the transfer function form current to the voltage at the ultracapacitor terminals.

$$G(s) = \frac{V(s)}{I(s)} = C \cdot (s \cdot I - A)^{-1} \cdot B + D \tag{10}$$

D term from the equations (7) and (10) can be neglected due to very small value. With this assumption, the resulting transfer function is:

$$G(s) = \frac{s^2 \cdot \left(R_c + \frac{R_s \cdot R_a}{R_s + R_a}\right) + s \cdot \left(\frac{1}{C_o} + \frac{R_s^2}{C_a \cdot (R_s + R_a)^2} + \frac{R_c}{C_a \cdot (R_s + R_a)} + \frac{R_s \cdot R_a}{C_a \cdot (R_s + R_a)^2}\right) + \frac{1}{C_o \cdot C_a \cdot (R_s + R_a)}}{s \cdot \left(s + \frac{1}{C_a \cdot (R_s + R_a)}\right)} \tag{11}$$

$$G(s) = \frac{s^2 \cdot a + s \cdot b + c}{s \cdot (s + p)} \tag{12}$$

The transfer function shows that there is a pole in the origin, as expected since capacitor voltage is integral of current. Also there is a real pole at $-\dfrac{1}{C_a \cdot (R_s + R_a)}$ that results in the additional exponential response term in the capacitor voltage. The ultracapacitor model posses also a real zero whose location depends on the parameter Co. The pole and zero locations of the ultracapacitor model for capacitor voltages from 2.2V to 3.8V are shown in Figure 4.7. The pole and zero introduce additional dynamics in the system with ultracapacitors as energy storage, and this dynamics has to be taken into account in order to design high performance systems. In the research reported in this thesis, ultracapacitor energy storage replaces standard DC link capacitor in the double conversion system that connects wind turbine to the utility grid. Standard control algorithms for double conversion systems have been being widely used with electrolytic capacitor in the DC link. In order to add ultracapacitor energy storage in the DC link, the standard control algorithms have to be modified, and a method based on direct output power control is proposed in the next section.
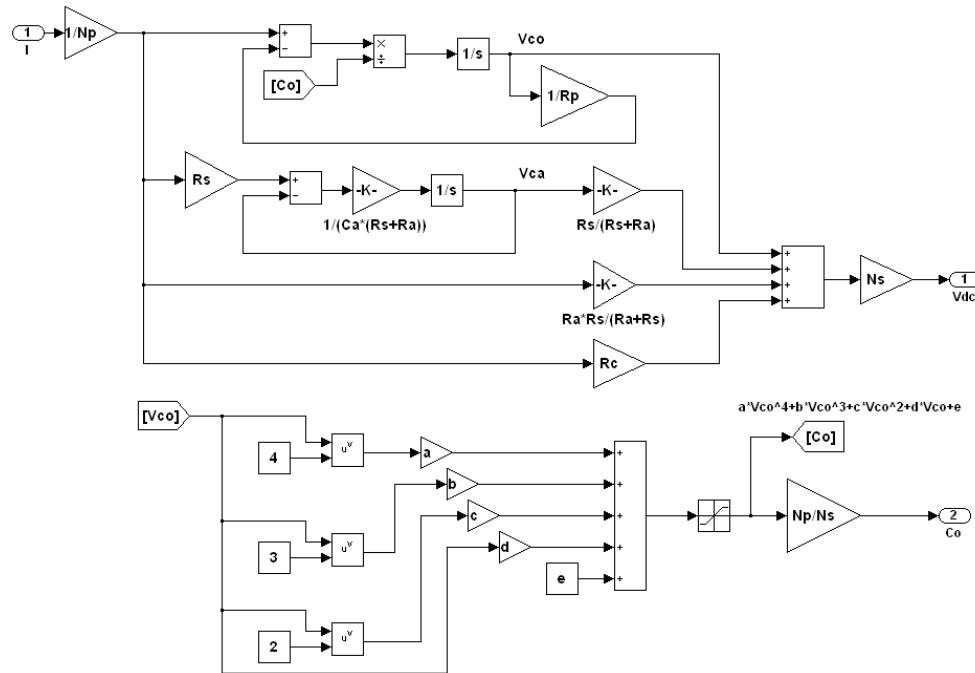
Figure 4.6. Simulink model of a ultracapacitor module
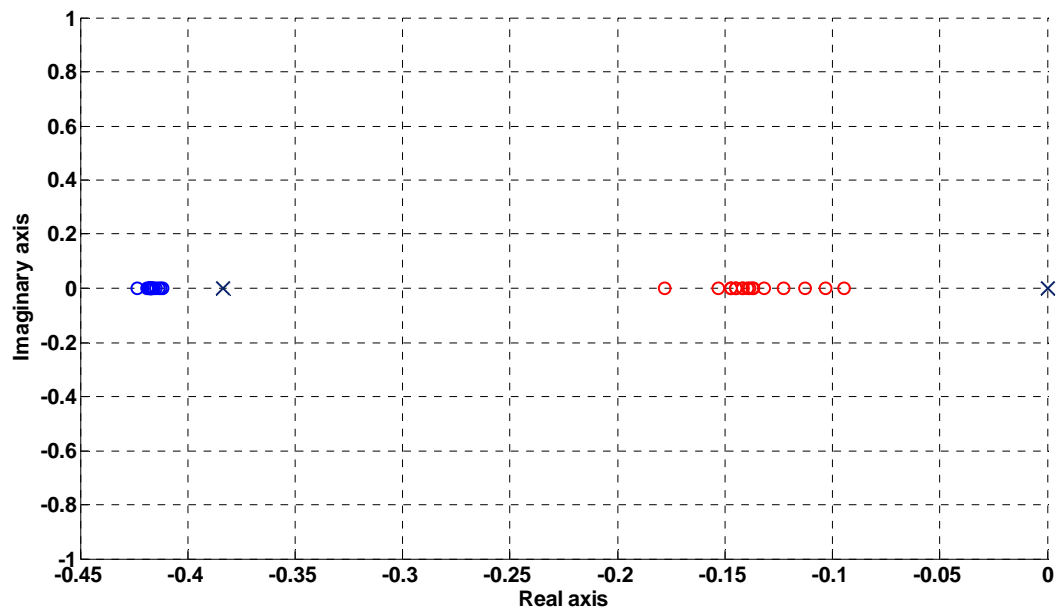
Figure 4.7. Voltage dependent zero-pole locations of the ultracapacitor model

4.3. Ultracapacitors in the DC link of double conversion system of a wind turbine

Conventional wind turbines based on full rated power conversion system have electrolytic capacitor in DC link. This capacitor only filters voltage ripple of the DC link voltage and cannot store significant amount of energy, relative to the energy produced by the wind turbine. DC link voltage is kept constant by control action of the outer control loop of the grid side converter (inverter). Variable input power from the generator acts as a disturbance which is compensated by proper adjusting of the current reference for the inner current control loops of the inverter. In order to keep DC link voltage constant, the DC side current of the inverter has to be equal to the DC current of the generator side converter (rectifier) resulting in no charging or discharging current of the DC link capacitor. Therefore, input power of the generator, and output power of inverter are strongly coupled. Addition of a large capacitance in the DC link would enable additional degree of freedom as energy can be stored in the capacitor making possible control of the output power independently of the input power from the generator. DC link voltage would be no longer constant, as it depends of the integral of the DC current difference of inverter or rectifier, as illustrated in Figure 4.8. Output power becomes indirectly dependent on DC link voltage reference, which would be limited between maximum and minimum values that guarantee safe and reliable operation of the power conversion system.
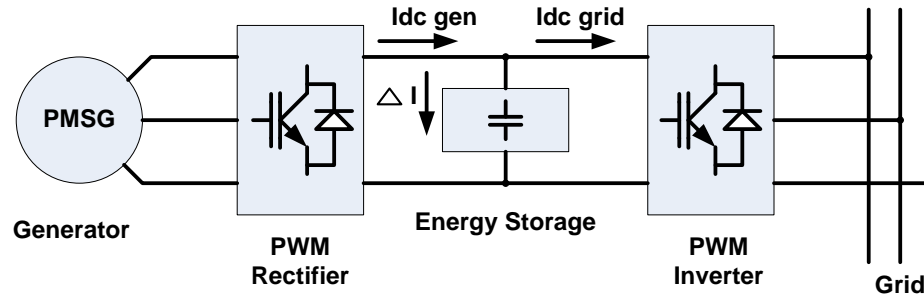
Figure 4.8. Energy storage in DC link

Dynamic behavior of lithium-ion ultracapacitors is significantly different than the behavior of standard capacitor. Even though standard capacitors possess parasitic effects such as equivalent series resistance or nonlinearities of the isolating material, these effects are much smaller than the parasitic effects in ultracapacitors. In the systems with ultracapacitor based energy storage device, the dynamic behavior that is significantly different than that of ideal capacitors has to be taken into account. Major issue with lithium-ion utracapacitor based energy storage is large voltage drop on parasitic equivalent series-parallel Ra-Rs-Ca circuit during charging or discharging processes. The dynamic behavior of an ideal capacitor with voltage directly proportional to the charge or the integral of the charging or discharging current, makes it more desirable over the behavior of ultracapacitors. Since ultracapacitor voltage is not proportional only to the integral of the current, indirect output power control by controlling DC link voltage, becomes more difficult. At the same time, due to limits on DC link voltage necessary for regular operation of the double conversion system, indirect control of output power by controlling DC link voltage reference would ensure that this voltage is always within the prescribed limits. The method proposed in this thesis controls the output power directly, while DC link voltage control is indirect. Also, this control method optimizes DC link voltage by introducing the additional component into output power reference that is

proportional to the deviation of the DC link voltage from the optimal point which maximizes available energy storage buffer.

4.3.1 Output power smoothing – Direct output power control

In steady state, energy stored in the ultracapacitor module is equal to:

$$E = \frac{1}{2} \cdot C_n \cdot V_{DC}^2$$

(13)

Where C_n is rated capacitance of the ultracapacitor module. Due to the low voltage limit of the DC link, as well as low voltage limitation on a lithium-ion ultracapacitor cell, total available energy that can be stored in the ultracapacitor module is:

$$\Delta E = E_{max} - E_{min} = \frac{1}{2} \cdot C_n \cdot \left(V_{DC\,max}^2 - V_{DC\,min}^2 \right)$$

(14)

When the wind turbine produces power while operating in regions 2 and 2 ½ , generated power varies as wind velocity changes. In order to reduce power variations at the output of the wind turbine, ultracapacitor energy storage should be able to store energy when wind speed increases or release energy when it decreases. Therefore, the ultracapacitor storage should never be fully charged or fully discharged since it would not have capacity to further store or release energy resulting in inability of the output power control system to reduce power fluctuations. In order to maximize output power smoothing capability, the DC link voltage should be kept as close as possible to the optimal value which maximizes charging or discharging capability of the ultracapacitor energy storage system.

$$\Delta E_{store} = \frac{1}{2} \cdot C_n \cdot \left(V_{DC\,max}^2 - V_{DCopt}^2 \right)$$

(15)

V_{DCopt} is the optimal DC link voltage with respect to the available energy storage buffer ΔE_{store}.

At the same time, the ultracapacitor energy storage has to be able to provide energy for the output:

$$\Delta E_{available} = \frac{1}{2} \cdot C_n \cdot \left(V_{DCopt}^2 - V_{DC\min}^2 \right)$$

(16)

$\Delta E_{available}$ is stored amount of energy available to be delivered to the output. Now, the optimal DC link voltage can be calculated, by assuming that capacitance is constant.

$$\Delta E_{available} = \Delta E_{store}$$

(17)

$$\frac{1}{2} \cdot C_n \cdot \left(V_{DCopt}^2 - V_{DC\min}^2 \right) = \frac{1}{2} \cdot C_n \cdot \left(V_{DC\max}^2 - V_{DCopt}^2 \right)$$

(18)

$$V_{DCopt}^2 - V_{DC\min}^2 = V_{DC\max}^2 - V_{DCopt}^2$$

(19)

$$2 \cdot V_{DCopt}^2 = V_{DC\max}^2 - V_{DC\min}^2$$

(20)

$$V_{DCopt} = \sqrt{\frac{V_{DC\max}^2 - V_{DC\min}^2}{2}}$$

(21)

Nonlinear dependence of capacitance to the stored energy and voltage is neglected in this calculation. Also, series capacitance C_a can store or release significant amount of energy thus contributing dynamically to the storage capacity is neglected too.

As mentioned earlier, energy storage decouples output power from the generated power, while operating turbine in regions 2 or 2 ½ :

$$P_{out} = P_{generator} \pm P_{storage}$$

(22)

The equation (22) is the basis for direct output power method where P_{out} is commanded directly by the output power controller. Energy storage then provides additional power buffering depending on output power demand and available incoming power from the generator. In order to achieve effective power smoothing, proper selection of the output power command is the main challenge. The output power should vary less than input power from the generator, but at the same time the storage power $P_{storage}$ should not lead to fully charging or discharging of the energy storage. Therefore, depending on the size of the storage, output power will be variable too, but with much slower variations.

The method for direct output power smoothing proposed here is based on adaptive low pass filtering with DC link voltage optimization. The block diagram of the proposed controller is illustrated in figure 4.9.
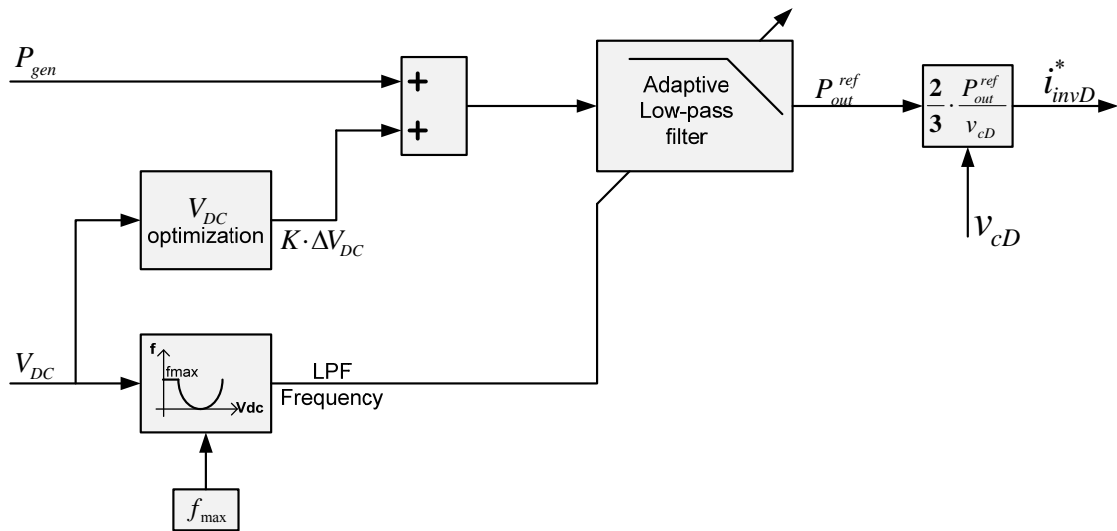
Figure 4.9. Adaptive filtering method for direct output power smoothing

The output power reference is the result of low pass filtering (LPF) of the generator power P_{in}. However, depending on the bandwidth of the LPF, DC link voltage would either reach upper or lower limits if the bandwidth is too low, or storage capacity would

not be used in the most optimal way if the bandwidth is too high, thus allowing larger power variations at the output. In order to avoid this problem, the LPF cut-off frequency is variable and it depends on DC link voltage, therefore forming an adaptive system. Now, as DC link voltage approaches lower or upper limits, large output power variations are allowed by increasing the bandwidth of LPF. On the other hand, closer the DC link voltage is to the optimal point V_{DCopt}, smaller power fluctuations appear in the output power by reducing the bandwidth of the LPF. The function that maps dc link voltage to LPF cut off frequency should have minimum at V_{DCopt}, and should monotonously increase as voltage moves away from this point in any direction. Quadratic function naturally satisfies this requirement.

$$f_{LPF}[Hz] = a \cdot V_{DC}^2 + b \cdot V_{DC} + c \qquad (23)$$

Coefficients a,b, and c are design parameters that depend on maximum and minimum DC link voltage as well as maximum frequency at these points. Since optimum voltage is not in the middle of the allowed voltage range, the negative portion of the quadratic function is simply limited to f_{LPF}^{min}.

$$a \cdot V_{DC\,max}^2 + b \cdot V_{DC\,max} + c = f_{LPF}^{max} \qquad (24)$$

$$a \cdot V_{DC\,min}^2 + b \cdot V_{DC\,min} + c = f_{LPF}^{max} \qquad (25)$$

$$a \cdot V_{DCopt}^2 + b \cdot V_{DCopt} + c = f_{LPF}^{min} \qquad (26)$$

Parameters a,b, and c are solution of this system of linear equations. The minimum frequency f_{LPF}^{min} should be smaller for an order of magnitude then f_{LPF}^{max} resulting in maximum filtering when DC link voltage is close to the optimum point.

Additional and very important feature of the proposed method is the DC link voltage optimization. Even with adaptive filtering, nothing prevents the algorithm to reach an equilibrium point where frequency f_{LPF} would be greater than $f_{LPF}^{\min}$ but less than $f_{LPF}^{\max}$. Moreover, any positive or negative trend in input power P_{in} would move DC link voltage toward positive or negative limits thus increasing f_{LPF} and suboptimal use of the energy storage. To prevent this from happening, the DC link voltage optimization term is added to the input power P_{in}. This optimizing component is proportional to the DC link voltage difference from the optimal point V_{DCopt}. It is added before the filter to avoid injecting a variable output power component into the output power reference when the DC link voltage oscillates around V_{DCopt}.

$$P_c(t) = K \cdot \left(V_{DC}(t) - V_{DCopt} \right)$$
(27)

If DC link voltage is greater than V_{DCopt} then optimizing component P_c is going to be positive, resulting in increased output power reference P_{out}. Increased P_{out} leads to discharging the ultracapacitor module resulting in decrease in the DC link voltage. Therefore, a negative feedback loop is established that keeps DC link voltage near V_{DCopt}. In case when DC link voltage is smaller than V_{DCopt}, P_c becomes negative, thus reducing the output power reference P_{out} which in turn leads to charging the ultracapacitor energy storage and increasing of DC link voltage. Gain K is a design parameter. It should be large enough to effectively keeps DC link voltage near V_{DCopt}, but not too large to prevent increased output power fluctuations due to the DC link voltage optimization algorithm. The value of this parameter can also be adaptive, depending on the turbulence level at a

particular site where the wind turbine equipped with the ultracapacitor energy storage is installed. For the purpose of research reported in this thesis, this value is kept constant. Wind turbine control structure which include the gearbox vibration damping from the previous chapter and output power smoothing algorithm is shown in figure 4.10. The Simulink model of a wind turbine from the previous chapter is modified by adding the model of the ultracapacitor module (figure 4.6) and adaptive filtering algorithm in place of the DC link voltage controller. The effectiveness of the algorithm described in this section was tested by extensive simulations under various wind speed profiles and size of energy storage. Following section describes Simulink implementation and simulation results.

Figure 4.10. Wind turbine control structure with drivetrain

vibration damping and output power smoothing

4.3.2. Simulink implementation of the output power smoothing algorithm

Wind turbine model developed in the chapter 2 is expanded to include ultracapacitor energy storage and output power smoothing algorithm. Figure 4.11 shows new Simulink model of the electrical block of the wind turbine model from chapter 2.

Generator side, as well as the grid side of the double conversion system, is the same as in previous case used to test active vibration damping control. The differences are the DC link block which now contains the model of the lithium-ion ultracapacitor module, as well as the direct output power control block (DPC) responsible for output power smoothing replacing the previous PI controller of the DC link voltage. Figure 4.12 shows the new DC link block. The model of ideal capacitor from chapter 2 has been replaced by the model from figure 4.6. The DC link currents of the rectifier and inverter are calculated from d and q components of the generator and inverter AC side voltages and currents. The difference between these currents charges or discharges the ultracapacitor module.
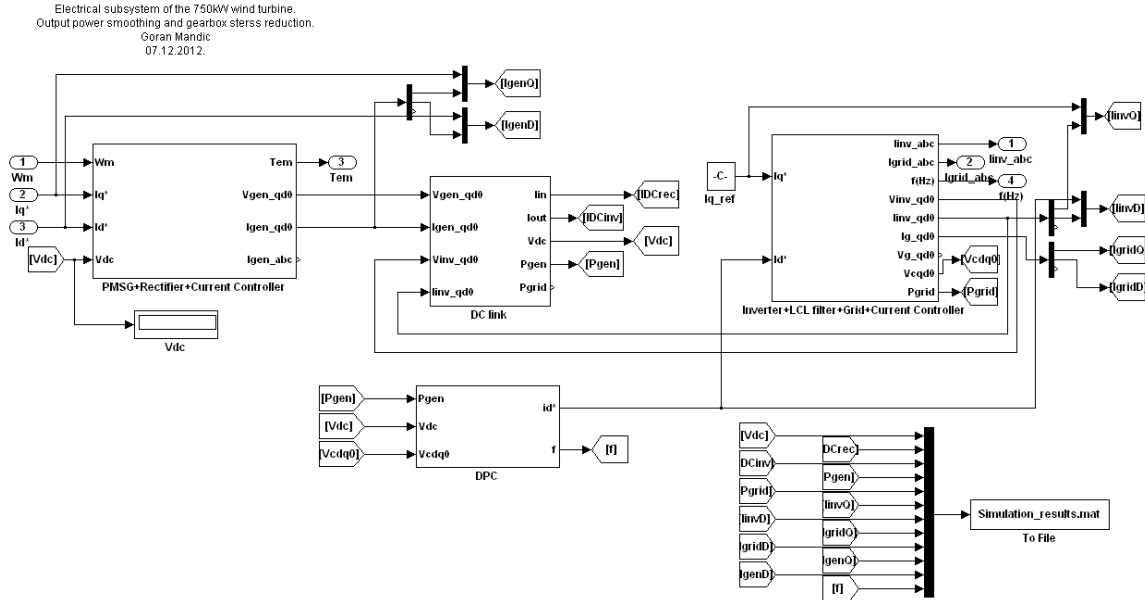
Figure 4.11. Electrical subsystem of the 750kW wind turbine

with output power smoothing controller
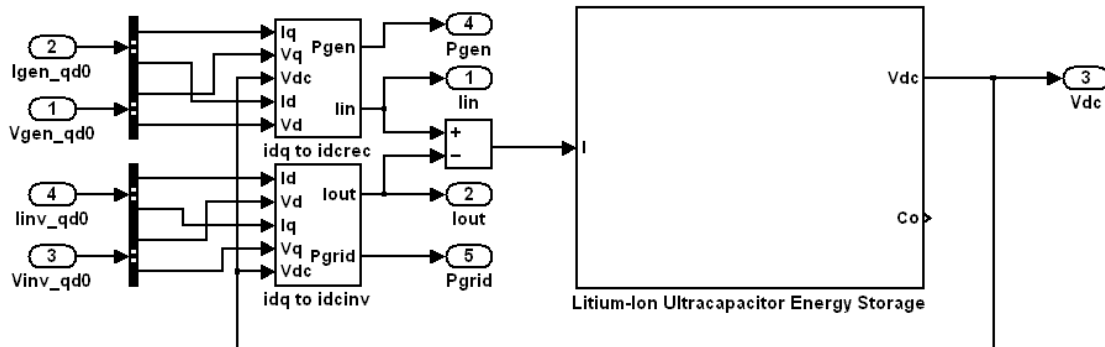
Figure 4.12. Lithium-ion energy storage in the DC link

Simulink implementation of the algorithm from figure 4.9. is shown in figure 4.13. Three major components are adaptive low-pass filter , f_{LPF} calculation, and dc link voltage optimization. Implementations of these blocks are shown in figures 4.14, 4.15, and 4.16 respectively. Step source in the adaptive low-pass filter determines initial state of the low pass filter and starting point of output power smoothing. Corner value of the LPF frequency is set to 0.06Hz.
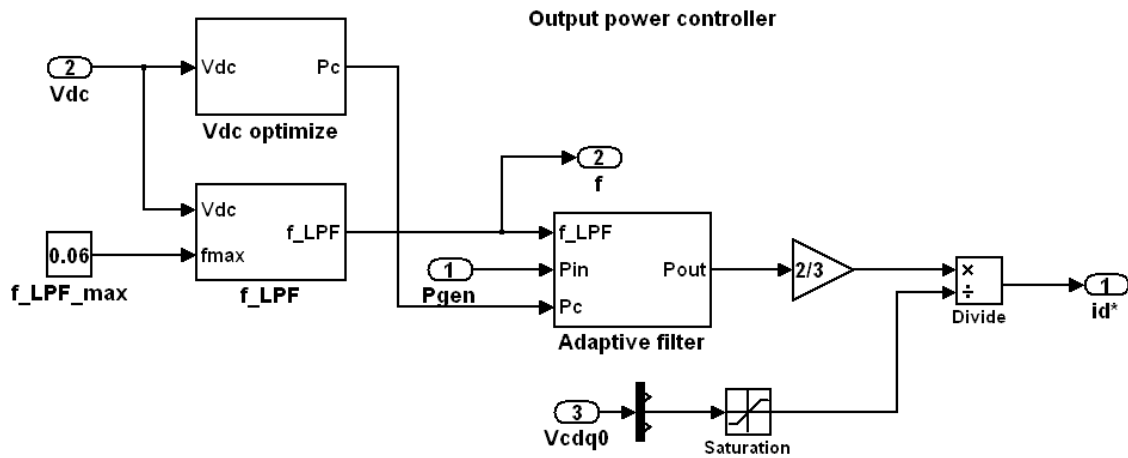
Figure 4.13. Output power smoothing controller

In chapter 2, the minimum DC link voltage for the 750kW turbine has been determined as 1120V. Assuming that the minimum DC link voltage is 1150V, and by choosing the minimum allowed voltage across an individual lithium-ion ultracapacitor cell as 2.4V, the number of cells connected in series is:

$$Ns = \frac{V_{DC\,min}}{V_{LIC\,min}} = \frac{1150V}{2.4V} \approx 480$$

By allowing individual ultracapacitors to charge up to 3.6V, the maximum dc link voltage is:

$$V_{DC\,max} = Ns \cdot V_{LIC\,max} = 480 \cdot 3.6V \approx 1730V$$
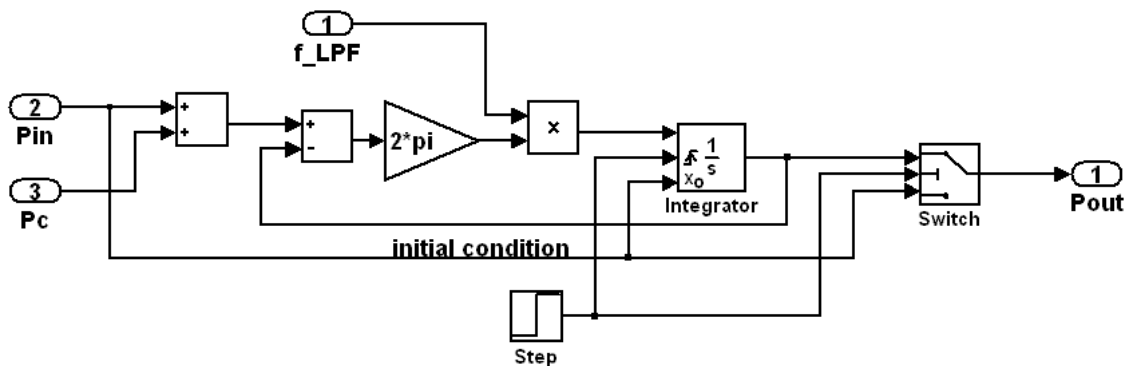
Figure 4.14. Adaptive low-pass filter
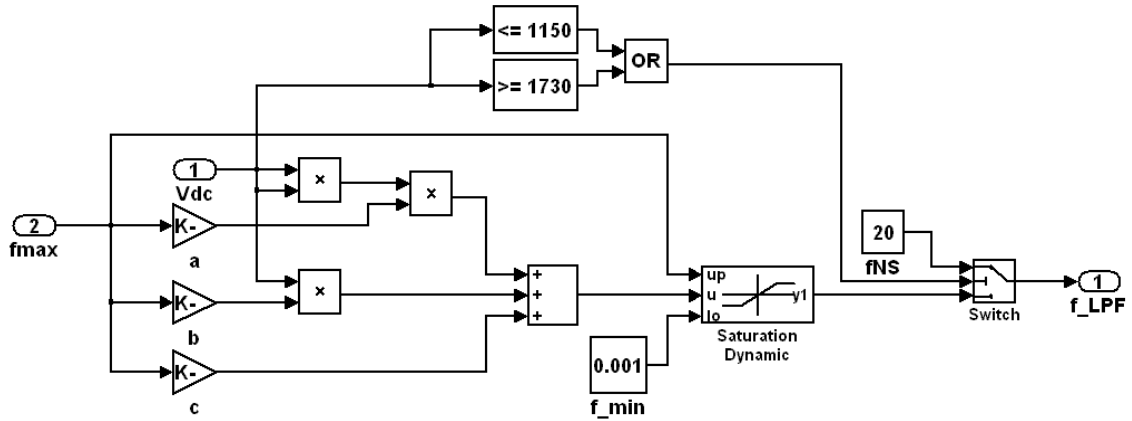
Figure 4.15. Cut-off frequency calculation for the adaptive low-pass filter
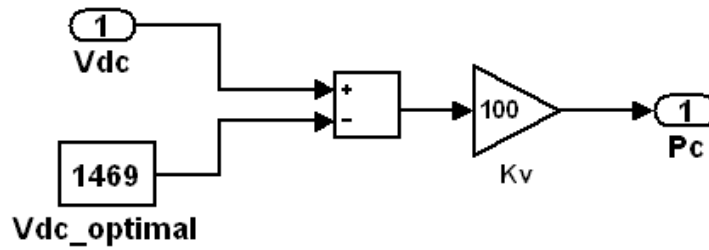
Figure 4.16. DC link voltage optimization block

With known minimum and maximum DC link voltages, the optimal point voltage of the DC link can be calculated as:

$$V_{DCopt} = \sqrt{\frac{V_{DC\,max}^2 - V_{DC\,min}^2}{2}} = \sqrt{\frac{1730^2 - 1150^2}{2}} \approx 1469V$$

In order to increase the storage capacity of the ultracapacitor energy storage, additional parallel strings of ultracapacitor cells can be added. However, each string has to have the same number of ultracapacitor connected in series. Finally, as the additional protection from crossing the upper or lower dc link voltage limit, the mean of bypassing the output power smoothing is provided. In case when DC link voltage is equal to either upper or lower limit the LPF frequency is instantly switched to 20Hz, thus allowing all power fluctuations from input to pass to the output. However, DC link optimization will still be

able to drive dc link voltage back inside the normal operational interval resulting in bypass intervals to be very brief, as shown in simulation results presented later in this chapter. In the simulations presented in following section, the power smoothing algorithm is tested under the same condition with 4, 2, and 1 string of ultracapacitors.

4.4. Simulation results

The same turbulent wind speed profiles used to test drivetrain vibration damping algorithm in the chapter 3 are used for test the output power smoothing algorithm. The TurbSim input file for generating the wind profiles are listed in the Appendix. Simulation time is much longer, 600 seconds as the power smoothing effects are better observed over longer time intervals.

4.4.1. Wind speed profile A1

Wind profile I is used in the first set of simulations. Simulations were repeated for the cases when the ultracapacitor storage has 4, 2, and 1 parallel strings. Wind speed profile and rotational speed are shown in figure 4.17. They are the same for all three simulation cases. As it can be seen on figure 4.17, there is a period of about 50s starting at 400s when the turbine was operating in the region 3, delivering constant power to the grid.

4.4.1.1. Simulation with 4 parallel ultracapacitor strings

Generator and output power are shown in figure 4.18 and storage power is shown in figure 4.19. As shown in the figure 4.18, power variations of the output power are significantly reduced compared to input power from the generator. In case when ultracapacitor storage would not be used, the input and the output power would be the same. The storage power plot shows that large peaks of power are needed in some instances, to compensate for input power variations.
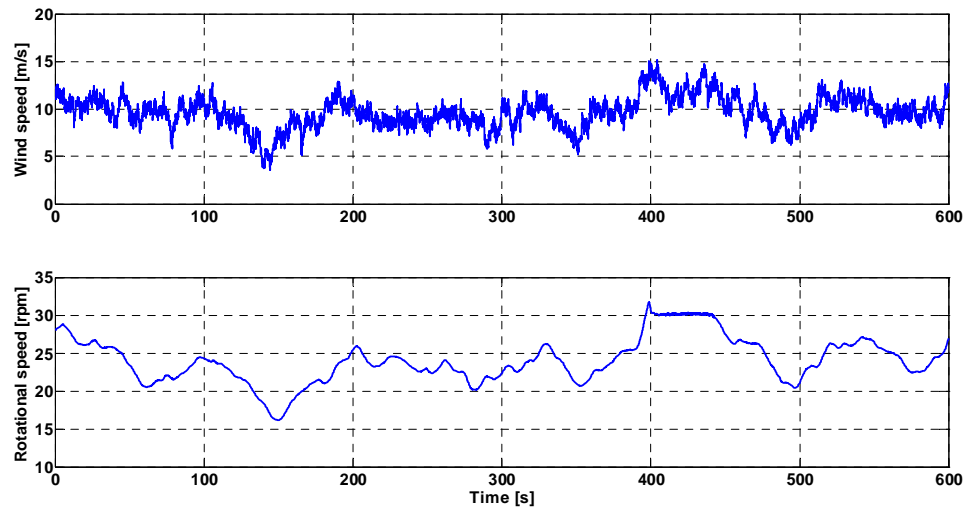
Figure 4.17.Wind speed profile and rotational speed
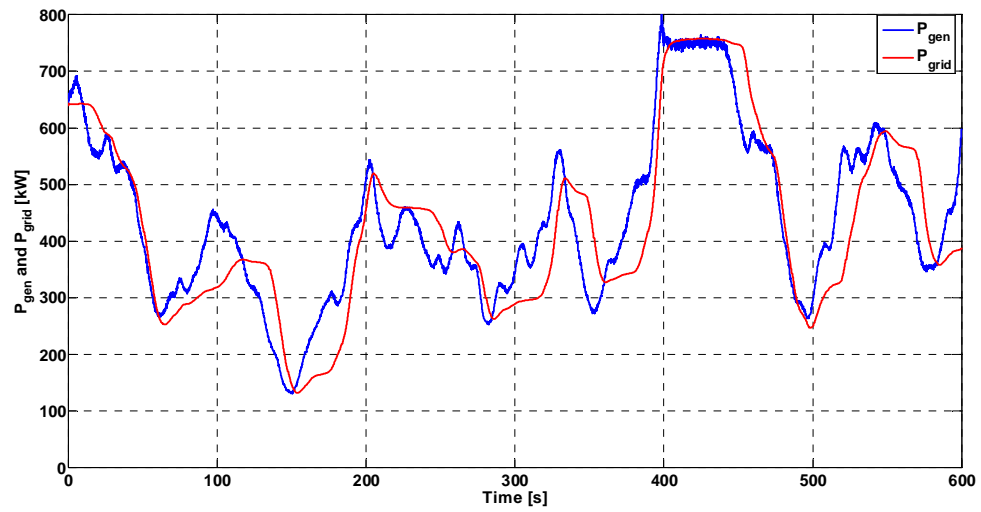
Figure 4.18. Generator and output power
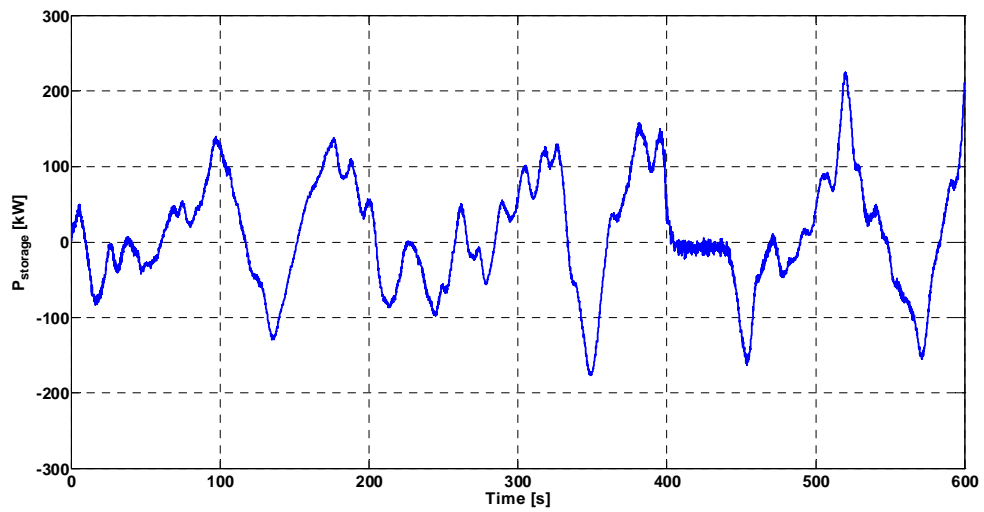
Figure 4.19. Ultracapacitor energy storage power
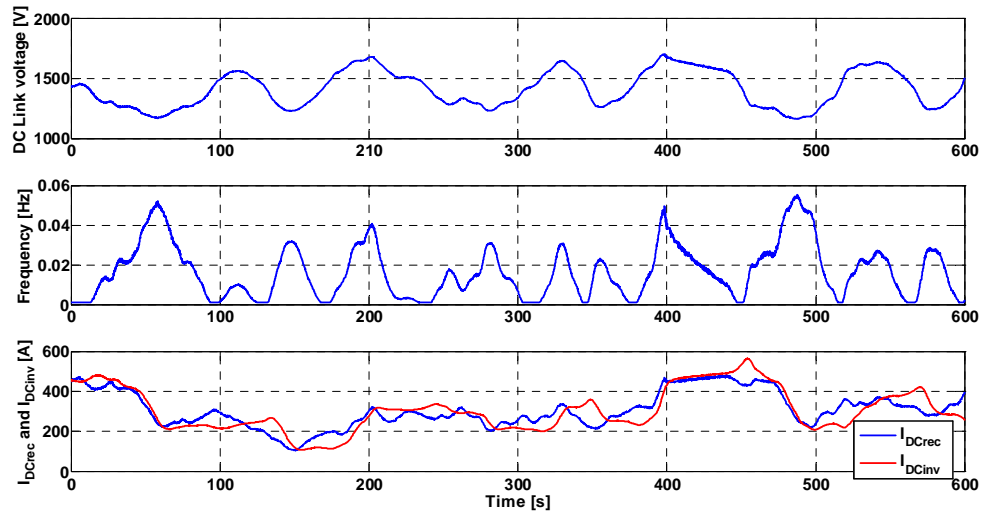
Figure 4.20. DC link voltage, LPF frequency, and DC link currents

DC link voltage, LPF frequency and dc link currents are shown in figure 4.20. As result of medium level of turbulence of the wind profile I, there are no intervals when power smoothing was bypassed which leads to the conclusion that upper frequency of LPF can be reduced from 0.06Hz to the smaller value further reducing output power fluctuations.

4.4.1.2. Simulation with 2 parallel ultracapacitor strings

Generator and output power plots are shown in figure 4.21. Output power fluctuations are still significantly reduced, but not as much as in the previous case as the result of reduced storage capacity.
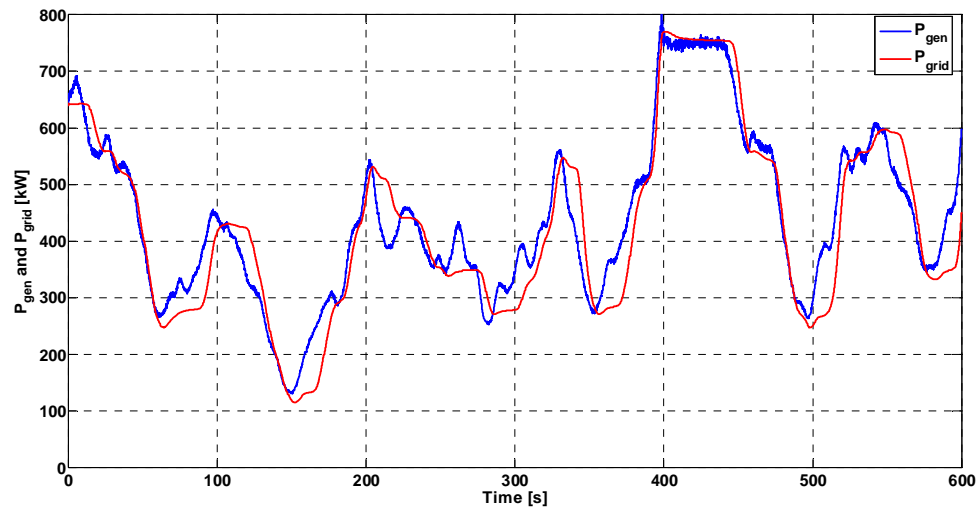
Figure 4.21. Generator and output power
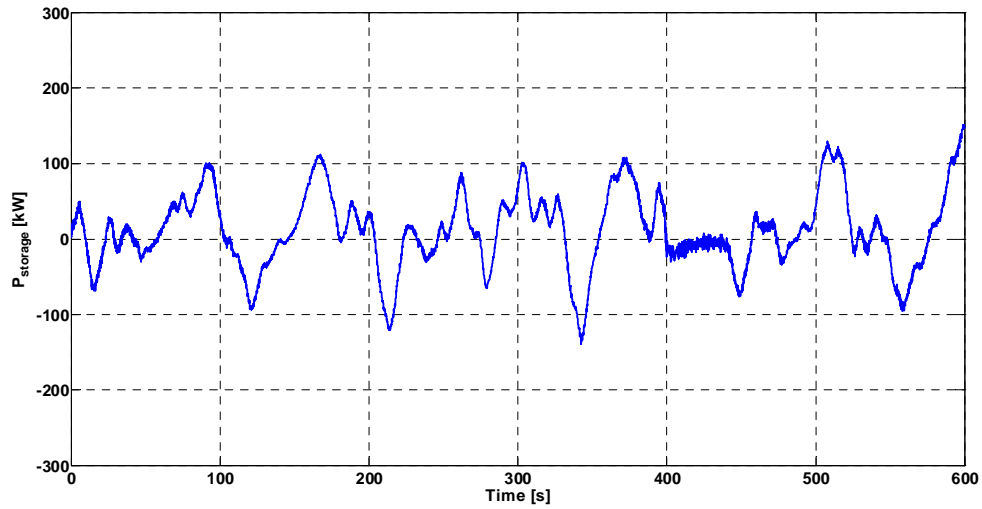
Figure 4.22. Ultracapacitor energy storage power

As the result of reduced size of energy storage, the ultracapacitor power peak is reduced as well, as shown in figure 4.22. Figure 4.23 shows DC link voltage, LPF cut-off frequency and DC link currents. LPF cut-off frequency reaches peak several times, including several intervals when power smoothing algorithm was bypassed.
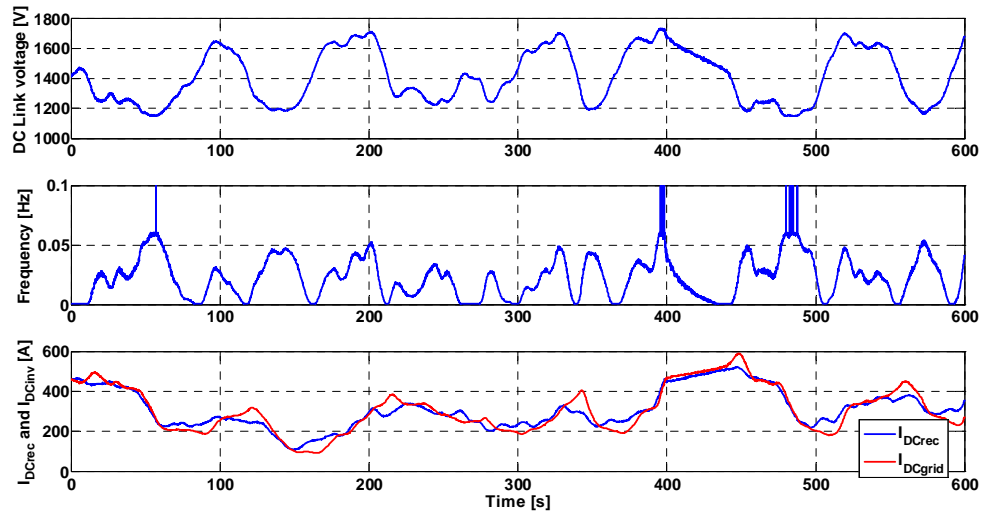
Figure 4.23. DC link voltage, LPF frequency, and DC link currents

4.4.1.3. Simulation with single ultracapacitor string

Finally, with only one ultracapacitor string the storage capacity is further reduced. Generator and output power are shown in figure 4.24. Power fluctuations are still reduced, but not as much as in the previous cases. The LPF cut-off frequency plot from figure 4.26 shows that peak is reached more frequently with greater number of bypass intervals when DC link voltage is at low or high limit.
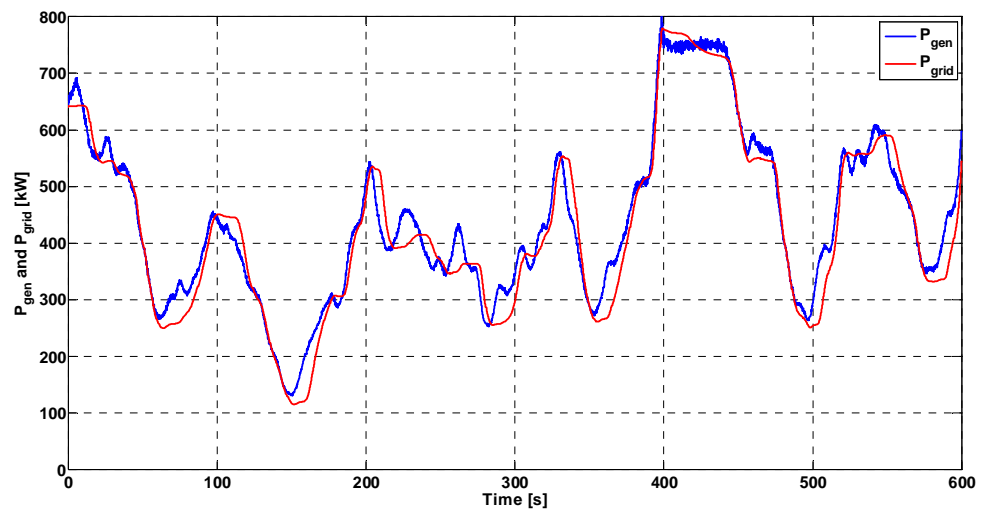
Figure 4.24. Generator and output power
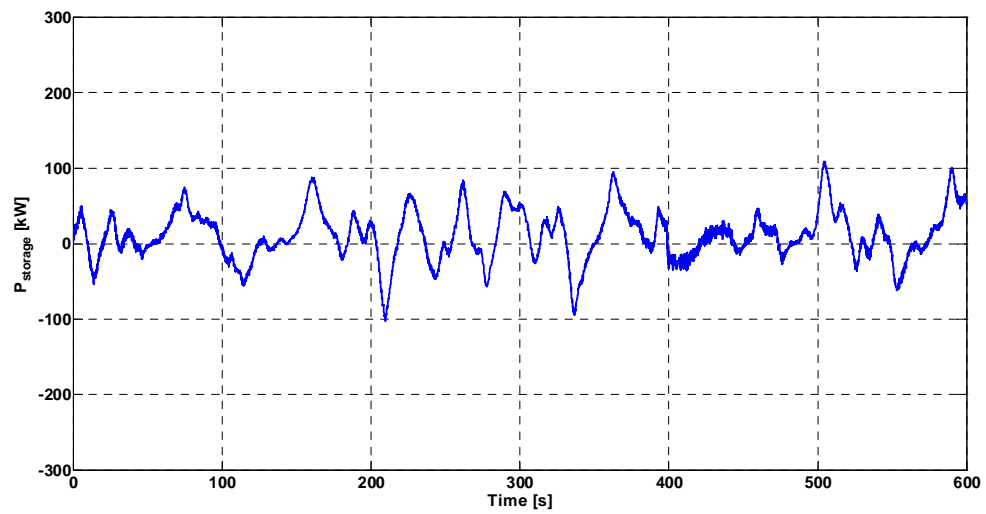
Figure 4.25. Ultracapacitor energy storage power
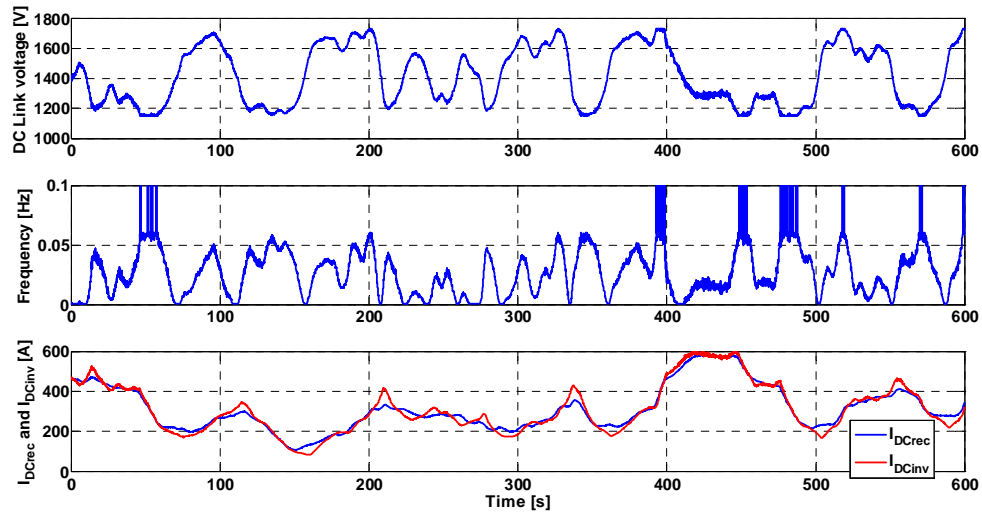
Figure 4.26. DC link voltage, LPF frequency, and DC link currents

4.4.2. Wind speed profile B

Next series of simulations was performed using wind profile B, with higher level of turbulence. Increased wind speed variations result in increased generator power variations and more challenging task for the output power smoothing system. Figure 4.27 shows wind speed profile and rotational speed of the wind turbine under wind profile B. Rotational speed plots show two intervals where rotational speed is constant, 30.18 rpm. In these intervals, the turbine operates in the region 3, due to high wind speed as described in the chapter 2. As the wind speed profile shows, large variations occur during 10 minutes of wind turbine operation making this wind profile good test case for the output power smoothing algorithm.

4.4.2.1. Simulation with 4 parallel ultracapacitor strings

Power produced by the generator and power delivered to the grid are shown in figure 4.28. As the figure shows, the output power (red curve) has significantly reduced fluctuations as result of the integrated energy storage and power smoothing algorithm.
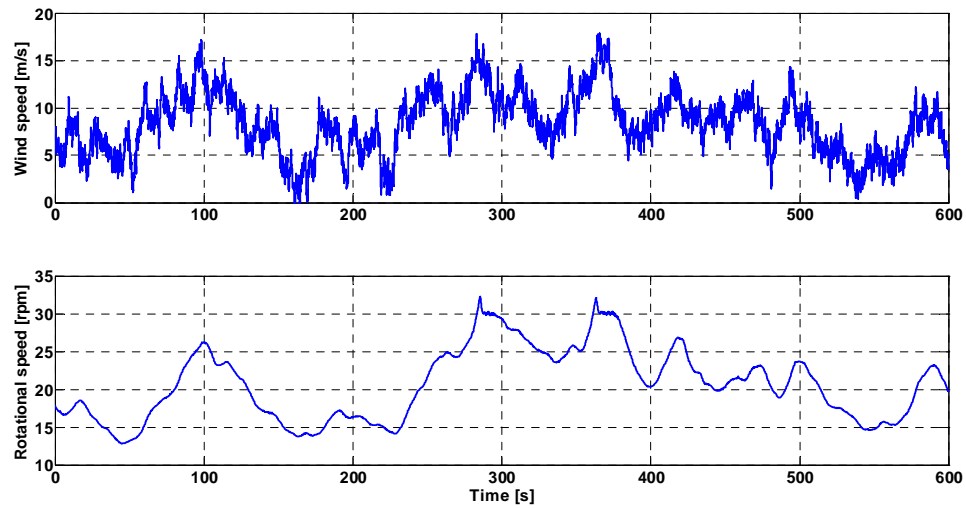
Figure 4.27. Wind speed profile and rotational speed
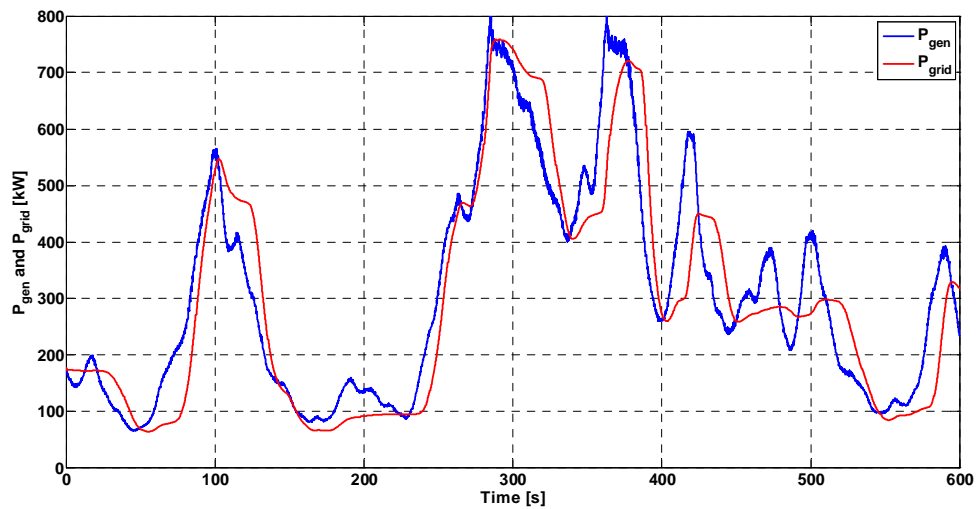
Figure 4.28. Generator and output power
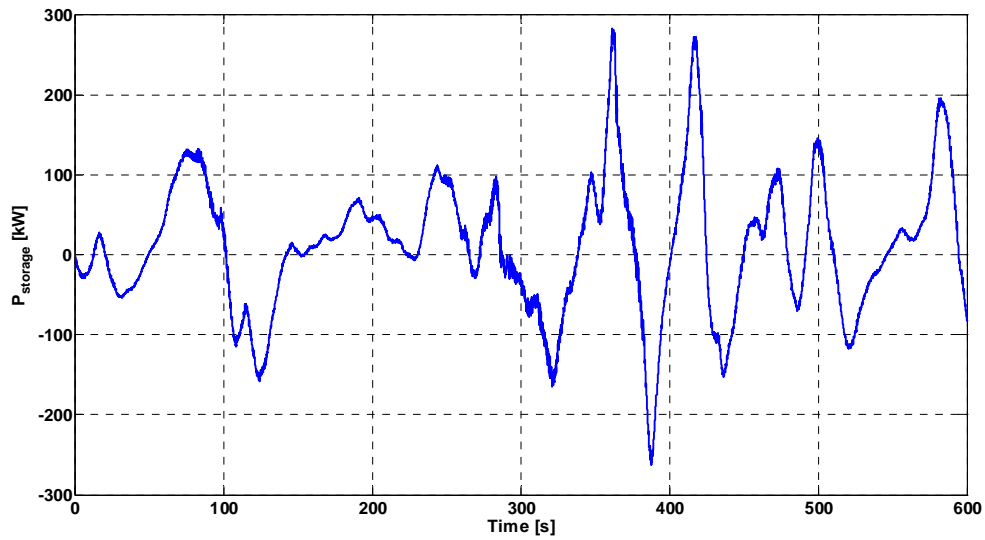
Figure 4.29. Ultracapacitor storage power
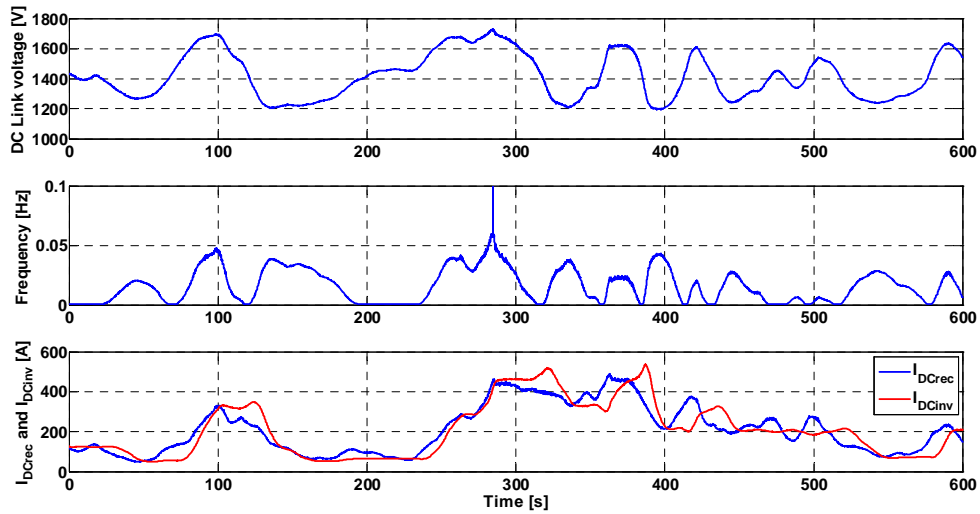
Figure 4.30. DC link voltage, frequency of the LPF, and DC link currents

The energy storage power is shown in figure 4.29. The peak power is larger than in cases when wind profile A was used with the same number of parallel ultracapacitor strings, as the result of larger turbulence level. The peak power is slightly less than 300kW which is significant percent of the rated power of 750kW. The major advantage of ultracapacitors is their ability to deliver large amounts of power for short periods of

time, and this is shown in figure 4.29. Figure 4.30 shows DC link voltage, variable LPF cut-off frequency and DC link currents. As shown in this figure, DC link voltage varies around the average of 1469V, as the result of dc link voltage optimization technique described earlier. Variable frequency plot shows that most of the time the LPF cut-off frequency is bellow 0.06Hz, except for short period of time near 280s when dc link voltage reached the peak of 1730V and power smoothing was bypassed.

4.4.2.2. Simulation with two parallel ultracapacitor strings

In the second simulation, the ultracapacitor energy storage has only two parallel strings of 480 series connected capacitors. Wind speed profile is the same as in the previous case, resulting in the same rotational speed. Generator and output power are shown in figure 4.31. As expected, output power variations are greater than in the previous case.
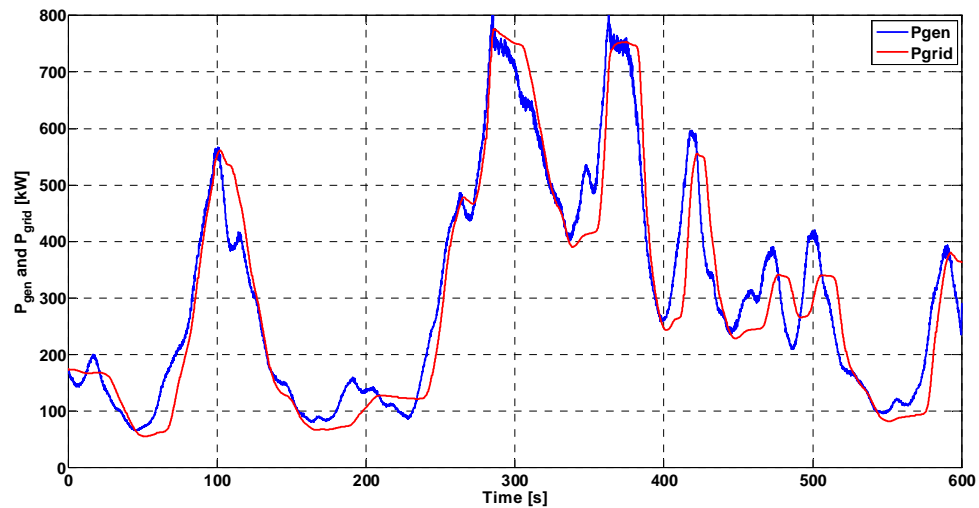
Figure 4.31. Generator and output power

Energy storage power is shown in figure 18. The peak is now lower than in the previous case due to reduced storage capacity.
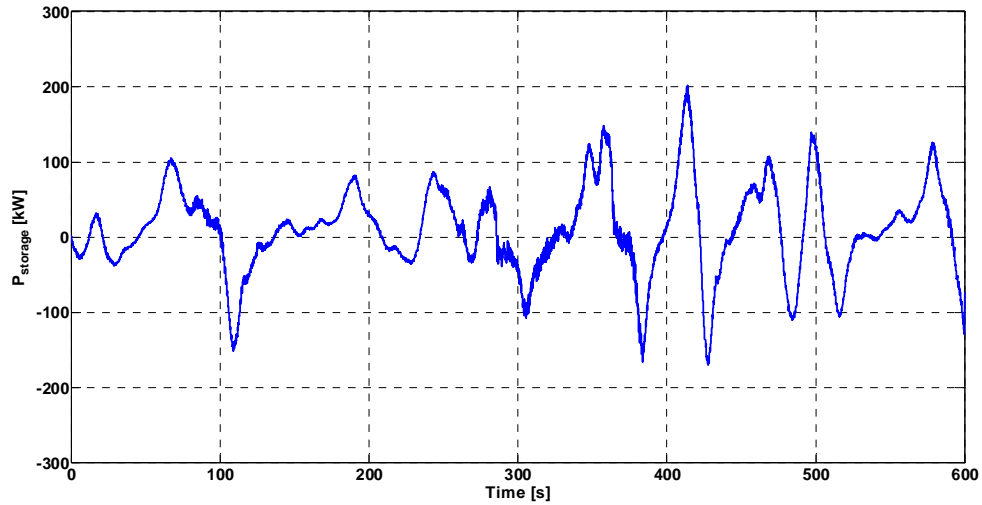
Figure 4.32. Ultracapacitor storage power

Figure 4.33 shows DC link voltage, LPF cut-off frequency, and DC link currents. Variations of dc link voltage are increased, and frequency shows several intervals when power smoothing algorithm was bypassed.
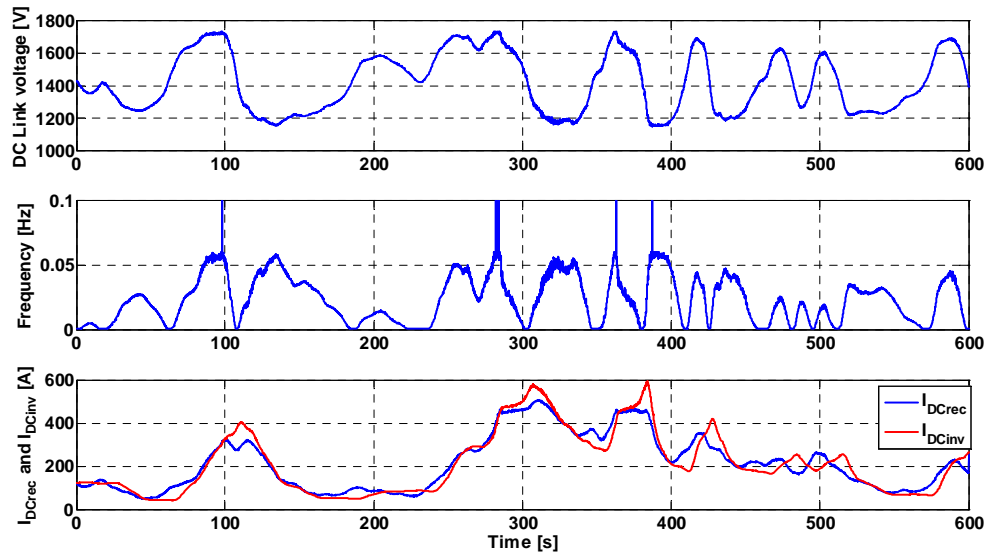
Figure 4.33. DC link voltage, LPF frequency, and DC link currents

4.4.2.3. Simulation with single ultracapacitor string

In the third case, only one string of 480 series connected ultracapacitors was used. Generator and output power are shown in figure 4.34. Figure 4.35 shows energy storage power, while figure 4.36 shows DC link variables and LPF cut-off frequency. As expected, level of power filtration is reduced and DC link voltage more often reaches upper or lower limit. In order to reduce the number of intervals when power smoothing is bypassed, the maximum LPF cut-off frequency should be increased in this case, increasing the bandwidth, but still providing power smoothing capacity for faster power fluctuations.
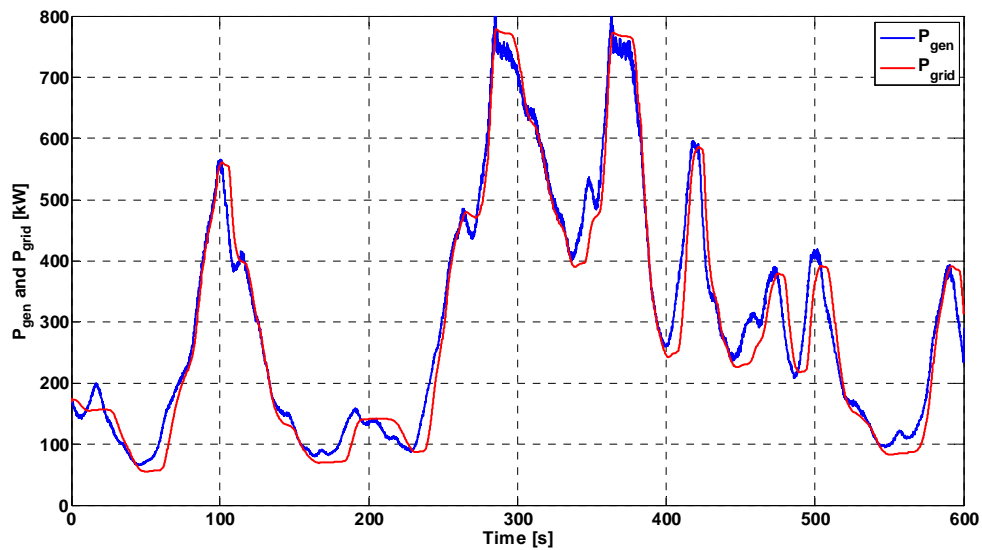
Figure 4.34. Generator and output power
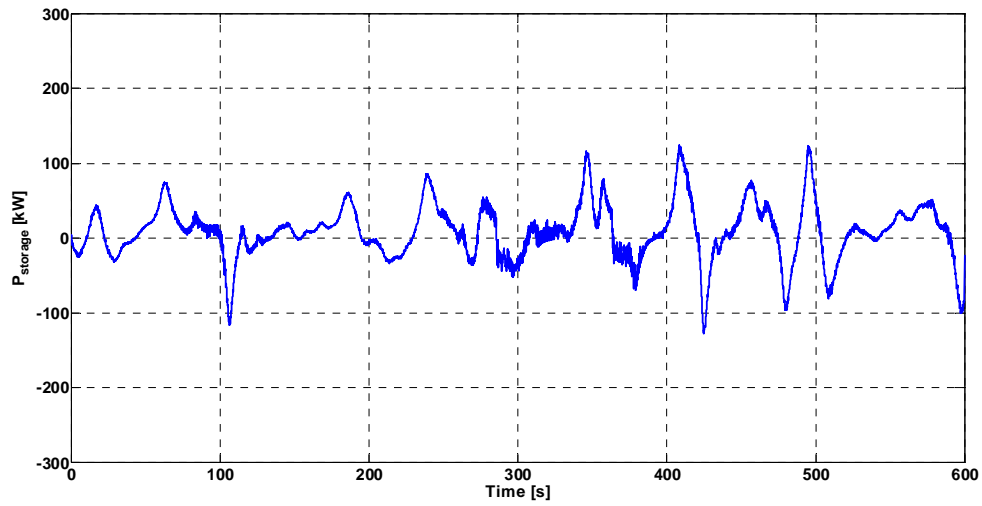
Figure 4.35. Ultracapacitor storage power
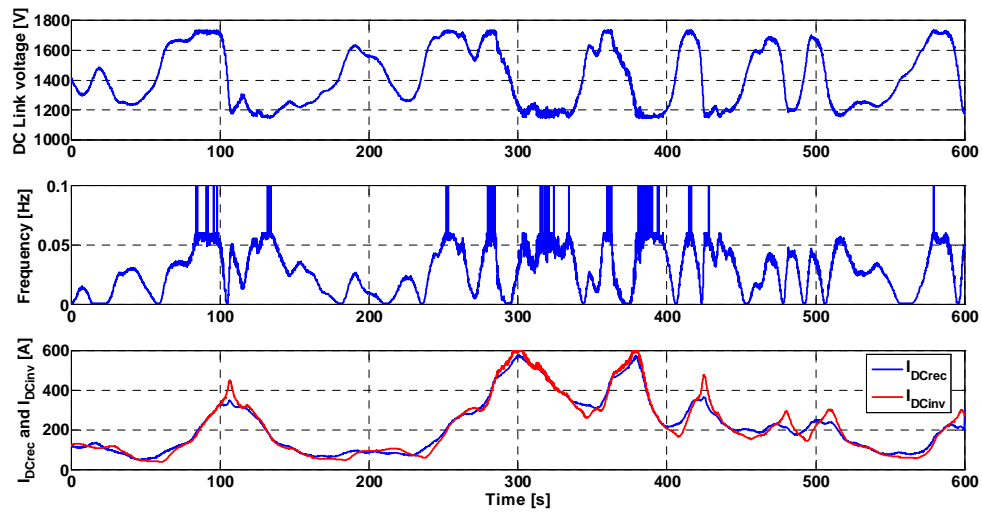
Figure 4.36. DC link voltage, LPF frequency, and DC link currents

To better compare all three cases, the energy storage power, DC link voltage and LPF frequency are shown together in figures 4.37, 4.38 and 4.39 respectively. Reduced size of energy storage results in reduced storage power peaks, increases DC link voltage variations as well as variations of the LPF cut-off frequency resulting in increasing the output power variations.
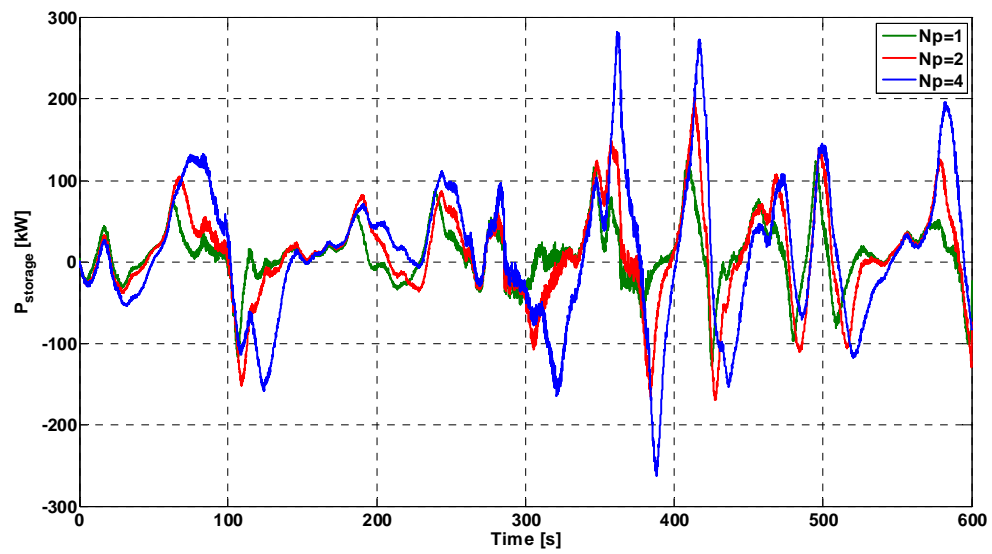
Figure 4.37. Energy storage power for 1, 2, and 4 parallel ultracapacitor strings
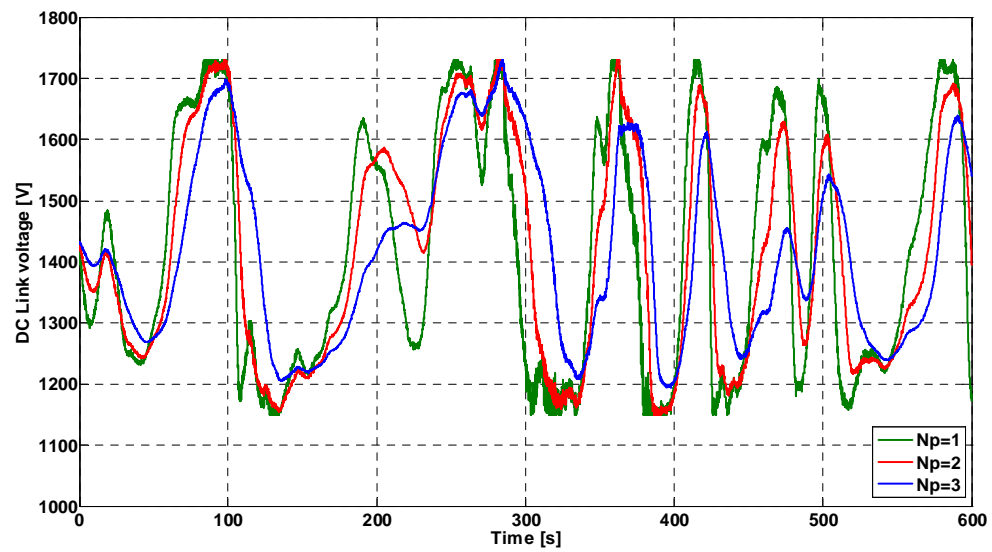
Figure 4.38. DC link voltage for 1, 2, and 4 parallel ultracapacitor strings
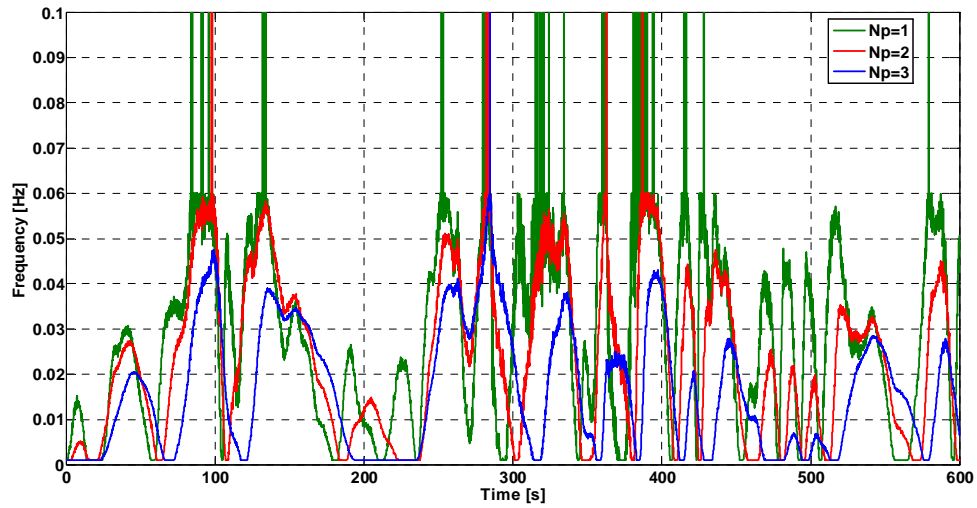
Figure 4.39. LPF frequency for 1, 2, and 4 parallel ultracapacitor strings

4.4.2.4. Simulation with 6 parallel ultracapacitor strings

In the final simulation case for this wind profile, six parallel ultracapacitor strings were used. Since in the first case when four parallel strings were used, only at one instance the DC link voltage limit was reached, the maximum LPF frequency is reduced to 0.04Hz in this case. Generator and the output power are shown in figure 4.40. Power variations are significantly reduced, due to the larger capacity of energy storage. Figure 4.41 shows DC link variables and LPF cut-off frequency. As this figure illustrates, six parallel strings of ultracapacitor provide good power filtering capability since maximum LPF cut-off frequency can be reduced without frequent reaching upper or lower DC link voltage limits that would result in bypassing of the output power smoothing algorithm. Figure 4.42 shows frequency spectrums of the generator and output power.
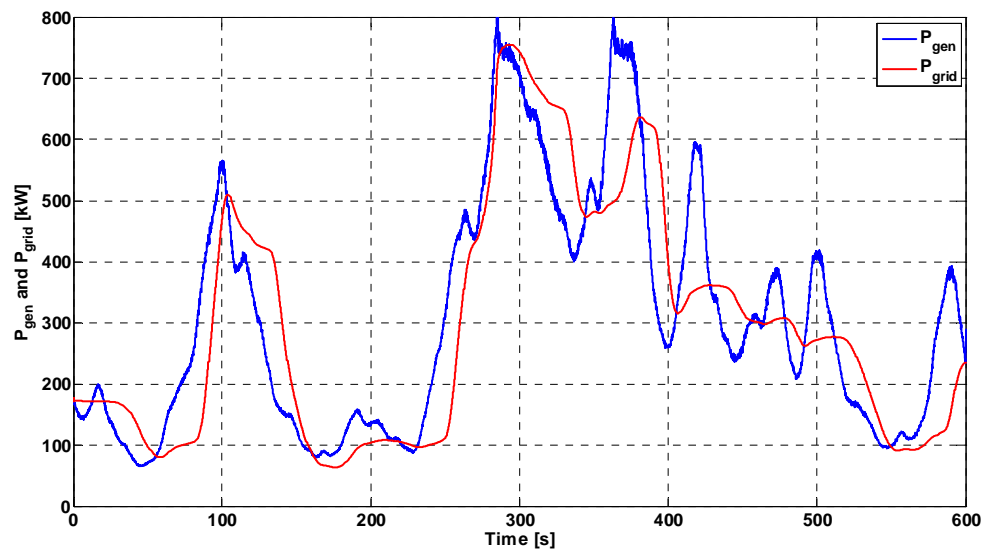
Figure 4.40. Generator and output power
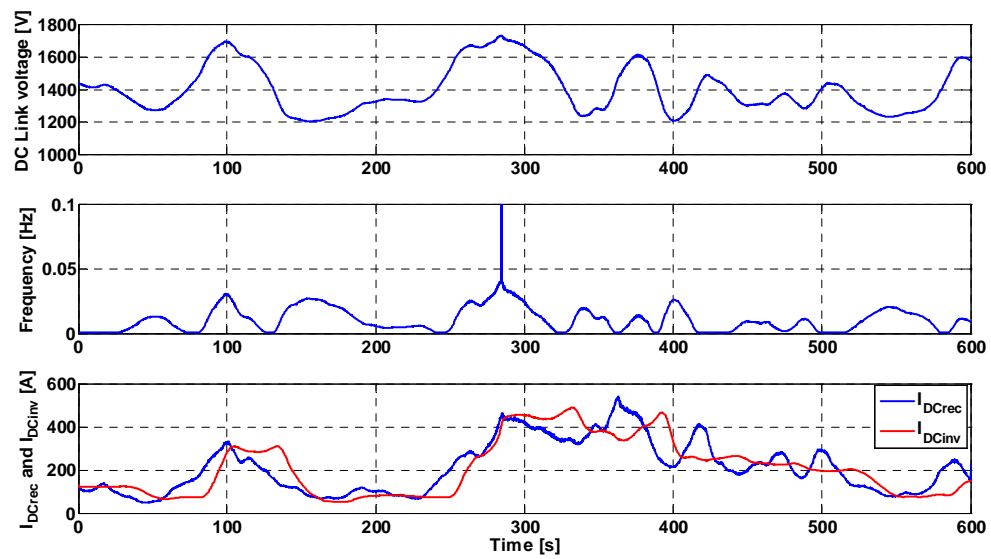
Figure 4.41. DC link voltage, LPF frequency, and DC link currents
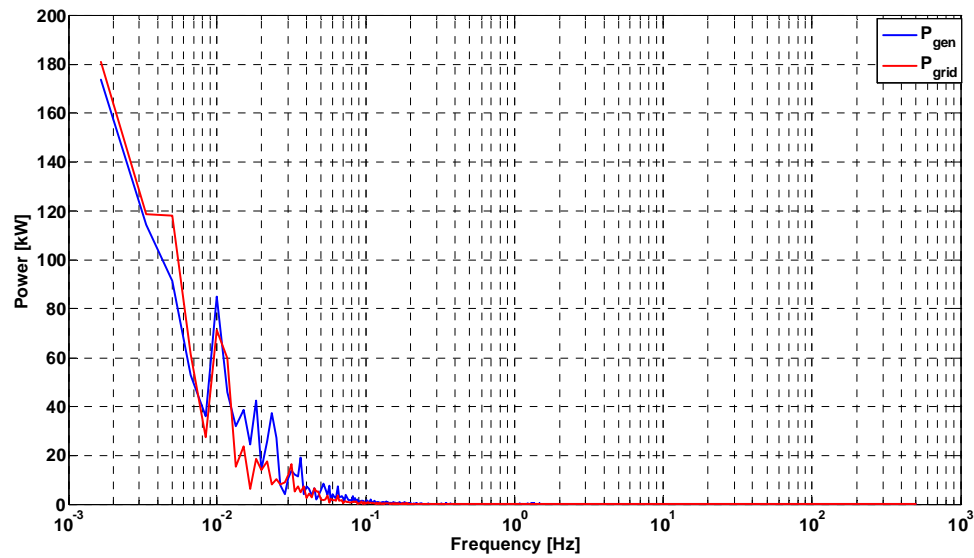
Figure 4.42. Frequency spectrum of generator and output power

Ultracapacitor energy storage and proposed control algorithm result in significant reduction of power variations in the 10^{-1} Hz to 10^{-2} Hz region defined as region 2 [1] with larger impact on frequency stability. From the simulation results presented in this section, it can be concluded that number of ultracapacitor string as well as peak frequency directly affect the level of the reduction of output power smoothing. The number of ultracapacitor strings is a parameter that should be determined during the turbine design phase, according to the wind speed and turbulence level data. Maximum LPF cut-off frequency can later be fine tuned to maximize output power smoothing according to the present conditions of the wind turbine installation site.

4.5. Experimental tests on double conversion system with ultracapacitor energy storage

This section describes the experimental setup built for the purpose of experimentally verifying behavior of lithium-ion ultracapacitor bank in the DC link of a double conversion system and its power smoothing capabilities. The setup was built in the Power Electronics and Electrics Drives laboratory at the University of Wisconsin-Milwaukee. Block diagram of the experimental setup is shown in figure 4.43. The setup consists of two three-phase power converters that share common DC link. The ultracapacitor bank that consists of 120 lithium-ion ultracapacitors connected in series is connected directly to the DC link. Power modules of Rockwell 750 motor drives, with control boards removed, are used as rectifier and inverter. The entire control logic has been implemented externally, on NI CompactRIO real-time controller.
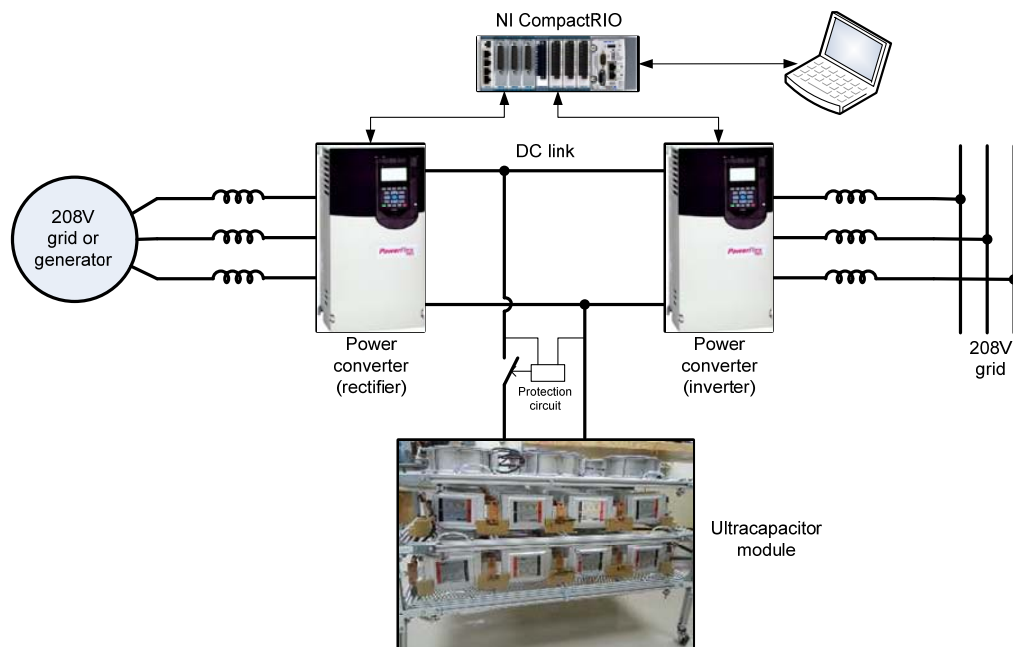
Figure 4.43. Experimental setup

Power module that acts as a rectifier can be connected to the synchronous generator, or 208V three phase power grid. Inverter side of the double conversion system is connected to the 208V three phase power grid from the separate feed than the one used for rectifier. Three 500μH inductances are used to filter ripple current. If the generator is not used, power circulates from 208V grid through double conversion system back to 208V grid. Rectifier is then connected to the grid through 500μH inductances as well. By modulating reference of the rectifier current, it is possible to achieve similar behavior as of a rectifier connected to the generator of a variable speed wind turbine. Grid side inverter is controlled in the same way as inverter of a real wind turbine. In the experiments presented in this section, output power is controlled directly by keeping it constant while input power varies. NI Compact RIO controller, that is responsible for control tasks in the setup, has two hardware layers that can be programmed separately and that can exchange informations among themselves. Hardware architecture of NI CompactRIO consists of the FPGA module and real-time controller. FPGA module is responsible for PWM signal generation, phase locked loops, current controllers, and short circuit protection of both power module. The software architecture of the experimental setup is illustrated in figure 4.44. Unlike software run on a single core processor, FPGA allows true hardware parallelism of software tasks executed by various hardware structures within the same chip. This functionality is widely used in the software that runs the experimental setup. As shown in figure 4.44, there are several tasks that are all run in parallel, synchronized by signal generated at the end of each analog to digital conversion scan.
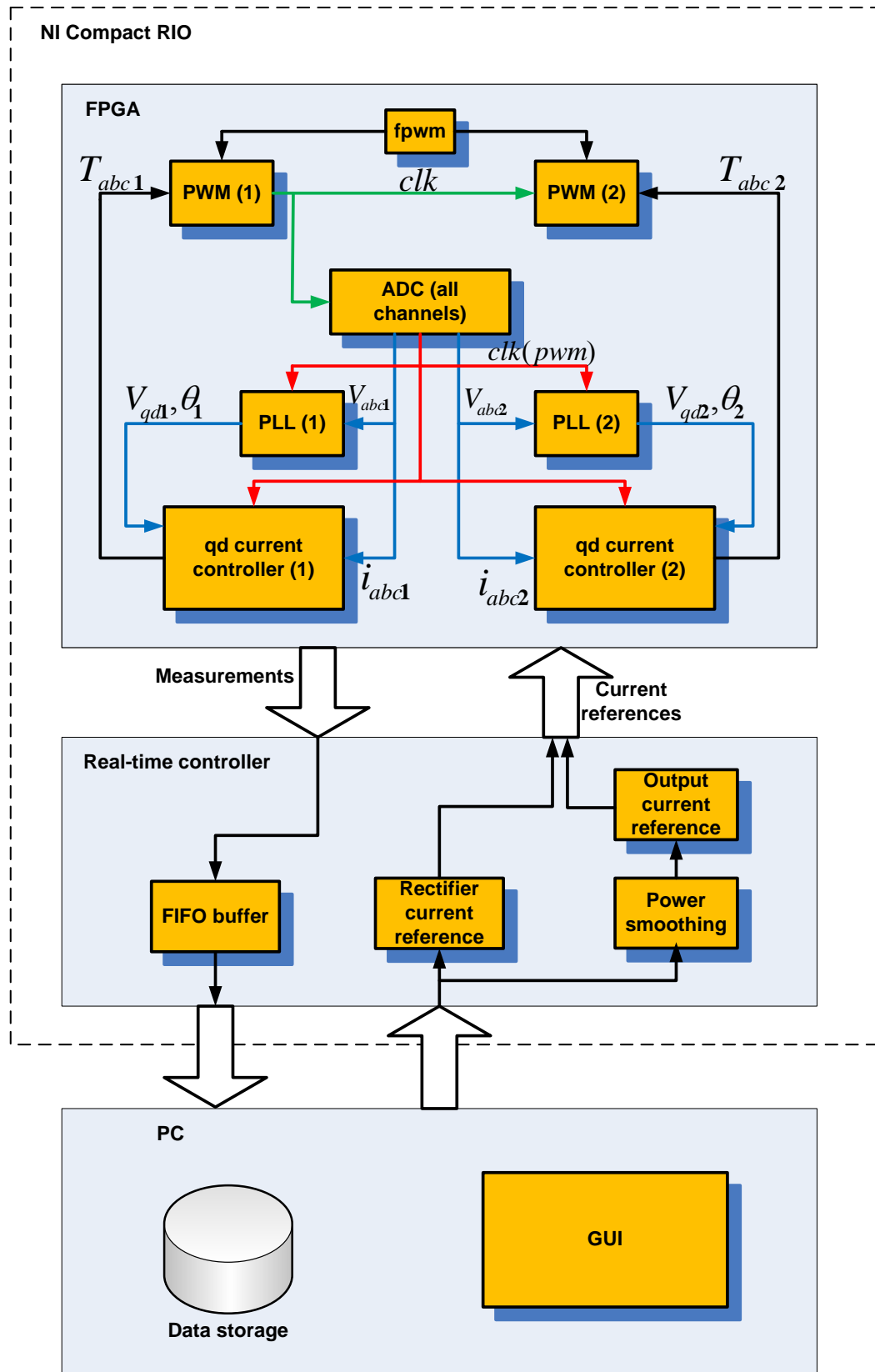
Figure 4.44. Experimental setup – software organization

The FPGA chip of the NI Compact RIO controller can directly communicate to the I/O modules. There are eight modules installed in the system. They are: three fast digital I/O modules used to generate PWM and other control signals for power modules. Three analog to digital converter modules, with total of 12 analog inputs, measure voltages and currents within the double conversion system for feedback control loops. Clock frequency of the FPGA is 200MHz, which combined with parallelism enables very complex tasks of control two power converters to be run on a single controller. Two synchronized PWM modules generate signals for each power converter, based on pulse duration information from current controllers. Two PLL blocks synchronize rotating reference frames to three phase voltages at the terminals of each power converter. Analog to digital control module is synchronized to the PWM interval and it scans all analog inputs once per PWM cycle. At the end of each scan, it generates a pulse that triggers the current control blocks. Current controllers are implemented in QD reference frame, as described in the chapter 2. They calculate pulse durations for PWM blocks. The current references for each controller are supplied from the real time controller. All data from ADC block are available to the real time controller through FIFO buffer used for communication with the higher layer of software.

Second layer of software is run on the real time controller. Real time controller is based on PowerPC processor that runs at 500MHz of clock frequency. Real time controller also has 256MB of RAM, LAN network port, USB port, and the RS232 port. LAN network port is used for communication with host PC computer with the graphical user interface, which is the next layer of software of this setup. Real time controller is responsible for control tasks that do not require speed of the FPGA. In this case, real time controller is

responsible for computing current references for the current control loops on FPGA. Real time controller has access the data from analog to digital controller. The main strengthens of the real time controller is the floating point arithmetic, which makes it suitable for performing complex mathematical calculations such as power smoothing or power management algorithms.

Finally, the real time controller can communicate to the host PC computer. Graphical user interface was developed for the experimental setup and it allows user to control power reference for the rectifier, power reference of the inverter, and data acquisition and monitoring. Figures 4.45 and 4.46 show oscilloscope pictures of currents and grid voltages of the double conversion system. In both cases, converters were operated with power factor equal to one.
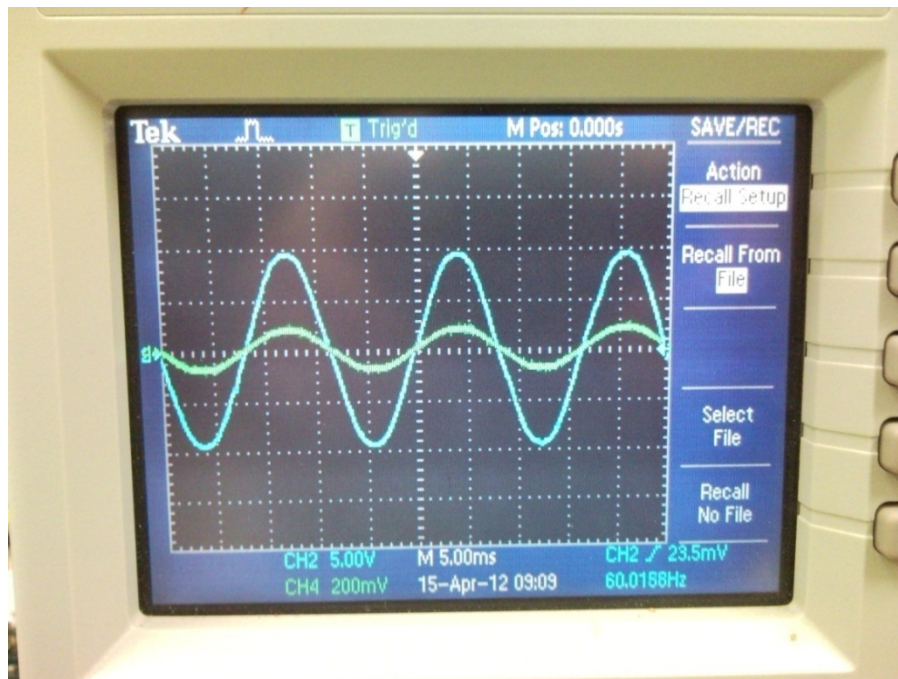
Figure 4.45. Inverter voltage and current
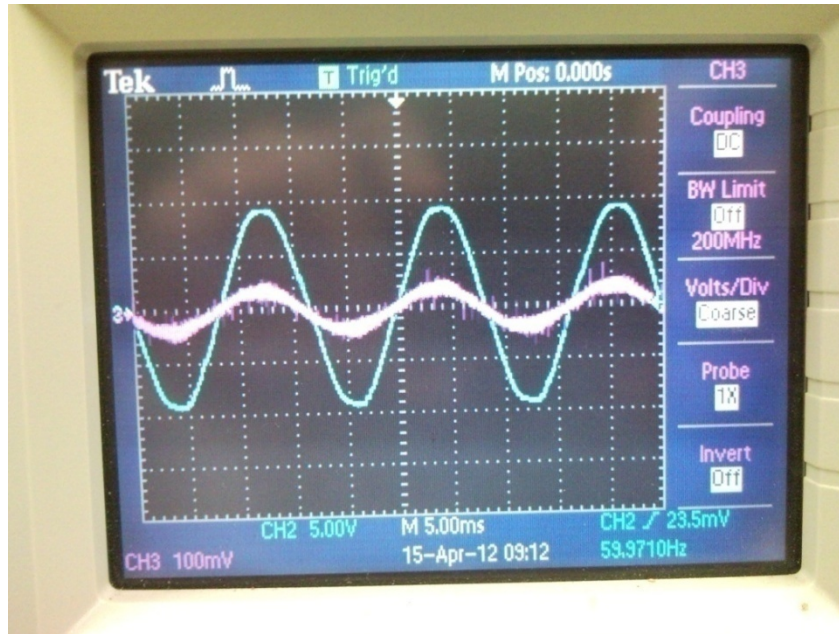
Figure 4.46. Rectifier voltage and current

4.5.1. Experimental results

Series of experimental tests were run to test applicability of ultracapacitors as short term energy storage for wind power applications. In the first case, power reference for the rectifier is a sinusoidal signal with 1kW amplitude added to the constant average value of 1.5kW. Output power reference is held constant at 2kW. Since output power is greater than average, the ultracapacitor module supplies additional power. Figure 4.47 shows DC link voltage and input and output power.
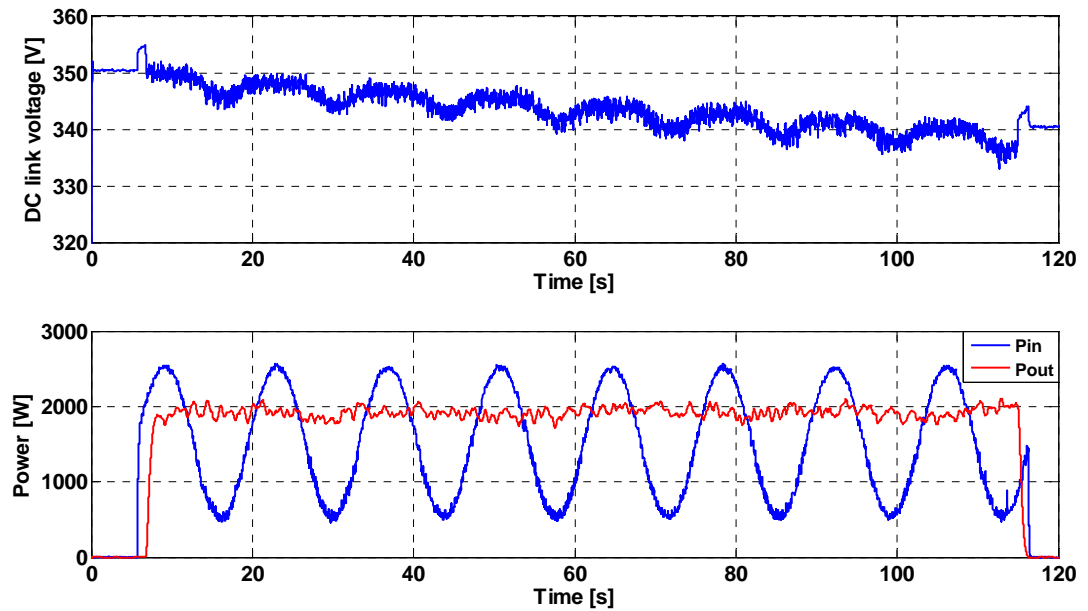
Figure 4.47. DC link voltage; input and output power

DC link slowly reduces, as result of discharging of the ultracapacitor module. In order to verify Simulink model used in simulations, the data files of measured current profiles were loaded in Matlab, and used in Simulink as programmed current source/sink that charges and discharges the model of ultracapacitor module consisting of 120 ultracapacitor connected in series. DC link voltage resulting from simulation is plotted versus measured DC link voltage in figure 4.48. Good matching between simulation and experimental results confirm accuracy of the ultracapacitor model, and validity of simulation results from the previous section.
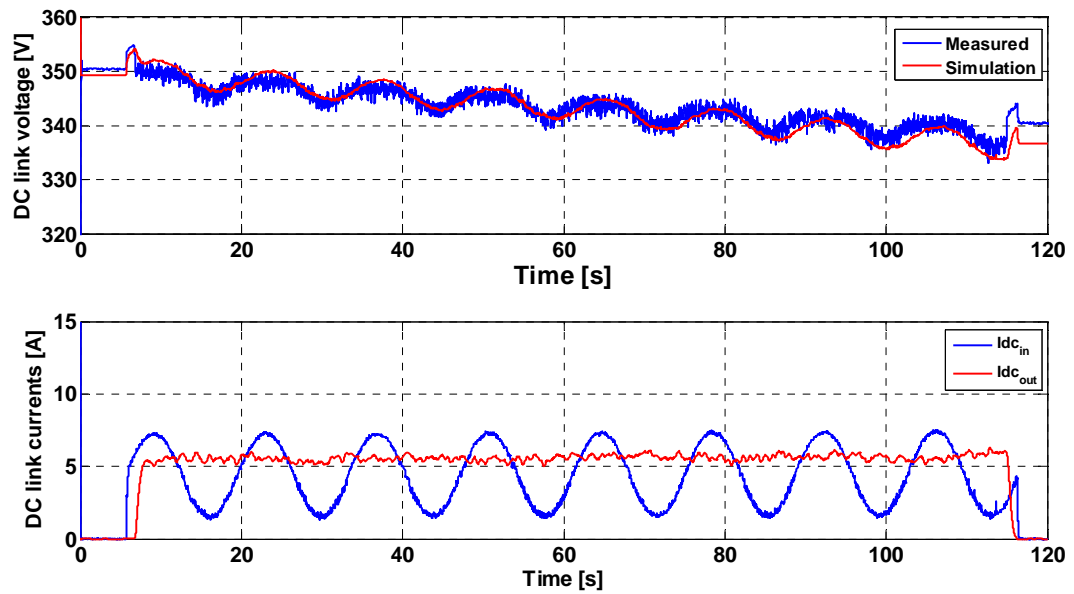
Figure 4.48. DC link voltage and currents

In the case 2, the input current reference is a square wave signal that causes input power variations between 500W and 2500W. Output power is held constant at 1600W. DC link voltage, input and output power is shown in figure 4.49. Figure 4.50 shows DC link voltage and currents.
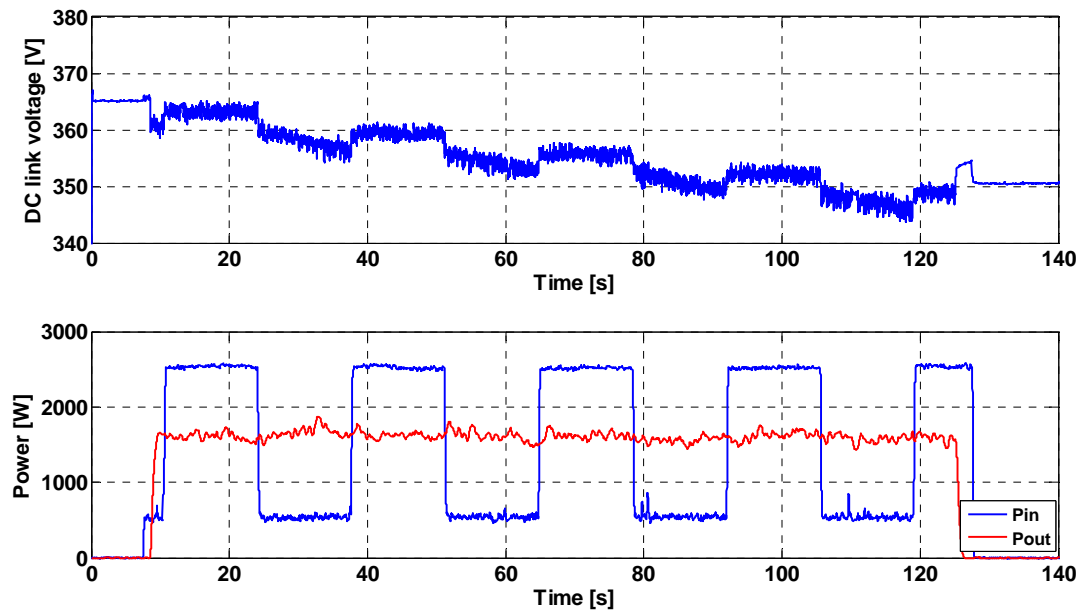
Figure 4.49. DC link voltage, input and output power
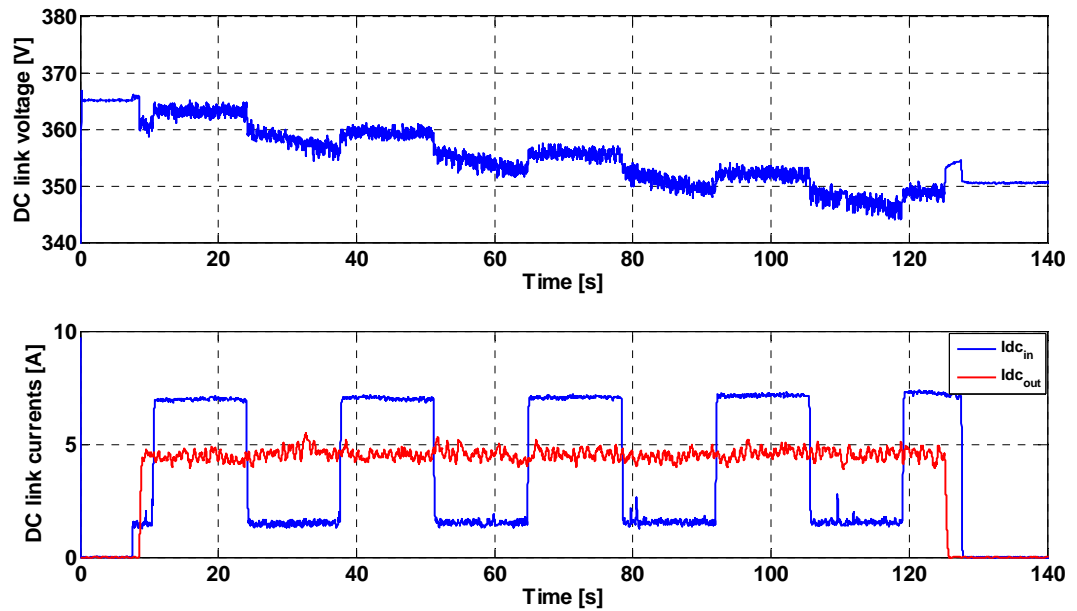
Figure 4.50. DC link voltage and currents

In the third case, input power is varied sinusoidally with frequency of 2.96Hz, which is the frequency of the first resonant mode of the gearbox model developed in chapter 3. Output power is held constant. The purpose of this test is to show that ultracapacitor energy storage effectively removes higher frequency power variations that can be result of applied active drivetrain vibration damping technique that injects additional power variations on the rectifier side of the double conversion system. Figure 4.51 shows DC link voltage, input and output power, while figure 4.52 is the closer look into 10 seconds interval of the figure 4.51.
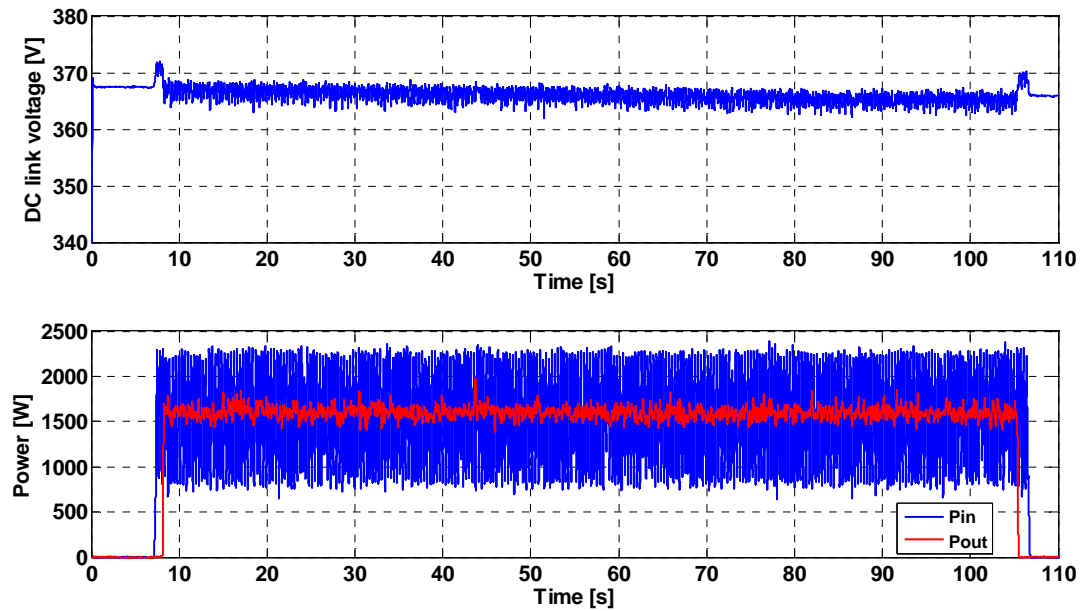
Figure 4.51. DC link voltage, input and output power
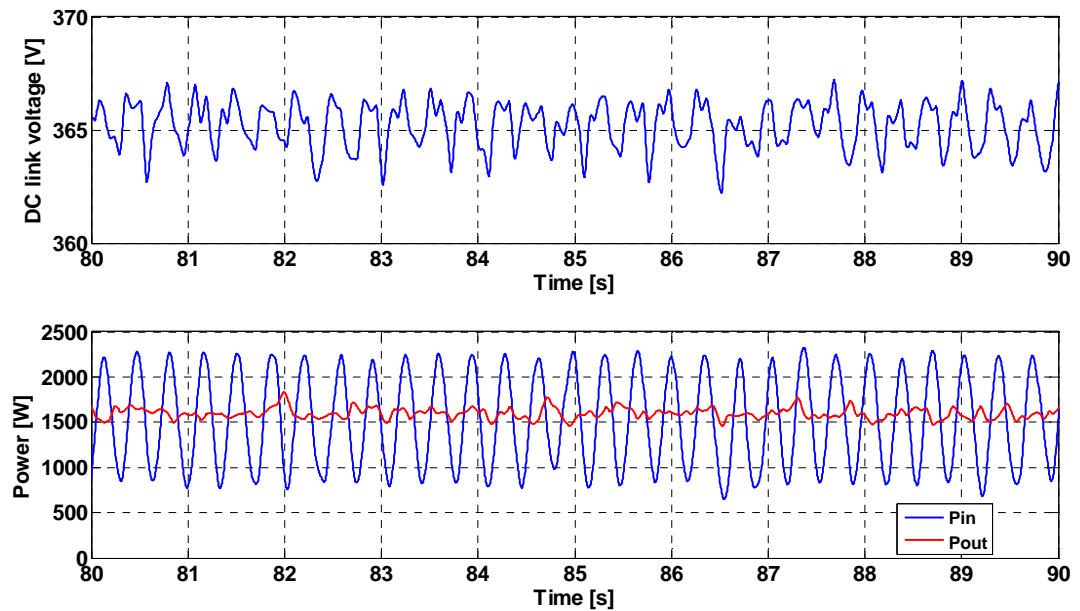
Figure 4.52. DC link voltage, input and output power (zoom in)

In the fourth case, a triangular input power reference was used. Output power was kept constant. Start and stop commands for inverter and rectifier were given manually, in order to create intervals when only one converter was working either charging or

discharging the module. DC link voltage and input and output power are shown in figure 4.53. As shown in the figure, ultracapacitor module was able to receive power from the source even without delivering power to the output, or to deliver power to the output when there is no input power.
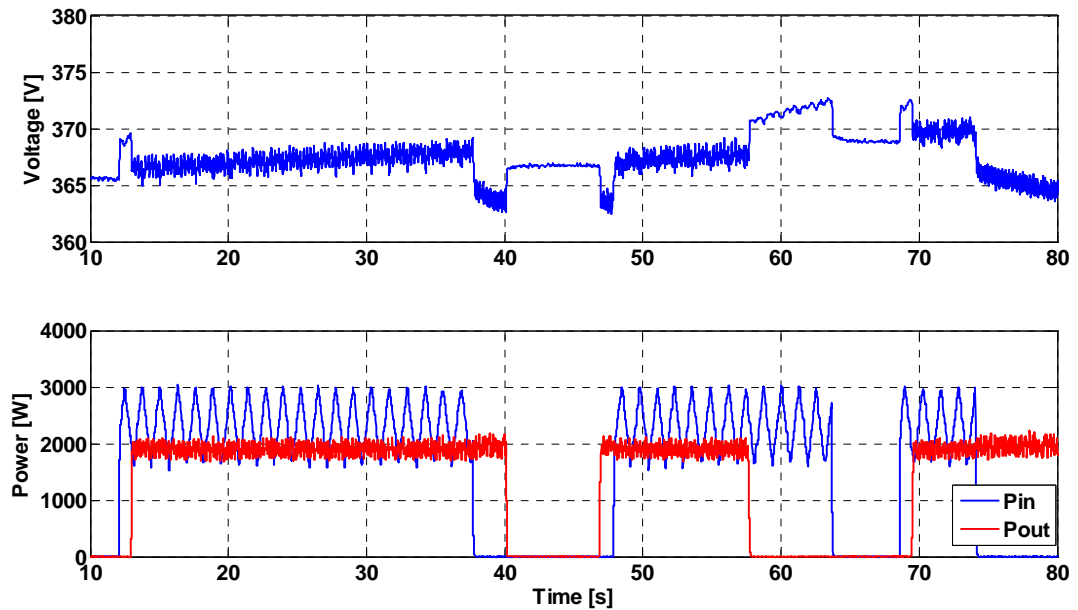
Figure 4.53. DC link voltage, and input and output power. Triangular waveform

Experimental results from the setup that consists of two three phase power converter operated as inverter and rectifier with ultracapacitor module in the common DC link show that it is possible to integrate lithium-ion ultracapacitors into such system which has large ripple current in the DC link due to relatively low switching frequency. Output power can be controlled independently on input power, provided that DC link voltage is between voltage limits defined by the number of ultracapacitors connected in series and allowed maximum and minimum voltage per cell. Simulation results, with imported experimental data and scaled model of energy storage, used in simulations of power

smoothing algorithm, show good matching between measured and simulated DC link voltage, thus verifying the model of ultracapacitor energy storage.

5. Conclusion and future research

Simulation and experimental results show that improvements in power quality can be made by integrating lithium-ion ultracapacitor energy storage with a wind turbine. Vibration damping control strategy shows great reduction in resonant vibrations on the shafts of the drivetrain. Further progress in vibration damping control can be made by using the multivariable control system approach and H∞ optimization for controller design. Such method may result in even more increase in damping of resonant modes.

Presented vibration damping strategy reduces only torsional vibrations within the drivetrain assembly. Results of dynamic simulations of the wind turbine are torque loads at all points within the flexible multi-body drivetrain model. These torque loads within the assembly can be further used as input for finite element based models to precisely calculate loading of individual components. This analysis would then provide more precise insight into mechanical stress and effect of vibration damping controller. Also, the feedback from finite element analysis can be used to further tune vibration damping controller in order to reduce damaging vibration effect on gear teeth and their contact surfaces. Multiphysics model of the drivetrain, generator with all nonlinearities saturation effects and harmonics in space distribution of magnetic field, power converter with its own nonlinearities, would give more detailed picture on processes within the drivetrain. Development of such large scale model with all associated control loop would make possible use of parameter optimization algorithm, similar to one described in chapter 3, to find optimal parameters of vibration damping controller that would reduce vibrations even of the other modes that cannot be selectively damped by using bandpass filters.

Finally, experimental results on a wind turbine are invaluable to definitely assess effectiveness of any mechanical load reduction strategy on extension of the gearbox lifetime.

Extension of the power smoothing algorithm described in the chapter 4 would include development of centralized controller on the level of WPP that would decide on low-pass filter cut-off frequencies of each individual wind turbine equipped with ultracapacitor energy storage, based on total power output and information on availability of storage capacity of each turbine. Such controller would be able to control ramp rates of the entire WPP by optimal use of available decentralized storage capacity. Also, the centralized controller can provide additional functionality such as inertia emulation when the output of the entire WPP would behave in the same way as the output of large synchronous generator connected to the grid. The inertia emulation algorithm would use distributed energy storage capacity to emulate kinetic energy storage behavior of the rotating mass of the equivalent synchronous generator, thus allowing easier integration of WPPs into power systems and increase level of wind power participation in the total electric power production.

6. References

[1] C. Luo and B. -T. Ooi, "Frequency deviation of thermal power plants due to wind farms," *IEEE Trans. Energy Convers.*, vol. 21, no. 3, pp. 708–716, Sep. 2006.

[2] H. Banarkar, C. Luo, and B.-T. Ooi, "Power system response to wind power fluctuations," *Transmission and Distribution Conference and Exhibition, 2005/2006 IEEE PES* , vol., no., pp.1445-1452, 21-24 May 2006.

[3] C. Luo, H.G. Far, H. Banarkar, P.K. Keung, and B.-T. Ooi, "Estimation of wind penetration as limited by frequency deviation," *IEEE Trans. Energy Convers.*, vol. 22, no. 3, pp. 783–791, Sep. 2007.

[4] M.T. Do, J. Sprooten, S. Clenet, and B. Robyns, "Influence of wind turbines on power system reliability through probabilistic studies," *Innovative Smart Grid Technologies Conference Europe (ISGT Europe), 2010 IEEE PES* , vol., no., pp.1-6, 11-13 Oct. 2010.

[5] E. Muljadi, C.P. Butterfield, and M. L. Buhl, "Effects of turbulence on power generation for variable-speed wind turbines," *ASME Wind Energy Symposium,* Reno, NV, Jan. 6-9. 1997.

[6] C. Luo, H. Banakar, B. Shen; B.-T. Ooi , "Strategies to Smooth Wind Power Fluctuations of Wind Turbine Generator," *IEEE Trans. Energy Convers.*, vol.22, no.2, pp.341-349, Jun. 2007.

[7] J. L. Rodriguez-Amenedo, S. Arnalte, and J.C. Burgos, "Automatic generation control of a wind farm with variable speed wind turbines," *IEEE Trans. Energy Convers.*, vol.17, no.2, pp.279-284, Jun. 2002.

[8] R. G. de Almeida and J.A.P. Lopes, "Participation of doubly fed induction wind generators in system frequency regulation," *IEEE Trans. Power Systems*, vol. 22, no. 3, pp. 944–950, Aug. 2007.

[9] T. Senjyu, M. Tokudome, A. Uehara, T. Kaneko, A. Yona, H. Sekine, and C. H. Kim, "A new control methodology of wind farm using short-term ahead wind speed prediction for load frequency control of power system," *Power and Energy Conference, 2008. PECon 2008. IEEE 2nd International* , vol., no., pp.425-430, 1-3 Dec. 2008.

[10] C. Jauch, "Stability and control of wind farms in power systems," Ph.D. dissertation, Risø Nat. Lab., Roskilde, Denmark, 2006.

[11] E. Muljadi and H.E. McKenna, "Power quality issues in a hybrid power system," *IEEE Trans. Ind. Appl.,* vol.38, no.3, pp.803-809, May/Jun 2002.

[12] J. P. Barton and D.G. Infield, "Energy storage and its use with intermittent renewable energy," *IEEE Trans. Energy Convers.*, vol. 19, no. 2, pp. 441–448, Jun. 2004.

[13] T. Hennessy and M. Kuntz, "The multiple benefits of integrating electricity storage with wind energy," *IEEE Power Engineering Society General Meeting, 2005.*, vol., no., pp. 1952- 1954 Vol. 2, 12-16 Jun. 2005.

[14] E. Muljadi, C.P. Butterfield, R. Yinger, and H. Romanowitz, "Energy storage and reactive power compensator in a large wind farm," 42nd AIAA Aerosp. Sci. Meeting Exib., Reno, NV, Jan. 5-8, 2004.

[15] S. Teleke, M.E. Baran, A. Q. Huang, S. Bhattacharya,and L. Anderson, "Control strategies for battery energy storage for wind farm dispatching," *IEEE Trans. Energy Convers.*, vol. 24, no. 3, pp. 725–732, Sep. 2009.

[16] A. Arulampalam, M. Barnes, N. Jenkins, and J.B. Ekanayake, "Power quality and stability improvement of a wind farm using STATCOM supported with hybrid battery energy storage," *IEE Proceedings - Generation, Transmission and Distribution*, vol.153, no.6, pp.701-710, Nov. 2006.

[17] T.K.A. Brekken, A. Yokochi, A. von Jouanne, A, Z.Z. Yen, H.M. Hapke, and D.A. Halamay, "Optimal Energy Storage Sizing and Control for Wind Power Applications," *IEEE Trans. Sustainable Energy*, vol.2, no.1, pp.69-77, Jan. 2011.

[18] Z. Jie, Z. Buhan, M. Chengxiong, W. Yunling , "Use of Battery Energy Storage System to Improve the Power Quality and Stability of Wind Farms," *in Proc. International Conference on Power System Technology PowerCon 2006.*, vol., no., pp.1-6, 22-26 Oct. 2006.

[19] T-Y. Lee, "Optimal wind-battery coordination in a power system using evolutionary iteration particle swarm optimization," *Generation, Transmission & Distribution, IET,* vol. 2, no. 2, pp. 291-300, Mar. 2008.

[20] S. Nomura, Y. Ohata, T. Hagita, H. Tsutsui, S. Tsuji-Iio, and R. Shimada, "Wind farms linked by SMES systems," *IEEE Trans. Applied Superconductivity*, vol. 15, no. 2, pp. 1951–1954, June. 2005.

[21] T. Ise, M. Kita, and A. Taguchi, "A hybrid energy storage with a SMES and secondary battery," *IEEE Trans. Applied Superconductivity*, vol. 15, no. 2, pp. 1915–1918, June. 2005.

[22] S.S. Chen, L. Wang, W.-J. Lee, and Z. Chen, "Power flow control and damping enhancement of a large wind farm using a superconducting magnetic energy storage unit," *Renewable Power Generation, IET* , vol.3, no.1, pp.23-38, March 2009.

[23] M.H. Ali, P. Minwon, I.K. Yu, T. Murata, and J. Tamura, "Improvement of Wind-Generator Stability by Fuzzy-Logic-Controlled SMES," *IEEE Trans. Ind. Applicat.*, vol.45, no.3, pp.1045-1051, May 2009.

[24] G. O. Cimuca, C. Saudemont, B. Robyns, and M. M. Radulescu, "Control and Performance Evaluation of a Flywheel Energy-Storage System Associated to a Variable-Speed Wind Generator," *IEEE Trans. Ind. Electrn.,* vol.53, no.4, pp.1074-1085, June 2006

[25] R. Cardenas, R. Pena, G. Asher, and J. Clare, "Control strategies for enhanced power smoothing in wind energy systems using a flywheel driven by a vector-controlled induction machine ," *IEEE Trans. Ind. Electrn.,* vol.48, no.3, pp.625-635, Jun 2001.

[26] J. Morren, J., S.W.H. de Haan, and J.A. Ferreira, "Primary power/frequency control with wind turbines and fuel cells," *in Proc. IEEE Power Engineering Society General Meeting, 2006.* Montreal, Canada, Oct. 2006.

[27] K. Agbossou, M. Kolhe, J. Hamelin, and T. K. Bose, "Performance of a stand-alone renewable energy system based on energy storage as hydrogen," *IEEE Trans. Energy Convers.*, vol. 19, no. 3, pp. 633–640, Sep. 2004.

[28] M. Korpas and A. T. Holen, "Operation planning of hydrogen storage connected to wind power operating in a power market," *IEEE Trans. Energy Convers.*, vol. 21, no. 3, pp. 742–749, Sep. 2006.

[29] D. J. Swider, "Compressed air energy storage in an electricity system with significant wind power generation," *IEEE Trans. Energy Convers.*, vol. 22, no. 1, pp. 95–102, Mar. 2007.

[30] S.C. Smith and P.K Sen, "Ultracapacitors and energy storage: Applications in electrical power system," *40th North American Power Symposium, NAPS '08.*, pp.1-6, 28-30 Sept. 2008

[31] C. Abbey and G. Joos, "Supercapacitor energy storage for wind energy applications," *IEEE Trans. Ind. Appl.*, vol. 43, no. 3, pp. 769–776, May/Jun. 2007.

[32] T. Kinjo, T. Senjyu, N. Urasaki, and H. Fujita, "Output leveling of renewable energy by electric double-layer capacitor applied for energy storage system," *IEEE Trans. Energy Convers.*, vol. 21, no. 1, pp. 221–227, Mar. 2006.

[33] M. Bottu, M.L. Crow, and A.C. Elmore, "Design of a conditioner for smoothing wind turbine output power," in *Proc. North American Power Symposium (NAPS), 2010*, pp.1-6, 26-28 Sept. 2010.

[34] W. Li, G. Joos, and J. Belanger, "Real-time simulation of a wind turbine generator coupled with a battery supercapacitor energy storage system," *IEEE Trans. Ind. Electron.*, vol. 57, no. 4, pp. 1137–1145, Apr. 2010.

[35] A. Abedini, and A. Nasiri, "Applications of super capacitors for PMSG wind turbine power smoothing," *in Proc. IECON 2010 - 34th Annual Conference of IEEE Industrial Electronics Society*, pp. 3347-3351, 10-13 Nov. 2008.

[36] T. Luu, and A. Nasiri, "Power smoothing of doubly fed induction generator for wind turbine using ultracapacitors," *in Proc. IECON 2010 - 36th Annual Conference of IEEE Industrial Electronics Society* ,pp. 3293-3298, 7-10 Nov. 2010.

[37] X. Li, C. Hu, C. Liu, and D. Xu, "Modeling and control of aggregated super-capacitor energy storage system for wind power generation," *in Proc. IECON 2010 - 34th Annual Conference of IEEE Industrial Electronics Society*, pp. 3370-3375, 10-13 Nov. 2008.

[38] L. Qu, and W. Qiao, "Constant power control and fault ride through enhancement of DFIG wind turbines with energy storage," in *Proc. Industry Applications Society Annual Meeting*, pp.1-8, 4-8 Oct. 2009.

[39] I. Boldea *Variable Speed Generators,* CRC Press, 2005.

[40] B. Ruzojcic, D. Zarko, and D. Ban, "Interior permanent-magnet motor for ship propulsion, design and testing," in *Proc. EPE 2009 – 13th European Conference on Power Electronics and Applications*, pp. 1-10, 8-10 Sept. 2009.

[41] P. Asmus and M. Seitzler, "The Wind Energy Operation & Maintenance Report," *Wind Energy Update,* Feb. 2010.

[42] F. Oyague, "Gearbox Modeling and Load Simulation of a Baseline 750-kW Wind Turbine Using State-of-the-Art Simulation Codes," NREL, Golden, CO, Tech. Rep. NREL/TP-500-41160, February 2009.

[43] J. Peeters, "Simulation of Dynamic Drive Train Loads in a Wind Turbine," Ph.D. dissertation, Dept. Mech. Eng., K.U. Leuven, Leuven, Belgium, Jun. 2006.

[44] T. L. Sullivan, D.R. Miller, and D.A, "Drive Train Normal Modes Analysis for the ERDA/NASA 100-Kilowatt Wind Turbine Generator," NASA Report No. NASA-TM-73718, Jul. 1977.

[45] H. Polinder, F. F. A. van der Pijl, G. J. de Vilder, and P. J. Tavner, "Comparison of Direct-Drive and Geared Generator Concepts for Wind Turbines," *IEEE Trans. Energy. Convers.*, vol. 21, pp. 725-733, Sep. 2006.

[46] E. A. Bossanyi, "The Design of Closed Loop Controllers for Wind Turbines," *Wind Energy,* vol. 3, pp. 149-163, 2000.

[47] R. Muszynski and J. Deskur, "Damping of Torsional Vibrations in High-Dynamic Industrial Drives," *IEEE Trans. Ind. Electron.*, vol. 57, pp. 544-552, Feb. 2010.

[48] K. Sugiura and Y. Hori, "Vibration suppression in 2- and 3-mass system based on the feedback of imperfect derivative of the estimated torsional torque," *IEEE Trans. Ind. Electron.*, vol. 43, pp. 56–64, Feb. 1996.

[49] J. K. Ji and S. K. Sul, "Kalman filter and LQ based speed controller for torsional vibration suppression in a 2-mass motor drive system," *IEEE Trans. Ind. Electron.*, vol. 42, pp. 564–571, Dec. 1995.

[50] Y. Hori, H. Sawada, and Y. Chun, "Slow Resonance Ratio Control for Vibration Suppression and Disturbance Rejection in Torsional System," *IEEE Trans. Ind. Electron.*, vol. 46, pp. 162–168, Jan. 1999.

[51] T. Zoller, T. Leibfried, and A.M. Miri, "Application of Power Electronics for Damping of Torsional Vibrations," in *Proc. 7th PEDS,* Bangkok, Thailand, Nov. 27-30, 2007.

[52] S.N. Vukosavic and M.R. Stojic, "Suppression of Torsional Oscillations in a High-Performance Speed Servo Drive," *IEEE Trans. Ind. Electron.,* vol. 45, pp. 108-117, Feb. 1998.

[53] M. Molinas, J. A. Suul, and T. Undeland, "Torque transient alleviation in fixed speed wind generators by indirect torque control with STATCOM," in *Proc. 13th EPE-PEMC*, pp. 2318–2324, Poznan, Poland, Sep. 1–3, 2008.

[54] E. Al-nabi, B. Wu, and N. Zargari, "Proposed Resonant Compensator for High Performance Drive Train Systems With Large Time Delay," *in Proc. 23th APEC*, Austin, TX, USA, Feb. 2008.

[55] H. Geng, D. Xu, B. Wu, and G. Yang, "Active Damping for PMSG based WECS With DC-Link Current Estimation," *IEEE Trans. Ind. Electron.,* vol.58, pp. 1110-1119, Apr. 2011.

[56] C. Sourkounis, "Active Dynamic Damping of Torsional Vibrations by H∞-Control," *in Proc. 12th International Conference on Optimization of Electrical and Electronic Equipment (OPTIM)*, Brasov, Romania, May 2010.

[57] T. N. Chang and N. Ansari, "Passband Cont*rol of Lightly Damped Systems With Mode Separation," IEEE Trans. Ind. Electron.,* vol. 55, pp. 2169-2176, May 2008.

[58] K. Itoh, M. Iwasaki, and N. Matsui, "Optimal Design of Robust Vibration Suppression Controller Using Genetic Algorithms," *IEEE Trans. Ind. Electron.,* vol. 51, pp. 947-953, Oct. 2004.

[59] A. Cavallo, G. De Maria, C. Natale, and S. Pirozzi, "H-∞ Strongly Stabilizing Bandpass Controllers for Flexible Systems," *in Proc. 45th IEEE Conference on Decision & Control,* San Diego, CA, USA, Dec. 2006.

[60] S.H. Kia, H. Henao, and G.-A Capolino, "Torsional Vibration Effects on Induction Machine Current and Torque Signatures in Gearbox-Based Electromechanical System," *IEEE Trans. Ind. Electron.,* vol. 56, no. 11, pp. 4689-4699, Nov. 2009.

[61] A. Dixit and S. Suryanarayanan, "Towards Pitch-Scheduled Drive Train Damping in Variable Speed, Horizontal-Axis Large Wind Turbines," in *Proc. 44th CDC-ECC,* Seville, Spain, Dec. 12-15, 2005.

[62] B.J. Jonkman, J.M., Buhl Jr., M.L. *FAST User's Guide*, NREL/EL-500-29798. Golden, CO: National Renewable Energy Laboratory, Aug. 2005.

[63] B. J. Jonkman, M. L. Buhl Jr, *TurbSim user's guide*, NREL/EL-500-36970, Golden, CO: National Renewable Energy Laboratory, Sep. 2005.

[64] K. Szabat and T. Orlowska-Kowalska, "Vibration suppression in a two-mass drive system using PI-speed controller and additional feedbacks—Comparative study," *IEEE Trans. Ind. Electron.*, vol. 54, no. 2, pp. 1193–1206, Apr. 2007.

[65] M. Cychowski, K. Szabat, and T. Orlowska-Kowalska, "Constrained model predictive control of the drive system with mechanical elasticity," *IEEE Trans. Ind. Electron.*, vol. 56, no. 6, pp. 1963–1973, Jun. 2009.

[66] Y. Hori, H. Iseki, and K. Sugiura, "Basic consideration of vibration suppression and disturbance rejection control of multi-inertia system using SFLAC (state feedback and load acceleration control)," *IEEE Trans. Ind. Appl.*, vol. 30, no. 4, pp. 889–896, Jul./Aug. 1994.

[67] G. Mandic, A. Nasiri, E. Muljadi, and F. Oyague, "Active torque control for gearbox load reduction in a variable speed wind turbine," accepted of publication in *IEEE Trans. Ind. Appl.*, 2012

[68] M.L. Buhl Jr., and A. Manjock, "A Comparison of Wind Turbine Aeroelastic Codes Used for Certification," 44th AIAA Aerospace Sciences Meeting and Exhibit Reno, NV, Jan., 2006.

[69] A. Miller, E. Muljadi, and D. S. Zinger, "A variable speed wind turbine power control," *IEEE Trans. Energy Convers*, vol. 12, no. 2, pp. 181–186, Jun. 1997.

[70] M. Chinchilla, S. Arnaltes, and J. C. Burgos, "Control of Permanent-Magnet Generators Applied to Variable-Speed Wind-Energy Systems Connected to the Grid," *IEEE Trans. Energy Convers.,* vol. 21, no. 1, pp. 130-135, Mar. 2006.

[71] R.Fadaeinedjad, M.Moallem, and G.Moschopoulos, "Simulation of a Wind Turbine With Doubly Fed Induction Generator by FAST and Simulink," *IEEE Trans. Energy Convers.,* vol. 23, no. 2, pp. 690-700, Jun. 2008.

[72] B. Beltran, T. Ahmed-Ali, and M.E.H. Benbouzid, "High-Order Sliding-Mode Control of Variable-Speed Wind Turbines," *IEEE Trans. Ind. Electron.,* vol. 59, no. 9, pp. 3314-3321, Sep. 2006.

[73] E.Koutroulis, and K.Kalaitzakis, "Design of a Maximum Power Tracking System for Wind-Energy-Conversion Applications," *IEEE Trans. Ind. Electron.,* vol. 53, no. 2, pp. 486-494, Apr. 2006.

[74] K.E. Johnson, "Adaptive Torque Control of Variable Speed Wind Turbines," Ph.D. thesis, University of Colorado, Boulder, CO, 2004.

[75] P.J. Moriarty and A.C. Hansen, "AeroDyn Theory Manual," NREL/EL-500-36881. Golden, CO: National Renewable Energy Laboratory, Dec. 2004.

[77] D.S. Zinger and E. Muljadi, "Annualized wind energy improvement using variable speeds," *IEEE Trans. Ind. Appl.*, vol.33, no.6, pp.1444-1447, Nov/Dec 1997.

[78] S. M. Muyeen, M. Hasan Ali, R. Takahashi, T. Murata, J. Tamura, Y. Tomaki, A. Sakahara, and E. Sasano, "Comparative study on transient stability analysis of wind turbine generator system using different drive train models," *IET Renew. Power Gener.*, vol. 1, no. 2, pp. 131–141, Jun. 2007.

[79] J. Carrasco, L. Franquelo, J. Bialasiewicz, E. Galvan, R. Guisado, M. Prats, J. Leon, and N. Moreno-Alfonso, "Power-electronic systems for the grid integration of renewable energy sources: A survey," *IEEE Trans. Ind. Electron.*, vol. 53, no. 4, pp. 1002–1016, Jun. 2006.

[80] Y. Chen, P. Pillay, and A. Khan, "PM wind generator topologies," *IEEE Trans. Ind. Appl.*, vol. 41, no. 6, pp. 1619–1626, Nov./Dec. 2005.

[81] P.W. Carlin, A.S. Laxson, and E.B. Muljadi, "The History and State of the Art of Variable-Speed Wind Turbine Technology," Technical Report NREL/TP-500-28607,NREL, Feb. 2001.

[82] E. Muljadi and C.P. Butterfield, "Pitch-controlled variable-speed wind turbine generation," *IEEE Trans. Ind. Appl.,* vol.37, no.1, pp.240-246, Jan/Feb 2001.

[83] G. Mandic, and A. Nasiri, "Modeling and simulation of a wind turbine system with ultracapacitors for short-term power smoothing," IEEE ISIE 2010, Bari, Italy, July 2010.

[84] O. Anaya-Lara, N. Jenkins, J. Ekanayake, P. Cartwright, M Hughes, *Wind Energy Generation : Modeling and Control.* John Wiley & Sons, 2009.

[85] B. J. Johnson, "State space based individual blade pitch control design for NREL 5MW wind turbine," Master's thesis, The University of Wisconsin-Milwaukee, May 2010.

[86] L. Zubieta and R. Bonert, "Characterization of double-layer capacitor (DLCs) for power electronics application," *IEEE Trans. Ind. Appl.*, vol. 36, no. 1, pp. 199–205, Jan./Feb. 2000.

[87] L. Shi, M. L. Crow, "Comparison of Ultracapacitor Electric Circuit Models," in *Proc. IEEE PES General Meeting*, pp. 1-6., Jul. 20-24., 2008.

[88] S. Buller, E. Karden, D. Kok and R.W. De Doncker, "Modeling the Dynamic Behavior of Supercapacitors Using Impedance Spectroscopy," *IEEE Trans. Ind. Applicat.*, vol. 38, no. 6, pp. 1622-1626, Nov/Dec 2002.

[89] T. Wei, X. Qi, and Z. Qi, "An Improved Ultracapacitor Equivalent Circuit Model for the Design of Energy Storage Power Systems," in *Proc.6th ICEMS*, pp. 69-73.,Oct. 8-11, 2007.

[90] A.Grama, L. Grama, D. Petreus, and C. Rusu, "Supercapacitor Modelling Using Experimental Measurements," in *Proc. ISSCS*, pp. 1-4., Jul. 9-10, 2009.

[91] W. Yang, J. E. Carletta, T. T. Hartley, and R. J. Veillette, "An ultracapacitor model derived using time-dependent current profiles," in *Proc. 51st MWSCAS*, pp. 726–729, Aug. 10–13, 2008.

[92] F. Belhachemi, S. Rael, B.Davat, "A physical based model of power electric double-layer supercapacitors," Proceeding of the IEEE Industry Applications Conference, Vol. 5, pp. 3069-3076, October 2000.

[93] V. Srinivasan, J.W. Weidner, "Mathematical Modelling of Electrochemical Capacitors", *Journal Electrochem Society*, Vol. 146 (1999), p.1650.

[94] N. Bertrand, O. Briat, J.-M. Vinassa, J. Sabatier, and H. El Brouji, "Porous electrode theory for ultracapacitor modeling and experimental validation," in *Proc. IEEE VPPC*, Sep. 3–5, 2008, pp. 1–6.

[95] N. Bertrand, J. Sabatier, O. Briat, and J. M. Vinassa, "Embedded Fractional Nonlinear Supercapacitor Model and Its Parametric Estimation Method," *IEEE Trans. Ind. Electron.,* vol. 57, no. 12, pp. 3991-4000, Dec. 2010.

[96] J. N. Marie-Francoise, H. Gualous, A. Berthon, "Supercapacitor thermal- and electrical-behaviour modelling using ANN," IEEE Proc. on Electric Power Applications, Vol. 153, pp. 255-262, March 2006.

[97] E. Manla, G. Mandic, and A. Nasiri, "Testing and Modeling of Lithium-ion Ultracapacitors" in Proc. *IEEE Energy Conversion Congress and Exposition (ECCE),* pp.2957-2962, 17-22 Sep. 2011.

[98] F. Blaabjerg, R. Teodorescu, M. Liserre, and A.V. Timbus, "Overview of Control and Grid Synchronization for Distributed Power Generation Systems," , *IEEE Trans. Ind. Electrn.*, vol.53, no.5, pp.1398-1409, Oct. 2006.

[99] A. V. Timbus,M. Liserre, R. Teodorescu, and F. Blaabjerg, "Synchronization methods for three phase distributed power generation systems. An overview and evaluation," in *Proc. IEEE PESC*, pp. 2474–2481, 2005.

[100] S.-K. Chung , "Phase-locked loop for grid-connected three-phase power conversion systems," *IEE Proc. Electric Power Applications, - ,* vol.147, no.3, pp.213-219, May 2000.

[101] M. Malinowski and S. Bernet, "A simple sensorless active damping scheme for three-phase PWM converters with an LCL filter," *IEEE Trans. Ind. Electron.,* vol. 55, no. 4, pp 1876-1880, Apr. 2008.

[102] V. Blasko and V. Kaura, "A novel control to actively damp resonance in input LC filter of a three-phase voltage source converter," *IEEE Trans. Ind. Applicat.,* vol. 33, no. 2, pp. 542-550, Mar./Apr. 1997.

[103] M. P. Kazmierkowski and L. Malesani, "Current control techniques for three-phase voltage source PWM converters: A survey," *IEEE Trans. Ind. Electron.,* vol. 45, no. 5, pp. 691–703, Oct. 1998.

[104] J. Dannehl, C. Wessels, and F. W. Fuchs, "Limitations of voltage-oriented PI current control of grid-connected PWM rectifiers with LCL filters," *IEEE Trans. Ind. Electron.,* vol. 56, no. 2, pp 380-388, Feb. 2009.

[105] D.G. Holmes and T.A. Lipo, *Pulse Width Modulation for Power Converter,* IEEE Press, 2003.

APPENDIX A: Space vector pulse width modulation
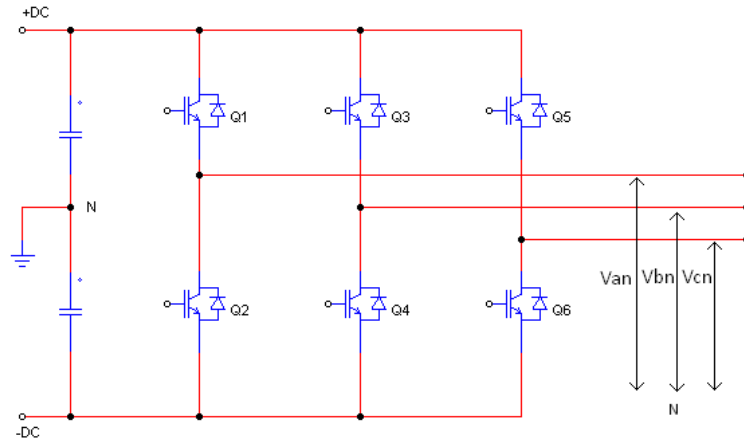
Figure A.1. A three phase DC/AC converter

Schematic diagram of a three phase DC/AC (or AC/DC) converter is shown in figure A.1. Transistors Q1-Q6 are operated as switches by applying gate voltages. Each phase terminals can be connected either to +DC or -DC pole of the DC link. Transistors in the same branch, called a phase leg, must not conduct at the same time. The switching state of the lower three transistors (Q2, Q4, and Q6) is always complement of the corresponding upper transistor. Therefore, there are total 8 switching states that are allowed. By applying PWM technique, it is possible to generate any waveform, including the sinusoidal which is of the main interest. The following table summarizes phase voltages in each possible switching state.

	Q1	Q3	Q5	V_{AN}	V_{BN}	V_{CN}	$V_{\alpha n}$	$V_{\beta n}$
V0	0	0	0	0	0	0	0	0
V1	1	0	0	$\frac{2}{3}V_{DC}$	$-\frac{1}{3}V_{DC}$	$-\frac{1}{3}V_{DC}$	$\frac{2}{3}V_{DC}$	0
V2	1	1	0	$\frac{1}{3}V_{DC}$	$\frac{1}{3}V_{DC}$	$-\frac{2}{3}V_{DC}$	$\frac{1}{3}V_{DC}$	$\frac{\sqrt{3}}{3}V_{DC}$
V3	0	1	0	$-\frac{1}{3}V_{DC}$	$\frac{2}{3}V_{DC}$	$-\frac{1}{3}V_{DC}$	$-\frac{1}{3}V_{DC}$	$\frac{\sqrt{3}}{3}V_{DC}$
V4	0	1	1	$-\frac{2}{3}V_{DC}$	$\frac{1}{3}V_{DC}$	$\frac{1}{3}V_{DC}$	$-\frac{2}{3}V_{DC}$	0
V5	0	0	1	$-\frac{1}{3}V_{DC}$	$-\frac{1}{3}V_{DC}$	$\frac{2}{3}V_{DC}$	$-\frac{1}{3}V_{DC}$	$-\frac{\sqrt{3}}{3}V_{DC}$
V6	1	0	1	$\frac{1}{3}V_{DC}$	$-\frac{2}{3}V_{DC}$	$\frac{1}{3}V_{DC}$	$\frac{1}{3}V_{DC}$	$-\frac{\sqrt{3}}{3}V_{DC}$
V7	1	1	1	0	0	0	0	0

By applying a three phase to equivalent two phase (αβ) coordinate transformation, voltages in alpha beta reference frame are calculated and listed in last two columns in the table.

$$\begin{bmatrix} V_\alpha \\ V_\beta \end{bmatrix} = \frac{2}{3} \cdot \begin{bmatrix} 1 & -\frac{1}{2} & -\frac{1}{2} \\ 0 & \frac{\sqrt{3}}{2} & -\frac{\sqrt{3}}{2} \end{bmatrix} \cdot \begin{bmatrix} V_a \\ V_b \\ V_c \end{bmatrix}$$

Two axes of the alpha-beta reference frame are ninety degrees apart. The vector diagram of the terminal voltage in alpha-beta coordinates is shown in figure A.2. If switching control of the transistors only applies vectors V1 to V6 in sequence, with equal duration the well known six-step voltage waveforms are generated [105]. Six-step switching is equivalent to rotation of the voltage vector in alpha-beta plane on figure A.2, where voltage vector rotate in discrete steps from one switching vector to another.
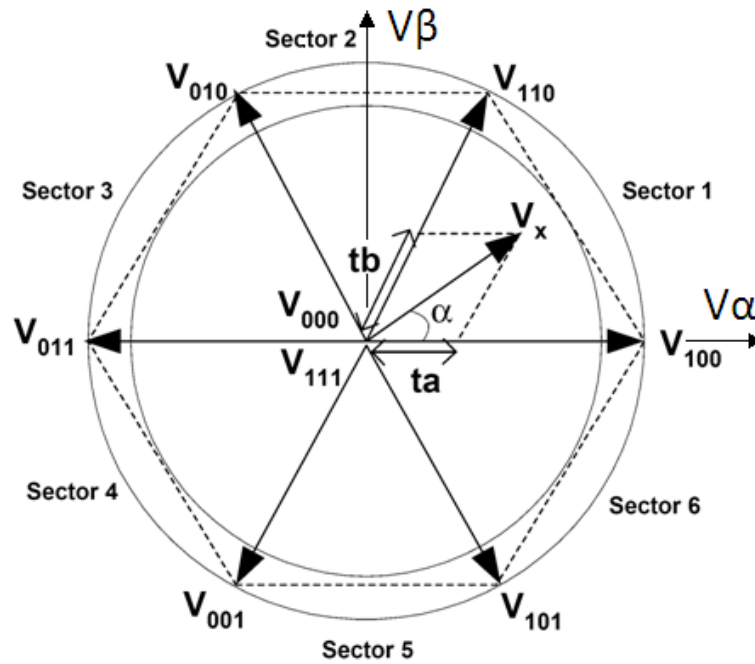
Figure A. 2. Voltage vectors of a three phase converter

The method to generate any arbitrary voltage vector within the interior circle inside the hexagon defined by switching vector is called Space-Vector Pulse Width Modulation (SVPWM). SVPWM is widely used in modern three phase power converters and it is adopted as a switching strategy for both converters of the wind turbine double conversion system described in this thesis. The main principle of SVPWM is to apply adjacent switching vectors, for a fraction of a switching cycle, to generate equivalent voltage vector Vx inside a sector defined by the switching voltage vectors. Target voltage vector rotates in the desired direction with desired rotational speed that corresponds to the output voltage frequency. Amplitude of the voltage vector can also be controlled resulting in a power converter with fully controllable three phase voltage and frequency. Higher level control system has to provide target alpha and beta voltage components, and SWPWM modulator determines switching sequence for each switching cycle. Durations

of vectors V1 (V100) and V2 (V110) on figure A.2. are ta and tb. These time intervals are calculated by using the following formulas:

$$T_a = \frac{V_{\max LN}}{V_X} \cdot \sin\left(\frac{\pi}{3} - \alpha\right)$$ (1)

$$T_b = \frac{V_{\max LN}}{V_X} \cdot \sin(\alpha)$$ (2)

The difference between the switching cycle Ts and sum of time durations of switching vector is a period of time when either all switches are on or off (vectors V000 and V111). During these periods voltage on all three phases is equal to zero. This period of time is called zero sequence.

$$t_0 = T_S - T_a - T_b$$ (3)

The maximum amplitude of the voltage vector is equal to the radius of the interior circle of the hexagon :

$$V_{\max LN} = \frac{2}{3} \cdot V_{DC} \cdot \frac{\sqrt{3}}{2} = \frac{V_{DC}}{\sqrt{3}}$$ (4)

The maximum voltage of the output line to neutral voltage for sine triangular PWM is one half of the DC link voltage. Therefore, the SVPWM allows higher output voltage then sine triangular PWM with the same DC link voltage. This is the main advantage of the SVPWM. SVPWM also allows flexible placement of voltage vectors and zero sequence intervals within the switching cycle. One of the most widely used method is called symmetrical SVPWM, and the principle of the voltage vector distribution within the switching cycle is shown in figure A.3.
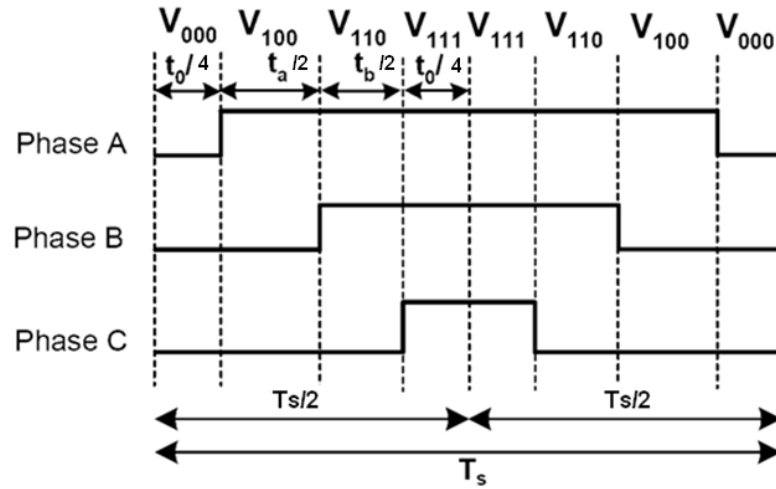
Figure A.3. Symmetrical SVPWM

The symmetrical SVPWM minimizes switching transitions between therefore minimizing switching losses in the transistors of the three phase converter. It also results in reduced voltage harmonics of the output voltage. For practical application of the SVPWM, the last step is to calculate the duration times of conducting for each transistor in every phase leg of the three phase converter. Following table summarizes the time durations for each sector in the figure A.2.

Table A.2.

Sector	1	2	3	4	5	6
TQ1	$t_0/2$	$T_b + t_0/2$	$T_s - t_0/2$	$T_s - t_0/2$	$T_a + t_0/2$	$t_0/2$
TQ3	$T_a + t_0/2$	$t_0/2$	$t_0/2$	$T_b + t_0/2$	$T_s - t_0/2$	$T_s - t_0/2$
TQ5	$T_s - t_0/2$	$T_s - t_0/2$	$T_a + t_0/2$	$t_0/2$	$t_0/2$	$T_b + t_0/2$

Time intervals TQ1, TQ3, and TQ5 are intervals during which upper transistors in the power converter are conducting during each switching cycle. The implementation of SVPWM that would use the table A.2 would be very complex, due to time interval

calculation dependence on the sector in alpha-beta plane. It is shown in literature [105] that SVPWM equivalent voltage waveform can be generated by addition of the offset voltage to each phase voltage reference for PWM modulator. This offset reference for the case of symmetrical SVPWM is [105]:

$$V_{offset} = -\frac{\max(V_{an}^*, V_{bn}^*, V_{cn}^*) + \min(V_{an}^*, V_{bn}^*, V_{cn}^*)}{2}$$

(5)

Functions min and max return minimum and maximum values of three voltage references $V_{an}^*, V_{bn}^*, V_{cn}^*$. The offset voltage is called the zero sequence voltage, due to its role in placing time intervals when output voltages are equal to zero within the switching cycle. Finally, voltage references for the PWM modulator become:

$$V_a = V_{an}^* + V_{offset}$$

(6)

$$V_b = V_{bn}^* + V_{offset}$$

(7)

$$V_c = V_{cn}^* + V_{offset}$$

(8)

Simulink block of the zero sequence offset voltage addition to the voltage references for a power converter is shown in figure A.4.
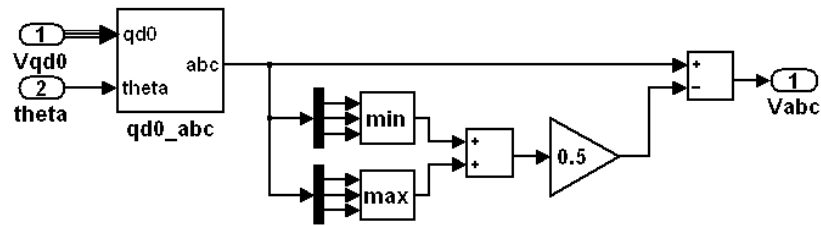
Figure A.4. Zero sequence voltage addition for SVPWM

APPENDIX B: Wind profile A1 – TurbSim input file

TurbSim Input File. Valid for TurbSim v1.50, 25-Sep-2009

---------Runtime Options----------------------------------
531274928   RandSeed1   - First random seed (-2147483648 to 2147483647)
-84236723   RandSeed2   - Second random seed (-2147483648 to 2147483647) for intrinsic pRNG, or an alternative pRNG: "RanLux" or "RNSNLW"
False   WrBHHTP   - Output hub-height turbulence parameters in binary form? (Generates RootName.bin)
True   WrFHHTP   - Output hub-height turbulence parameters in formatted form? (Generates RootName.dat)
False   WrADHH   - Output hub-height time-series data in AeroDyn form? (Generates RootName.hh)
False   WrADFF   - Output full-field time-series data in TurbSim/AeroDyn form? (Generates Rootname.bts)
True   WrBLFF   - Output full-field time-series data in BLADED/AeroDyn form? (Generates RootName.wnd)
False   WrADTWR   - Output tower time-series data? (Generates RootName.twr)
False   WrFMTFF   - Output full-field time-series data in formatted (readable) form? (Generates RootName.u, RootName.v, RootName.w)
False   WrACT   - Output coherent turbulence time steps in AeroDyn form? (Generates RootName.cts)
True   Clockwise   - Clockwise rotation looking downwind? (used only for full-field binary files - not necessary for AeroDyn)
 0   ScaleIEC   - Scale IEC turbulence models to exact target standard deviation? [0=no additional scaling; 1=use hub scale uniformly; 2=use individual scales]

--------Turbine/Model Specifications-----------------------
9   NumGrid_Z   - Vertical grid-point matrix dimension
9   NumGrid_Y   - Horizontal grid-point matrix dimension
0.05   TimeStep   - Time step [seconds]
800   AnalysisTime   - Length of analysis time series [seconds] (program will add time if necessary: AnalysisTime = MAX(AnalysisTime, UsableTime+GridWidth/MeanHHWS))
630   UsableTime   - Usable length of output time series [seconds] (program will add GridWidth/MeanHHWS seconds)
54.8   HubHt   - Hub height [m] (should be > 0.5*GridHeight)
60.00   GridHeight   - Grid height [m]
60.00   GridWidth   - Grid width [m] (should be >= 2*(RotorRadius+ShaftLength))
0   VFlowAng   - Vertical mean flow (uptilt) angle [degrees]
0   HFlowAng   - Horizontal mean flow (skew) angle [degrees]

--------Meteorological Boundary Conditions-------------------
"IECKAI"   TurbModel   - Turbulence model ("IECKAI"=Kaimal, "IECVKM"=von Karman, "GP_LLJ", "NWTCUP", "SMOOTH", "WF_UPW", "WF_07D", "WF_14D", or "NONE")
"3"   IECstandard   - Number of IEC 61400-x standard (x=1,2, or 3 with optional 61400-1 edition number (i.e. "1-Ed2"))
"B"   IECturbc   - IEC turbulence characteristic ("A", "B", "C" or the turbulence intensity in percent) ("KHTEST" option with NWTCUP model, not used for other models)
"NTM"   IEC_WindType   - IEC turbulence type ("NTM"=normal, "xETM"=extreme turbulence, "xEWM1"=extreme 1-year wind, "xEWM50"=extreme 50-year wind, where x=wind turbine class 1, 2, or 3)
default   ETMc   - IEC Extreme Turbulence Model "c" parameter [m/s]

default   WindProfileType - Wind profile type ("JET","LOG"=logarithmic,"PL"=power law,"IEC"=PL on rotor disk,LOG elsewhere, or "default")
54.8   RefHt   - Height of the reference wind speed [m]
10.0   URef   - Mean (total) wind speed at the reference height [m/s] (or "default" for JET wind profile)
default   ZJetMax   - Jet height [m] (used only for JET wind profile, valid 70-490 m)
default   PLExp   - Power law exponent [-] (or "default")
default   Z0   - Surface roughness length [m] (or "default")

--------Non-IEC Meteorological Boundary Conditions------------
default   Latitude   - Site latitude [degrees] (or "default")
0.05   RICH_NO   - Gradient Richardson number
default   UStar   - Friction or shear velocity [m/s] (or "default")
default   ZI   - Mixing layer depth [m] (or "default")
default   PC_UW   - Hub mean u'w' Reynolds stress (or "default")
default   PC_UV   - Hub mean u'v' Reynolds stress (or "default")
default   PC_VW   - Hub mean v'w' Reynolds stress (or "default")
default   IncDec1   - u-component coherence parameters (e.g. "10.0 0.3e-3" in quotes) (or "default")
default   IncDec2   - v-component coherence parameters (e.g. "10.0 0.3e-3" in quotes) (or "default")
default   IncDec3   - w-component coherence parameters (e.g. "10.0 0.3e-3" in quotes) (or "default")
default   CohExp   - Coherence exponent (or "default")

--------Coherent Turbulence Scaling Parameters-------------------
"M:\coh_events\eventdata" CTEventPath   - Name of the path where event data files are located
"Random"   CTEventFile   - Type of event files ("LES", "DNS", or "RANDOM")
true   Randomize   - Randomize the disturbance scale and locations? (true/false)
 1.0   DistScl   - Disturbance scale (ratio of wave height to rotor disk). (Ignored when Randomize = true.)
 0.5   CTLy   - Fractional location of tower centerline from right (looking downwind) to left side of the dataset. (Ignored when Randomize = true.)
 0.5   CTLz   - Fractional location of hub height from the bottom of the dataset. (Ignored when Randomize = true.)
30.0   CTStartTime   - Minimum start time for coherent structures in RootName.cts [seconds]

APPENDIX C: Wind profile A2 – TurbSim input file

TurbSim Input File. Valid for TurbSim v1.50, 25-Sep-2009

---------Runtime Options----------------------------------
23967284   RandSeed1   - First random seed (-2147483648 to 2147483647)
-6578942   RandSeed2   - Second random seed (-2147483648 to 2147483647) for intrinsic pRNG,
or an alternative pRNG: "RanLux" or "RNSNLW"
False   WrBHHTP   - Output hub-height turbulence parameters in binary form? (Generates
RootName.bin)
False   WrFHHTP   - Output hub-height turbulence parameters in formatted form? (Generates
RootName.dat)
False   WrADHH   - Output hub-height time-series data in AeroDyn form? (Generates
RootName.hh)
False   WrADFF   - Output full-field time-series data in TurbSim/AeroDyn form? (Generates
Rootname.bts)
True   WrBLFF   - Output full-field time-series data in BLADED/AeroDyn form? (Generates
RootName.wnd)
False   WrADTWR   - Output tower time-series data? (Generates RootName.twr)
False   WrFMTFF   - Output full-field time-series data in formatted (readable) form?
(Generates RootName.u, RootName.v, RootName.w)
False   WrACT   - Output coherent turbulence time steps in AeroDyn form? (Generates
RootName.cts)
True   Clockwise   - Clockwise rotation looking downwind? (used only for full-field binary files
- not necessary for AeroDyn)
 0   ScaleIEC   - Scale IEC turbulence models to exact target standard deviation? [0=no
additional scaling; 1=use hub scale uniformly; 2=use individual scales]

--------Turbine/Model Specifications-----------------------
9   NumGrid_Z   - Vertical grid-point matrix dimension
9   NumGrid_Y   - Horizontal grid-point matrix dimension
0.05   TimeStep   - Time step [seconds]
800   AnalysisTime   - Length of analysis time series [seconds] (program will add time if
necessary: AnalysisTime = MAX(AnalysisTime, UsableTime+GridWidth/MeanHHWS))
630   UsableTime   - Usable length of output time series [seconds] (program will add
GridWidth/MeanHHWS seconds)
54.8   HubHt   - Hub height [m] (should be > 0.5*GridHeight)
60.00   GridHeight   - Grid height [m]
60.00   GridWidth   - Grid width [m] (should be >= 2*(RotorRadius+ShaftLength))
0   VFlowAng   - Vertical mean flow (uptilt) angle [degrees]
0   HFlowAng   - Horizontal mean flow (skew) angle [degrees]

--------Meteorological Boundary Conditions-------------------
"IECKAI"   TurbModel   - Turbulence model ("IECKAI"=Kaimal, "IECVKM"=von Karman,
"GP_LLJ", "NWTCUP", "SMOOTH", "WF_UPW", "WF_07D", "WF_14D", or "NONE")
"3"   IECstandard   - Number of IEC 61400-x standard (x=1,2, or 3 with optional 61400-1 edition
number (i.e. "1-Ed2"))
"B"   IECturbc   - IEC turbulence characteristic ("A", "B", "C" or the turbulence intensity in
percent) ("KHTEST" option with NWTCUP model, not used for other models)
"NTM"   IEC_WindType   - IEC turbulence type ("NTM"=normal, "xETM"=extreme turbulence,
"xEWM1"=extreme 1-year wind, "xEWM50"=extreme 50-year wind, where x=wind turbine class 1, 2, or
3)
default   ETMc   - IEC Extreme Turbulence Model "c" parameter [m/s]

default   WindProfileType - Wind profile type ("JET","LOG"=logarithmic,"PL"=power law,"IEC"=PL on rotor disk,LOG elsewhere, or "default")
54.8   RefHt   - Height of the reference wind speed [m]
10.0   URef   - Mean (total) wind speed at the reference height [m/s] (or "default" for JET wind profile)
default   ZJetMax   - Jet height [m] (used only for JET wind profile, valid 70-490 m)
default   PLExp   - Power law exponent [-] (or "default")
default   Z0   - Surface roughness length [m] (or "default")

--------Non-IEC Meteorological Boundary Conditions------------
default   Latitude   - Site latitude [degrees] (or "default")
0.05   RICH_NO   - Gradient Richardson number
default   UStar   - Friction or shear velocity [m/s] (or "default")
default   ZI   - Mixing layer depth [m] (or "default")
default   PC_UW   - Hub mean u'w' Reynolds stress (or "default")
default   PC_UV   - Hub mean u'v' Reynolds stress (or "default")
default   PC_VW   - Hub mean v'w' Reynolds stress (or "default")
default   IncDec1   - u-component coherence parameters (e.g. "10.0   0.3e-3" in quotes) (or "default")
default   IncDec2   - v-component coherence parameters (e.g. "10.0   0.3e-3" in quotes) (or "default")
default   IncDec3   - w-component coherence parameters (e.g. "10.0   0.3e-3" in quotes) (or "default")
default   CohExp   - Coherence exponent (or "default")

--------Coherent Turbulence Scaling Parameters-------------------
"M:\coh_events\eventdata" CTEventPath   - Name of the path where event data files are located
"Random"   CTEventFile   - Type of event files ("LES", "DNS", or "RANDOM")
true   Randomize   - Randomize the disturbance scale and locations? (true/false)
 1.0   DistScl   - Disturbance scale (ratio of wave height to rotor disk). (Ignored when Randomize = true.)
 0.5   CTLy   - Fractional location of tower centerline from right (looking downwind) to left side of the dataset. (Ignored when Randomize = true.)
 0.5   CTLz   - Fractional location of hub height from the bottom of the dataset. (Ignored when Randomize = true.)
30.0   CTStartTime   - Minimum start time for coherent structures in RootName.cts [seconds]

APPENDIX D: Wind profile B – TurbSim input file

TurbSim Input File. Valid for TurbSim v1.50, 25-Sep-2009

---------Runtime Options-----------------------------------
231853901   RandSeed1   - First random seed (-2147483648 to 2147483647)
-568021329   RandSeed2   - Second random seed (-2147483648 to 2147483647) for intrinsic pRNG,
or an alternative pRNG: "RanLux" or "RNSNLW"
False   WrBHHTP   - Output hub-height turbulence parameters in binary form? (Generates
RootName.bin)
True   WrFHHTP   - Output hub-height turbulence parameters in formatted form? (Generates
RootName.dat)
False   WrADHH   - Output hub-height time-series data in AeroDyn form? (Generates
RootName.hh)
False   WrADFF   - Output full-field time-series data in TurbSim/AeroDyn form? (Generates
Rootname.bts)
True   WrBLFF   - Output full-field time-series data in BLADED/AeroDyn form? (Generates
RootName.wnd)
False   WrADTWR   - Output tower time-series data? (Generates RootName.twr)
False   WrFMTFF   - Output full-field time-series data in formatted (readable) form?
(Generates RootName.u, RootName.v, RootName.w)
False   WrACT   - Output coherent turbulence time steps in AeroDyn form? (Generates
RootName.cts)
True   Clockwise   - Clockwise rotation looking downwind? (used only for full-field binary files
- not necessary for AeroDyn)
 0   ScaleIEC   - Scale IEC turbulence models to exact target standard deviation? [0=no
additional scaling; 1=use hub scale uniformly; 2=use individual scales]

--------Turbine/Model Specifications-----------------------
9   NumGrid_Z   - Vertical grid-point matrix dimension
9   NumGrid_Y   - Horizontal grid-point matrix dimension
0.05   TimeStep   - Time step [seconds]
800   AnalysisTime   - Length of analysis time series [seconds] (program will add time if
necessary: AnalysisTime = MAX(AnalysisTime, UsableTime+GridWidth/MeanHHWS))
630   UsableTime   - Usable length of output time series [seconds] (program will add
GridWidth/MeanHHWS seconds)
54.8   HubHt   - Hub height [m] (should be > 0.5*GridHeight)
60.00   GridHeight   - Grid height [m]
60.00   GridWidth   - Grid width [m] (should be >= 2*(RotorRadius+ShaftLength))
0   VFlowAng   - Vertical mean flow (uptilt) angle [degrees]
0   HFlowAng   - Horizontal mean flow (skew) angle [degrees]

--------Meteorological Boundary Conditions------------------
"IECKAI"   TurbModel   - Turbulence model ("IECKAI"=Kaimal, "IECVKM"=von Karman,
"GP_LLJ", "NWTCUP", "SMOOTH", "WF_UPW", "WF_07D", "WF_14D", or "NONE")
"3"   IECstandard   - Number of IEC 61400-x standard (x=1,2, or 3 with optional 61400-1 edition
number (i.e. "1-Ed2"))
"A"   IECturbc   - IEC turbulence characteristic ("A", "B", "C" or the turbulence intensity in
percent) ("KHTEST" option with NWTCUP model, not used for other models)
"3ETM"   IEC_WindType   - IEC turbulence type ("NTM"=normal, "xETM"=extreme turbulence,
"xEWM1"=extreme 1-year wind, "xEWM50"=extreme 50-year wind, where x=wind turbine class 1, 2, or
3)

default ETMc - IEC Extreme Turbulence Model "c" parameter [m/s]

default   WindProfileType - Wind profile type ("JET","LOG"=logarithmic,"PL"=power law,"IEC"=PL on rotor disk,LOG elsewhere, or "default")

54.8 RefHt - Height of the reference wind speed [m]

8.0   URef - Mean (total) wind speed at the reference height [m/s] (or "default" for JET wind profile)

default ZJetMax - Jet height [m] (used only for JET wind profile, valid 70-490 m)

default PLExp - Power law exponent [-] (or "default")

default Z0 - Surface roughness length [m] (or "default")

--------Non-IEC Meteorological Boundary Conditions------------

default Latitude - Site latitude [degrees] (or "default")

0.05 RICH_NO - Gradient Richardson number

default UStar - Friction or shear velocity [m/s] (or "default")

default ZI - Mixing layer depth [m] (or "default")

default PC_UW - Hub mean u'w' Reynolds stress (or "default")

default PC_UV - Hub mean u'v' Reynolds stress (or "default")

default PC_VW - Hub mean v'w' Reynolds stress (or "default")

default IncDec1 - u-component coherence parameters (e.g. "10.0 0.3e-3" in quotes) (or "default")

default IncDec2 - v-component coherence parameters (e.g. "10.0 0.3e-3" in quotes) (or "default")

default IncDec3 - w-component coherence parameters (e.g. "10.0 0.3e-3" in quotes) (or "default")

default CohExp - Coherence exponent (or "default")

--------Coherent Turbulence Scaling Parameters-------------------

"M:\coh_events\eventdata" CTEventPath - Name of the path where event data files are located

"Random" CTEventFile - Type of event files ("LES", "DNS", or "RANDOM")

true Randomize - Randomize the disturbance scale and locations? (true/false)

1.0 DistScl - Disturbance scale (ratio of wave height to rotor disk). (Ignored when Randomize = true.)

0.5 CTLy - Fractional location of tower centerline from right (looking downwind) to left side of the dataset. (Ignored when Randomize = true.)

0.5 CTLz - Fractional location of hub height from the bottom of the dataset. (Ignored when Randomize = true.)

30.0 CTStartTime - Minimum start time for coherent structures in RootName.cts [seconds]

CURRICULUM VITAE

Goran Mandic

EDUCATION
University of Belgrade, Serbia
Dipl. Ing. Degree in Electrical Engineering, December 2004
- Area of concentration: Power Electronics and Electric Drives
- Thesis title : Digital electric drive controller based on an intelligent power module and ATmega8 microcontroller

PROFESSIONAL ENGINEERING EXPERIENCE

Eaton Corporation, Raleigh, North Carolina, USA
<u>Lead Electrical Engineer</u>, November 2011-present
- Responsible for firmware development for new lines of high power three phase uninterruptible power supplies
- Control system design for three phase multi level inverters and rectifiers
- Embedded software development in C++
- Modeling and simulation of complex power conversion systems
- Research and development of parallel power conversion topologies and control algorithms

Electrical Engineering Institute "Nikola Tesla", Belgrade, Serbia
<u>Engineer</u>, February 2005- January 2008
- Worked in a team of engineers responsible for development, design, deployment, and maintenance of field excitation controllers for synchronous generators in several power plants in Serbia.
- Designed an embedded data acquisition system with human-machine interface for field excitation controller of a 300MW synchronous generator. The system has been in operation for over three years in a power plant.
- Developed a DSP based universal controller board for the Institute's next generation of embedded controllers for power converters. Designed a multi-layer mixed-signal printed circuit board using OrCAD. Tested the prototype and wrote test functions in C programming language. The board has been in use as a control platform of an electrostatic precipitator (ESP) in a power plant.
- Worked on several other projects that included PLC and microcontroller programming.

RESEARCH EXPERIENCE
University of Wisconsin-Milwaukee, College of Engineering & Applied Sciences, Department of Electrical Engineering
<u>Research Assistant</u>, January 2008 – December 2011

- Work on the research project funded by U.S. Department of Energy. Grid integration of wind turbines combined with ultracapacitor energy storage and full rated power conversion.
- Developed control algorithms for power smoothing and active vibration damping in the turbine's drivetrain
- Conduct modeling, simulation, prototype building, and experimental verification of developed power conversion topology and control algorithms. Power conversion topology includes a three phase active PWM rectifier and a grid connected three phase PWM inverter in a full rated back-to-back configuration. Designed controllers for the rectifier and inverter for active and reactive power control and DC bus voltage control.
- Extensive use of Matlab/Simulink, LabView, and PSIM
- Rapid prototyping hardware tools used: dSPACE and National Instruments CompactRIO embedded controller

University of Belgrade, School of Electrical Engineering, Laboratory for Digital Control of Electric Drives, Belgrade, Serbia
Lab Assistant, June 2004-July 2005

- Member of a student team at the International Future Energy Challenge 2005. Worked on hardware and software design of a microcontroller based low-cost electric motor drive. Implemented Space Vector PWM modulation algorithm and control and protection routines on a low-cost microcontroller in C programming language. The team built the prototype that won the first place on the competition that took place in Chicago, IL in 2005
- Developed and built prototype of a 1kW electric motor drive based on integrated power module and Motorola/Freescale DSP56F801 processor. Wrote hardware abstraction layer in C programming language for simplified I/O programming. Implemented Space-Vector PWM algorithm, protection routines, and speed control algorithm based on voltage/frequency constant ratio. Designed a mixed signal printed circuit board

AWARDS

- University of Wisconsin-Milwaukee Research Foundation: Research Fellowship Award (2009-2010)
- University of Wisconsin-Milwaukee: Chancellor's Graduate Student Award
- University of Wisconsin-Milwaukee: Graduate Student Travel Award (2011)
- International Future Energy Challenge 2005: <u>First Place</u>. IEEE sponsored student competition that took place in Chicago, Il, August 2005.

MEMBERSHIPS
IEEE Industrial Electronics, Power Electronics, and Control Systems Societies

PUBLICATIONS

G. Mandic, A. Nasiri, E. Muljadi, and F. Oyague, "Active torque control for gearbox load reduction in a variable speed wind turbine," accepted of publication in IEEE Trans. Ind. Appl., 2012

G. Mandic, and A. Nasiri, "Modeling and simulation of a wind turbine system with ultracapacitors for short-term power smoothing," IEEE ISIE 2010, July 2010, Bari, Italy.

G. Mandic, A. Nasiri, and E. Muljadi, "Mechanical Stress Reduction on the Gearbox of the Variable Speed Wind Turbines," WindPower 2011, May 2011, Anaheim, CA.

E. Manla, G. Mandic, and A. Nasiri, "Testing and Modeling of Lithium-ion Ultracapacitors," IEEE Energy Conversion Congress & Exposition 2011, September 2011, Phoenix, AZ.

A. Nasiri, S. A. Zabalawi, and G. Mandic, "Indoor Power Harvesting Using Photovoltaic Cells for Low-Power Applications," IEEE Transactions on Industrial Electronics, Vol. 56, Issue 11, Nov. 2009, pp. 4502 – 4509.

A. Abedini, G. Mandic, and A. Nasiri, "Wind power smoothing using rotor inertia aimed at reducing grid susceptibility," Int. J. of Power Electronics, vol. 1, no. 2, pp. 227 - 247, 2008.